Citation: Turley, A. J. (1977). Mathematical modelling and computer-aided design of diaphragms and capsules for instrument transducers. (Unpublished Doctoral thesis, The City University)

MATHEMATICAL MODELLING AND COMPUTER-AIDED DESIGN OF DIAPHRAGMS AND CAPSULES FOR INSTRUMENT TRANSDUCERS

Alan J. Turley

A Thesis submitted for the Degree of
Doctor of Philosophy

The City University, London
Department of Systems Science

December, 1977

CONTENTS

Chapter 6.0 The Design of Corrugated Diaphragms and Capsules 223

Chapter 7.0 Conclusions 274

ACKNOWLEDGEMENTS

The Author and the Instrument Systems Centre, The City University wish to express their grateful thanks to KDG Instruments Ltd., Rustington, West Sussex, for their financial support throughout this project.

The Author wishes to express particular thanks to [redacted] [redacted] [redacted] (Technical Director, KDG Instruments Ltd.) without whom the work would not have been attempted, and his project supervisors, Dr. F. Abdullah and Professor L. Finkelstein for their continual guidance throughout the project.

Thanks are also due to the staff at KDG Instruments Ltd. for their help especially [redacted] [redacted] [redacted] and [redacted] [redacted] [redacted] who helped type and prepare the thesis.

Thanks also to [redacted] [redacted] [redacted] who typed the final copy.

ABSTRACT

Mathematical models have been developed for the purpose of analysis and design of corrugated diaphragms and capsules. The models based on the geometric and material properties are presented as computer programs, and are therefore powerful tools for replacing the largely empirical design techniques previously employed.

The equations are based on thin elastic shell theory and are solved by a fast finite difference approximation. Both the linear and non-linear solutions have been found and validated against experimental results.

The linear model is also used to predict the fundamental natural frequency of both diaphragms and capsule using a standard energy method (Rayleigh's method) and by a technique based on the dynamic deflection curve.

A systematic approach to design has been adopted and the possible applications detailed; two industrial design problems were tackled and one, the design of a nesting capsule, was successfully followed through to a finished product.

1.0 Introduction

This thesis is concerned with the development and application of mathematical models to the design of elastic deformation elements.

One of the most common instrument elements after the ordinary coil type spring is the diaphragm element, used mainly for measuring pressure, but, unlike a spring, diaphragm analysis and design has been a very empirical science, described by some as almost a "black art". The reason for this is the geometrical complexity of such elements and the non-existence of analytically tractable design formulae. The few formulae that have been developed are of very limited validity. The availability of fast digital computers has enabled a fresh computer-aided design approach to be made for practical problems where corrugated diaphragms or diaphragm capsules are used. In the thesis computer models are developed and validated and novel design procedures are proposed and implemented; thus removing the empiricism in design.

The use of computers, particularly digital computers, for design, is now common practice in many branches of Engineering, so much so that realistic and complex mathematical models are often constructed for systems and components of systems; and these are tested for desired characteristics prior to any hardware construction.

The use of mathematical models, both for description and design, is particularly widespread in the fields of communication and control. This approach is not widely used for the description and design of instrument transducers; most books on instruments provide a descriptive catalogue with scant information on design and design principles. In recent years attempts have been made at the Instrument Systems Centre (the author's institution) to remedy this situation by exploring the feasability of using mathematical models for both teaching and research into design. It has been found that mathematical modelling can be conveniently divided into two types: functional and physical (IMEKO paper, appendix V).

Functional models are black box models which present the mathematical functional relation between input and output variables without reference to the construction of the instrument or instrument components. The functional relationship may be determined by experiment or some physical model. Functional models of complete instruments may be derived from functional models of their components together with the manner of interconnection. Such models can be used for prediction of static, dynamic and disturbance responses and would be useful for early system design as well as for later diagnostic use. The required functional relationship of an instrument is often a simple linear one.

Physical models are models which describe the functional characteristics in terms of geometrical features and material properties. Thus for a diaphragm used as pressure sensor, in a displacement model, such a model would predict the pressure deflection functional characteristic in terms of geometrical features (diameter and thickness, number and shape of corrugations, etc.) and the material properties (Young's modulus, Poisson's ratio).

It is with this Physical modelling that this thesis is concerned. Zographos ref. (1) has considered the functional modelling of a complex differential pressure transducer and Abdullah (Appendix V) has refined and concluded the work, by showing that such modelling can adequately predict system behaviour.

1.1 Corrugated diaphragms and capsules

A corrugated metal diaphragm is a disc which has had axisymmetric, concentric ridges pressed into it by a forming process. The device is usually restrained at the outer edge by welding or soldering around the periphery; it is then able to sense a pressure difference and convert it into a displacement. This displacement is generally measured at the centre of the device, shown by (w) in the schematic diagram, Figure 1.1.

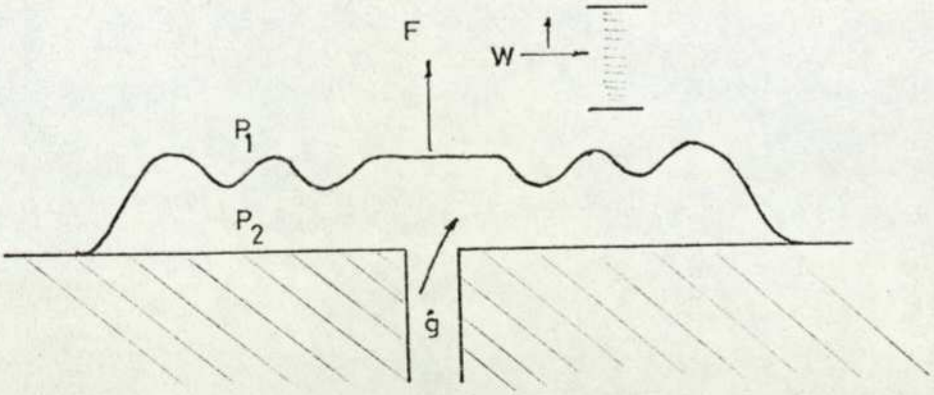

Figure 1.1: Schematic diaphragm

Using the "through" and "across" variable approach, ref. (2) to represent a diaphragm illustrates its operations simply and systematically by the functional model:

$$\begin{bmatrix} F \\ \\ \dot{g} \end{bmatrix} = \begin{bmatrix} ms + R + C_f/s & -A_e \\ \\ A_e & \end{bmatrix} \begin{bmatrix} \dot{w} \\ \\ P \end{bmatrix} \quad \text{where } (\dot{\ }) = \frac{d(\ )}{dt}$$

S = Laplace operator

$$A_e = C_f/C_p = \frac{\text{force constant}}{\text{pressure constant}}$$

$$P_1 - P_2 = P$$

(The directions shown are the positive values.)

Consider only the steady state:

$$F = C_f w - A_e p$$

$$g = A_e w$$

then, as an example, consider the case of $F = 0$ (no force) and p is therefore directly proportional to w (the constant of proportionality being the pressure constant (C_p)); the most common usage described above.

A corrugated diaphragm is used to sense pressure in preference to a flat plate because of its increased working range. The reason why is given by the relative amounts of bending and stretching during deformation; the stretching contributes to the non-linearity effect and most of the deformation of a flat circular plate is taken up with stretching, whereas a corrugated diaphragm is able to bend much more. A circular flat plate becomes considerably non-linear after the centre deflection/thickness ratio (w/t) exceeds 0.45, whereas a corrugated diaphragm exhibiting the same amount of non-linearity may have a (w/t) ratio of up to 8.0 - 10.0. This is achieved at the expense of sensitivity, but the range of the initial sensitivity for a flat plate is so small that it is not a practical device for sensing pressure by measuring displacement. Circular flat plate diaphragms which sense pressure by measuring strain are in common use. The diaphragm characteristic can thus be varied by changing the shape and dimensions of the corrugations.

To improve the sensitivity further, without impairing the linearity and increasing the overall size of the device, capsules are produced. These are basically two diaphragms joining at the outer edge by welding or soldering. The underside diaphragm is now clamped at or near its centre and the displacement sensed at the centre of the top one; this effectively doubles the displacement for the same applied pressure and hence capsules are widely used in industry.

1.2 Need for models of diaphragms

The analysis and design of corrugated diaphragms is a very complex problem; the two main reasons for this are listed:

(i) The actual analysis of a diaphragm is complicated by the way in which the physical and geometric properties are related to the input and output characteristics. By reference to the matrix equation, section 1.1, the matrix elements which have been shown directly relate the input and output are the complex functions of the physical and geometric properties. The mathematical model developed for a diaphragm is then only soluble by the use of a digital computer.

(ii) The number of possible design variables, basically a function of the corrugations, is very large. Fortunately, the number of variables can sensibly be reduced to about ten, of which most are inter-related, e.g. to change the number of corrugations without altering the diameter would change the wavelength, and vice-versa. In contrast, a flat circular plate which has an analytical expression for the pressure deflection characteristic, has only three variables, namely material constant, thickness and diameter, all of which are independent of each other, making the design problem considerably simpler.

The model therefore needs to be (a) flexible, (b) have the prescribed outputs, and (c) consider the environmental effects.

(a) The flexibility aspect is self-evident when the design side is to be considered. The model needs to predict adequately the performance under various loadings for a large number of diaphragm shapes and configurations. The diaphragm profile needs to be generated automatically from a simple description of its basic design parameter, thereby allowing a systematical sensitivity analysis to be made.

(b) The ideal pressure transducer responds to an input of pressure and pressure alone, has a unique and preferably simple transfer function. The real transducer, of course, does not achieve this and its accuracy is characterised by the amount by which it deviates from ideal under the effect of pressure (the primary influence), or secondary influences.

The most important factors to be considered by a designer are:

(1) Sensitivity (w/p)

(2) The linear range or deviation for a particular pressure range

(3) On-set of plasticity

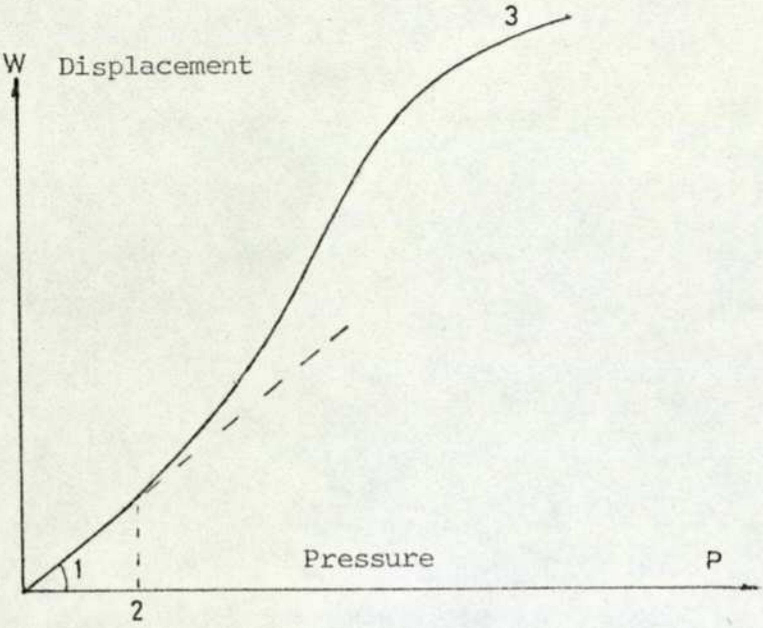

Figure 1.2: Pressure deflection characteristic

Therefore the major requirement for a model is that it is geometrically non-linear, and, although diaphragms would not be operated outside the Hookian region, it is useful to be able to predict the on-set of plasticity. Other causes of deviation from the ideal produced by the primary influence are hysteresis, elastic after-effect and creep. It is not possible to model these effects because imperfections, which are characteristic features of all materials, are too random to be allowed for in the model, and hence it is convenient to assume an isotropic-homogeneous material.

Fortunately for elastic deformation elements which register a displacement the hysteresis is an order of magnitude smaller than the non-linearity; typical figures will be: non-linearity 0.5 per cent, hysteresis 0.01 per cent. Even if it is not possible to handle certain error sources with a model, the user must be aware of them and make allowances accordingly.

(c) Environmental effects are secondary influences and the main ones which a model would be required to handle are temperature and vibration. A simple overall temperature rise and its effect on the centre deflection can be modelled easily with the knowledge of the materials coefficient of expansion and again the assumption that the material is homogeneous and isotropic.

Diaphragms and capsules are not normally used in a vibrating mode, but can occasionally, when used in a pressure instrument, be subjected to a vibration as an unwanted environmental disturbance. Hence, a knowledge of their behaviour under such conditions, particularly the fundamental frequency, would be an advantage for instrument design.

1.3 Arrangement of thesis

The presentation of the models is in their chronological order of development; the non-linear capsule model was developed after an unsuccessful attempt to design a specific capsule using the non-linear diaphragm, and linear capsule model.

The experimental validation can also be chronologically split into two parts, the second part being the more extensive study of capsule stacks, undertaken more as an industrial evaluation project applied to original designs. The dynamics of diaphragms and capsules appears after the modelling and validation because the basic assumption of the dynamic model is that there exists an accurate static model.

Sensitivity analysis of a general diaphragm profile, along with various design approaches derived from the sensitivity analysis, is presented in the chapter on overall design aspects: this serves to illustrate the possible applications and limitations of the models and the possibility of optimising the design procedure. Finally, an actual industrial design problem is tackled and followed through from the finished design to manufacture, testing and installation in a pre-production instrument.

1.4 Note on units

Generally the units used in the thesis are empirical followed by their S.I. equivalent; for stress and pressure the unit is the same, i.e. lbs/in^2. This is equivalent to Newtons per metre squared (N/m^2), but the preferred S.I. unit for pressure measurement is the Pascal (Pa) (1 N/m^2 ≡ 1 Pa). Therefore it is proposed to use N/m^2 when referring to stress levels and Pascals when referring to actual pressures.

When an actual pressure range of a particular sensor is quoted its range may be specified by a pressure of inches of water gauge (Wg) by the manufacturer; to be consistent this is also used in the thesis. The conversion factor is 1 lb/in^2 ≡ 27.6799 Wg (at 20°C).

1.5 Note on symbols

Throughout the text symbols used to represent variables are defined in the body of the text and these need no further explanation, except where an unavoidable over-use of a particular symbol may be confusing.

The radius of curvature is expressed by R_ξ, rl and Rl. The R_ξ is used in the mathematical analysis, the rl is used in reference to the computer program and refers to the ith value of radius of curvature, and Rl is associated with the input data for the program and refers to the radius of curvature at the peaks and troughs of the corrugated profile.

2.0 Review of Past Work

In this review of previous work it is intended to look at different approaches to predicting the performance of corrugated diaphragms and capsules. This has been broken down into three main groups: experimental work, analytical methods, and numerical methods (using computers). The question arises, why use computers? On reading the Sections on experimental and analytical work, it becomes evident that the inherent restrictions make it impossible in a general manner to predict performance. With the availability of fast digital computers, problems hitherto insoluble can now be tackled, i.e. practical design problems. In the latter group a closer review is given to work done in the Instrument Systems Centre of The City University as this is more directly relevant to the thesis. It is by no means an exhaustive review and intuitively one would expect many more papers on the experimental investigations than are presented here. However, the salient points can easily be brought out in the two experimental papers reviewed. The papers do not necessarily fall into each of the above categories. There is some overlapping: for example, D. Rajanna et al, ref. (3), uses algebraic formula as a basis for design from which diaphragms were produced and then experimentally tested.

Initially, systematic experimental investigations into the behaviour of corrugated diaphragms were very important as this was the only way of obtaining design data for future reference. This therefore ought not to be overlooked in the proceeding studies on the mathematics of the problem.

2.1 Experimental work on diaphragms and capsules

The first paper, ref. (4), is concerned with producing a particular diaphragm characteristic. The Bendix Aviation Corporation in 1958 had a requirement for a non-linear pressure deflection curve from a capsule, to use in a 1000-knot airspeed indicator. To achieve this aim they produced more than 875 corrugated diaphragms of 17 basic corrugation designs. A single diaphragm was made for each of the following design parameter changes: a uniform change in the depth of the corrugations, for each of several heat treatments and for different thicknesses, and initial hardnesses of the chosen material (Beryllium Copper). This was done in order to determine the effect of these factors on the performance. From these experiments a large amount of empirical data was collected and discussed under these headings:

(1) Heat treatment
(2) Initial hardness of diaphragm blank
(3) Lack of uniformity of material
(4) Thickness of diaphragm blank
(5) Corrugation depth, design otherwise identical
(6) Corrugation design
(7) Elastic defects.

Although it was stated that "generally the effects are so complicated and inter-related that no complete empirical or theoretical analysis of deflection and stresses as a function of pressure is possible at present", some conclusions were drawn. The main conclusions on design were that primary control of the deflection pressure curve is achieved by:

(a) Varying the thickness of the material
(b) Varying uniformly the depth of corrugation and
(c) Varying the corrugation design.

(b) and (c) can be varied independently for this case because the forming dies were mechanical, as opposed to hydraulic, and adjustable by use of shims. As secondary measures of control, the hardness of the material and the heat treatment can be varied. Other factors also enter, but these are largely to do with obtaining uniformity of performance. To a large extent, but with important exceptions, factors (a) and (b) control the deflection curve, but not its shape. Therefore, the primary curve shape control is, as would be expected, the corrugation design. Finally, after all this effort, no one capsule was able to meet the requirements up to 1000 knots, the maximum reached being 800 knots.

The second paper, ref. (5), is concerned with obtaining experimental design information by systematically changing one geometric variable at a time, and noting the effect on linearity and deflection. This was a rather limited investigation confined to the particular diaphragm configuration chosen, but it was possible to reveal some information about hysteresis and "spring back", subjects which are very complex to consider on a theoretical basis. In contrast to the previous paper, the diaphragms were formed using a rubber pad and a hydraulic press. The pressure applied was 1.5 times predicted forming pressure to make sure that they were fully formed. As the dies were not adjustable, the variation of shape was restricted; one basic shape was chosen and the design parameters were varied about that, but not strictly on the "one variable at a time" principle. Fourteen dies were used and the various combinations increased by using different materials and thicknesses.

From the results "spring back" is reported to be "only an effective change in cone angle whether the tool has a zero cone angle or not" (the cone angle is the angle formed between the centre line of the corrugations and the flat centre portion of the die). This could have been only a superficial observation as the actual "spring back" of each convolution was ignored and only the overall "spring off" considered. From the investigation into hysteresis the results show materials like Beryllium Copper and Phosphor Bronze to be less affected by hysteresis than Stainless Steel.

Interestingly, some work was performed on capsules; these were made of two identical diaphragms which were soldered together to produce a capsule of the kind likely to be found in an aneroid barometer box. The main disadvantage with this type of construction is that there is no overload protection. This experiment was conducted to see how the capsule performance could be predicted from a knowledge of the individual diaphragm performance. The results showed that the linearity of the capsule was almost exactly the same as the diaphragms and the deflection was approximately three per cent greater than the sum of the separate diaphragm deflections. This is a useful result for comparison with numerical results presented later. Another investigation carried out in this paper, which has practical significance when considering a pressure element operating a mechanism, is that of finding the actuating energy. The description is somewhat arbitrary and based on the formula:

$E_n = K C_f W^2$, where E_n = energy available
K = constant
C_f = force constant
W = full-scale deflection.

It is assumed that the energy available is large enough to overcome the resisting force, but it is usual for this force to be small so that the element is not deflected very far from its equilibrium position at any pressure. Thus, to determine the actuating energy of an element one must first decide on the allowable deflection from the equilibrium position that the load can produce. For example, one-tenth of a per cent of full-scale deflection giving $K = 0.001$.

Considering three diaphragms of differing material under identical conditions, i.e. same form, thickness and pressure, the following normalised results were obtained:

Material	Actuating energy
Phosphor bronze	1.00
Beryllium copper	0.70
316 Stainless steel	0.54

Again, except for its limitation, this appears a useful result, but going on to consider the maximum allowable diaphragm deflection for a given form, Beryllium copper exceeds Phosphor bronze. So for a constant profile not dependent on thickness Beryllium copper out performs Phosphor bronze on actuating energy and Stainless Steel a poor third, a result which could probably be inferred by knowing values of Young's Modulus and Yield point. The paper concludes very general effects of diaphragm profile on performance and suggests large areas of work for investigation.

2.2 Analytical methods

Researchers have attempted for many years to produce algebraic expressions which predict the performance of corrugated diaphragms. Grover and Bell, ref. (6), produced a paper in 1948, and as recently as 1975 a paper was published by C. Rubin, ref. (7).

But the main contributors in this area are Haringx, ref. (8), ref. (9) and Andreeva, ref. (10). Haringx produced four papers concerned with diaphragms, the first on the rigidity of corrugated diaphragms, the second on stresses in sheet material, the third on the non-linearity of corrugated diaphragms, and the fourth was on the design of diaphragms using the results of the other three papers.

Haringx was able to work from the known solution of a flat plate and then simply replace the corrugated diaphragm by a fictitious flat plate of similar properties (tensile stiffness and bending stiffness). He then calculated successively the rigidity, the stresses, and for large deformation the degree of non-linearity. This restricted the author to consider diaphragms of specific profile types: all the corrugations had to be the same size and shape and equidistant above and below the middle plane, also no initial flat section or enlarged end bead for clamping could be incorporated.

2.2.1 Rigidity (pressure-deflection prediction)

The linear deflection for a flat plate is given by:

$$f_o = \frac{3 P R^4}{16 E' t^3} \quad \ldots\ldots\ldots\ldots\ldots\ldots\ldots\ldots \quad (2.1a)$$

Then the deflection of a diaphragm of the same overall dimensions is

$$f_o = \frac{3 P R^4}{16 E' t^3} \varepsilon \quad \ldots\ldots\ldots\ldots\ldots\ldots\ldots\ldots \quad (2.1b)$$

where $E = {}^{E}/(1 - \nu^2)$: ε = coefficient of reduction.

The coefficient ε is then a very involved algebraic function containing a fundamental quantity referred to as q, which is itself a complex function of the geometry.

2.2.2 Stresses

The assumptions applied to finding the stresses were more restrictive than finding the deflection. The three stresses found were the maximum tangential and radial stresses plus the extreme radial stress at the outer rim; these were all functions of the quantity q.

2.2.3 Non-linearity

The non-linearity calculation was again more restrictive than the corresponding rigidity; extracting the pressure from Eqn. 2.1,

$$P = \frac{16}{3(1 - \nu^2)} \frac{E t^3}{R^4 \varepsilon} f_o$$

and employing the energy method used for the non-linearity calculation:

$$P = 2(q + 1)(q + 3) \frac{E t^3}{3 R^4} f_o \left(1 + \frac{f_o^2}{Q^2 t^2}\right) \quad \ldots\ldots \quad (2.2)$$

Hence the total pressure deflection characteristic Eqn. (2.2) is of cubic form similar to a flat plate. From the foregoing results non-dimensional groups of variables were formed and these were used in "carpet plot" type design charts. By way of an example a diaphragm was designed from the plots, but the great disadvantage was that the design had to be of a standard trapezoidal corrugation profile.

Andreeva's work on diaphragms forms part of her book on Elastic Elements of Instruments, ref. (10), and is a much longer and more thorough treatment of the subject than would be expected in a paper. Her approach is similar to Haringx in many ways: she assumes in the case of a corrugated diaphragm, resistance to bending in a radial direction is much smaller when compared to the tangential direction. Hence the corrugated diaphragm is anisotropic and the mathematical model of such a device is taken as a flat anisotropic diaphragm. Based on this analogy the equivalent flexural (bending) and tensile rigidities are determined. Then the diaphragm deflection is related to pressure by a cubic of the same form as before.

$$P = A w + B w^3 \quad \ldots\ldots\ldots\ldots\ldots\ldots\ldots\ldots \quad (2.3)$$

Here the linear term corresponds to bending rigidity and the cubic term is related to resistance to tension, e.g. (2.3) is equivalent to:

$$P = \frac{E\,t}{R^4}(\alpha\, t^2\, w + \beta\, w^3) \quad \ldots\ldots\ldots\ldots\ldots\ldots \quad (2.4)$$

where α and β are constants depending on the profile and Poisson's ratio. Again, the major disadvantage is the fact that the shape is so restricted, i.e. a large number of regular symmetric corrugations. The book not only provides a mathematical model for pressure deflection characteristics, but with modification to the constants in Eqn. (2.4) it can handle the addition of a rigid centre boss and the application of a point load on the boss; from this information an expression for the effective area of the diaphragm can be found. Also, convex snap-action and non-metallic diaphragms are considered. Like Haringx, Andreeva forms non-dimensional design parameters which are used in design charts, and some examples are given in the text.

The work of both Haringx and Andreeva was used at the N.A.L. Bangalore, ref. (3), to attempt the design of diaphragms. These were successfully used in pressure transducers for the range (0 - 0.2) to (0 - 500) lbs/in^2 (0 - 1.38) to (0 - 3450) KPa; the combined non-linearity and hysteresis error were less than ± 0.5 per cent, but the results achieved did not reflect the theoretical predictions from Andreeva and Haringx, the error in sensitivity being (23 - 40) per cent higher from Andreeva's predictions and from -34.5 per cent to 28 per cent out for Haringx.

Later work by C. Rubin, ref. (7) 1975, is still taking an algebraic approach; the general equation for the bending of a polar orthotropic plate with a uniformly distributed load is considered. A series solution with four constants is obtained; these constants are found from the knowledge of the four distinct boundary conditions and this will give the displacements and stresses as a function of radial distance. Four cases are cited for a diaphragm clamped to a displaced centre shaft: (a) the shaft axially displaced with and without a pressure difference, and (b) the shaft angularly displaced with and without a pressure difference. An optimum design is sought by producing a table of maximum radial and tangential stresses for various inner to outer diameter ratios. This again was very limiting in profile scope and did not always give an optimum.

For the case of an applied pressure difference, the optimum was inferred as the stress values quoted above, approached an asymptotic value; this was for a pressure difference of 9.8×10^{-5} Pa (1.4214×10^{-8} $\mathrm{lbs/in^2}$). Although this was an interesting theoretical result, a pressure difference that small has little practical significance.

2.3 Computer studies of diaphragms and capsules

The first computer simulator of a corrugated diaphragm was done by W. A. Wildhack, R. F. Dressler and E. C. Lloyd, ref. (11), and this was followed up by a paper on bending and stretching of corrugated diaphragms by R. F. Dressler, ref. (12). The overall approach compared their computer prediction to the Grover-Bell results for the same shape. The corrugated diaphragm was treated as a rotationally symmetric elastic shell, and the linear equations of thin shell theory were applied with the appropriate geometry. This was a sixth-order non-homogeneous system of equations in terms of V (tangential deflection), W (normal deflection) and Q (normal shear) as functions of S (the curve distance). These three equations can be reduced (although it is not mentioned in the paper), to Reissner's formulation of linear thin shell equations, ref. (26); as an example, the rotation equation is formulated from the Wildhack et al first equation:

$$\overset{①}{r\,\overset{'''}{W}} + \overset{②}{\cos\phi\,\overset{''}{W}} - \left(\overset{③}{\frac{\cos^2\phi}{r}} + \overset{④}{\nu\,K\,\mathrm{Sin}\phi}\right)\overset{'}{W} + \overset{⑤}{r\,K\,\overset{''}{V}} + (\overset{⑥}{K\cos\phi} + \overset{⑦}{2r\,\overset{'}{K}})\overset{'}{V}$$

$$\left(\overset{⑧}{\overset{'}{K}\cos\phi} + \overset{⑨}{\overset{''}{K}\,r} - \overset{⑩}{K\,\frac{\cos^2\phi}{r}} - \overset{⑪}{\nu\,K^2\,\mathrm{Sin}\phi}\right)V + \left(\frac{r}{D}\right)Q = 0$$

where K(s) is the curvature function.

$$\text{Then}\quad \beta(\text{rotation}) = KV + W' \quad (\text{given})$$

$$\text{Hence}\quad \beta' = K'V + KV' + W''$$

$$\text{and}\quad \beta'' = K''V + 2K'V' + KV'' + W'''$$

Now collecting terms

$$① + ⑤ + ⑦ + ⑨ \equiv r\beta''$$

$$② + ⑥ + ⑧ \equiv \cos\phi\, \beta'$$

$$③ + ④ + ⑩ + ⑪ \equiv -\left(\frac{\cos\phi}{r} + \nu K \operatorname{Sin}\phi\right)\beta$$

and dividing by r

$$\beta'' + \left(\frac{\cos\phi}{r}\right)\beta' - \left(\frac{\cos^2\phi}{r^2} + \nu K \frac{\operatorname{Sin}\phi}{r}\right)\beta + \frac{Q}{D} = 0$$

This equation can be compared with Eqn. (3.40a), Chapter 3.

The method employed to solve these equations was a fourth order Runga-Kutta integration. The details of the method of solution is described in the first paper, ref. (11), and the elasticity solutions obtained with their interpretation is described in ref. (12) by Dressler. A fundamental point to note here is that they were using an initial value method to solve a two-point boundary value problem.

The Grover-Bell diaphragm which was extensively analysed by these authors is shown schematically in Figure 2.1.

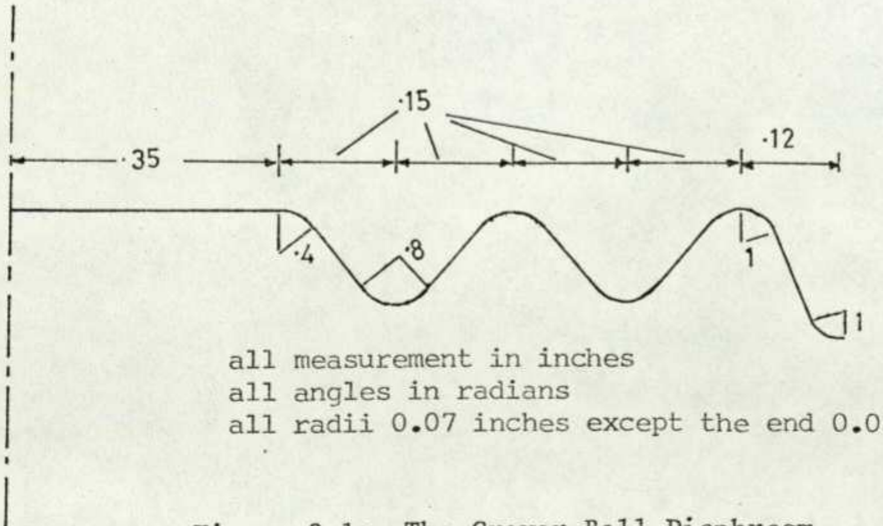

all measurement in inches
all angles in radians
all radii 0.07 inches except the end 0.03 inches

Figure 2.1: The Grover-Bell Diaphragm

It consists of short circular arcs joined by straight conical sections. This has discontinuities where the straight lines become tangential to the circles; at these eleven junctions the curvature K(s), as a function of generator length, changes quite radically. And for this reason smoothing functions were applied to aid the solution. The accuracy of the computation was checked by the static equilibrium at the horizontal points, where the exact relation:

$$2\pi \, r \, Q = P \, \pi \, r^2 \quad \text{holds,}$$

therefore $Q = -\frac{Pr}{2}$, where Q = shear force/unit length.

The stress resultants were subsequently calculated as functions of displacements by the following relations:

$$M_\phi = -\frac{Et^3}{12(1-\nu^2)} \left[K' V + K V' + W'' + \frac{\nu \cos\phi}{r} (K V + W') \right]$$

$$M_\theta = -\frac{Et^3}{12(1-\nu^2)} \left[\frac{\cos\phi}{r} (K V + W') + \nu (K' V + K V' + W'') \right]$$

$$N_\phi = \frac{Et}{(1-\nu^2)} \left[V' - K W + \nu \left(\frac{\cos\phi \, V}{r} - \frac{\mathrm{Sin}\phi \, W}{r} \right) \right]$$

$$N_\theta = \frac{Et}{(1-\nu^2)} \left[\frac{\cos\phi \, V}{r} - \frac{\mathrm{Sin}\phi \, W}{r} + \nu (V' - K W) \right]$$

The stresses are assumed to be linearly distributed through the thickness of the shell, but only the stresses in the radial and circumferential directions are considered as the normal and shear stresses are assumed negligible compared with the first two, (σ_ϕ) and (σ_θ), respectively.

The actual (total) stress components at the top and bottom faces may be obtained by adding or subtracting the membrane (N) and bending (M) parts as follows. This relationship is derived in the chapter on modelling.

$$\sigma_\phi\left(\frac{t}{2}\right) = N_\phi/t + 6M_\phi/t^2$$

$$\sigma_\phi\left(-\frac{t}{2}\right) = N_\phi/t - 6M_\phi/t^2$$

$$\sigma_\theta\left(\frac{t}{2}\right) = N_\theta/t + 6M_\theta/t^2$$

$$\sigma_\theta\left(-\frac{t}{2}\right) = {}^{N_\theta}/_{t} - {}^{6M_\theta}/_{t^2} .$$

These foregoing quantities were expressed graphically as a function of generator length. As a concluding remark on the first paper the computer time involved in one run, i.e. to compute the linear displacements, forces and stresses, took seven hours!

The Grover-Bell (Figure 2.1) diaphragm was 2.14" (52.43 mm) diameter (d) and 0.007" (.1778 mm) thick (t), giving a t/d ratio of 0.00327. Dressler considers a diaphragm of the same shape but three times as thick and one three times thinner giving t/d ratios of 0.0098 and 0.0011, respectively. These values would be well within the acceptable limits of thin shell theory if the shell had no curvature. Unfortunately, the diaphragm considered has a peak and trough radius of curvature of 0.07" (1.778 mm) which, for the two fictitious and one actual diaphragms considered, gives thickness to radius of curvature ratios of 30, 10 and 3.333, the last one being the "thick" diaphragm. Within the assumptions of thin shell theory this ratio ought to be at least five, therefore it is doubtful if the results for the thick case are meaningful. Conversely, considering the thin case, the same value of pressure (15 lbs/in^2 (103.5 kPa)) was applied to all three cases so the thin diaphragm which was only 0.00233" (0.059182 mm) thick received the same pressure and there was no justification for assuming that an actual diaphragm of that shape, thickness and material properties would still be performing in the linear region, for which the equations were only valid.

Nevertheless, the results were able to confirm some empirical design assumptions and indicated the problem could be solved numerically given sufficient computer time. Also, without losing sight of the limitations of a model, it should be realised that variations or uncertainties in material properties, such as Young's modulus, Poisson's ratio, effective thickness or residual stresses, make it unlikely that diaphragm manufacture will become "exact" to anywhere near the precision that the model would suggest.

2.4 The Instrument Systems Centre

Work on mathematical modelling corrugated diaphragms used as pressure sensors within the Instrument Systems Centre at The City University was first attempted by H. Schricker, ref. (13). He also considered a diaphragm as a thin axisymmetric shell and proposed a solution using thin shell equations and a digital computer. He chose a different approach from Wildhack et al and used a finite difference approximation for the first and second differentials. This was reasonable because in solving two simultaneous second order equations by a Runga-Kutta method would require four boundary conditions to be specified at one boundary, but with this type of shell problem only two are expressed at each end; also with shell problems boundary values at one boundary have very little effect on values found at the distant boundary. Basically Schricker was able to take Meissner's ref. (15) equations which were H. Reissner's original formulation, formulated for different dependent variables and program them in the manner indicated by Penny, ref. (16), and elaborated by Kraus, ref. (17). The two resulting variables from the solution were the rotation (β) and the normal shear force per unit length (Q). This was convenient because he could then force the computation to be correct at the points where the tangent to the curve was horizontal by substituting the relationship $Q = -\frac{Pr}{2}$. This was done at the peaks and troughs and also simplified the boundary conditions at each end, making them straightforward algebraic expressions. Again, the formulation provided only a linear model. Using central finite differences the system of equations reduced to a large matrix equation of the form:

$$\left[\begin{array}{c|c} X_1 & Y_1 \\ \hline Y_2 & X_2 \end{array}\right] \left[\begin{array}{c} R \\ \hline Q \end{array}\right] = \left[\begin{array}{c} K_1 \\ \hline K_2 \end{array}\right] \quad \ldots\ldots\ldots\ldots\ldots\ldots \quad (2.6)$$

where X_1 and X_2 are triagonal (N-2) by (N-2) matrices

Y_1 and Y_2 are unit matrices x a constant

R = Rotation

Q = Normal shear

K_1 = Zero

K_2 = Loading terms.

A method of reducing this 2.(n-2) square matrix was proposed but not used, even though it would have reduced the storage by three-quarters of the amount required for Eqn. (2.6). But a more significant feature was that only two per cent of the above matrix was non-zero, which meant that most of the operations were trivial, i.e. multiplying zero by zero, this would naturally increase the computational time unnecessarily. To solve for linear pressure deflection characteristic took 13.579 seconds on a C.D.C. 7600 machine with N = 106. Using the partitioned approach mentioned in Schricker's work and a Gaussian elimination technique which only stored the non-zero terms, the same Schricker program could be solved in 7.627 seconds, and the additional storage required to solve the matrix reduced from 42.85 K words to 0.5 K words.

Schricker applied his program to three production diaphragms and found that in all cases the predicted deflections were consistently lower than the experimental results; this he concluded to be mainly due to uncertainty in the values of the material constants, i.e. Young's Modulus. But investigations carried out since have shown this not to be the case, in fact, measurements on Young's Modulus by the author have shown that Schricker underestimated the value and this would have made his predictions worse!

The three diaphragms considered were all approximated to a regular shape, i.e. each convolution the same as the next, but in the actual situation this is not practically possible because the diaphragm forms either the top or bottom of a nesting capsule. From the computational side some unexplained anomalies arise. The step length associated with the finite difference approximation, a very sensitive parameter numerically, is changed when going from the regular convolutions to the end bead, and no adjustment for this is allowed; this may not have been significant but more striking is the result for the horizontal displacement. It is not quoted in the report but printed out in the programs: this displacement has no sign change along the whole diaphragm generator, which is statically incorrect because the horizontal displacement is constrained to zero at both boundaries. It therefore appears that the equations were inadequate to handle this type of problem.

The reasons for the inadequacies in Schricker's work were investigated by the author, and it appears that although Penny, ref. (16), successfully used the same formulation to solve a general thin shell by finite differences, the example he chose was only slightly curved and had a finite angle between the Z axis and the normal to the shell middle surface. The equations programmed by both Penny and Schricker are as follows:

$$\frac{d^2\beta}{ds^2} + A\frac{d\beta}{ds} + B_\beta + \frac{Q}{D} = 0$$

$$\frac{d^2Q}{ds^2} + J\frac{dQ}{ds} + G_Q - C_\beta = F$$

where $D = \dfrac{Et^3}{12(1 - \nu^2)}$; $C = Et$

A, B, J, G = functions of geometry and material properties
F = loading term.

The equations are more attractive to use than Reissner's because coefficients of loading terms and boundary conditions become rather more complicated with Reissner's equations and this increases the preliminary numerical work.

However, inspection of the above coefficients and loading terms shows that a multiplication of Cotangent (ϕ) is quite common. Payne, ref. (18), in his paper on axi-symmetric bending of a toroidal shell, found that when applying the above-mentioned equations to a toroid the angle ϕ goes through zero twice:

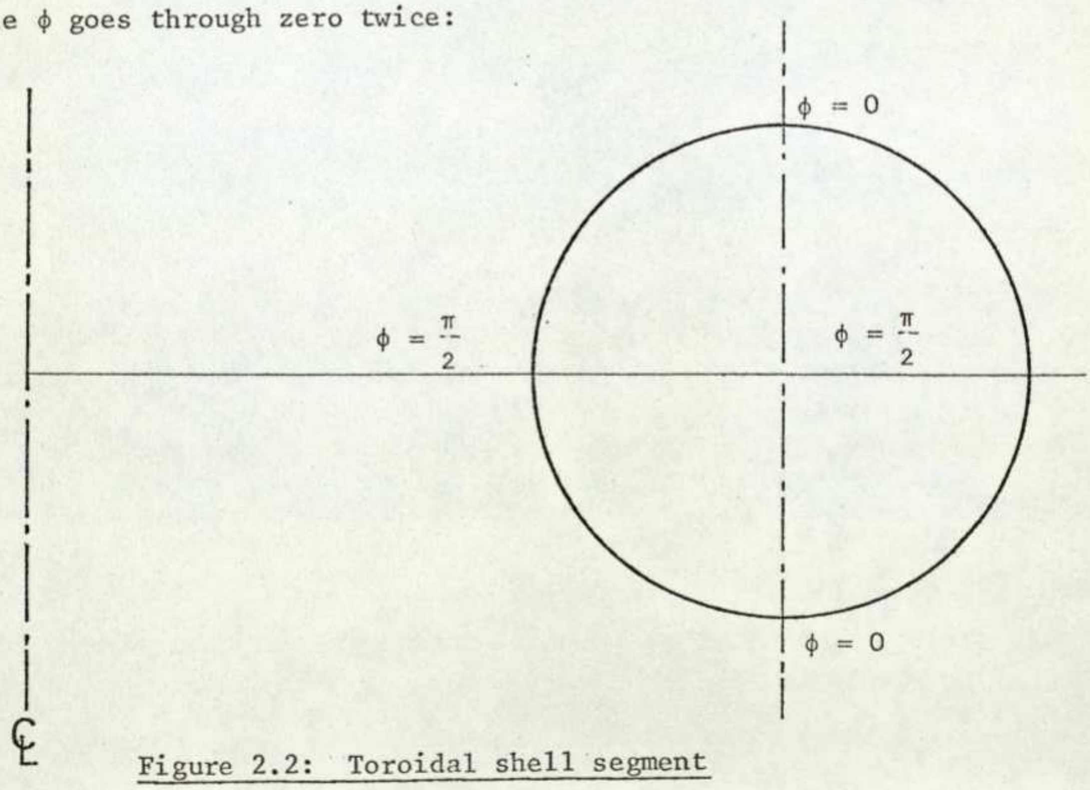

Figure 2.2: Toroidal shell segment

And hence Cotangent (ϕ) will be infinite at these two points. Similarly, for a corrugated diaphragm (ϕ) goes through zero at each peak and trough. Schricker attempted to eliminate this difficulty by forcing the finite difference mesh points to fall exactly on a peak and trough, and then use the identity $Q_i = -\frac{Pr_i}{2}$. This must have helped the solution, but if the mesh was small enough the points either side of the ϕ = zero point were also very small, causing large numbers to appear in the coefficients. Payne solved the toroid problem using both sets of equations, Reissner's being formulated in terms of (Hr) (the horizontal force/unit circumference, multiplied by the radial distance) and the rotation β. Reissner's equations avoid the possibility of a singularity if ϕ = zero by not having a term which tends to zero in the denominator or one which tends to infinity in the numerator of any of the coefficients. Payne's results showed that even if a solution is found for cases where ϕ = zero using Meissner's formulation there is a sharp discontinuity around this point, whereas Reissner's formulation appears to be quite adequate.

F. Abdullah, ref. (19) took a different approach to the linear thin shell problem; with the equations formulated as six first order differential equations, he applied state variable techniques to solve them. The equations were integrated using a predictor corrector method, which ensures that all the integrations are performed to a previously prescribed accuracy. This involved a Runga-Kutta integration to start the process as it was not self-starting. The program was thought to be much more flexible than a finite difference program because variations in environmental conditions and material properties could be handled relatively easily. The main disadvantage was the computational time which was later shown to be about five hundred times slower than a finite difference program, both being run on a CDC 7600 machine. All the digital simulations so far mentioned have only been linear models. From a pressure element viewpoint, two basic parameters are obviously important: the linear sensitivity of the element and the linear range. To cover both requirements, a geometric non-linear model is needed. F. Abdullah, ref. (19), developed a non-linear model which used the linear model for initial starting values. The formulation of the equations was similar, i.e. first order differential equations in state variable form (Kalnis formulation, ref. (20)), but using a shooting method, together with a computer optimisation routine to match boundary conditions at the far end of the diaphragm. Again, this method was very slow, each pressure point taking approximately the same time as a linear model solution.

3.0 The Mathematical Model

To analyse corrugated diaphragms and capsules, the initial problem is one of choosing a mathematical model. In the detailed level of modelling considered here, it becomes necessary to relate the pressure deflection characteristics to the geometry and the elastic constants of the diaphragm. With a future requirement for design, it is also desirable to automate and generalise the operation of such a model. It has been shown, and it is reasonable to assume, that a corrugated diaphragm is a rotationally symmetric thin elastic shell of complex convoluted geometry. Therefore, a mathematical analysis of stresses and displacements in the diaphragm could logically be based on axisymmetric thin shell theory; a theory derived from applying basic physical laws (in this case elastic laws) to a finite element of the shell and leading to a set of differential equations. This approach has been used in previous analytic and computer studies (outlined in Chapter 2) and will be further developed here. The differential equations are solved by numerical techniques on a digital computer and the model is therefore a computer program.

The chapter as presented is a chronological development of basically four models which build on the experience and techniques of the previous models in some way. This is best illustrated in the flow chart (Figure 3.1); much of the work is covered in the linear diaphragm model as it is basic to the others.

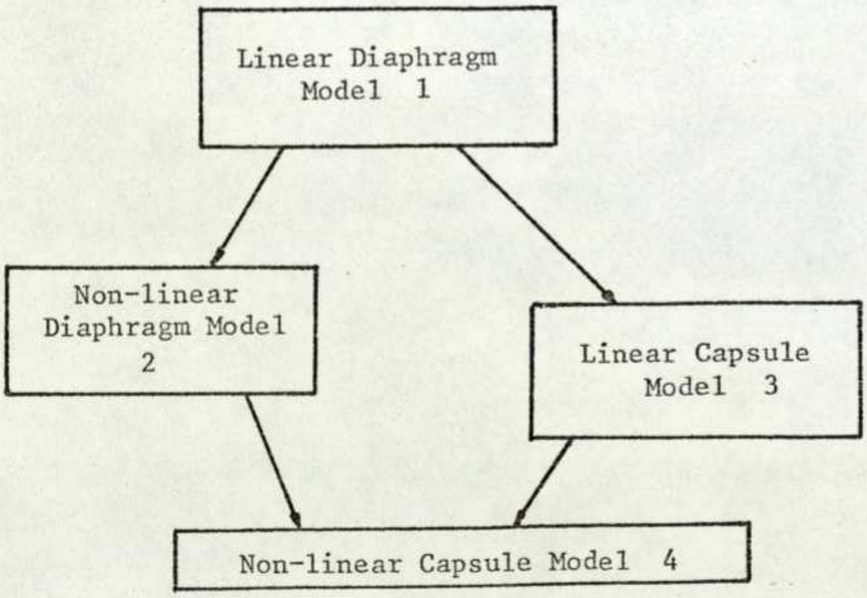

Figure 3.1: Model development

Perhaps a more logical way of presenting the equations would have been to obtain the non-linear equations first and show by making certain approximations how some terms may be neglected and a linear model results; but from the programming point of view it is easier to show how the non-linear model is developed from the linear and the extra terms which arise from not assuming a very small displacement.

3.1 The linear model

3.1.1 Assumptions of thin shell theory stress-strain relationship

Any theory must be based on a set of assumptions, and for thin shell theory, A. E. H. Love, ref. (21), first proposed a set of postulates, known as Love's first approximation to the theory of thin elastic shells:

(1) The shell is thin;
(2) The deflection of the shell is small;
(3) The transverse normal stress is negligible;
(4) Normals to the reference surface of the shell remain normal to it, and undergo no change in length during deformation.

The assumptions and their implications may now be discussed:

The assumption of thinness sets the scene for the entire theory. Indeed, as will be noted presently, the rest of Love's postulates seem to be appropriate only to thin shells and are, therefore, consequences of this postulate. Although no precise definition of thinness is available, it will be sufficient in our subsequent derivations of the theory to neglect the ratio of the thickness to the radius of curvature of the reference surface in comparison to unity. However, it is suggested that the resulting theory be applied only to shells whose thickness is everywhere less than one-tenth of the radius of curvature of the reference surface. By how far this suggested ratio can be reduced without drastically affecting the accuracy is considered in other chapters.

The assumption that the deflections of the shell are small permits us to refer all derivations and calculations to the original configuration of the shell and, together with Hooke's law, assures us that the resulting theory will be a linear elastic one.

The two remaining hypotheses of the Love theory deal with the constitutive equations of thin elastic shells and represent the most significant features of the first approximation. For these discussions consider Hooke's law for a homogeneous isotropic elastic medium. In such a material there are three mutually perpendicular planes of elastic symmetry that, in anticipation of our latter choice of the lines of principal curvature as co-ordinates ξ and θ, are the normal directions

$$\begin{aligned} \varepsilon_1 &= \left[\sigma_1 - \nu\,\sigma_2 - \nu\,\sigma_n\right]\frac{1}{E} \\ \varepsilon_2 &= \left[\sigma_2 - \nu\,\sigma_1 - \nu\,\sigma_n\right]\frac{1}{E} \qquad \ldots\ldots\ldots\ldots\ldots\ldots\ldots \quad (3.1) \\ \varepsilon_n &= \left[\sigma_n - \nu\,\sigma_1 - \nu\,\sigma_2\right]\frac{1}{E} \end{aligned}$$

$$\gamma_{12} = \tau_{12}/G, \quad \gamma_{1n} = \tau_{1n}/G, \quad \gamma_{2n} = \tau_{2n}/G \quad \ldots\ldots\ldots\ldots \quad (3.2)$$

where σ_1, σ_2, σ_n are normal stresses along three mutually perpendicular directions,

ε_1, ε_2, ε_n are the corresponding normal strains,

γ_{12}, γ_{1n}, γ_{2n} and τ_{12}, τ_{1n}, τ_{2n} are, respectively, the shearing strains and stresses, and

E, G and ν are the elastic constants (only two of which are independent for an isotropic medium).

Returning to the discussion of Love's postulates and noting that the fourth hypothesis concerns the preservation of the normal element, this represents an extension to the case of a thin elastic shell of the familiar Bernoulli-Euler hypothesis of beam theory which states that "plane sections remain plane". The assumption of the preservation of the normal implies that all the strain components in the direction of the normal to the reference surface vanish, or that

$$\varepsilon_n = \gamma_{1n} = \gamma_{2n} = 0.0 \quad \ldots\ldots\ldots\ldots\ldots\ldots\ldots\ldots \quad (3.3)$$

therefore from (3.2) the shearing stress components τ_{1n} and τ_{2n} also vanish.

Also, the restriction to thin shells makes reasonable the third assumption of the Love theory, that is expressed as:

$$\sigma_n = 0.0 \quad \ldots\ldots\ldots\ldots\ldots\ldots\ldots\ldots\ldots\ldots\ldots\ldots \quad (3.4)$$

As a consequence of the third and fourth postulates of the Love theory ((3.3), (3.4)), the system of stress-strain relations given by (3.1) is reduced to the following two dimensional constitutive law of thin elastic shells:

$$\varepsilon_1 = \frac{1}{E}\left[\sigma_1 - \nu\,\sigma_2\right]$$

$$\varepsilon_2 = \frac{1}{E}\left[\sigma_2 - \nu\,\sigma_1\right] \quad \ldots\ldots\ldots\ldots\ldots\ldots\ldots\ldots \quad (3.5)$$

$$\gamma_{12} = \tau_{12}/G$$

3.1.2 Stress-strain and stress resultant relationship

Having obtained a system of stress-strain relations in general directions (1, 2), Eqn. (3.5), for the shell, we can re-write them with a new notation defining the axial direction (ξ) and the circumferential direction (θ):

$$\sigma_\xi = \frac{E}{1-\nu^2}\left(\varepsilon_\xi + \nu\,\varepsilon_\theta\right)$$

$$\sigma_\theta = \frac{E}{1-\nu^2}\left(\varepsilon_\theta + \nu\,\varepsilon_\xi\right) \quad \ldots\ldots\ldots\ldots\ldots\ldots\ldots \quad (3.6)$$

This is just a statement of Hooke's law in two dimensions, and to derive the stress resultants Hooke's law, in conjunction with the shell geometry, is applied.

To analyse the internal forces we cut from the shell an infinitely small element formed by two pairs of adjacent planes which are normal to the middle surface of the shell and which contain its principal curvature R_ξ, R_θ (Figure 3.2). The internal forces (stress resultants) are also shown on the figure. It then follows that by integrating across the thickness $\left(\frac{t}{2}\right)$ to $\left(-\frac{t}{2}\right)$,

$$N_\xi = \int_{-t/2}^{t/2} \sigma_\xi \left(1 - \frac{Z}{R_\theta}\right) dz \quad \ldots\ldots\ldots\ldots\ldots\ldots\ldots\ldots \quad (3.7a)$$

$$N_\theta = \int_{-t/2}^{t/2} \sigma_\theta \left(1 - \frac{Z}{R_\xi}\right) dz \quad \ldots\ldots\ldots\ldots\ldots\ldots\ldots\ldots \quad (3.7b)$$

$$M_\xi = \int_{-t/2}^{t/2} \sigma_\xi\, Z \left(1 - \frac{Z}{R_\theta}\right) dz \quad \ldots\ldots\ldots\ldots\ldots\ldots\ldots \quad (3.7c)$$

$$M_\theta = \int_{-t/2}^{t/2} \sigma_\theta\, Z \left(1 - \frac{Z}{R_\xi}\right) dz \quad \ldots\ldots\ldots\ldots\ldots\ldots\ldots \quad (3.7d)$$

In the following discussion we shall invoke the first assumption and assume the thickness t is very small in comparison with the radii R_ξ, R_θ and omit terms $\frac{Z}{R_\xi}$, $\frac{Z}{R_\theta}$.

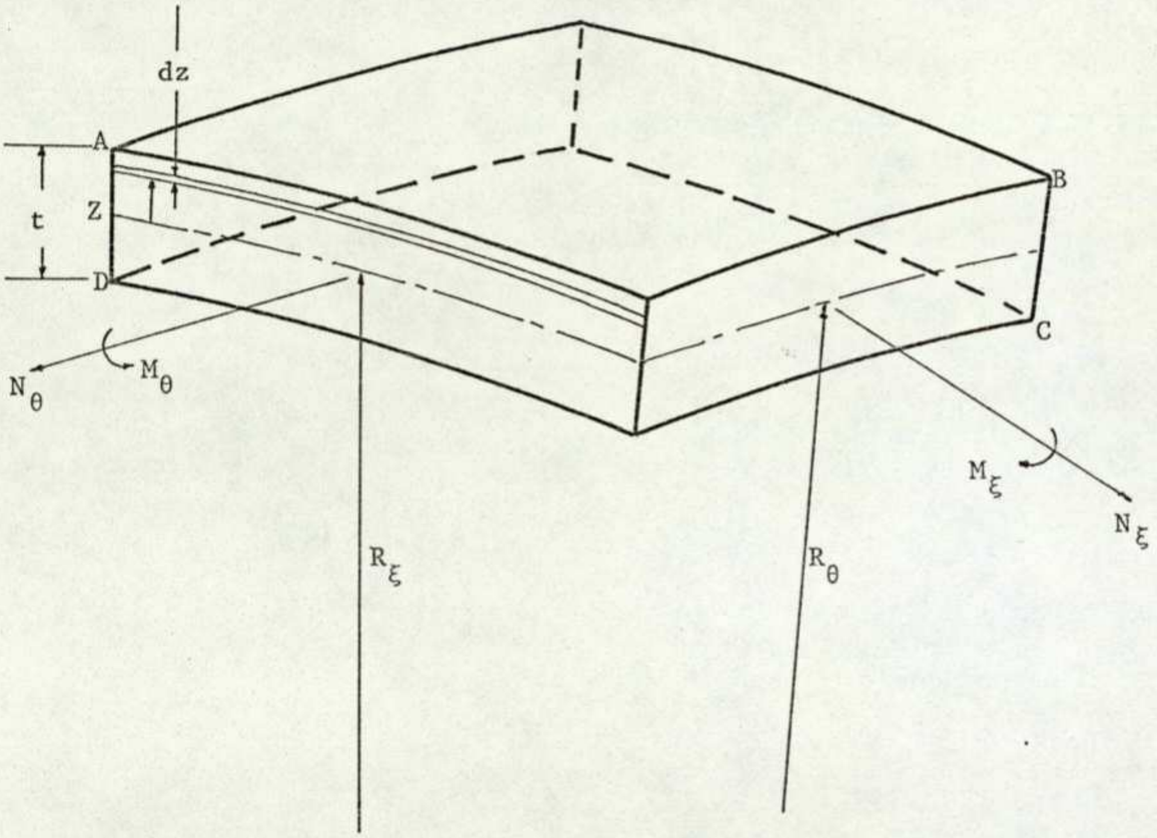

Figure 3.2: Elemental shell

Now apply assumption four of the thin shell theory and begin with a simple case, in which during bending the lateral faces of the element A B C D rotate only with respect to their lines of intersection with the middle surface. If $\bar{R}_\xi$ and $\bar{R}_\theta$ are the values of the radii of curvature after deformation, the unit elongations of a thin lamina at a distance Z from the middle surface are:

$$\varepsilon_\theta = -\frac{Z}{1 - \frac{Z}{R_\theta}}\left(\frac{1}{\bar{R}_\theta} - \frac{1}{R_\theta}\right) \quad \ldots\ldots\ldots\ldots\ldots\ldots \quad (3.8a)$$

$$\varepsilon_\xi = -\frac{Z}{1 - \frac{Z}{R_\xi}}\left(\frac{1}{\bar{R}_\xi} - \frac{1}{R_\xi}\right) \quad \ldots\ldots\ldots\ldots\ldots\ldots \quad (3.8b)$$

[Note: These equations of strain are due to bending only]

If, in addition to rotation, the lateral sides of the element are displaced parallel to themselves, owing to stretching of the middle surface, and if the corresponding unit elongations of the middle surface in the two directions are ε_1 and ε_2, the elongation ε_ξ of the lamina, as seen from Figure 3.3, is $\varepsilon_\xi = (\ell_2 - \ell_1)/\ell_1$.

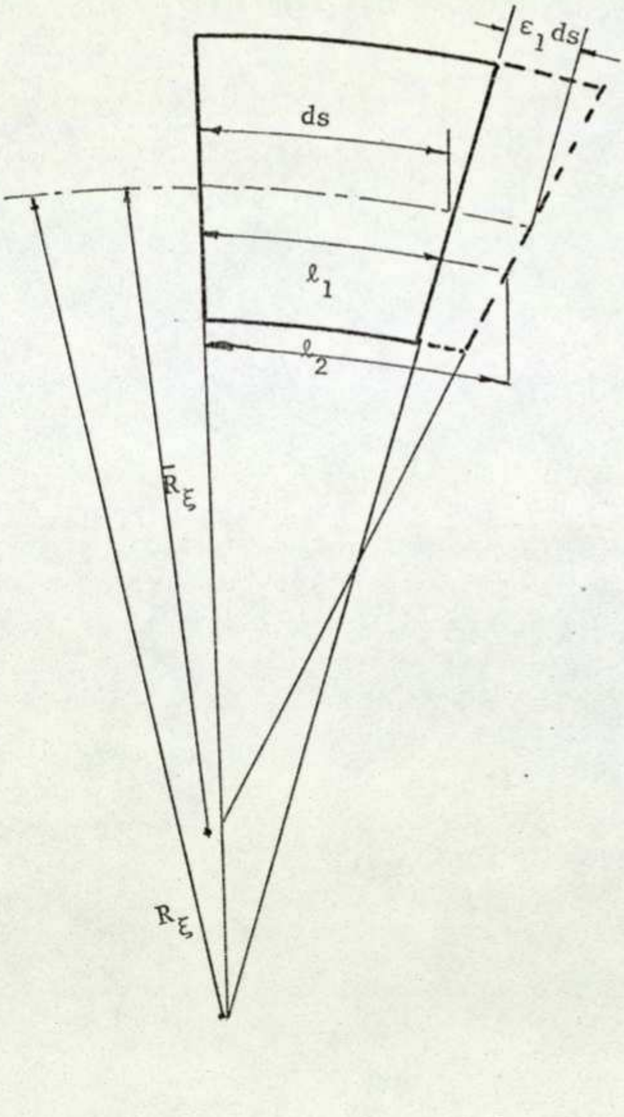

Figure 3.3

Substituting $\ell_1 = ds\left(1 - \frac{Z}{R_\xi}\right)$ and $\ell_2 = ds\left(1 + \varepsilon_1\right)\left(1 - \frac{Z}{R_\xi}\right)$, we obtain

$$\varepsilon_\xi = \frac{\varepsilon_1}{\left(1 - \frac{Z}{R_\xi}\right)} - \frac{Z}{\left(1 - \frac{Z}{R_\xi}\right)}\left[\frac{1}{(1 - \varepsilon_1)\bar{R}_\xi} - \frac{1}{R_\xi}\right] \quad \ldots\ldots\ldots \quad (3.9a)$$

A similar expression can be obtained for the elongation

$$\varepsilon_\theta = \frac{\varepsilon_2}{\left(1 - \frac{Z}{R_\theta}\right)} - \frac{Z}{\left(1 - \frac{Z}{R_\theta}\right)}\left[\frac{1}{(1 - \varepsilon_2)\bar{R}_\theta} - \frac{1}{R_\theta}\right] \quad \ldots\ldots \quad (3.9b)$$

(These are of the same form as (3.8), but contain the stretching effects of the mid-surface.)

Now applying the stated assumptions and neglecting $\varepsilon_{1,2}$ in comparison to unity, then

$$\varepsilon_\xi = \varepsilon_1 - Z\left(\frac{1}{\bar{R}_\xi} - \frac{1}{R_\xi}\right) = \varepsilon_1 - Z\,\chi_\xi \quad \ldots\ldots\ldots\ldots\ldots\ldots \quad (3.10a)$$

$$\varepsilon_\theta = \varepsilon_2 - Z\left(\frac{1}{\bar{R}_\theta} - \frac{1}{R_\theta}\right) = \varepsilon_2 - Z\,\chi_\theta \quad \ldots\ldots\ldots\ldots\ldots\ldots \quad (3.10b)$$

where χ_ξ and χ_θ denote the changes of curvature. Using these expressions for the components of strain of the lamina and assuming that there are no normal stresses between lamina (σ_Z = Zero), the following expressions for the components of stress are obtained:

$$\sigma_\xi = \frac{E}{1 - \nu^2}\left[\varepsilon_1 + \nu\,\varepsilon_2 - Z(\chi_\xi + \nu\,\chi_\theta)\right] \quad \ldots\ldots\ldots\ldots \quad (3.11a)$$

$$\sigma_\theta = \frac{E}{1 - \nu^2}\left[\varepsilon_2 + \nu\,\varepsilon_1 - Z(\chi_\theta + \nu\,\chi_\xi)\right] \quad \ldots\ldots\ldots\ldots \quad (3.11b)$$

Substituting these in Eqns. (3.7, a-d) gives

$$N_\xi = \frac{Et}{1 - \nu^2}\left[\varepsilon_1 + \nu\,\varepsilon_2\right] \quad \ldots\ldots\ldots\ldots\ldots\ldots\ldots\ldots \quad (3.12a)$$

$$N_\theta = \frac{Et}{1 - \nu^2}\left[\varepsilon_2 + \nu\,\varepsilon_1\right] \quad \ldots\ldots\ldots\ldots\ldots\ldots\ldots\ldots \quad (3.12b)$$

$$M_\xi = -D\left[\chi_\xi + \nu\,\chi_\theta\right] \quad \ldots\ldots\ldots\ldots\ldots\ldots\ldots\ldots \quad (3.12c)$$

$$M_\theta = -D\left[\chi_\theta + \nu\,\chi_\xi\right] \quad \ldots\ldots\ldots\ldots\ldots\ldots\ldots\ldots\ldots \quad (3.12d)$$

Here we can change our notation to be consistent: ε_1 is the strain of the middle surface in the ξ direction and ε_2 in the θ direction, therefore, re-arranging (3.12a) and (3.12b),

$$C\,\varepsilon_{\xi m} = N_\xi - \nu N_\theta \quad \ldots\ldots \quad (3.13a)$$

$$C\,\varepsilon_{\theta m} = N_\theta - \nu N_\xi \quad \ldots\ldots \quad (3.13b)$$

where $C = Et.$

3.1.3 Surface definition

Consider a general shell of revolution (Figure 3.4):

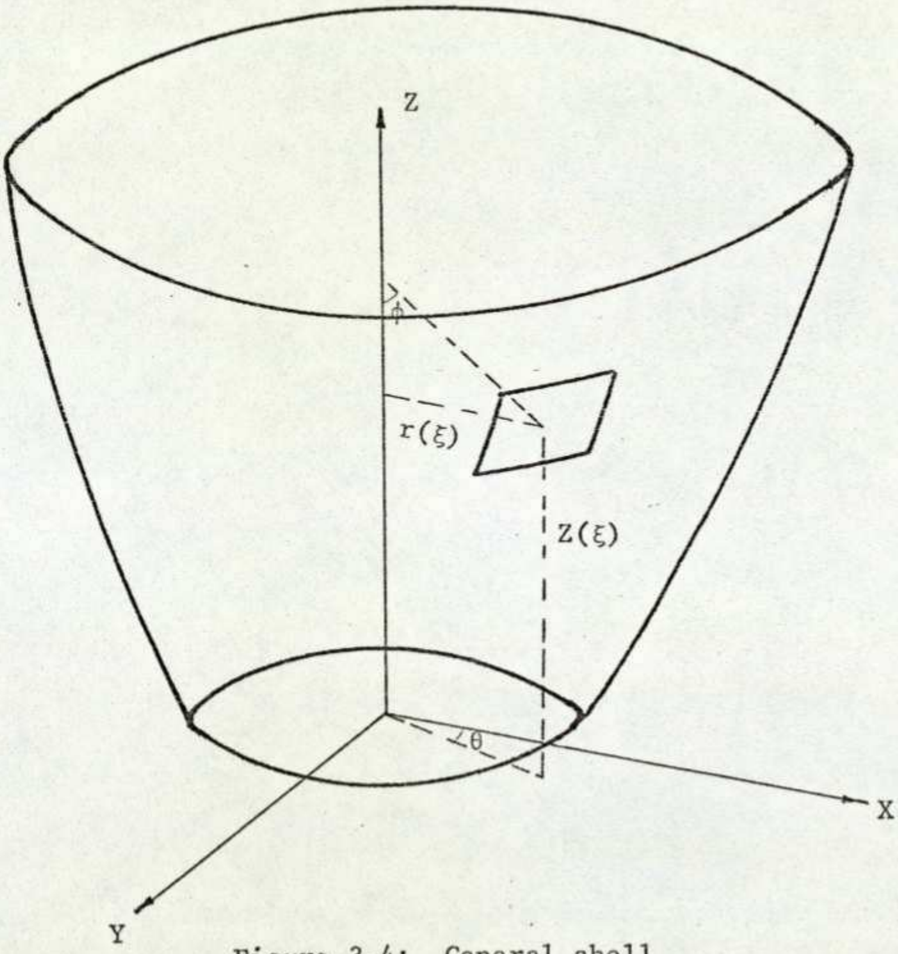

Figure 3.4: General shell

And suppose that a surface is defined by co-ordinates $r(\xi)$ and $Z(\xi)$, where ξ is a parameter on the surface.

Then, by differential geometry, the first fundamental form of such a surface, neglecting the thickness terms, is given by:

$$(ds)^2 = \alpha^2(d\xi)^2 + r^2(d\theta)^2 \quad \ldots\ldots \quad (3.14)$$

and then the condition

$$\alpha^2 = (r')^2 + (Z')^2 \text{ holds if}$$

$$\cos\phi = \frac{r'}{\alpha} \text{ and } \sin\phi = \frac{Z'}{\alpha}\ ; \quad (\ '\ ) \equiv \frac{d(\ )}{d\xi}\ .$$

Also, $R_\xi = \frac{\alpha}{\phi'}$, and $R_\theta = \frac{r}{\sin\phi}$

These are useful conditions owing to the fact that in the final formulation of the equations, the vertical height Z is eliminated and any differential of Z can be substituted for, i.e.

$$Z' = \alpha \sin\phi$$

$$Z'' = \alpha' \sin\phi + \alpha^2 \cos\phi / R_\xi$$

Hence the shell may be completely specified by knowledge of the variables r, α, ϕ and R_ξ.

3.1.4 Moment balance and compatability

Reissner derived his equations of thin shell theory from two basic equations: a moment balance,

$$(rM_\xi)' - \alpha \cos\phi\ M_\theta - \alpha(rQ) = 0 \quad \dots\dots\dots\dots\dots\dots \quad (3.15)$$

and a compatability equation,

$$(r\ \varepsilon_{\theta m})' - \alpha \cos\phi\ \varepsilon_{\xi m} + \alpha(\cos\phi_o - \cos\phi\ ) = 0 \quad \dots\dots \quad (3.16)$$

Taking the moment balance, consider two views of the small element of Figure 3.4 shown in Figures 3.5a and 3.5b:

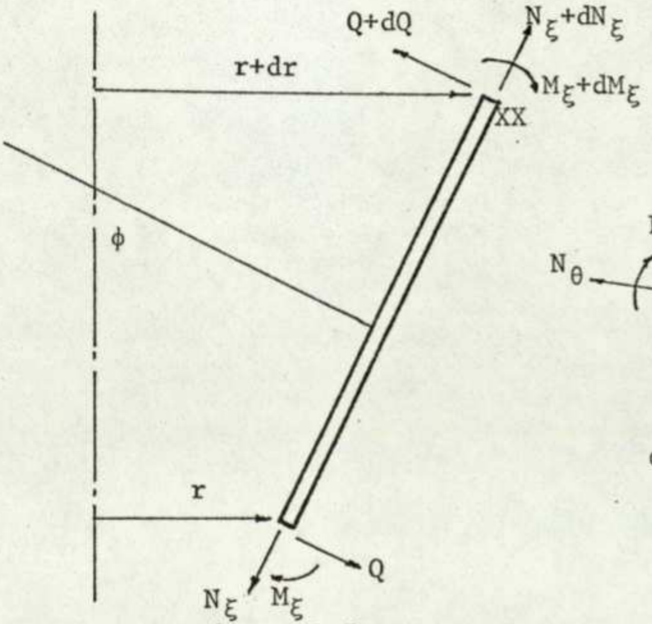

Figure 3.5a

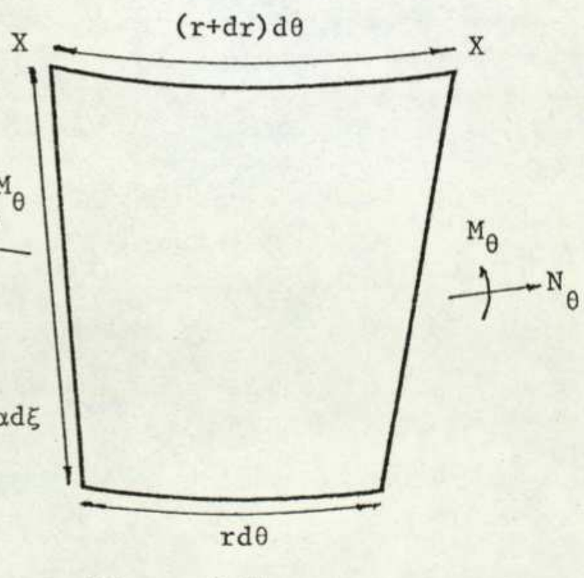

Figure 3.5b

Taking moments about XX ↻ direction,

$$(M_{\xi} + dM_{\xi})(r + dr)d\theta - M_{\xi}rd\theta - Qrd\theta d\xi\alpha - M_{\theta}\alpha d\xi \cos\phi \, d\theta \;=\; 0$$

(Terms containing the loading and body forces have been left out because they are of an order of magnitude smaller, and can be neglected any way.)

Collecting terms and dividing by dθ,

$$(M_{\xi}.dr + dM_{\xi}.r) - Qr\alpha d\xi - \alpha M_{\theta}\cos\phi d\xi \;=\; 0$$

therefore

$$(r.M_{\xi})' - \alpha\cos\phi.M_{\theta} - \alpha(rQ) \;=\; 0 \quad \ldots\ldots\ldots\ldots\ldots\ldots\ldots\ldots \quad (3.15)$$

The compatability equation, written straight down as Eqn. (3.16), arises from the Gauss-Codazzi conditions for the deformed middle surface, and will not be derived as it comes under the general topic of differential geometry; an example is given in ref. (22). Compatability basically ensures that no gaps will occur in the body during deformation.

3.1.5 Derived forces

Looking at the shell element in more detail, certain other equations and relationships may be derived, referring to Figure 3.6a and Figure 3.6b.

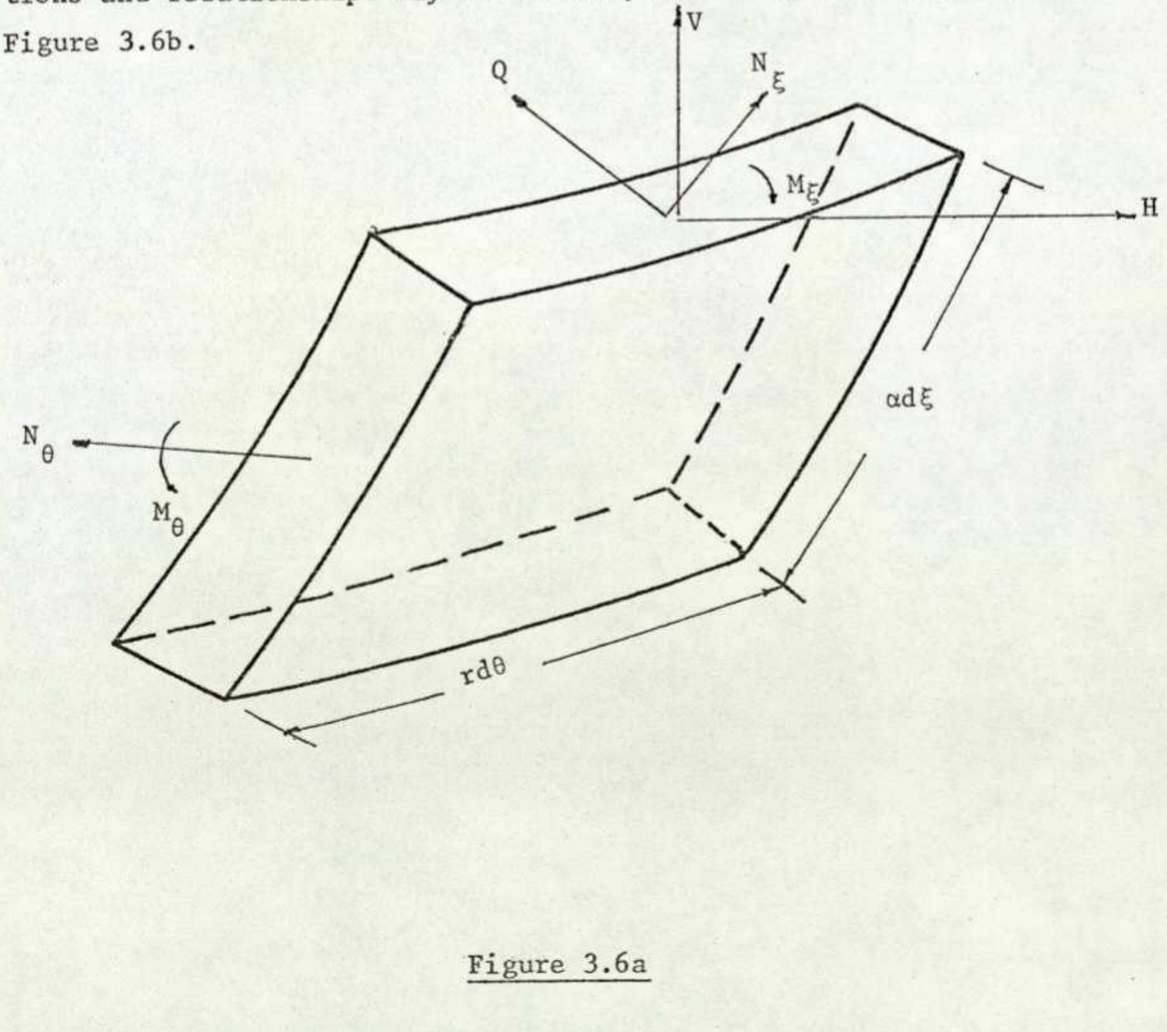

Figure 3.6a

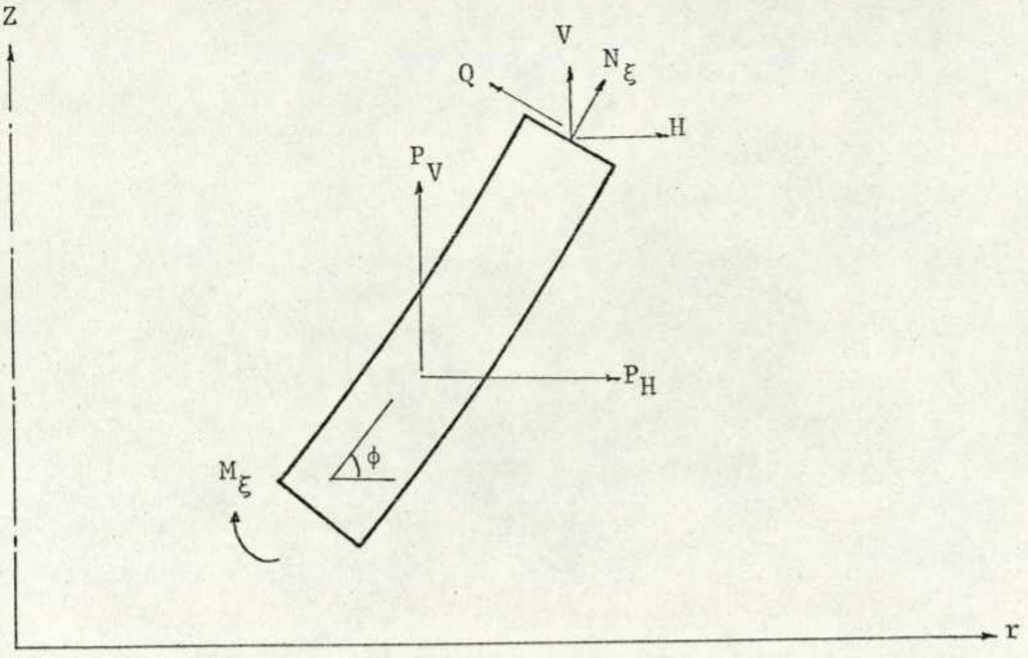

Figure 3.6b

Figure 3.6: Shell element showing derived forces

Then $N_\xi = \cos\phi \, H + \sin\phi \, V$

or $\alpha N_\xi = r'H + Z'V$ .... (3.17)

and $Q = -\sin\phi \, H + \cos\phi \, V$

or $\alpha Q = -Z'H + r'V$ .... (3.18)

It is clear that the shear force per unit length may be presented by a horizontal (H) and a vertical (V) internal force; this is a more convenient way of representing the forces because future equations are in terms of the so-called stress function $\psi = (rH)$.

Two more equations can now be derived by considering force balance in two directions. Figure 3.5a is repeated as Figure 3.7 with the relevant forces shown.

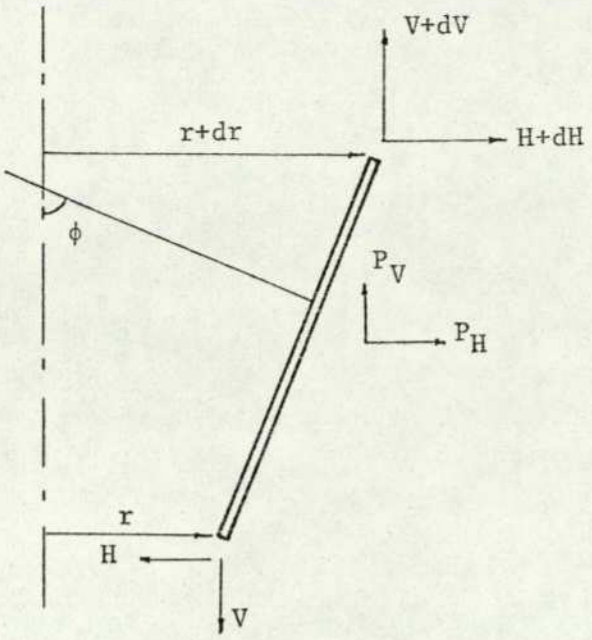

Figure 3.7: Derived and load forces

Referring to Figures 3.7 and 3.5b,

$$(H + dH)(r + dr) - Hr\ d\theta - N_\theta 2 \sin \frac{d\theta}{2}\ \alpha\ d\xi + P_H \cdot \left(r + \frac{dr}{2}\right) d\theta \alpha d\xi = 0$$

$$Hr + Hdr + rdH + dHdr - Hr - N_\theta \alpha d\xi + P_H r\alpha d\xi = 0$$

$$d(Hr) - N_\theta \alpha d\xi + P_H r\alpha d\xi = 0$$

$$(rH)' - N_\theta \alpha + P_H r\alpha = 0 \quad \ldots\ldots\ldots\ldots\ldots\ldots\ldots\ldots \quad (3.19)$$

$$(V + dV)(r + dr)d\theta - Vrd\theta + P_V\left(r + \frac{dr}{2}\right) \alpha d\xi d\theta = 0$$

$$Vrd\theta + Vdrd\theta + rdVd\theta + dVdrd\theta - Vrd\theta + P_V r\alpha d\xi d\theta + P_V \frac{dr}{2}\ \alpha d\xi d\theta = 0$$

$$r.dV + V.dr + P_V r\alpha d\xi = 0$$

$$= \ (rV)' + P_V r\alpha \quad \ldots\ldots\ldots\ldots\ldots\ldots\ldots\ldots\ldots\ldots \quad (3.20)$$

3.1.6 Reissner's Equations

From the foregoing expressions two simultaneous second order differential equations with variable coefficients can be derived. The two independent variables being the rotation β and the product of the radial distance and horizontal internal force (r.H) called the stress function ψ. These two equations are linear and are derived in Appendix 1; to be able to carry out the derivation the assumptions of thin shell theory have to be applied to Eqns. (3.15), (3.16), (3.12c) and (3.12d).

Equations (3.15) and (3.16) are:

$$(r\ M_\xi)' - \alpha\ \cos\phi\ M_\theta - \alpha(rQ) = 0$$

$$(r\ \varepsilon_{\theta m})' - \alpha\ \cos\phi\ \varepsilon_{\xi m} + \alpha(\cos\phi_o - \cos\phi) = 0$$

From the relationships of the surface, $\cos\phi = \frac{r'}{\alpha}$ therefore

$$(r\ M_\xi)' - r'\ M_\theta - \alpha(rQ) = 0 \quad \ldots\ldots\ldots\ldots\ldots\ldots\ldots \quad (3.21)$$

and $(\cos\phi_o - \cos\phi) = \cos\phi_o - \cos(\phi_o - \beta)$

If β is defined as $\beta = \phi_o - \phi$, therefore $\phi = \phi_o - \beta$

$$= \cos\phi_o - \left[\cos\beta\ \cos\phi_o + \sin\beta\ \sin\phi_o\right]$$

Again from assumption 2 β is very small

$$(\sin\phi \doteq \sin\phi_o = Z'/\alpha)$$

$$= -\beta\ \sin\phi_o = -\beta\ Z'/\alpha$$

therefore

$$(r\ \varepsilon_{\theta m})' - r'\ \varepsilon_{\xi m} - \beta\ Z' = 0 \quad \ldots\ldots\ldots\ldots\ldots\ldots\ldots \quad (3.22)$$

Equations (3.12c) and (3.12d):

$$M_\xi = -D\left[\chi_\xi + \nu\ \chi_\theta\right]$$

$$M_\theta = -D\left[\chi_\theta + \nu\ \chi_\xi\right]$$

and $\left(\frac{1}{\bar{R}_\xi} - \frac{1}{R_\xi}\right) = \chi_\xi$

$$\left(\frac{1}{\bar{R}_\theta} - \frac{1}{R_\theta}\right) = \chi_\theta,$$

where $(\bar{\ })$ refers to the deformed shell.

From our general surface definition:

$$\chi_\xi = \frac{\phi'}{\alpha} - \frac{\phi_o{}'}{\alpha} = -\frac{\beta'}{\alpha} \quad \ldots\ldots\ldots\ldots\ldots\ldots\ldots \quad (3.23)$$

$$\chi_\theta = \left(\frac{\sin\phi}{r} - \frac{\sin\phi_o}{r}\right) = -\frac{r'\beta}{r\alpha} \quad \ldots\ldots\ldots\ldots\ldots\ldots \quad (3.24)$$

The two equations thus obtained as (A1.6) and A1.17):

$$\beta'' + \frac{(rD/\alpha)'}{(rD/\alpha)}\ \beta' - \left[\left(\frac{r'}{r}\right)^2 - \nu\ \frac{(rD/\alpha)'}{(rD/\alpha)}\right]\beta + \frac{Z'}{(rD/\alpha)}\psi \ = \ \frac{r'(rV)}{(rD/\alpha)}$$

$$\psi'' + \frac{(r/C\alpha)'}{(r/C\alpha)}\ \psi' - \left[\left(\frac{r'}{r}\right)^2 + \frac{\nu(r'/C\alpha)}{(r/C\alpha)}\right]\psi - \frac{Z'}{(r/C\alpha)}\ \beta \ =$$

$$\left[\frac{Z'r'}{r^2} + \nu\ \frac{(Z'/C\alpha)'}{(r/C\alpha)}\right](rV) + \nu\ \frac{Z'}{r}\ (rV)' -$$

$$\left[\frac{(r/C\alpha)'}{(r/C\alpha)} + \nu\ \frac{r'}{r}\right](r\ \alpha\ P_H) - (r\ \alpha\ P_H)'$$

The dependent terms of the two equations contain only variables described by the geometric and material properties of the shell plus the loading terms and the vertical reaction force (rV). Assuming that it is possible to know the parameters required for the geometry and material properties, etc., it then remains to express the loading terms in known quantities.

From Eqn. (3.2),

$$(rV)' \ = \ -r\ \alpha\ P_V$$

therefore

$$(rV) \ = \ \int -r\ P_V\ \alpha\ d\xi$$

If the axi-symmetric loading is a pressure P(say), then from Figure 3.7,

$$P_V \ = \ P\cos\phi$$
$$P_H \ = \ -P\sin\phi$$

(P acting on the outside of the shell)

$$(rV) \ = \ \int -r\ P\ \cos\phi\ \alpha\ d\xi$$

and $\cos\phi = \frac{r'}{\alpha} \ = \ \frac{dr}{\alpha d\xi}$

$$(rV) \ = \ -P\int r\ dr \ = \ -\frac{Pr^2}{2} + \text{constant}$$

Hence (rV) may be expressed as a simple loading term, plus a constant which can be evaluated by considering the static equilibrium (Figure 3.8).

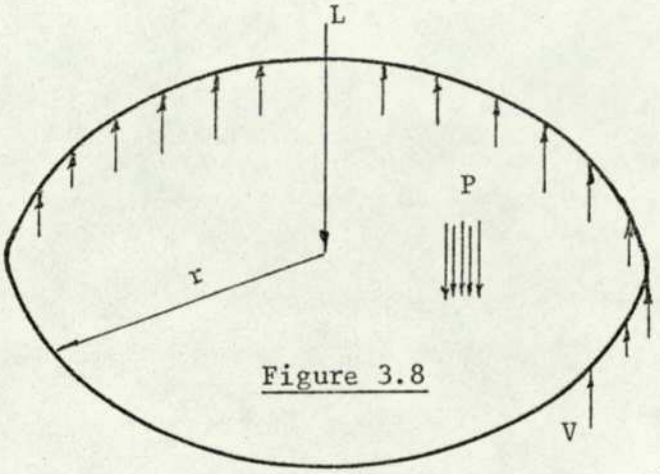

Figure 3.8

Consider the loading on a disc at a general radius r

$= P \pi r^2 + L,$ where P = pressure

L = load at centre

(Note only axi-symmetric loading).

This is then balanced by $2\pi rV$ around the edge of this fictitious disc, therefore $P\pi r^2 + L + 2\pi rV = 0$.

Then
$$(rV) = -\left(\frac{Pr^2}{2} + \frac{L}{2\pi}\right) \quad \ldots\ldots\ldots\ldots\ldots\ldots\ldots\ldots \quad (3.25)$$

In many cases

L = Zero, and

$$(rV) = -\frac{Pr^2}{2} .$$

From the solution of the two equations β and ψ are obtained. Then the stress resultants N_θ, N_ξ, M_θ, and M_ξ can be found by direct substitution from equations (3.12c), (3.12d), (3.23), (3.24), (3.19), and (3.17). Finally, the displacements may be found by substitution and integration.

3.1.7 Horizontal and vertical displacements

Horizontal displacement (U)

From Eqn. (3.13b),

$$\varepsilon_{\theta m} = \frac{1}{C}(N_\theta - \nu N_\xi)$$

This is the circumferential strain of the mid-plane. If strain is defined generally as the increase in length divided by the original length, then at any radial distance r the circumferential distance = $2\pi r$. Suppose after deformation this circumferential distance is increased to $2\pi\bar{r}$, when $\bar{r} = r + dr$ (Figure 3.9).

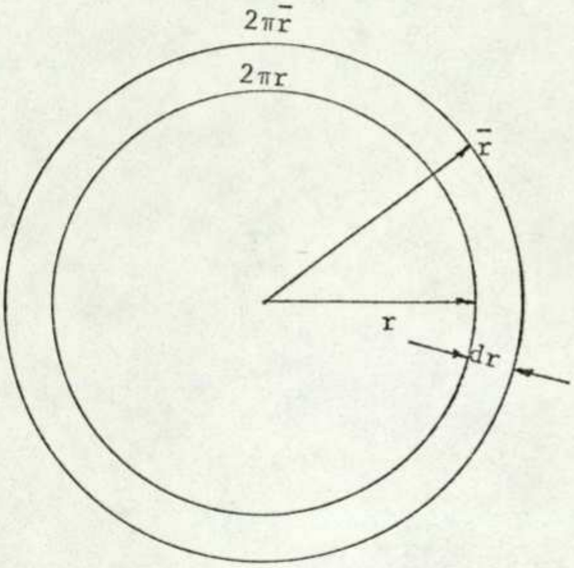

Figure 3.9

Then $$\varepsilon_{\theta m} = \frac{2\pi\,(r + dr) - 2\pi\, r}{2\,\pi\, r} = dr$$

The value dr is then the horizontal displacement U.

Hence, $$U = \frac{r}{C}\,(N_\theta - \nu\, N_\xi) \qquad (3.26)$$

Vertical displacement (W)

Considering the vertical displacement of an elemented ring dW as the sum of the bending and stretching effects due to the loading, i.e. the combined effect of rotation and radial strain:

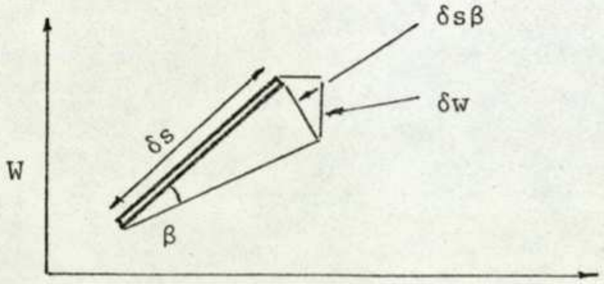

Figure 3.10a: Rotation

Figure 3.10a, the effect of rotation, gives

$$\delta w|_{\beta\,\text{only}} = -\,\beta\,\cos\phi\,\delta s.$$

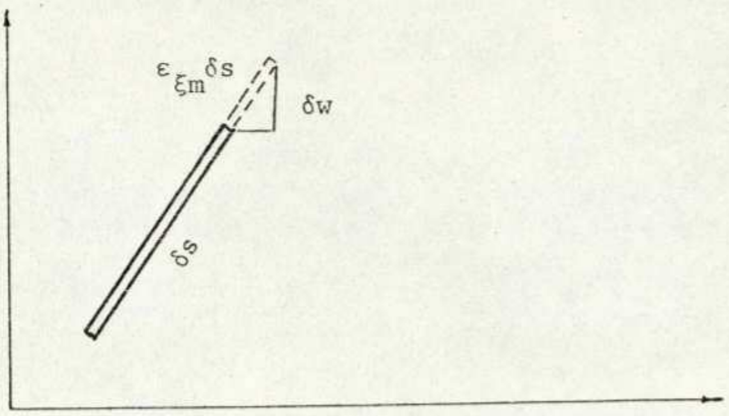

Figure 3.10b: Stretching

Figure 3.10b, the effect of direct straining, gives

$$\delta w\Big|_{\text{strain only}} = \varepsilon_{\xi m}\,\delta s\,\sin\phi,$$

therefore

$$\delta w = (\varepsilon_{\xi m}\sin\phi - \beta\cos\phi)\delta s$$

and in the limit

$$W = \int(\varepsilon_{\xi m}\sin\phi - \beta\cos\phi)ds \tag{3.27}$$

3.1.8 Method of solution of the equations

From the chapter on previous work and the discussions arising from the results of other researchers, the most hopeful, if not yet rewarding, method of solution of a shell of complex structure like a corrugated diaphragm would be finite differences. The main disadvantage in the past has been the inadequacies of methods for solving a necessarily large number of linear simultaneous equations, quickly and accurately. Implementation of a finite difference program meant that the generator of the diaphragm had to be divided up into a number of finite different stations not necessarily equally spaced along the curve (Figure 3.11).

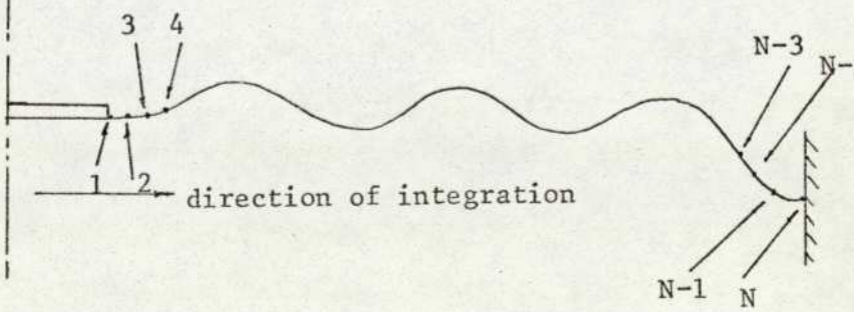

Figure 3.11: Diaphragm generator

The choice of the number of points and the direction of integration are discussed later, as they depend on having a solution anyway.

From Eqn. (3.14) it is seen that the independent variable is ξ which is related to the distance along the generator by $ds = \alpha d\xi$.

For the model we are at liberty to choose a value of α and for the linear model in particular this value will be constant; the obvious choice is unity, so $ds = d\xi$. It is fortuitous that S becomes the independent variable because any other variable would have drawbacks when considering a general shell shape. Z would be no good for a flat plate and r just as unsuitable for a cylinder.

For the formulation of the equations it was convenient to space the finite difference stations at equal distances along the curve. This was not necessary, but it does considerably simplify the coefficients. Central finite differences were chosen to represent the first and second derivatives at the i^{th} point.

$$\left(\frac{d\beta}{ds}\right)_i = \frac{\beta_{i+1} - \beta_{i-1}}{2(\delta s)} \quad \ldots\ldots\ldots\ldots\ldots\ldots\ldots\ldots\ldots \quad (3.28)$$

where $\delta s = S_{i+1} - S_i$ $\quad \left(\frac{d^2\beta}{ds^2}\right)_i = \frac{\beta_{i+1} - 2\beta_i + \beta_{i-1}}{(\delta s)^2}$

The associated error can be shown to be for the second derivative

$$-\frac{(\delta s)^2}{12} \cdot \Omega_1 \, y^{IV}(\zeta_1) \qquad \text{ref. (23)}$$

and the first derivative

$$-(\delta s)^2 \cdot \Omega_2 \, y^{III}(\zeta_2),$$

where $|\Omega_1|, |\Omega_2| \leq 1$, $S_{i-1} \leq \zeta_1$, $S_{i+1} \geq \zeta_2$

and $y^{III}(\zeta_2)$ and $y^{IV}(\zeta_1)$ represent the maximum (absolute) value of the respective derivatives in the interval (S_{i-1}, S_{i+1}).

The next step is to re-write equations (A1.6) and (A1.17) in a more manageable way:

$$\frac{d^2\beta}{ds^2} + A\frac{d\beta}{ds} + B\beta + \bar{E}\psi = F$$

$$\frac{d^2\psi}{ds^2} + G\frac{d\psi}{ds} + H\psi + J\beta = K \qquad (3.29a)$$

where $\quad A = \frac{(rD)'}{rD}, \quad B = -\left[\left(\frac{r'}{r}\right)^2 - \nu\frac{(r'D)'}{(rD)}\right],$

$$\bar{E} = \frac{Z'}{rD}, \qquad G = \frac{(r/C)'}{r/C},$$

$$H = - \left[\left(\frac{r'}{r}\right)^2 + \nu \, \frac{(r'/C)'}{(r/C)} \right], \quad J = - \frac{Z'}{r/C} , \quad \left. \begin{matrix} K \\ F \end{matrix} \right) = \text{loading terms.}$$

Then, if the generator is divided into N finite mesh points, we obtain at the i^{th} point, combining (3.28) and (3.29a),

$$\begin{aligned} \frac{\beta_{i+1} - 2\beta_i + \beta_{i-1}}{(\Delta S)^2} + A_i \frac{\beta_{i+1} - \beta_{i-1}}{2\Delta S} + B_i \, \beta_i + \bar{E}_i \, \psi_i &= F_i \\ \frac{\psi_{i+1} - 2\psi_i + \psi_{i-1}}{(\Delta S)^2} + G_i \frac{\psi_{i+1} - \psi_{i-1}}{2\Delta S} + H_i \, \psi_i + J_i \, \beta_i &= K_i \end{aligned} \qquad (3.29b)$$

and collecting terms:

$$\begin{aligned} a_i \, \beta_{i+1} - b_i \, \beta_i + c_i \, \beta_{i-1} + d_i \, \psi_i &= f_i \\ e_i \, \psi_{i+1} - g_i \, \psi_i + h_i \, \psi_{i-1} + j_i \, \beta_i &= k_i \end{aligned} \qquad \ldots\ldots\ldots\ldots\ldots \quad (3.30a)$$

If a multiplication of $(\Delta S)^2$ is made, then:

$$\begin{aligned} & a_i = 1 + \frac{\Delta S}{2} A_i, \quad b_i = -2 + (\Delta S)^2 \, B_i, \quad c_i = 1 - \frac{\Delta S}{2} A_i, \\ & d_i = \bar{E}_i (\Delta S)^2, \quad f_i = F_i (\Delta S)^2, \quad e_i = 1 + \frac{\Delta S}{2} G_i, \qquad (3.30b) \\ & g_i = -2 + (\Delta S)^2 \, H_i, \quad h_i = 1 - \frac{\Delta S}{2} G_i, \quad f_i = J_i (\Delta S)^2 , \quad k_i = K_i (\Delta S)^2 \end{aligned}$$

The variables a_i, b_i, etc. have now to be presented in a programable form, e.g.

$$A_i = \frac{(rD)'}{rD} = \frac{r'D + D'r}{rD} = \frac{r'}{r} + \frac{D'}{D} = \frac{\cos\phi}{r} + \frac{3}{t}\frac{dt}{ds} .$$

(For generality, the material thickness is a variable, but for most problems it is assumed constant; then $\frac{dt}{ds}$ = zero.)

$$B_i = - \left[\left(\frac{r'}{r}\right)^2 - \nu \left(\frac{r'D}{rD}\right)' \right]_i = - \left[\left(\frac{\cos\phi}{r}\right)^2 - \nu \left(\frac{\sin\phi}{r \, R_\xi} + \frac{3}{t} \frac{\cos\phi}{r} \frac{dt}{ds} \right) \right]_i$$

$$\bar{E}_i = \left(\frac{Z'}{rD}\right) = \left(\frac{\sin\phi}{rD}\right)_i$$

$$F_i = \frac{r'}{rD} \, (rV)_i = \left(\frac{\cos\phi}{rD} \, (rV) \right)_i$$

$$G_i = \frac{(r/C)'}{r/C} = \left(\frac{\cos\phi}{r} - \frac{1}{t} \frac{dt}{ds} \right)_i$$

$$H_i = -\left[\left(\frac{r'}{r}\right)^2 + \nu\,\frac{(r'/C)'}{r/C}\right]_i = -\left[\left(\frac{\cos\phi}{r}\right)^2 - \nu\left\{\frac{\sin\phi}{r\,R_\xi} + \frac{\cos\phi}{r}\;\frac{1}{t}\,\frac{dt}{ds}\right\}\right]_i$$

$$J_i = \left(-\frac{Z'}{r/C}\right)_i = \left(\frac{C}{r}\sin\phi\right)_i$$

$$K_i = \left[\frac{Z'r'}{r^2} + \nu\,\frac{(Z'/C)'}{r/C}\right](rV)_i + \nu\,\frac{Z'}{r}(rV)_i' - \left[\frac{(r/C)'}{r/C} - \nu\left(\frac{r'}{r}\right)\right](r\,P_H)_i - (r\,P_H)_i' = \left[\frac{\cos\phi\,\sin\phi}{r^2} + \nu\left\{\frac{\cos\phi}{r\,R_\xi} - \frac{\sin\phi}{r}\,\frac{1}{t}\,\frac{dt}{ds}\right\}\right]_i (rV)_i - (\nu\sin\phi\,P\cos\phi)_i$$

$$r\,P\sin\phi\left[\frac{\cos\phi}{r} - \frac{1}{t}\,\frac{dt}{ds} + \nu\,\frac{\cos\phi}{r}\right]_i - P\cos\phi\left[\sin\phi + \frac{r}{R_\xi}\right]_i$$

Now, if we know r, ϕ, R_ξ, E, t, ν, P, (rV), at every i^{th} point along the generator we have all the required information to find β and ψ at every i^{th} point. R, ϕ, R_ξ will come from the consideration of the geometry, E and ν are constant, and t is assumed constant, (although this is not absolutely true); P is a uniform pressure (constant), and (rV) was derived in an earlier section. The type of formulation usually leads to a matrix equation of the form $[A]\,\{x\} = \{b\}$.

Expanding and partitioning would give us:

$$\left[\begin{array}{c|c} A_1 & B_1 \\ \hline B_2 & A_2 \end{array}\right] \left[\begin{array}{c} \beta \\ \hline \psi \end{array}\right] = \left[\begin{array}{c} F \\ \hline K \end{array}\right]$$

where $[A_1] = \begin{bmatrix} b_1 & a_1 & & \\ c_2 & b_2 & a_2 & \\ & c_3 & b_3 & a_3 \\ & & & \\ & & & \end{bmatrix}$ and $[A_2] = \begin{bmatrix} g_1 & e_1 & & \\ h_2 & g_2 & e_2 & \\ & h_3 & g_3 & e_3 \\ & & & \\ & & & \end{bmatrix}$

two square tri-diagonal matrices

and $[B_1] = \begin{bmatrix} d_1 & & & \\ & d_2 & & \\ & & d_3 & \\ & & & \ddots \end{bmatrix}$ and $[B_2] = \begin{bmatrix} j_1 & & & & \\ & j_2 & & & \\ & & j_3 & & \\ & & & j_4 & \\ & & & & \ddots \end{bmatrix}$

two square diagonal matrices.

A method of solution was sought which was both fast and accurate, as well as being economical on computer storage. The method chosen was a step-by-step procedure, i.e. one in which the solution at each mesh point is derived from the solutions previously obtained. In order to accomplish this the equations had to be written in the following form:

$$\begin{aligned} \beta_j &= (BC)_j + (BB)_j\,\beta_{j+1} + (BH)_j\,\psi_{j+1} \\ \psi_j &= (HC)_j + (HB)_j\,\beta_{j+1} + (HH)_j\,\psi_{j+1} \end{aligned} \qquad \ldots\ldots\ldots\ldots\ldots \quad (3.31)$$

where β_j and ψ_j at each mesh point are expressed in terms of β_{j+1} and ψ_{j+1} at each mesh point: $(BC)_j$, $(BB)_j$, ... and so on, are constants and represent coefficients to be determined for each point. If there are N mesh points, then β_N and ψ_N can be obtained from the boundary conditions, and equations (3.31) will provide β_j and ψ_j for $j = 1, 2, 3 \ldots (N - 1)$ by recursion. Equations (3.31) are themselves obtained recursively by substituting the expressions (3.31) for β_j and ψ_j into equations (3.30) written for mesh point j+1, which thus provide two simultaneous equations in β_{j+1}, ψ_{j+1}, β_{j+2}, ψ_{j+2}. These can, in turn, be solved for β_{j+1} and ψ_{j+1}, resulting in Eqns. (3.31) for mesh point j+1.

This method used is essentially Gaussian elimination which assumes diagonal dominance. The algorithm for this is contained in Appendix 2.

3.1.9 Boundary conditions

At the boundary β and ψ need to be known explicitly. At the centre the rotation is assumed zero as well as the horizontal displacement U: this is a reasonable assumption owing to the axi-symmetric shape and finite stiffness coefficients (bending and tensile). At the outer edge (periphery) the boundary conditions are to some extent arbitrary, but two situations seemed the most reasonable to consider:

(a) that of a clamped edge (Figure 3.12a)

(b) and a "free edge" (Figure 3.12b).

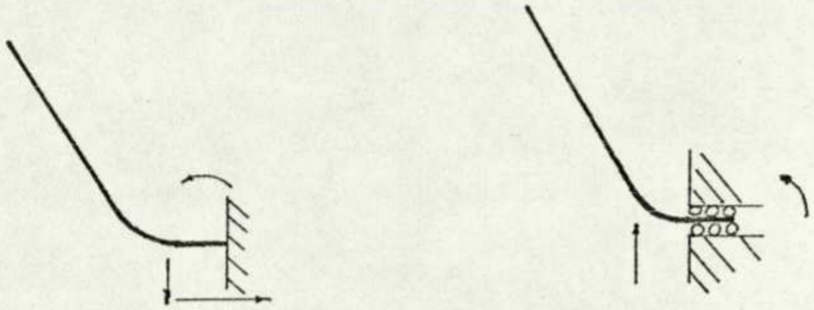

Figure 3.12a   Figure 3.12b

Figure 3.12: end conditions

The arrows in Figure 3.12 indicate the directions in which the end of the diaphragm is constrained from moving, therefore for

case (a) $W_N = 0$, $U_N = 0$, $\beta_N = 0$, and for

case (b) $W_N = 0$ and $\beta_N = 0$,

implying free horizontal movement, and hence $\psi_N = 0$.

For the centre, and for case (a) at the periphery, ψ must be inferred from the horizontal displacements which are zero in both cases.

From the equations derived earlier:

$$U = \frac{r}{C}(N_\theta - \nu N_\xi) \quad \ldots\ldots \quad (3.26)$$

$$\text{and} \quad \psi' - N_\theta + r P_H = 0 \quad \ldots\ldots \quad (3.19)$$

Now $N_\xi = H \cos\phi - V \sin\phi \quad (\alpha = 1)$

therefore

$$\frac{U}{r} C = N_\theta - \nu (H \cos\phi - V \sin\phi)$$

and substituting for N_θ and since U = zero,

$$\nu \left(\psi \frac{\cos\phi}{r} - (Vr) \frac{\sin\phi}{r} \right) = \psi' + r P_H$$

Now at the centre put $\psi' = \psi_2 - \psi_1/\Delta S$

$$\text{so} \quad \psi_1 \left(\frac{\cos\phi_1}{r_1} \right) - (Vr)_1 \frac{\sin\phi_1}{r_1} = \frac{\psi_2}{\nu\Delta S} - \frac{\psi_1}{\nu\Delta S} + \frac{(r P_H)_1}{\nu}$$

$$\psi_1 \left(\frac{\cos\phi_1}{r_1} + \frac{1}{\Delta S\nu} \right) = \frac{\sin\phi_1}{r_1} (Vr)_1 + \frac{(r P_H)_1}{\nu} + \frac{\psi_2}{\Delta S\nu}$$

therefore, $\psi_1 = K^I\psi_2 + K^{II}$, where K^I, K^{II} are constants.

In a similar way an expression for ψ_N may be obtained in terms of ψ_{N-1} using constants K^{III} and K^{IV}. This will add a complication to the solution algorithm and Eqn. (A2.6) will then become:

$$\psi_2 = k_2 - h_2\ (K^I\psi_2 + K^{II}) + -\frac{e_2}{g_2}\ \psi_3 + -\frac{j_2}{g_2}\ \beta_2$$

$$\psi_2 = \frac{k_2 - h_2\ K^{II}}{(g_2 + h_2\ K^I)} + \left(-\frac{e_2}{(g_2 + h_2\ K^I)}\right)\psi_3 + -\frac{j_2}{(g_2 + h_2\ K^I)}\ \beta_2$$

therefore in Eqn. (A2.8) $k_2 - h_2\ \psi_1$ becomes $k_2 - h_2\ K^{II}$, and and g_2 becomes $g_2 + h_2\ K^I$.

In the backward substitution to find β_i and ψ_i, $i = 2,3,4 \dots (N-1)$

$$\beta_{N-1} = (BC)_{N-1} + (BB)_{N-1}\ \beta_N + (BH)_{N-1}\ \psi_N$$

$$\psi_{N-1} = (HC)_{N-1} + (HB)_{N-1}\ \beta_N + (HH)_{N-1}\ \psi_N$$

$$\text{but}\quad \psi_N = \psi_{N-1}\ K^{III} + K^{IV}.$$

Therefore, if β_N = zero,

$$\psi_{N-1} = \frac{(HC)_{N-1}}{1 - (HH)_{N-1}\ K^{III}} + \frac{K^{IV}}{1 - (HH)_{N-1}\ K^{III}}$$

and $\beta_{N-1} = (BC)_{N-1} + (BH)_{N-1}\ (\psi_{N-1}\ K^{III} + K^{IV})$

and the loop starts at the N-2 elimination.

3.1.10 Numerical accuracy

The accuracy of a finite difference formulation is mainly dependent on the mesh size, and traditionally there has always been a trade-off between the truncation error and the round-off error. The truncation error is dependent upon the formulation, i.e. forward differences, centre differences, etc. and mesh size, the error decreasing as the mesh decreases. The round-off error is machine-dependent and is caused by subtracting two numbers whose difference is very small, and hence because the machine is only able to work to a certain number of significant digits, an error will certainly be generated.

By consideration of the computer used, the possibility of round-off errors was assessed to be negligible; the CDC 7600 computer used for this programing works to about the same number of significant digits in single precision as most computers work in double precision, i.e. 15. The problem then reduces to one of finding the minimum amount of truncation error which will give good results without increasing the dimensions of the problem unnecessarily. Schricker, ref. (13) undertook a direct comparison on the vertical deflection between his model and that of Wildhack et al, ref. (11); the overall deflection came out to be too small for 72 mesh points and the result just too great for 124 mesh points. He concluded then that a figure of 120 would be right. This might have given some confidence in his work but for the fact that in his programs he used only 106 mesh points, and also the shape of the diaphragm with which he compared his was not a typical diaphragm of the type he tested against experiment.

Whilst it was thought that a routine for generating a certain number of mesh points, dependent upon the geometry of the diaphragm, was not necessary, the program was written in a general form where the number of points N (say) was the first parameter set, and hence could be very simply adjusted if, say, a nine-corrugation diaphragm with small convolutions was being analysed. For a general value of N the radius of curvature was considered the limiting factor and the smallest practical radius found on production diaphragms was approximately 0.025" (0.635 mm). Now to put at least two mesh points on a segment this size would require a mesh of about 200 points. This proved to be a satisfactory general value for N, as the results from the experimental validation will show. To try to improve on this result an extrapolation routine was used: this was Richardson's deferred approach to a limit.

For a finite difference method the errors are of the order $(\delta s)^2$ so that for an arbitrary point we may write:

$$e(S) = c(S)\,(\delta s)^2 + \ldots\ldots\ldots$$

Neglecting the higher order terms, for a given point we have

$$e = c(\delta s)^2$$

in which c is an undetermined coefficient.

Now if the integration has been performed in the interval (a, b), which is then divided first into n_1 then n_2 equal parts:

$$\delta s_1 = \frac{b - a}{n_1}, \quad \delta s_2 = \frac{b - a}{n_2}$$

Let A_{n1} and A_{n2} be the corresponding values obtained for the unknown at the same point, and let A be the probable value, then the errors obtained in each of the two steps of the calculation are

$$e_1 = A - A_{n1} \doteqdot \frac{c(b - a)^2}{n_1^2}$$

$$e_2 = A - A_{n2} \doteqdot \frac{c(b - a)^2}{n_2^2}$$

Eliminating $c(b - a)^2$ and finding A explicitly, we obtain the so-called extrapolation formula in $(\delta s)^2$,

$$A = A_{n1}, A_{n2} = \alpha_1 A_{n1} + \alpha_2 A_{n2} = A_{n2} + \alpha_1 (A_{n1} - A_{n2}),$$

in which

$$\alpha_1 = -\frac{n_1^2}{n_2^2 - n_1^2} \qquad \alpha_2 = \frac{n_2^2}{n_2^2 - n_1^2} .$$

A program was written which took the ratio $\frac{n_2}{n_1} = 2$

therefore $\alpha_1 = -\frac{1}{3}$ and $\alpha_2 = 1\frac{1}{3}$

the values of $\beta_i\Big|_{n1}$ and $\psi_i\Big|_{n1}$ for $i = 1, 2 \ldots\ldots\ldots n_1$, where $n_1 = 200$

were found, then $\beta_i\Big|_{n2}$ and $\psi_i\Big|_{n2}$ for $i = 1, 2 \ldots\ldots n_2$, where $n_2 = 399$.

399 has to be used and not the intended 400 because of spacing, i.e.

$$\delta s_1 = \frac{(b - a)}{(n_1 - 1)} = \frac{(b - a)}{199}$$

and $$\delta s_2 = \frac{(b - a)}{(n_2 - 1)} = \frac{(b - a)}{398}$$

therefore $2(\delta s_1) = \delta s_2$.

Then
$$\beta_i = \frac{4}{3} \beta_{2i-1}\Big|_{n2} - \frac{1}{3} \beta_i\Big|_{n1}$$
$$(i = 1 \ldots\ldots 200)$$
$$\psi_i = \frac{4}{3} \psi_{2i-1}\Big|_{n2} - \frac{1}{3} \psi_i\Big|_{n1}$$

This routine gave an improvement of less than 1 per cent to the overall deflection when a three-corrugation diaphragm was being programmed, and increased the computational time by approximately 2.5 times. Nevertheless the program was still felt to be useful for analysing large diaphragms with many convolutions.

All the displacements and forces are found by direct substitution of β and ψ, or their first derivatives expect the vertical deflection which is an integration.

The integral being known at every i^{th} point,

$$\left(\frac{dW}{ds}\right)_i = (\varepsilon_{\xi m} \sin\phi - \beta\cos\phi)_i$$

A "Runga-Kutta" type integration was thought unnecessary to find $W_i (i = 1,2 \ldots\ldots N)$, therefore $\left(\frac{dW}{ds}\right)_i$ was formed into central differences and W solved by working in from the periphery.

Therefore $W_i = W_{i-2} - 2\,ds(\varepsilon_{\xi m} \sin\phi - \beta \cos\phi)_{i-1}$

This is only worth noting because as the deflection reached the flat centre portion, the value oscillated slightly due to the very small changes in $\left(\frac{dW}{ds}\right)_i$. This was smoothed out by taking the average of the central difference and single-sided forward difference approximation (F.D.A).

$$(\text{F.D.A.}) = W_i = W_{i-1} - ds(\varepsilon_{\xi m} \sin - \beta \cos\phi)_{i-1}$$

$$\text{therefore } W_i = \frac{(W_{i-1} + W_{i-2})}{2} - \frac{3}{2}\,ds(\varepsilon_{\xi m} \sin\phi - \beta \cos\phi)_{i-1} \quad .. \ (3.32)$$

3.1.11 Model versatility

The capabilities of the linear model, whether inferred from the previous sections or not, are listed below:

(1) Two types of edge clamping (section 3.1.9);
(2) Temperature effects;
(3) Variation in thickness;
(4) Loading - pressure and point;
(5) Initial stress at outer boundary.

(1) needs no elaboration as it is fully discussed in the section on boundary conditions, other than to consider the results. Figure 3.13 shows the vertical deflection for a diaphragm with the two types of edge

clamping under the same loading conditions; generally the clamped edge deflects about 5 per cent more than the free edge - not a very practical result for diaphragms alone, but useful for work on capsules of the aneroid box type.

(2) Temperature effects can be programmed as a positive or negative temperature gradient along the diaphragm generator: temperature gradients through the thickness of the diaphragm were not considered. The additional terms required are $-C(\bar{\alpha}\ T)'$ to the left hand side of the ψ equation, and the displacement equations become:

$$U = \frac{r}{C}\left(N_\theta - \nu N_\xi\right) + \bar{\alpha}\ T \quad \ldots\ldots\ldots\ldots\ldots\ldots \quad (3.33)$$

$$W = \int \left(\sin\phi_o \left(\varepsilon_{\xi m} + \bar{\alpha}\ T\right) - \beta \cos\phi_o\right) ds \quad \ldots\ldots\ldots\ldots \quad (3.34)$$

where $\bar{\alpha}$ = temperature coefficient of linear expansion,
T = temperature above that of zero stress and strain.

Therefore $-C(\bar{\alpha}\ T)' = -C\ \bar{\alpha}\ \frac{dT}{ds}$ assuming $\bar{\alpha}$ constant.

Now $\frac{dT}{ds}$ can be reduced to $\frac{dT}{dr}\cos\phi$.

Therefore $-C\ \bar{\alpha}\ \frac{dT}{dr}\cos\phi$ .... (3.35)

For most applications $\frac{dT}{ds}$ = zero and the diaphragm will only experience an overall temperature rise. A typical result of just applying a temperature rise is shown in Figure 3.14.

(3) From a practical point of view a diaphragm will vary in thickness along its generator, but observations have shown this to be quite small and, in the absence of any knowledge of exactly how the variation occurs, the effect is generally neglected. Diaphragms analysed were assumed to be of the same thickness as the original blank. To indicate that the effect of thickness variation was small, a metallurgical specimen was prepared for a particular production diaphragm and the actual thickness at a number of points measured and the variation programmed. These results are discussed in the chapter on experimental validation.

(4) Both pressure and point load at the centre, or both, may be applied to the diaphragm: in fact, numerically any axi-symmetric

Figure 3.13

The Variation of Computed Variables against radial distance (measured out from the centre boss) for a diaphragm undergoing pressure loading. (The solid lines represent the 'clamped' condition at the outer edge; the dotted the 'free' condition)

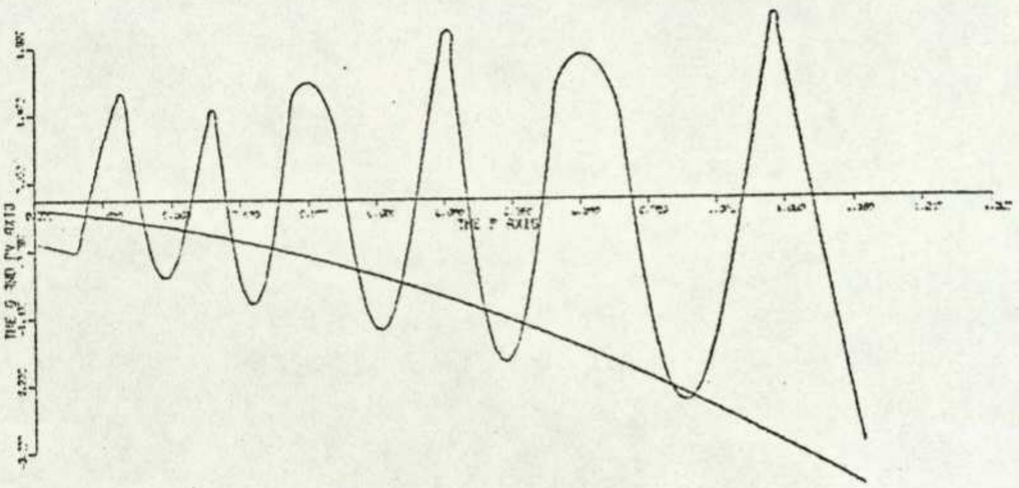

Normal shear force and (rV) loading

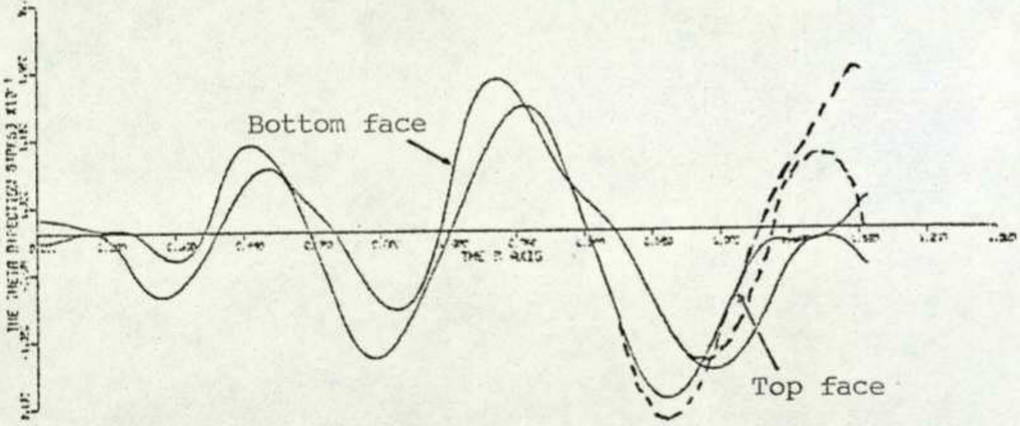

Circumferential stress

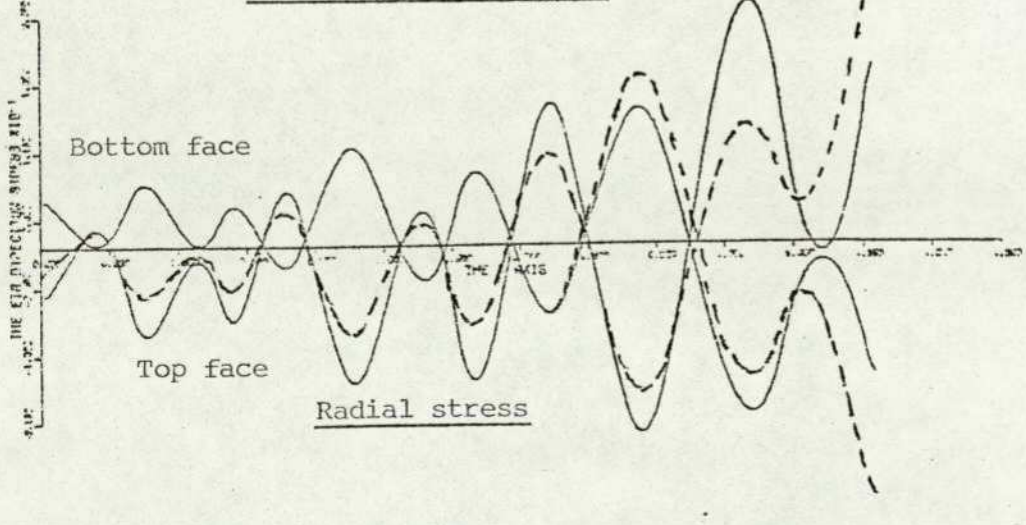

Radial stress

figure cont'd

Figure 3.13

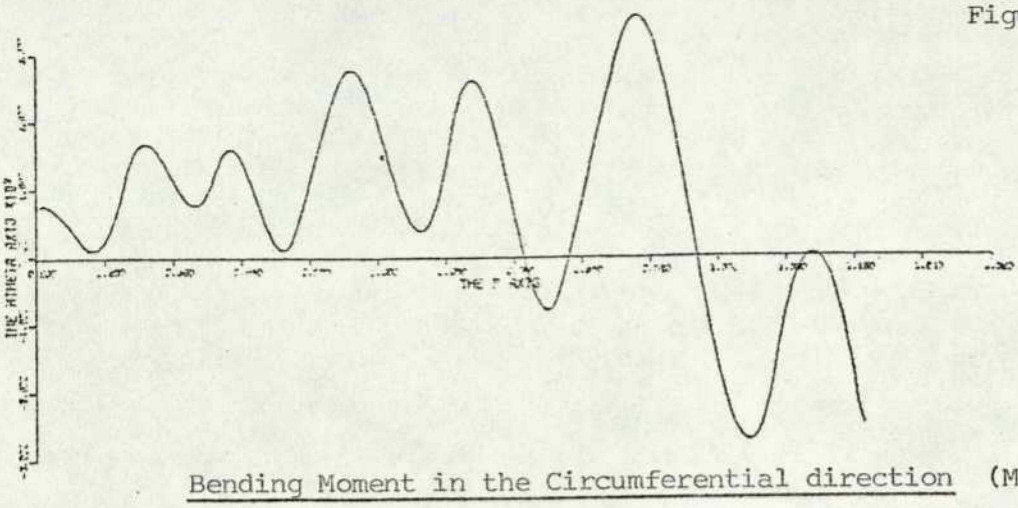

Bending Moment in the Circumferential direction (M_{θ})

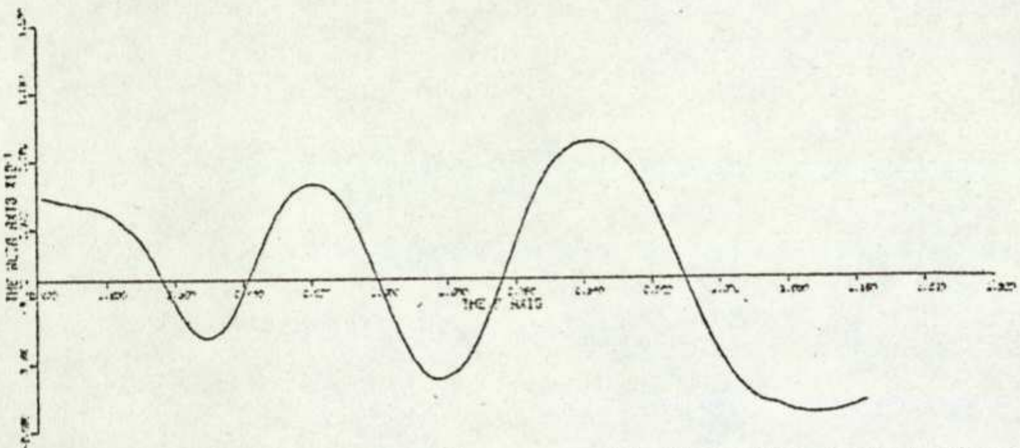

Stress resultant in the radial direction (N_{ξ})

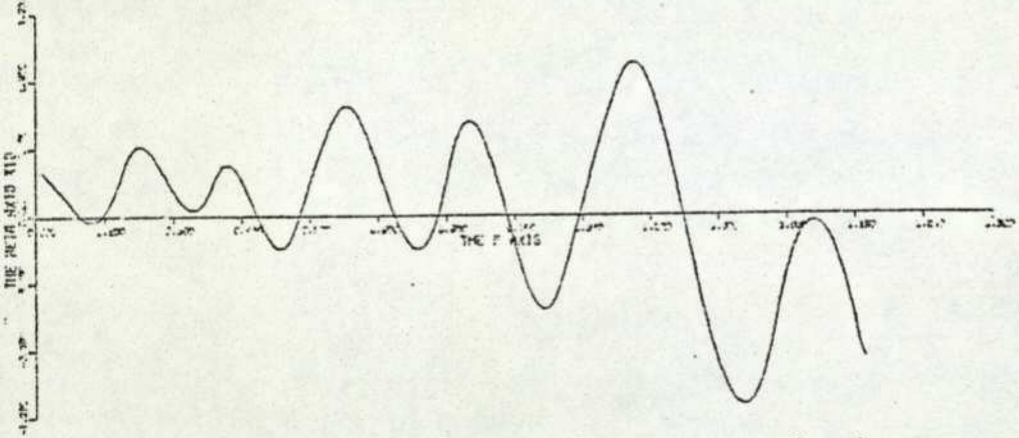

Bending Moment in the radial direction (M_{ξ})

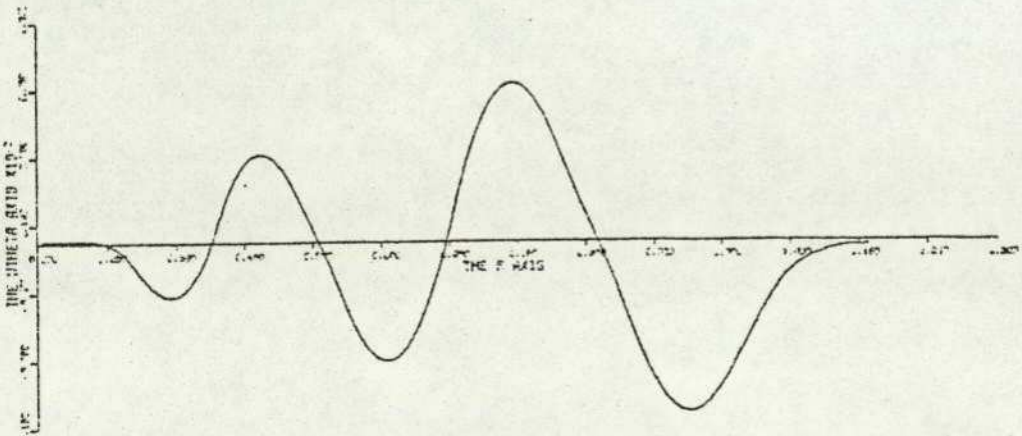

Stress resultant in the circumferential direction (N_{θ})

figure cont'd

Figure 3.13

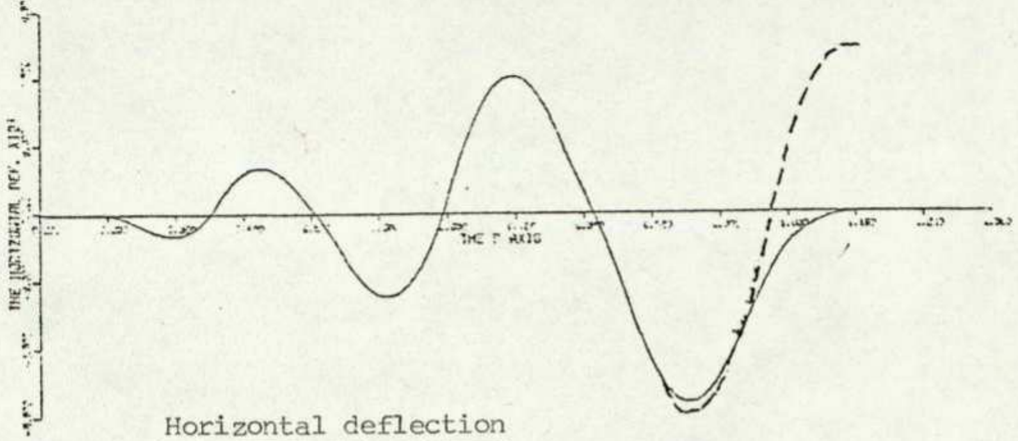

Horizontal deflection

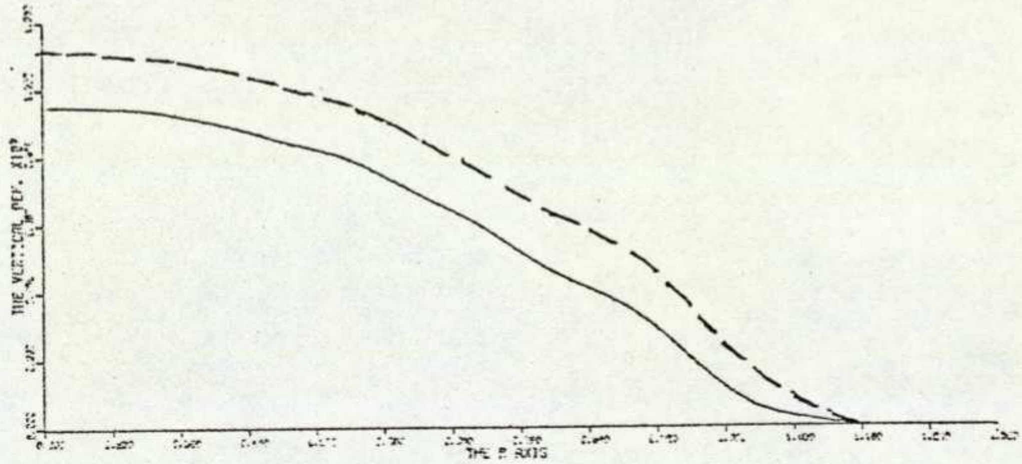

Vertical deflection

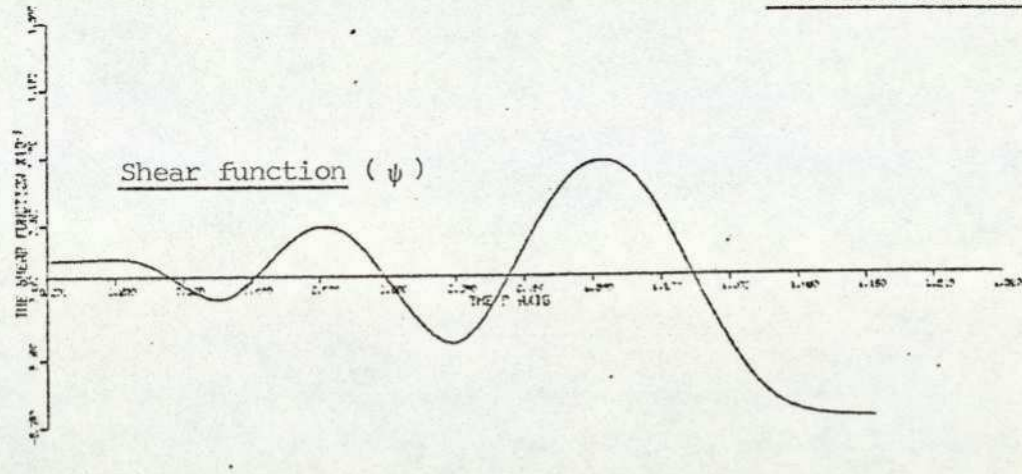

Shear function (ψ)

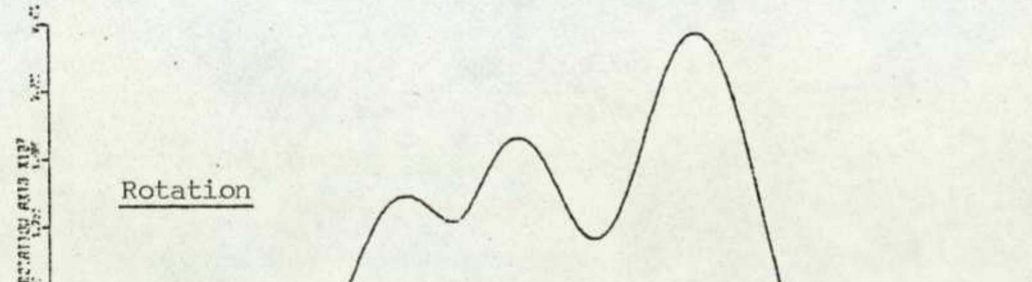

Rotation

Figure 3.14

The Variation of Computed Variables against radial distance (measured out from the centre boss) for a diaphragm subjected to an overall temperature rise

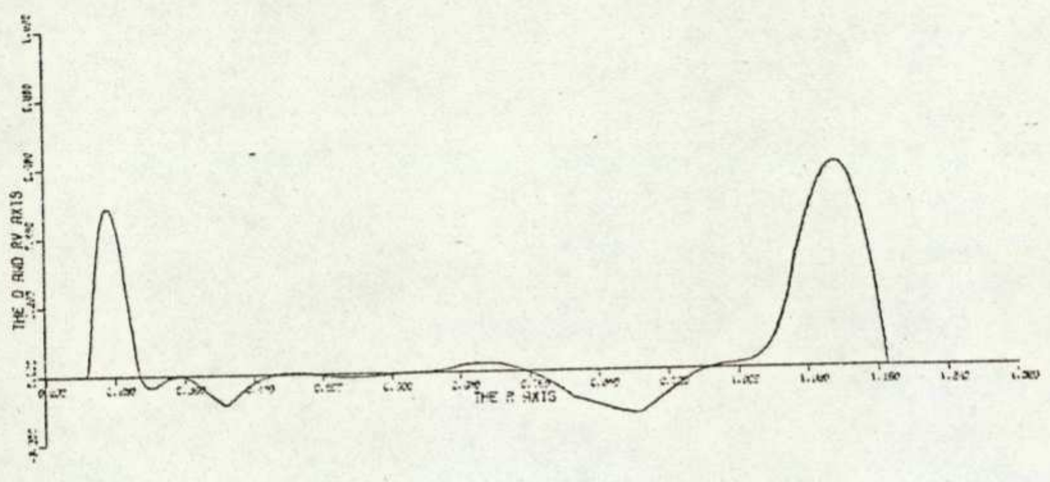

Normal shear force

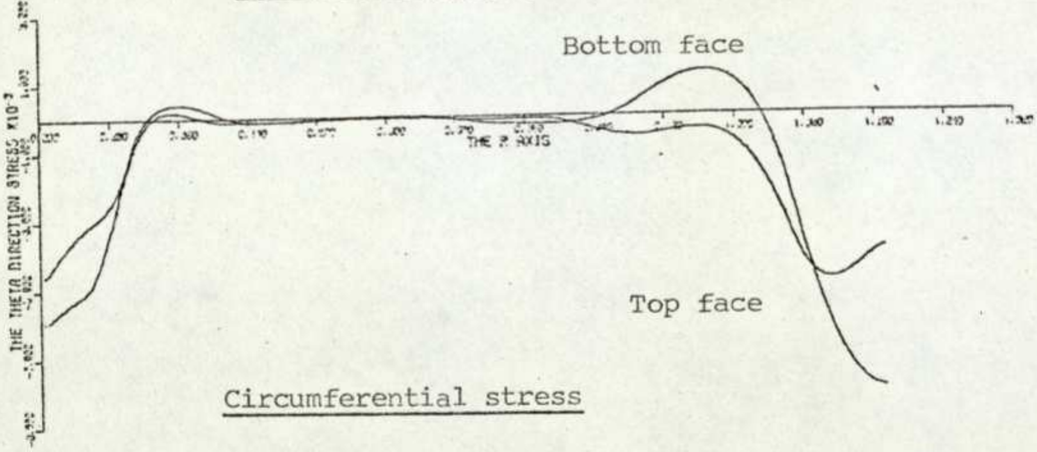

Circumferential stress

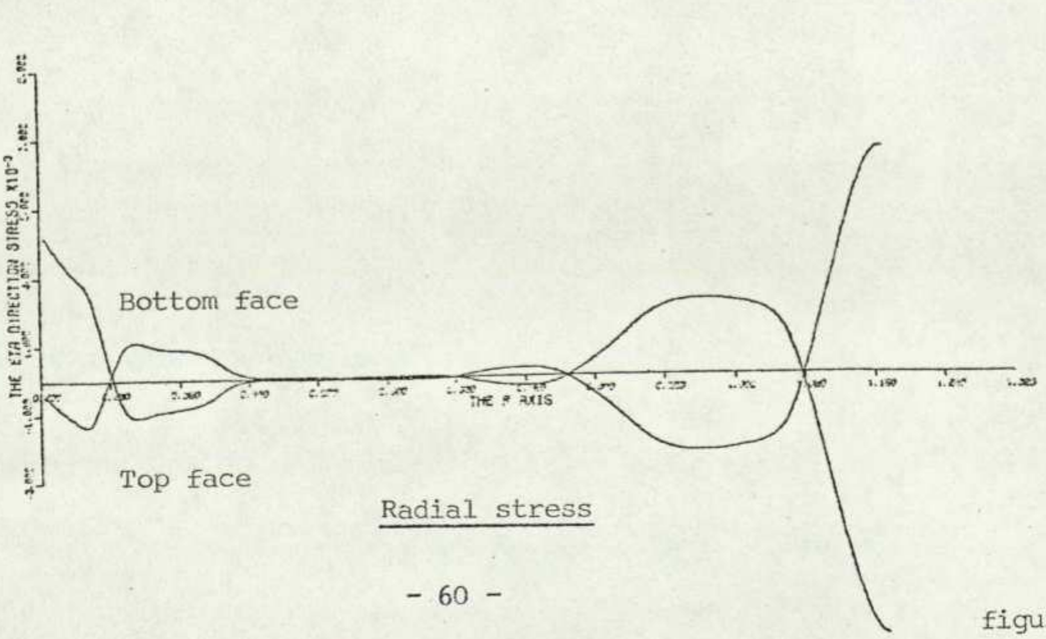

Radial stress

figure cont'

Figure 3.14

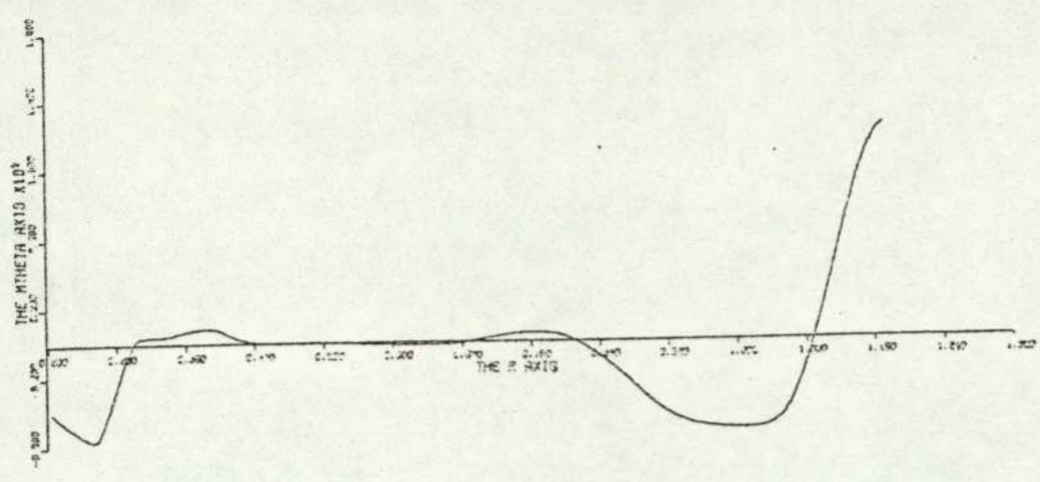

Bending Moment in the Circumferential direction (M_{θ})

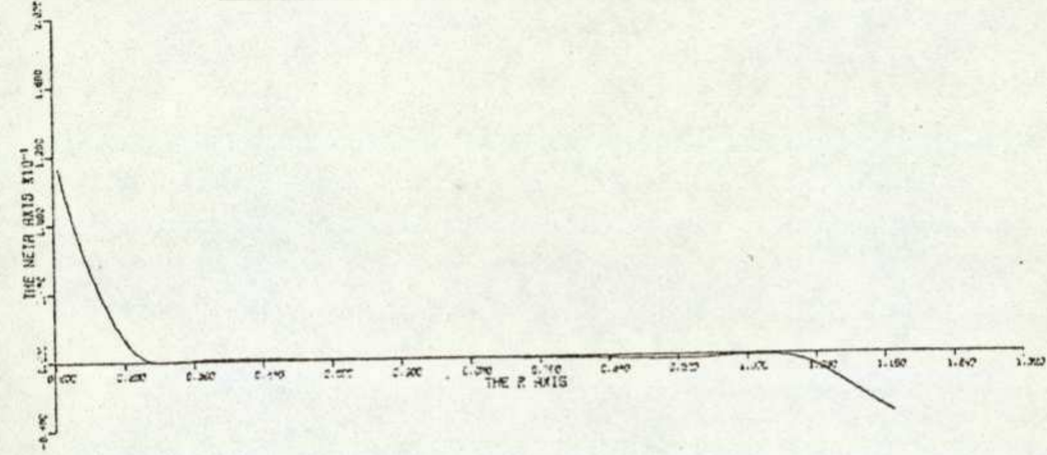

Stress resultant in the radial direction (N_{ξ})

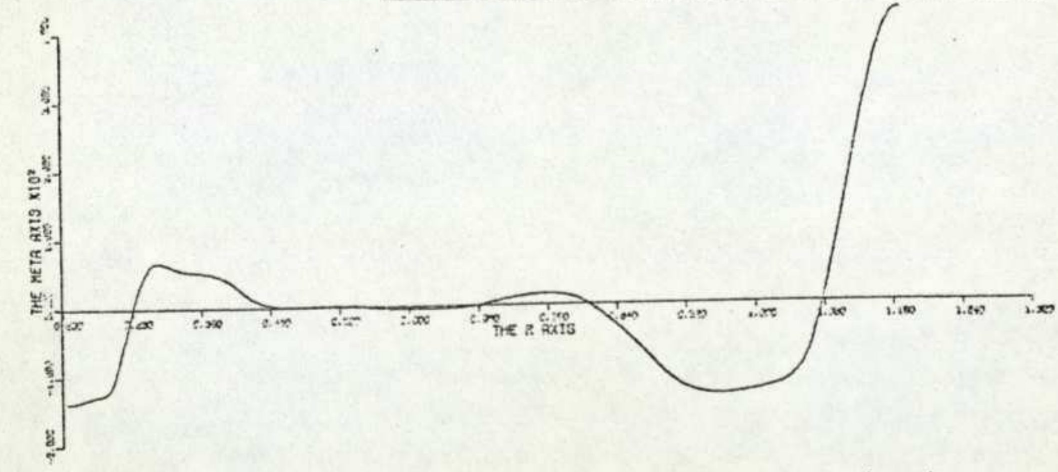

Bending Moment in the radial direction (M_{ξ})

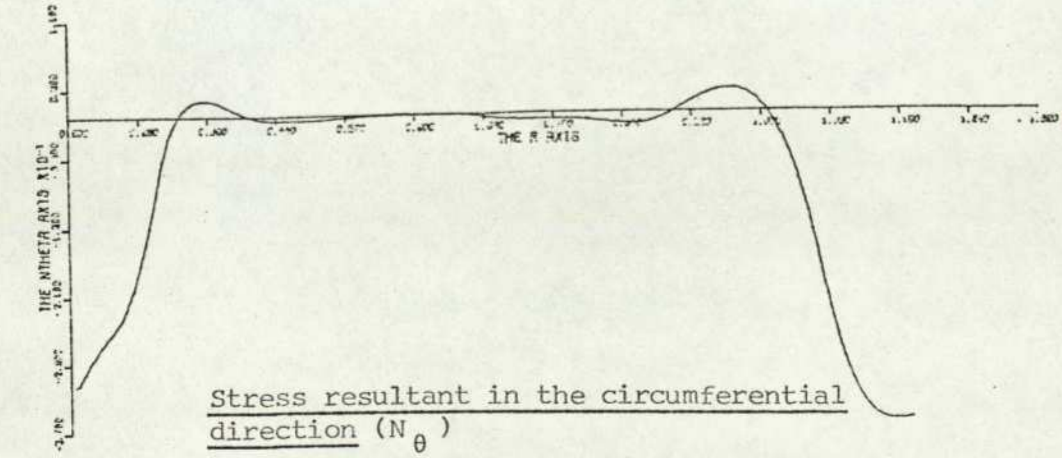

Stress resultant in the circumferential direction (N_{θ})

figure cont'd

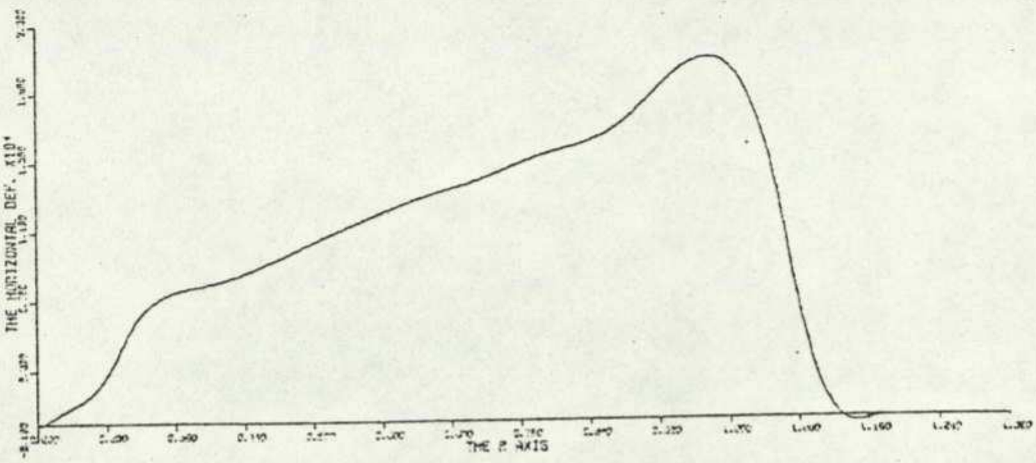

Horizontal deflection

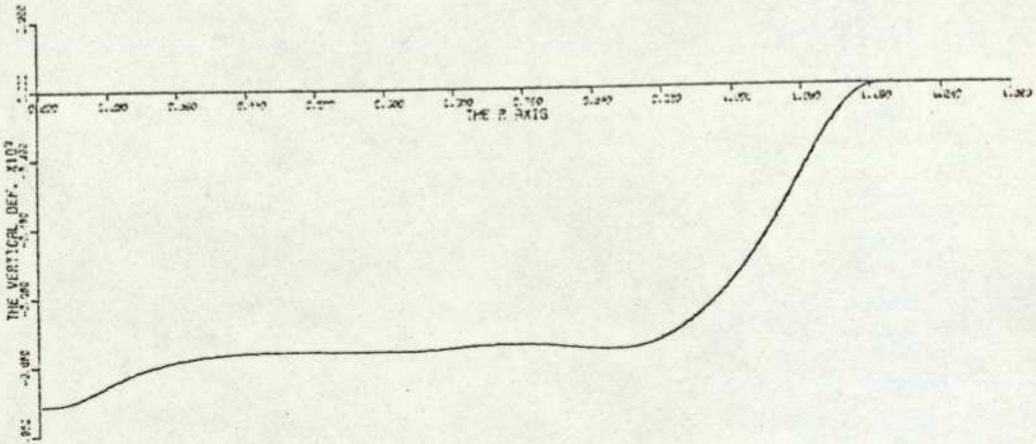

Vertical deflection

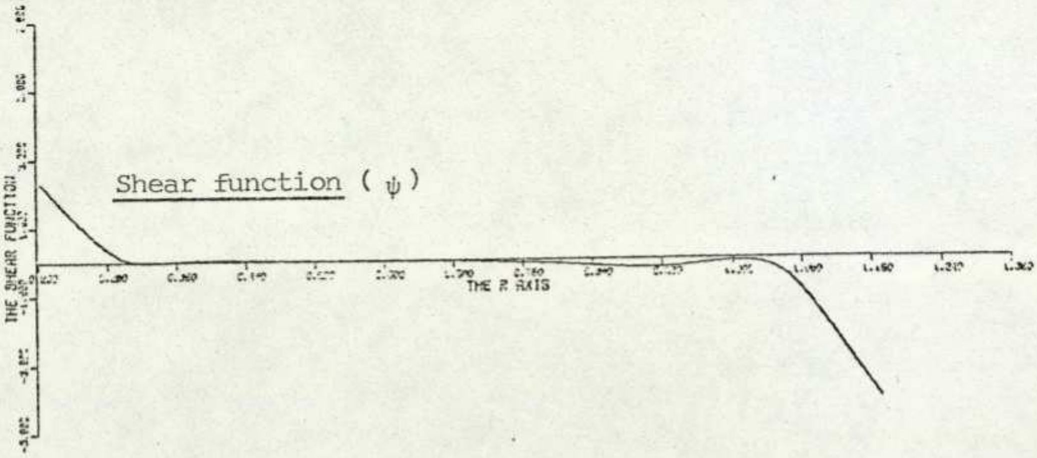

Shear function (ψ)

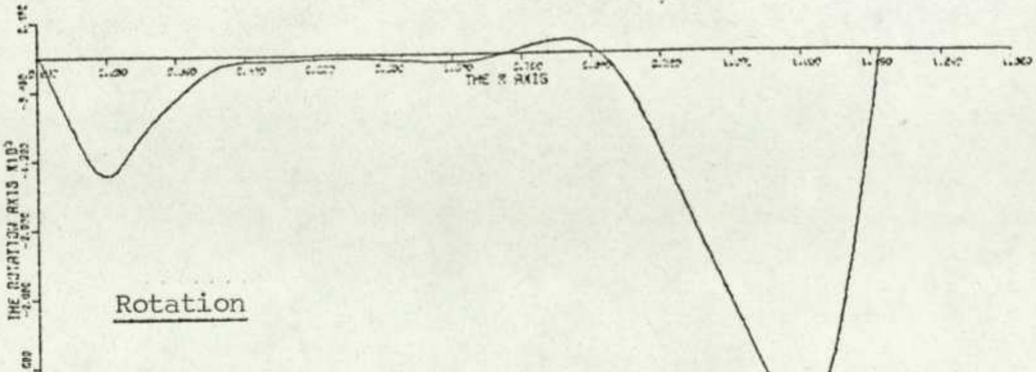

Rotation

Figure 3.15

The Variation of Computed Variables against radial distance (measured out from the centre boss) for a diaphragm loaded by a mass at the centre. (The solid lines represent the 'clamped' condition at the outer edge; the dotted the 'free' condition)

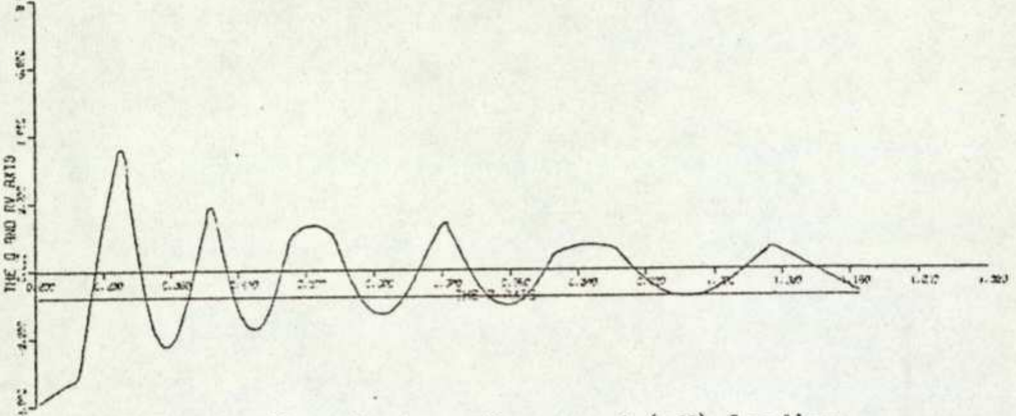

Normal shear force and (rV) loading

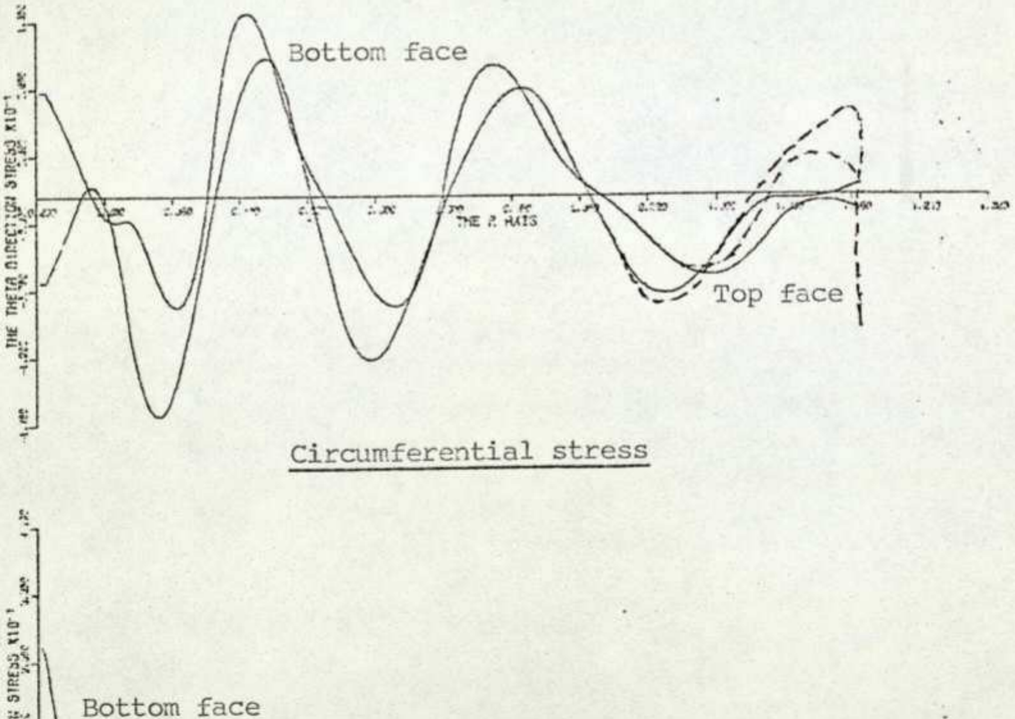

Circumferential stress

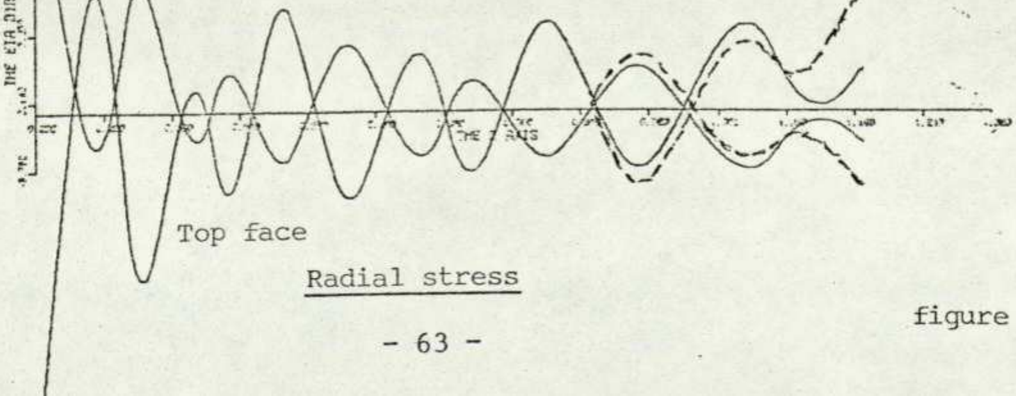

Radial stress

figure cont'd

Figure 3.15

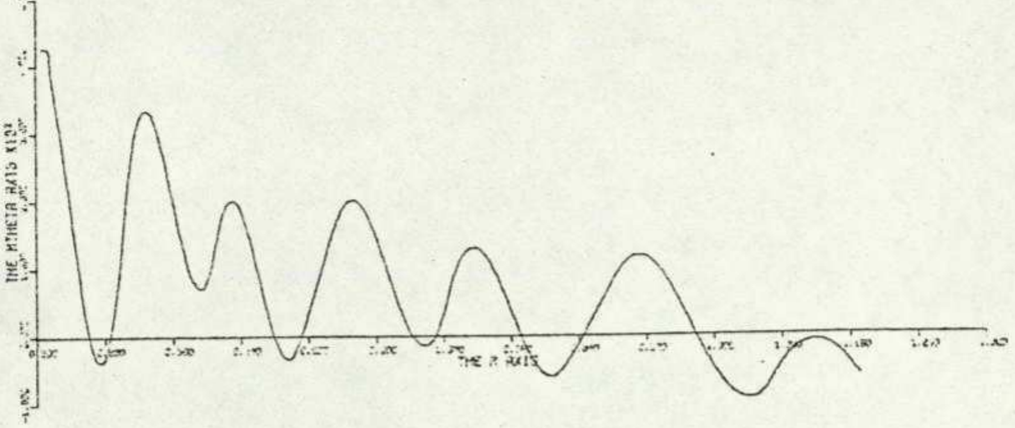

Bending Moment in the Circumferential direction (M_{θ})

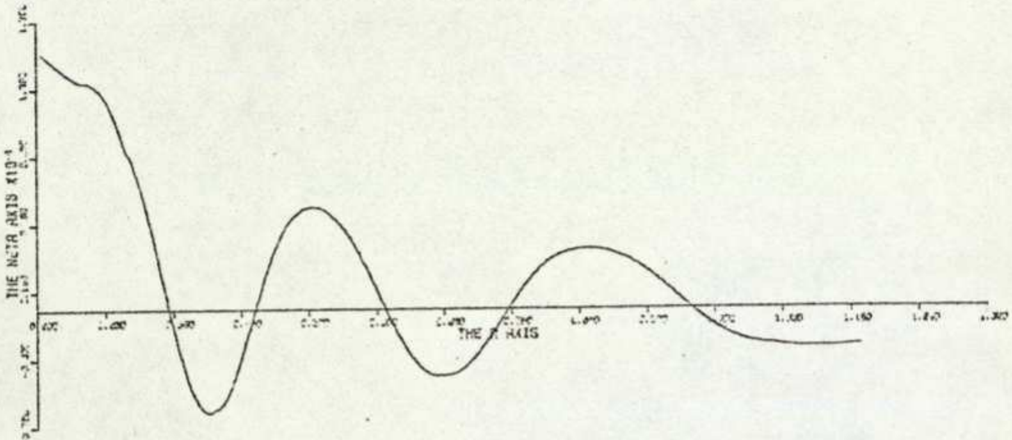

Stress resultant in the radial direction (N_{ξ})

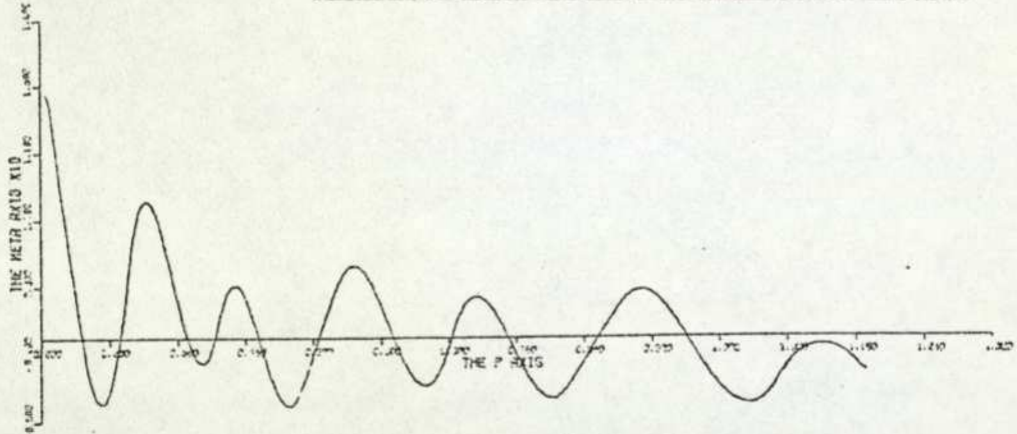

Bending Moment in the radial direction (M_{ξ})

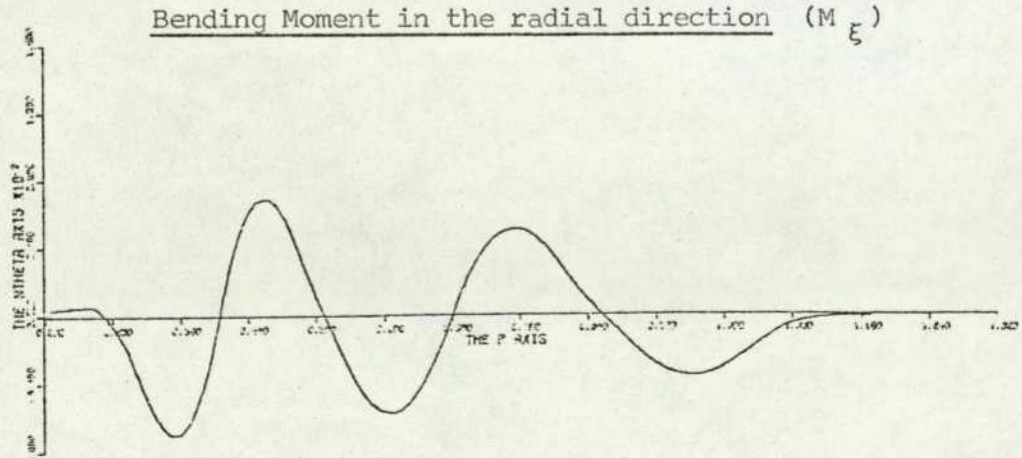

Stress resultant in the circumferential direction (N_{θ})

Figure 3.15

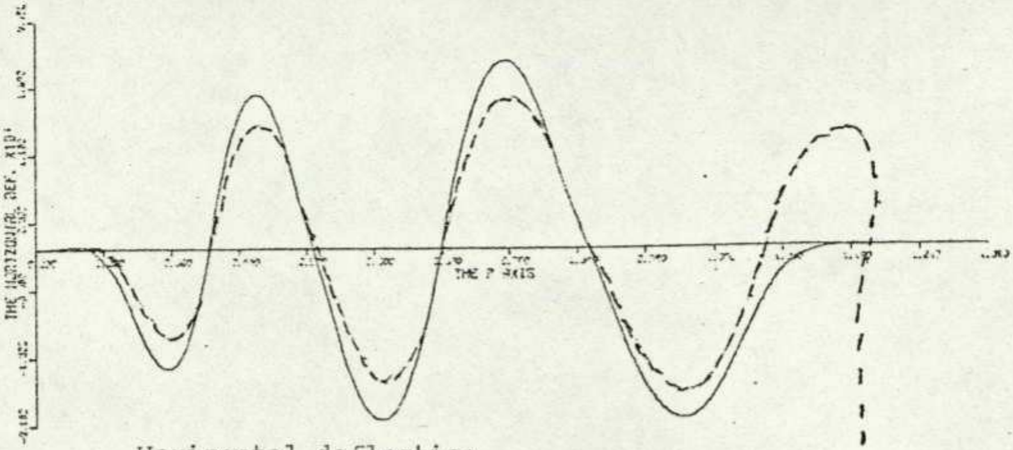

Horizontal deflection

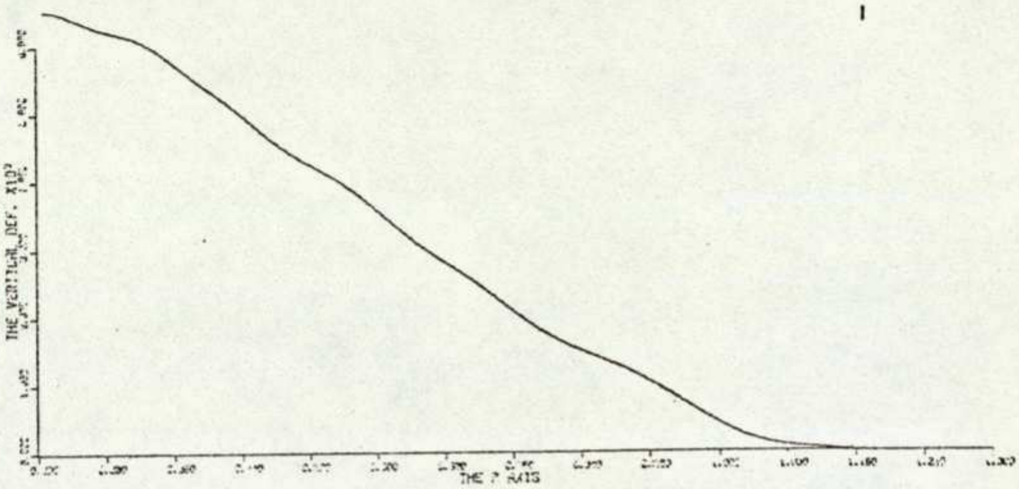

Vertical deflection

Shear function (ψ)

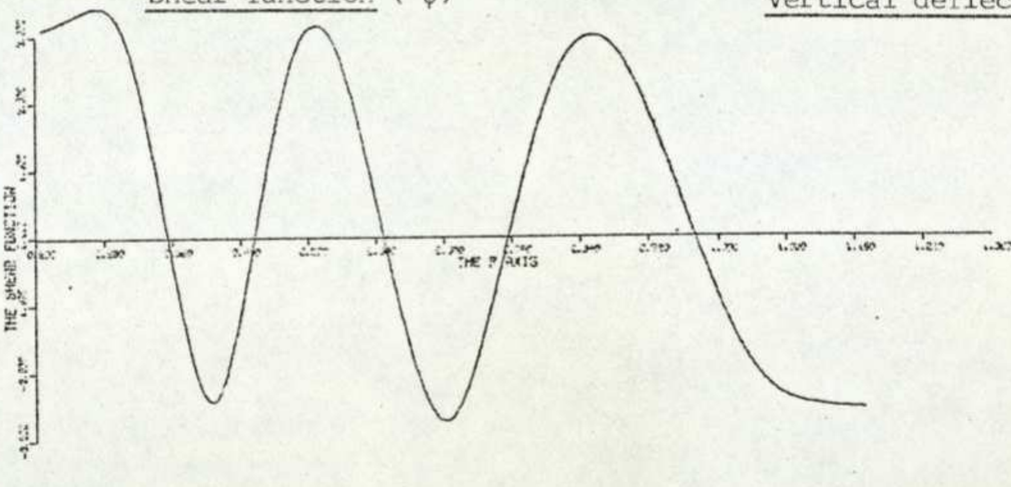

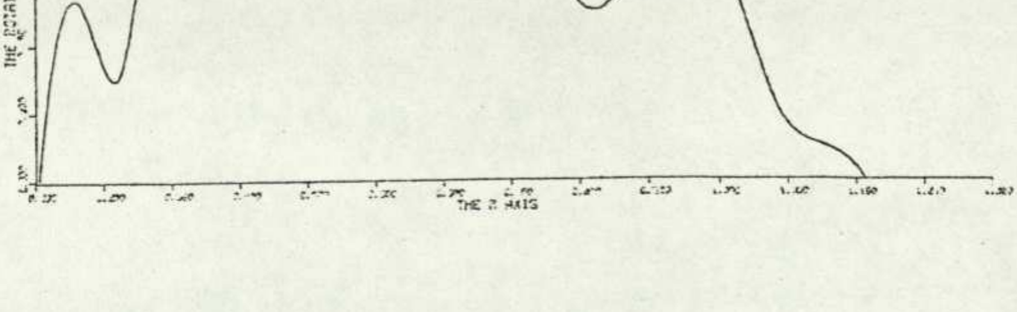
Rotation

Figure 3.16

The Variation of Computed Variables against radial distance (measured out from the centre boss) for a diaphragm stressed at the outer edge by applying a horizontal displacement towards the centre

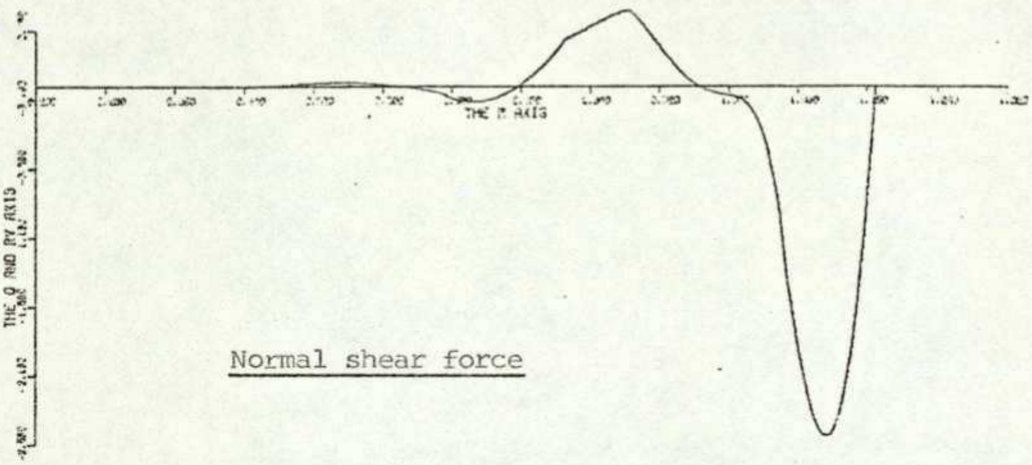

Normal shear force

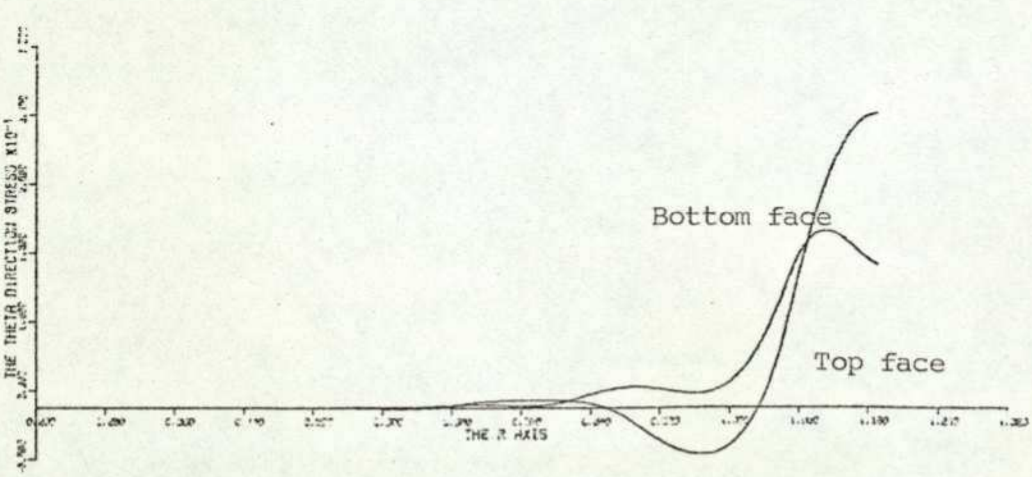

Circumferential stress

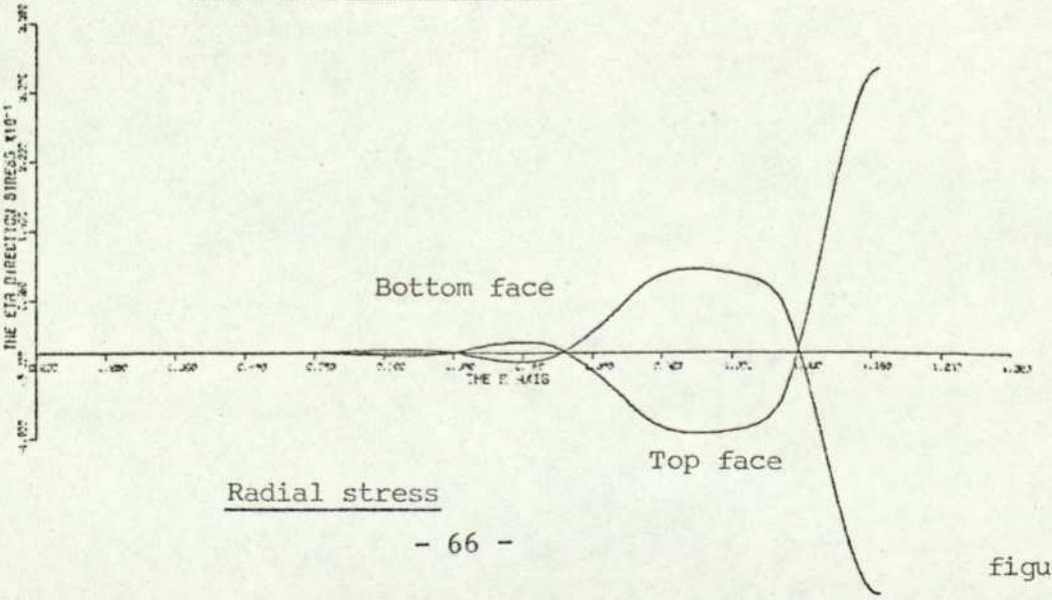

Radial stress

figure cont'd

Figure 3.16

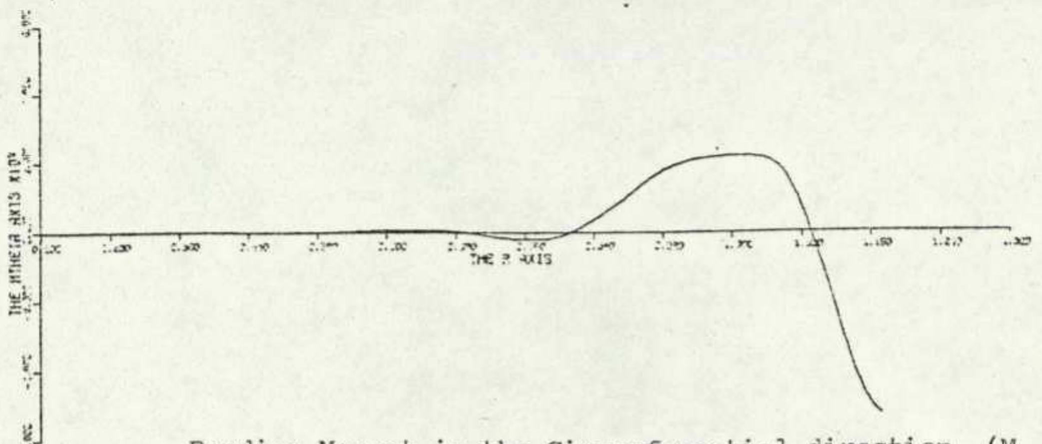

Bending Moment in the Circumferential direction (M_θ)

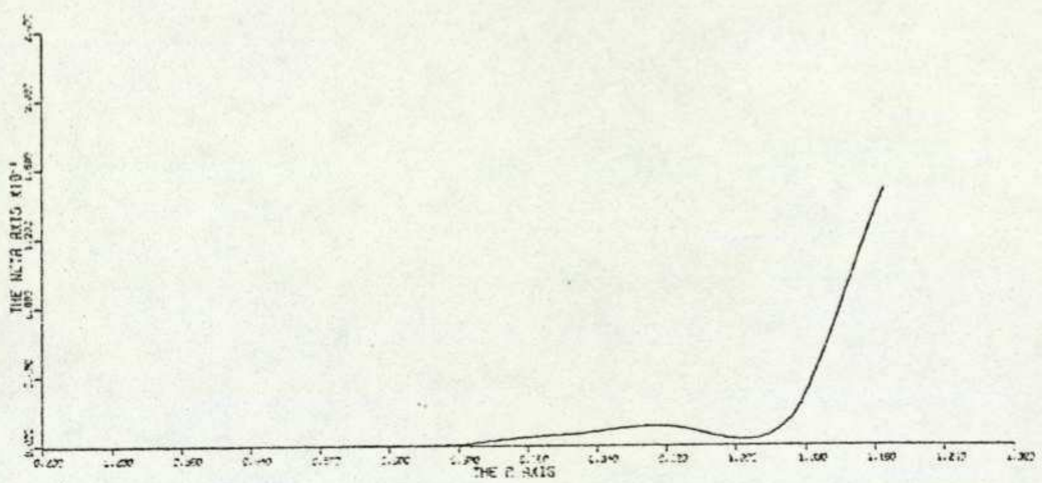

Stress resultant in the radial direction (N_ξ)

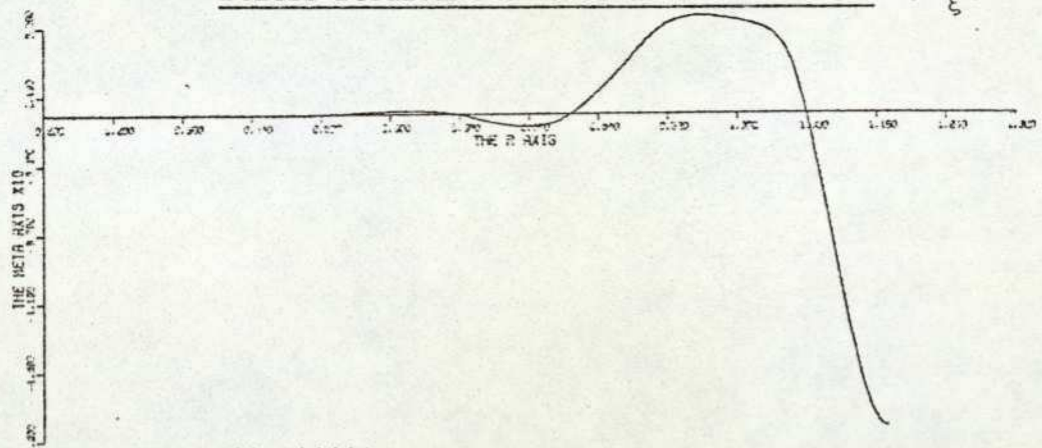

Bending Moment in the radial direction (M_ξ)

Stress resultant in the circumferential direction (N_θ)

figure cont

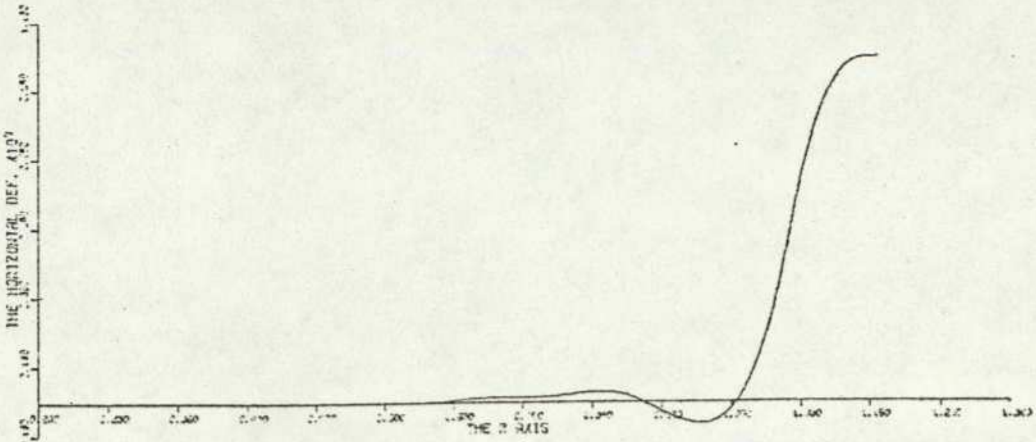

Horizontal deflection

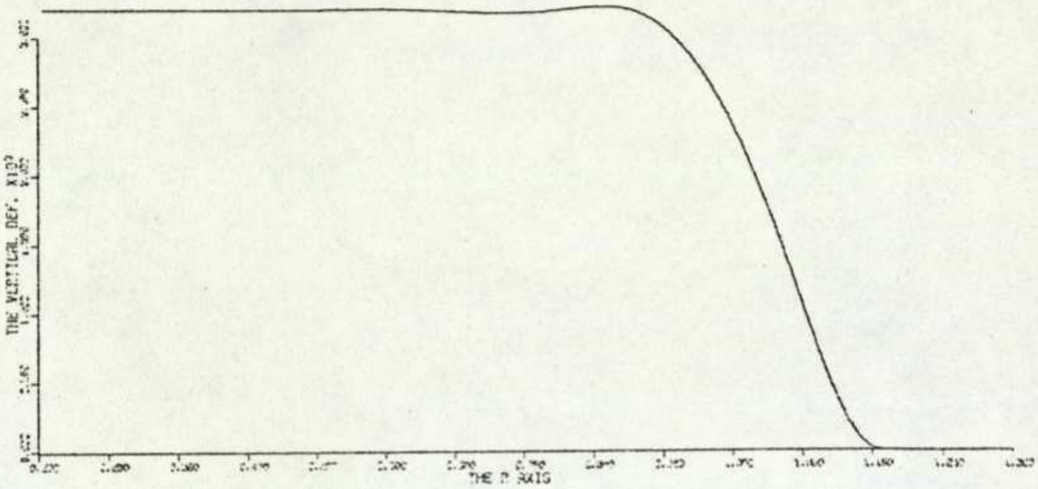

Vertical deflection

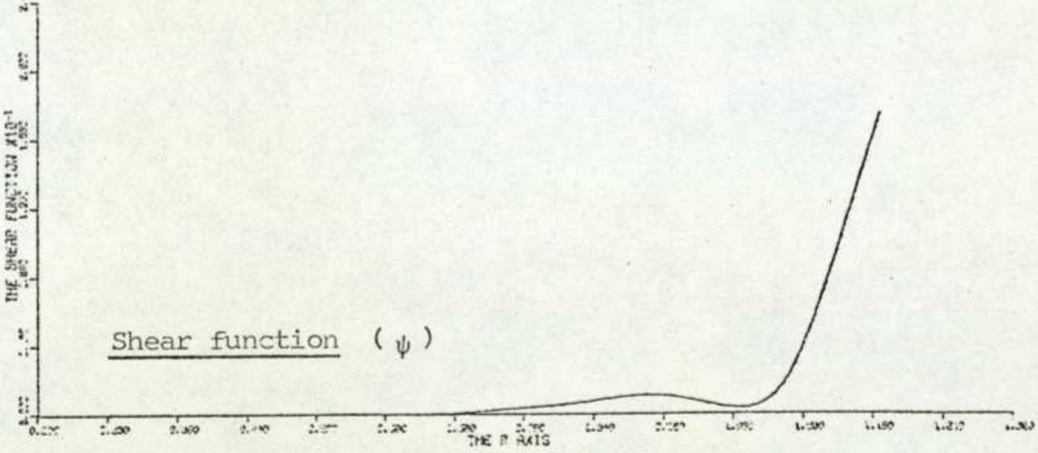
Shear function (ψ)

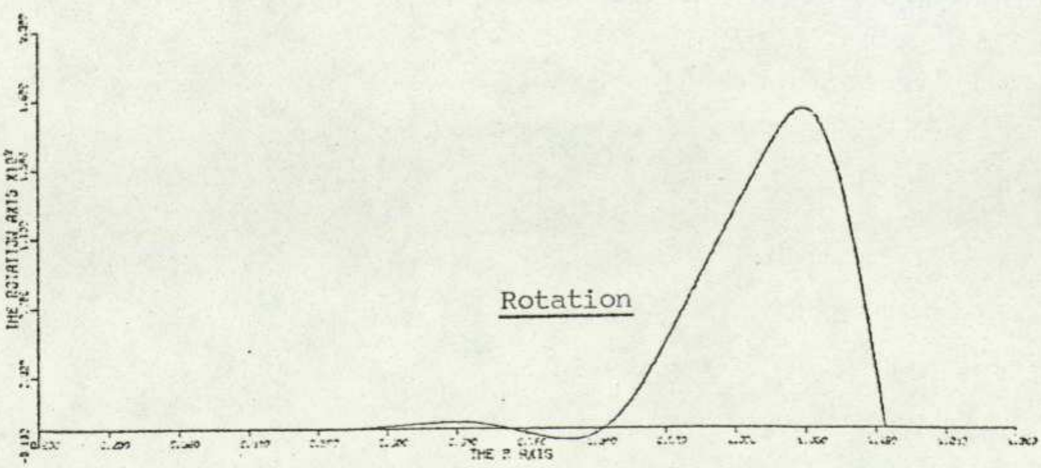
Rotation

loading can be applied. Examples of point and pressure loading are given in Figures 3.13 and 3.15.

(5) Initial stress, compressive or tensile, may be applied at the outer boundary by inducing an initial horizontal displacement U_N^I, then circumferential strain = U_N^I / r_N. Results of applying an initial compressive stress with no other loading are shown in Figure 3.16.

Program output: The program will output at every point (if desired) the vertical and horizontal displacements, U_i and W_i, along with ψ_i, β_i, $(M_\xi, M_\theta, N_\xi, N_\theta)_i$ and Q_i $(i = 1,2 \ldots\ldots N)$. From the stress resultants the actual stresses through the thickness of the diaphragm can be found. These will be a maximum at the top or bottom face depending on the direction of the applied pressure difference. If we assume the stresses in the ξ and θ directions to be both composed of a membrane stress which is constant, and a bending stress which varies linearly across the thickness of the shell,

$$\sigma\Big|_{\theta,\xi} = \sigma_o + Z\,\sigma_1\Big|_{\theta,\xi}.$$

At the two faces we have (Figure 3.17):

$$\sigma_{\theta,\xi}\left(\frac{t}{2}\right) = \sigma_o + \frac{t}{2}\sigma_1 \quad \ldots\ldots\ldots\ldots\ldots\ldots\ldots\ldots\ldots \quad (3.36)$$

$$\sigma_{\theta,\xi}\left(-\frac{t}{2}\right) = \sigma_o - \frac{t}{2}\sigma_1 \quad \ldots\ldots\ldots\ldots\ldots\ldots\ldots\ldots\ldots \quad (3.37)$$

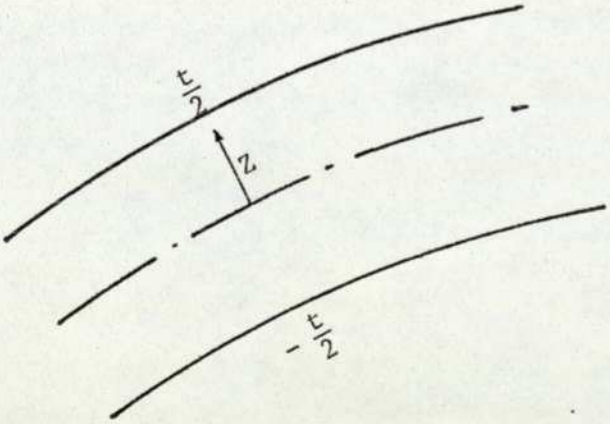

Figure 3.17

The stresses are related to the stress resultants by:

$$N = \int_{-t/2}^{t/2} \sigma \, dZ, \quad \text{and } M = \int_{-t/2}^{t/2} \sigma \, Z \, dZ$$

Substituting

$$N = \int_{-t/2}^{t/2} (\sigma_o + \sigma_1 Z)dZ = \sigma_o t$$

$$M = \int_{-t/2}^{t/2} (\sigma_o + \sigma_1 Z)ZdZ = \sigma_1 \frac{t^3}{12}$$

and into (3.36) and (3.37) gives:

$$\begin{aligned} \sigma_\theta\left(\frac{t}{2}\right) &= \frac{N_\theta}{t} + \frac{6\ M_\theta}{t^2} \\ \sigma_\theta\left(-\frac{t}{2}\right) &= \frac{N_\theta}{t} - \frac{6\ M_\theta}{t^2} \\ \sigma_\xi\left(\frac{t}{2}\right) &= \frac{N_\xi}{t} + \frac{6\ M_\xi}{t^2} \\ \sigma_\xi\left(-\frac{t}{2}\right) &= \frac{N_\xi}{t} - \frac{6\ M_\xi}{t^2} \end{aligned} \qquad (3.38)$$

Thus the stress at any point on the diaphragm can be assessed. Typical values of stresses on the top and bottom faces, as well as the other outputs, are shown for all types of loading in Figures 3.13 and 3.16.

3.1.12 The finite element approach

Structural analysis using digital computer techniques can be based upon three main methods: finite differences, direct integration and finite elements. The finite difference technique is the more established method; the direct integration method, although it has the use of highly developed integration routines, is fundamentally unsuited to boundary value problems; and the finite element technique, which is the most recently developed, is being rapidly applied to a very wide range of structural problems.

The approach used in this thesis was the finite difference method, and it was decided that a comparison should be made for the three types of numeric techniques, as applied to the diaphragm type problem. Fortunately, a comparison was available with the direct integration method, ref. (19), leaving the finite element approach, therefore the author has developed a linear diaphragm model using finite elements to compare with his previous finite difference model.

The finite element method is based on the concept that the actual structure can be idealized as a set of finite elements connecting nodal points. It is assumed that the displacements everywhere in the structure can be described in terms of the displacements of these nodal points, and the actual loading of the structure can be replaced by a set of equivalent loads at the nodal points (equivalent in the sense that the work done during any incremental deformation approximates to work done by the actual loading). Compatability of deformation is satisfied precisely only at the nodal points and approximately along the element boundaries.

For each element, relationships can be derived, based on the elastic properties of the elements and reasonable approximation of the interior deformation of the element, giving the forces at the node points (equivalent to the distributed forces on the element boundaries) in terms of the displacements at the node points. These algebraic equations, written in matrix form, are:

$$\{F\} = \left[k\right] \{\delta\}$$

where $\{F\}$ and $\{\delta\}$ are column matrices of forces and displacements at the nodes, and $\left[k\right]$ is the stiffness matrix for the element. For the entire structure, the total stiffness matrix is obtained by superposition (addition) of each of the element stiffness matrices. The force-displacement relation for the entire structure is then

$$\{F\} = \left[K\right] \{\delta\}$$

where $\left[K\right]$ is the total stiffness matrix.

The method applied particularly to thin axi-symmetric shells considers the generator to be composed of a number of short conical shells. The main problem is one of finding the element stiffness matrix which is a function of geometry, material properties and assumed deflection mode. Each element is a straight one-dimensional "hoop" type element, owing to the axi-symmetric nature of the problem and the thinness assumption. Full details are given by O. C. Zienkiewicz, ref. (24).

The problem run on the model was a four-convolution sinusoidal type diaphragm, clamped at the outer edge, a common problem applicable to the work. The number of elements chosen to represent the generator was varied by having a number of runs, from 20 up to 200, in steps of 20.

The normalised centre displacements (W/t) are listed below against the number of elements (Table 3.1).

(W/t)	n
4.9413	20
4.3432	40
4.1678	60
4.1500	80
4.1298	100
4.1118	120
4.0990	140
4.0923	160
4.0878	180
4.0823	200

Table 3.1: Comparison of displacement against Number of finite elements

The first striking feature is that even with only 20 elements the result is within about 20 per cent of the final answer, although, as the number of elements is increased, the value of (W/t) does not converge rapidly after about 120 elements. When a test problem was run using a flat plate, very little improvement could be achieved after increasing the number of elements above 10!, and after increasing above 50 there was no change at all in the displacement.

The above result is to be expected with a flat plate, because the elements themselves are flat. With a curved generator, like a diaphragm, the straight conical sections are only an approximation and the larger the number, the better the approximation. Unfortunately, the number of elements required appears to be in the same order as the number of finite difference points, which do have a curvature associated with them, and although the difference between the results at 180 finite elements and 200 is less than 0.2 per cent, convergence cannot be assured, especially as the difference between the 160 - 180 result is less than the 180 - 200 result, indicating a slight numerical instability.

3.1.13 Note on the presentation of data and computer run times

Figures 3.13 and 3.16 show plots of the variation of each parameter against radial distance r: plotted information of this form is extremely useful to obtain the overall picture of what is happening. Graphical information of this kind can be obtained in three forms, depending upon the machine used and its application. Using a suitable graphing routine a plot can be generated on one or two pages of line printer output: this is the quick but inaccurate method, because the distance across the page is normalised to the actual dimension value and then quanticized into 120 or 132, depending upon the number of spaces across the line printer. This results in a very rough thick line for the graph curve. The second method, which produces a graph scaled to any size, is to utilise the graph plotter by calling a series of purpose-written graphing routines. These fit a smooth curve through a series of five points automatically. The main disadvantages of this method are the extra amount of program writing required and the extra time taken by the plotting routine. The third method used was to produce the graphs on microfilm: this has the same disadvantage as the previous method, but has the advantage that the copy is more permanent and easier to store.

The solution time for F. Abdullah's computer model using the direct integration technique was about 20 seconds on a Control Data Corporation (C.D.C) 7600 computer. For the finite difference approach, using 200 mesh points, the same solution took 40 milliseconds, the results being equivalent to within 0.1 per cent.

The finite element model, which was also equivalent to within 0.1 per cent if greater than 160 elements were used, had a run time of about 800 milliseconds for the 160-element model.

3.2 Geometry

Having established in the previous section that certain geometric variables are required at each mesh point as input data for the mathematical model, the problem arises of how best to present them. With a computer-aided design approach in mind, the presentation ought to be as flexible as possible, subject to practical constraints. The shell equations apply to a shell of revolution, of an arbitrary shape, having either a positive or negative Gaussian curvature, i.e. not discontinuous, although in this particular work we wish to restrict ourselves to corrugated diaphragms and capsules.

From the considerations of the previous sections, the parameters of the diaphragm needed to solve the equations are:

(a) Radial distance to each mesh point r_i, measured from the axis of symmetry.

(b) The angle between the normal and the axis of symmetry ϕ_i.

(c) The radius of curvature at each mesh point rl_i (the R_ξ value from the previous analysis). These values are functions of the generator length S, not radial distance.

A study of a number of production diaphragms has shown that the generator curve may be considered as a series of circular arcs joined by short conical straight sections. This was done by sectioning a diaphragm and looking across a diameter magnified on a shadow graph. Initially it was hoped to implement a design procedure based on an analytical description of the corrugated curve - a good example would have been a sine wave - then different diaphragm shapes could be generated by varying the amplitude and phase.

Unfortunately, this approach had two disadvantages:

(1) The need to express the variables as a function of S would introduce a numerical integration since

$$S = \int_{o}^{x} \left(1 + \left(\frac{dy}{dx}\right)^2\right) dx \quad \text{for } y = f(x).$$

(2) The number and variation of profile shapes would be more limited than a piecewise approach based on circles and straight lines.

Therefore, data for simulating diaphragms was obtained by the sectioning method described above and reproducing the profile on paper and providing three measurements at each peak and trough, namely, the X and Y co-ordinates plus the radius of curvature (R) (Figure 3.18).

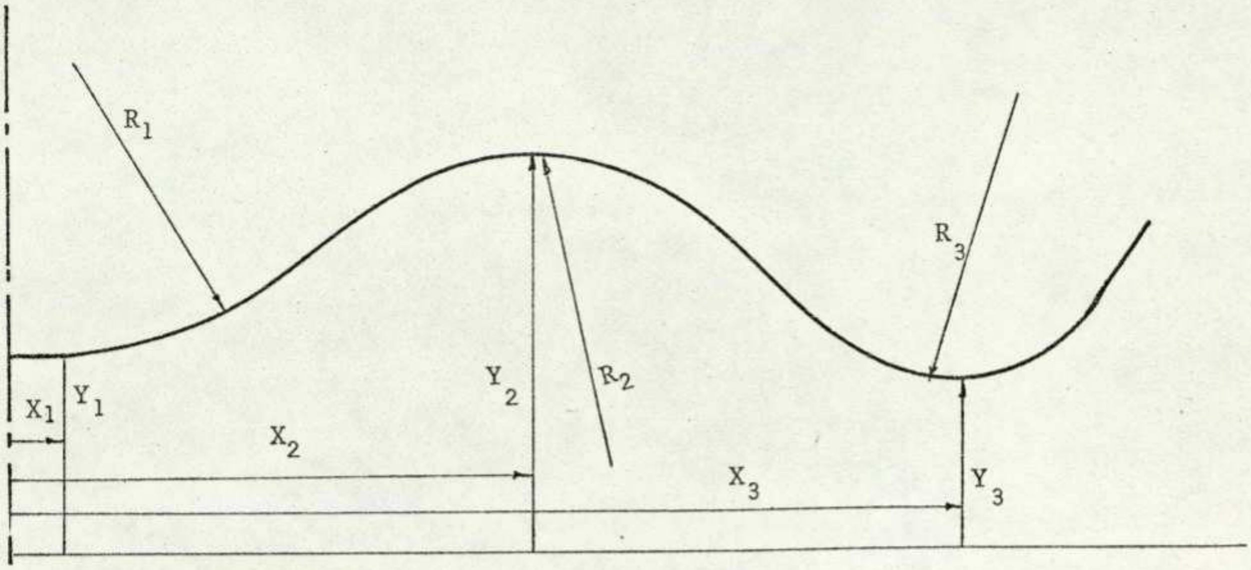

Figure 3.18: Diaphragm geometry

This was an adequate but simple method which uniquely describes the diaphragm profile. For simple structures (for which the flat plate diaphragm is a good example) it is possible to obtain an analytic expression for r_i, rl_i, ϕ_i ($i = 1, 2 \ldots\ldots N$) in terms of S.

Flat circular plate

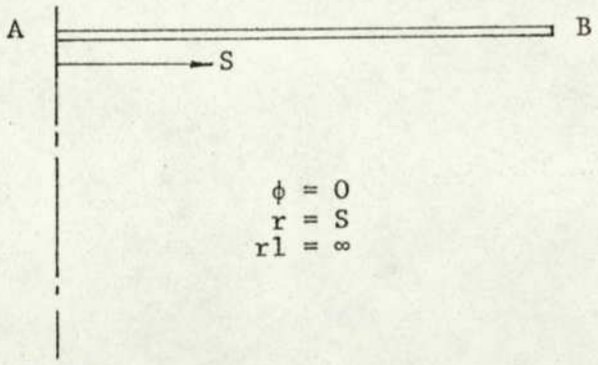

$$\phi = 0$$
$$r = S$$
$$rl = \infty$$

The flat circular plate is obtained by rotating B about the centre line

Figure 3.19a

Conical segment

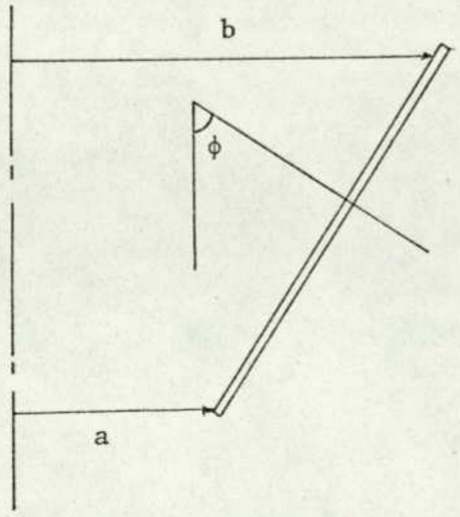

$$\phi = \tan^{-1} \frac{c}{(b-a)}$$
$$rl = \infty$$
$$r = a + S \cos\phi$$

Figure 3.19b

Circular segment (i.e. a segment of a torus)

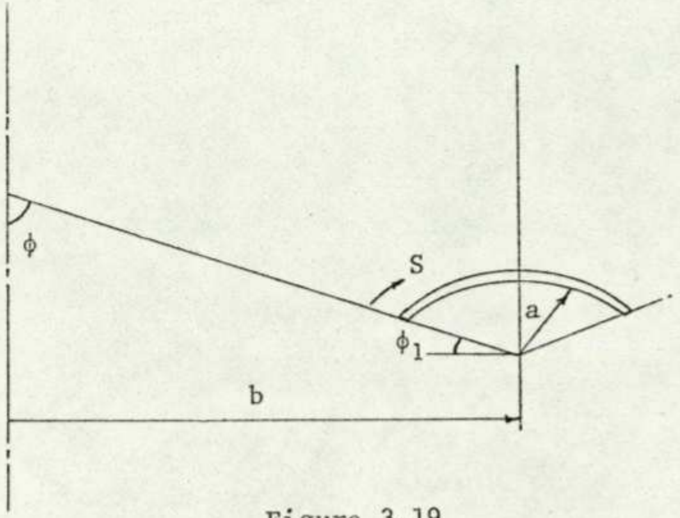

$$\phi = \frac{\pi}{2} - \phi_1 + \frac{S}{a}$$

$$rl = a$$

$$r = b - a \sin\phi$$

Figure 3.19c

Figure 3.19

These three simple structures will make up our more complex structural diaphragm.

From the X, Y, Rl measurements at the peaks and troughs, an algorithm is needed where the three simple cases are joined; mathematically the problem is one of joining two circles by a common tangent (Figure 3.20).

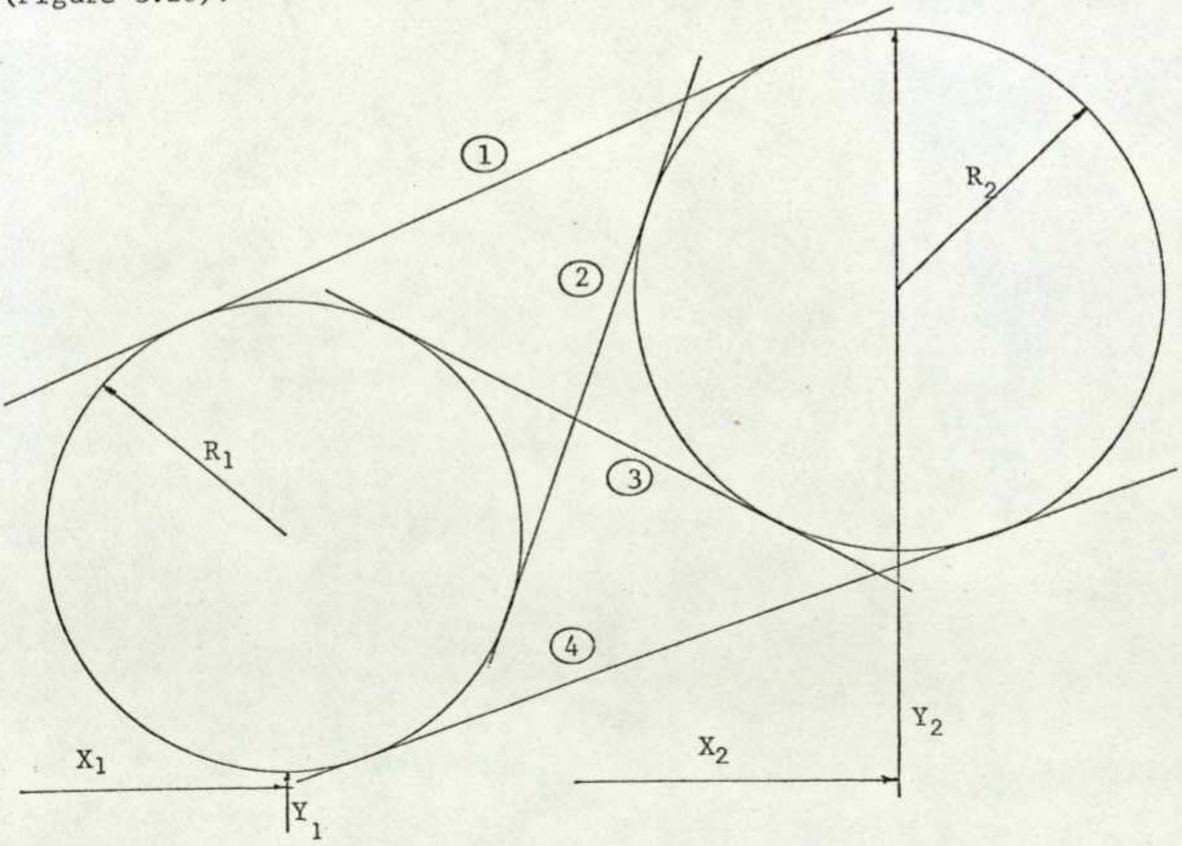

Figure 3.20: Circles and common tangents

As shown in Figure 3.20, there are four possibilities of which we wish to eliminate (1) and (4) as not applicable to the problem, and then choosing between (2) and (3), depending upon which part convolution is being considered.

The expression for the angle, the perpendicular from the tangent makes with the axis of symmetry, is given by:

$$\phi = \tan^{-1}\left(\frac{(Y \mp R)X \pm R\sqrt{X^2 - R^2 + (Y \mp R)^2}}{X^2 - R^2}\right) \quad \ldots\ldots\ldots \quad (3.39a)$$

$$\text{where} \quad \left.\begin{aligned} Y &= Y_2 - Y_1 \\ X &= X_2 - X_1 \\ R &= R_1 + R_2 \end{aligned}\right\} \text{ Figure 3.20}$$

which for case (2)

$$\phi = \tan^{-1}\left(\frac{(Y - R)X + R\sqrt{X^2 - R^2 + (Y - R)^2}}{X^2 - R^2}\right) \quad \ldots\ldots\ldots \quad (3.39b)$$

and for case (3) the sign change is reversed.

The sign of angle ϕ is then determined by which tangent is applicable, and the sign convention used. For corrugated diaphragms the angle ϕ will normally vary between $\frac{\pi}{2} > \phi > -\frac{\pi}{2}$, and the direction of integration for shell problems is taken from the lower edge boundary towards the upper edge boundary. This direction is meaningless for diaphragms, so the author has taken the direction of integration from the axis of symmetry to the outer periphery. This makes the sign convention for the angle ϕ and radius of curvature rl relatively simple. By considering ds (a small finite step in s) as equal to rl $d\phi$, which must be positive in the direction of integration (Figure 3.21) shows how the operation in the actual computer program is controlled by an integer switching between +1 and -1.

The automatic generation of the diaphragm variables was hence achieved by a single subroutine GEOM which took as input data X, Y, R co-ordinates at the peaks and troughs and from the updated value of generator length gave back the current values of $(r)_i$, $(rl)_i$, and $(\phi)_i$. By putting the subroutine in a loop with a predetermined value of steplength, an exact number of mesh points could be put along the generator length.

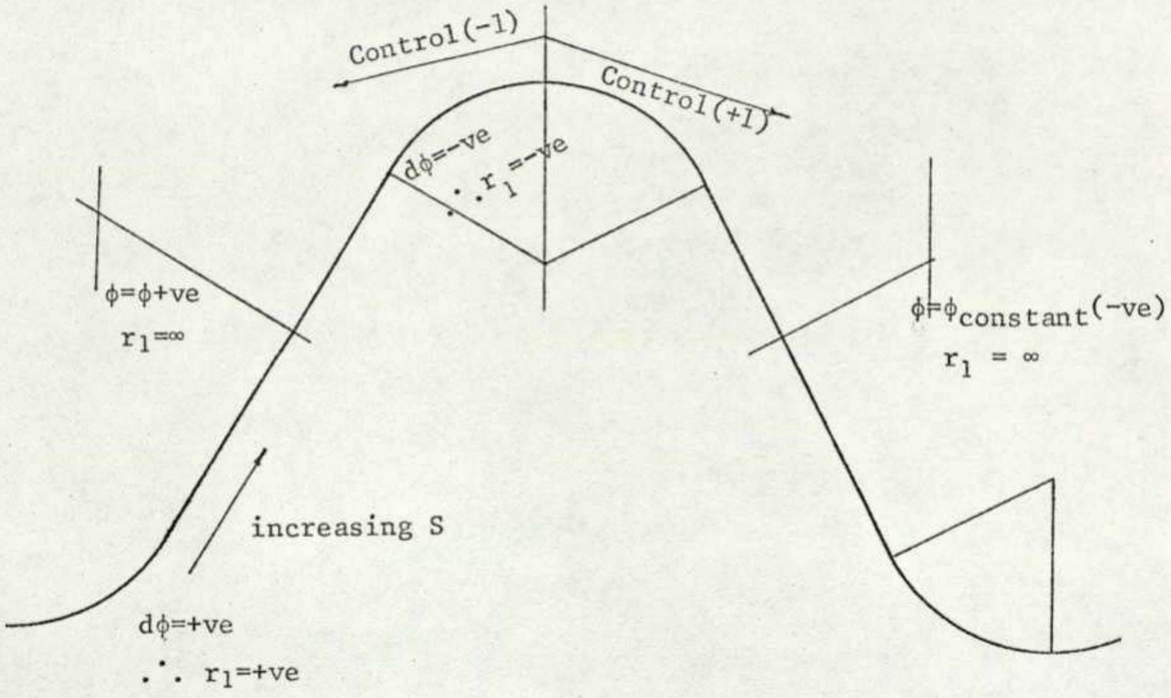

Figure 3.21: Computer generation of diaphragm profile

The variations of profile which can be achieved with this subroutine are immense, some of which are illustrated below:

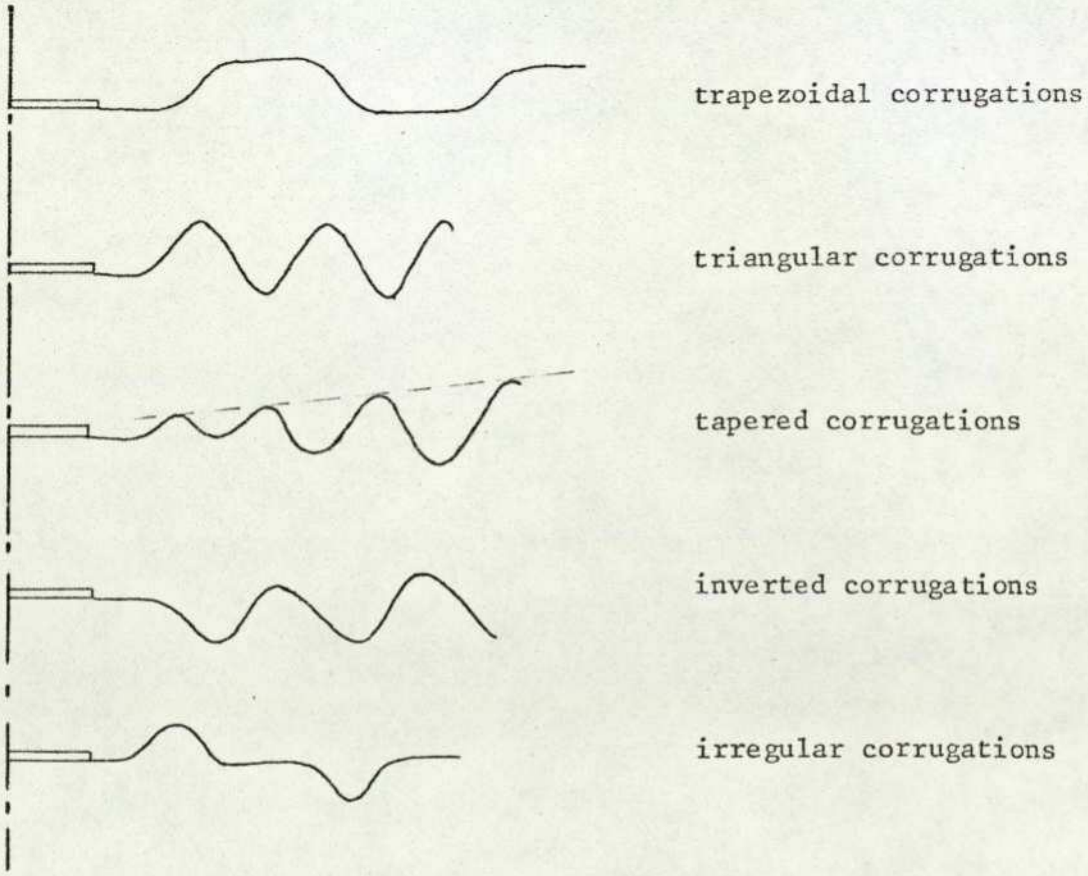

Figure 3.22: Diaphragm shapes

With slight modifications a subroutine was written to solve for a bellows shape (Figure 3.23).

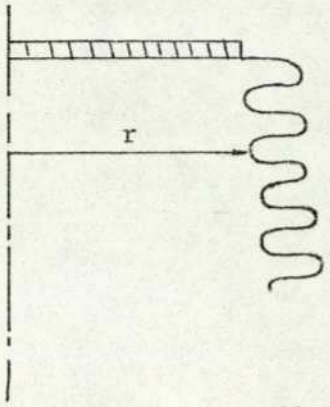

Figure 3.23: Bellows

An additional complication arises for bellows because the radius does not increase monotonically from one boundary to the other.

3.3 Non-linear model

The section is divided broadly in three parts: the equations which were used for programming (3.3.1), the numerical procedure for implementing them on the computer (3.3.2), and the various tests and investigations applied to the model.

In the deformation of elastic elements the geometric non-linearity will be much more important than the material non-linearity (i.e. plasticity). In fact, no pressure-sensing element would normally be required to operate even near the yield point of the material. Therefore, a model which is able to give both the non-linearity and sensitivity is extremely useful. Associated with any elastic element is a useful working range, above which the deviation from the tangent at the origin is too excessive. The non-linearity must then be known, and a limit set on the amount which can be tolerated. As an example consider a flat plate subjected to a uniform pressure; then the well-known equation for its centre deflection is:

$$\frac{P}{E}\left(\frac{R}{t}\right)^4 = \alpha\left(\frac{W}{t}\right) + \beta\left(\frac{W}{t}\right)^3 \qquad \left.\begin{matrix}\alpha\\ \beta\end{matrix}\right\} \text{constants}$$

An approximate figure quoted as the "linear range" of the flat plate is $\left(\frac{W}{t}\right) \leqslant 0.45$, but this gives a maximum deviation from linearity of 3.26 per cent when presented as

$$\left(\frac{\delta W}{W_N} \times 100\right)\%$$

where δW = maximum deviation of curve from a straight line between the origin and the end of the range W_N.

A full account of the representation of non-linearity is given in the chapter on capsules.

3.3.1 Equations to be programmed

Many additional theories of these elastic shells have been proposed in which one or another of Love's assumptions have been suspended, with the exception of the small deflection assumption. These are the so-called higher order linear theories, a good example being the Theory of Flügge, ref. (25). These theories were not considered as important as one in which Love's small deflection assumption is suspended. Here the work might appear to be ordered incorrectly because E. Reissner's equations are again used for the non-linear whereby the linear equations derived in the previous chapter can be obtained by neglecting the second order of magnitude terms and linearising the non-linearities. By presenting the work this way round the actual chronological development is presented, and also an indication of where the non-linearities arise can be given without a complete derivation.

As we are only interested in geometric non-linearities and we still wish to operate within the Hookian region, it is reasonable to neglect the strains with respect to unity and still neglect transverse shear and normal stress effects. Therefore, $\alpha = \alpha_o$ and $r = r_o$, i.e. no strain update. This is consistent with the assumption on the preservation of the normal because the change in length of the normal to the reference surface is expected to be negligible only for small strains any way.

Then we retain, as before:

$$(r_o V)' + r_o \alpha_o P_V = 0 \quad \ldots\ldots\ldots (3.20)$$

$$(r_o H)' - \alpha_o N_\theta + \alpha_o r_o P_H = 0 \quad \ldots (3.19)$$

Referring to Figure 3.6:

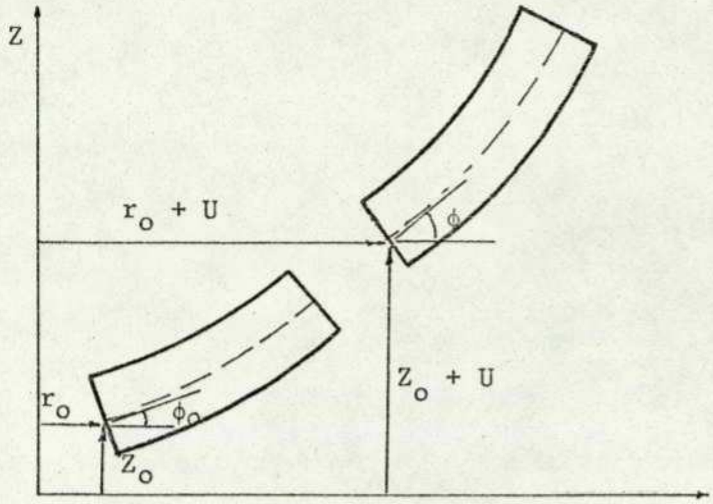

(rotation $\beta = \phi_o - \phi$)

Figure 3.24: Deformation

Then $\quad \alpha_o N_\xi = \cos\phi \, H + \sin\phi \, V \qquad$ from (3.17)

so $\quad \alpha_o N_\xi r_o = \cos\phi \, \psi + \sin\phi (r_o V)$

and $\quad \alpha_o N_\xi r_o = \psi \cos\phi_o + (r_o V)\sin\phi_o + \beta \left[\psi \sin \phi_o - (r_o V)\cos\phi_o \right]$

If β is small $\sin\beta \doteq \beta$ and $\cos\beta \doteq 1$,

also, $\quad r_o \alpha_o Q = -\psi \sin\phi_o + (r_o V)\cos\phi_o + \beta \left[\psi \cos\phi_o + (r_o V)\sin\phi_o \right]$

In the linear model the two terms containing β were neglected as being of an order of magnitude smaller than the preceding values.

Referring again back to the previous section,

χ_θ was linearised from $\dfrac{\sin\phi}{r} - \dfrac{\sin\phi_o}{r_o}$ to $-\beta \dfrac{\cos\phi_o}{r_o}$.

Now if we keep $r = r_o$,

$$\frac{\sin(\phi_o - \beta) - \sin\phi_o}{r_o} = \frac{\sin\phi_o \cos\beta + \cos\phi_o \beta - \sin\phi_o}{r_o}$$

$$= \frac{\sin\phi_o}{r_o} (\cos\beta - 1) + \frac{\cos\phi_o}{r_o} \beta$$

Now $\cos\beta = 1 + \frac{\beta^2}{2} + \ldots\ldots\ldots$ higher terms.

If we now include terms of up to β^2 in the approximation,

$$\chi_\theta = \frac{\sin\phi_o}{r_o} \left(\frac{\beta^2}{2} \right) + \frac{\cos\phi_o}{r_o} \beta$$

therefore,

$$M_\theta = D \left[\frac{\cos\phi_o}{r_o} \beta + \frac{1}{2} \frac{\sin\phi_o}{r_o} \beta^2 + \frac{\nu \, \beta'}{\alpha_o} \right]$$

and $M_\xi = D\left[\frac{\beta'}{\alpha_o} + \nu\left(\frac{\cos\phi_o}{r_o}\,\beta + \frac{1}{2}\,\frac{\sin\phi_o}{r_o}\,\beta^2\right)\right]$

It can now be seen that all the geometric variables, predominantly r and ϕ, are referred back to the undeformed shell. If the above expressions are treated in a similar fashion as in the previous section and Appendix 1, two non-linear simultaneous second-order differential equations of a similar form to the linear ones can be derived. For expediency, these equations are written straight down from ref. (29):

$$\left(\frac{r_o D}{\alpha_o}\right)\beta'' + \left(\frac{r_o D}{\alpha_o}\right)'\beta' - \left[\frac{D r_o'^2}{r_o \alpha_o} - \nu\left(\frac{r_o' D}{\alpha_o}\right)'\right]\beta + \alpha_o \psi \sin\phi_o = \Gamma_1 \quad \text{.. (3.40a)}$$

$$\left(\frac{r_o}{C\alpha_o}\right)\psi'' + \left(\frac{r_o}{C\alpha_o}\right)\psi' - \left[\frac{r_o'^2}{C r_o \alpha_o} + \nu\,\frac{r_o'}{C\alpha_o}\right]\psi - \alpha_o \beta \sin\phi_o = \Gamma_2 \quad \text{... (3.40b)}$$

where

$$\Gamma_1 = \left[\frac{3}{2}\,\frac{r_o'}{r}\,\frac{Z_o' D}{\alpha_o} - \frac{\nu}{2}\left(\frac{Z_o' D}{\alpha_o}\right)'\right]\beta^2 + \alpha_o (r_o V)\cos\phi_o + \alpha_o \beta\left[\psi\cos\phi_o + (r_o V)\sin\phi_o\right]$$

$$\begin{aligned}\Gamma_2 = {} & \left[2\,\frac{Z_o' r_o'}{C r_o \alpha_o} + \nu\left(\frac{Z_o'}{C\alpha_o}\right)'\right]\beta\psi + \frac{\nu\, Z_o' \beta' \psi}{\alpha_o C} - \frac{1}{2}\,\alpha\,\beta^2 \cos\phi_o \\ & + \left[\frac{r_o' Z_o'}{C r_o \alpha_o} + \nu\left(\frac{Z_o'}{C\alpha_o}\right)\right](r_o V) + \frac{\nu Z_o'}{C\alpha_o}\,(r_o V)' - \frac{\nu r_o'}{C\alpha_o}\,\beta'(r_o V) \\ & + \left[\frac{Z_o'^2 - r_o'^2}{C r_o \alpha_o} - \nu\left(\frac{r_o'}{C\alpha_o}\right)'\right](r_o V)\beta - \frac{\nu r_o'}{C\alpha_o}\,\beta\,(r_o V)' - \left(\frac{r_o^2 P_H}{C}\right)' \\ & - \left[\nu\left(\frac{r_o'}{C r_o} + \beta\,\frac{Z_o'}{C r_o}\right) - \frac{C'}{C^2}\right](r_o^2\, P_H).\end{aligned}$$

The vertical deflection expression is also modified by these foregoing considerations of :

$$W = \int \left[(\sin\phi - \sin\phi_o) + \frac{\sin\phi}{C}\,\varepsilon_{\xi m}\right] ds.$$

These complicated loading terms were initially thought to be too difficult to program and might suffer with convergence problems, so a set of equations, which are derived from Reissner's two basic equations of compatability and moment balance, were found which were simpler in form.

Billington, ref. (27), used the results of a more recent Reissner publication, ref. (28), to derive the following equations:

$$\bar{\beta}'' + \frac{(rD/\alpha)'}{(rD/\alpha)}\bar{\beta}' - \left(\frac{\alpha^2 \cos\phi_o}{r^2} - \frac{\nu D'}{(rD/\alpha)}\right) \bar{\beta} \cos\phi_o - \frac{\nu\alpha\phi_o'}{r}(r\Omega) = $$

$$= \left(-\frac{\alpha}{rD/\alpha}\right)(rQ) \;\ldots\ldots \quad (3.41a)$$

$$\psi'' + \frac{(r/C\alpha)'}{(r/C\alpha)}\psi' - \left(\frac{\alpha^2 \cos\phi_o}{r^2} - \frac{\nu C'}{(rC/\alpha)}\right) \psi \cos\phi_o - \frac{\nu\alpha\phi_o'}{r}(rQ)_L$$

$$= -\frac{\alpha(r\Omega)}{r/C\alpha} + \frac{\nu\alpha\sin\phi_o}{r}(rV)' + \left(\frac{\alpha^2}{r^2}\cos\phi_o - \frac{\nu C'}{(rC/\alpha)}\right)(rV)\sin\phi_o \;. \quad (3.41b)$$

The additional difference is that $\bar{\beta}$ is the negative of β from Eqns. (3.40).

The terms for P_H have been left out from (3.41b) as they are exactly the same as for the (3.40b) Eqn. Also the paper does not state whether r or α refers to the deformed or undeformed shell, but owing to the likeness to Eqns. (3.40a) and (3.40b), they were assumed to be referred to the deformed shell, but since strain is still assumed negligible compared to unity, the parameters may be referred to the undeformed shell.

The only non-linear terms appearing are:

$$(r\Omega) = -(\cos\phi - \cos\phi_o) \;\ldots\ldots\ldots\ldots\ldots\ldots \quad (3.42a)$$

$$(rQ) = -\psi\sin\phi - (rV)\cos\phi \;\ldots\ldots\ldots\ldots\ldots\ldots \quad (3.42b)$$

$$(rQ)_L = -\psi\sin\phi_o + (rV)\cos\phi_o \quad \{\text{is a linear term}\}$$

Thus, these equations appear a considerable simplification over (3.40a) and (3.40b) and are considered to be still appropriate for large deflections but very small strains.

3.3.2 Numerical procedure

The method of solution for the non-linear equations was the quasi-linearisation; by using this method the basic techniques used for the linear model could be applied with the appropriate programming for the linearisation.

The method actually solves for the error when a guess value is substituted into the equations; this error is then added to the guess value and re-substituted. A new error is found by the resulting solution; as the problem converges the error will tend to zero and β_i and ψ_i

(i = 1, 2 ..... N) will stabilise. The stress resultants, stresses and displacements can then be found at that particular pressure and the next pressure applied via the loading terms. The whole iteration procedure is then repeated until the pressure range is completed: the iterative loops are illustrated in the flow chart of Figure 3.25.

The Equations:

Taken in the general form these are very similar to Eqns. (3.30a):

$$a_i\beta_{i+1} + b_i\beta_i + c_i\beta_{i-1} + d_i\psi_i = \Gamma_{1i} \tag{3.43a}$$

$$e_i\psi_{i+1} + g_i\psi_i + h_i\psi_{i-1} + j_i\beta_i = \Gamma_{2i} \tag{3.43b}$$

the difference being that Γ_{1i} and Γ_{2i} are functions of β_i and ψ_i as well as various loading terms.

The equations are now transformed by writing $\beta_i = \beta_{oi} + \delta\beta_i$ and $\psi_i = \psi_{oi} + \delta\psi_i$, where β_o and ψ_o are guess or previous values from the last iteration and $\delta\beta$ and $\delta\psi$ are the errors.

The terms containing β and ψ on the right-hand side are substituted for in the same way, but in Γ_1 and Γ_2 non-linear functions of the two variables appear, e.g. $\beta\psi$, $\beta'\psi$, β^2, etc. Rather than dealing tediously with every case, an example of how these terms are handled, and the linearisation process applied, is given below:

Consider the term

$$\beta'\psi = \left(\frac{\beta_{i+1} - \beta_{i-1}}{2\Delta S}\right)\psi_i$$

$$\text{then} = \left(\frac{(\beta_o + \delta\beta)_{i+1} - (\beta_o + \delta\beta)_{i-1}}{2\Delta S}\right)(\psi_o + \delta\psi)_i$$

$$= \frac{(\beta_{o_{i+1}} - \beta_{o_{i-1}} + \delta\beta_{i+1} - \delta\beta_{i-1})(\psi_o + \delta\psi)}{2\Delta S}$$

$$= \frac{(\psi_{o_i}\beta_{o_{i+1}} - \psi_{o_i}\beta_{o_{i-1}} + \psi_{o_i}\delta\beta_{i+1} - \psi_{o_i}\delta\beta_{i-1})}{2\Delta S}$$

$$+ \frac{(\beta_{o_{i+1}}\delta\psi_i - \beta_{o_{i-1}}\delta\psi_i + \delta\beta_{i+1}\delta\psi_i - \delta\beta_{i-1}\delta\psi_i)}{2\Delta S}$$

The last two terms are neglected as being of second order in magnitude

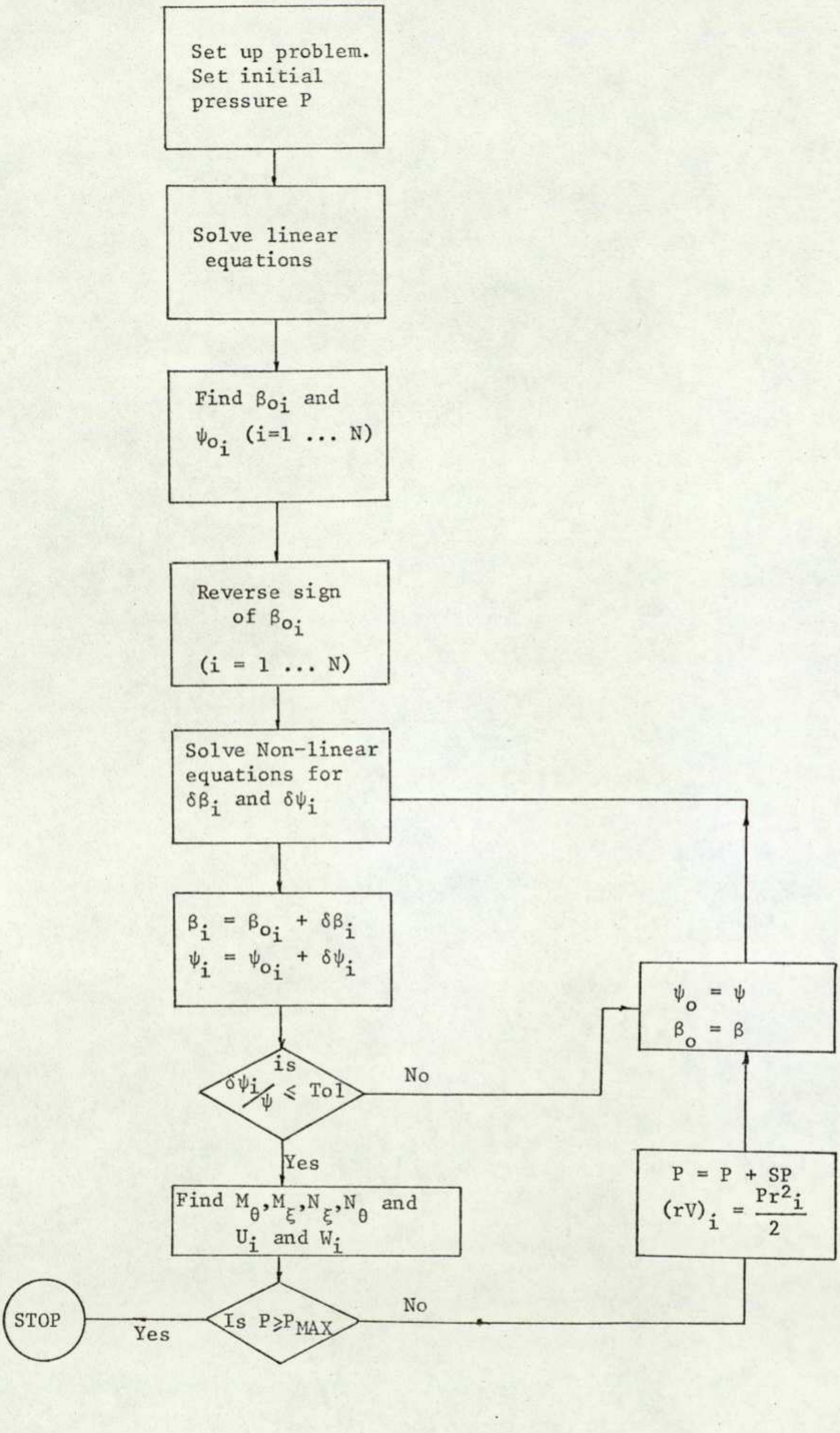

Figure 3.25: Flow chart for non-linear program

and then only linear terms of the dependent variables are left.

Returning to Eqn. (3.43), we now have

$$a_i \delta\beta_{i+1} + b_i \delta\beta_i + c_i \delta\beta_{i-1} + d_i \delta\psi_i = \Gamma_{1i} - EN1 \;\ldots\ldots \quad (3.44a)$$

$$e_i \delta\psi_{i+1} + g_i \delta\psi_i + h_i \delta\psi_{i-1} + j_i \delta\beta_i = \Gamma_{2i} - EN2 \;\ldots\ldots \quad (3.44b)$$

where $EN1 = (a_i \beta_{o_{i+1}} + b_i \beta_{o_i} + c_i \beta_{o_{i-1}} + d_i \psi_{o_i})$

$EN2 = (e_i \psi_{o_{i+1}} + g_i \psi_{o_i} + h_i \psi_{o_{i-1}} + j_i \beta_{o_i})$

The a_i .... j_i on the left hand side will, many cases, be different in (3.44): these coefficients will contain extra functions brought across from Γ_1 and Γ_2 (the linearised functions of $\delta\psi$ and $\delta\beta$).

Programming details - Billington's Equations

The two equations (3.41a) and (3.41b) are now re-written for programming; we assume $\alpha = 1$,

then (3.41a): $$\beta'' + C1\beta' - C2\beta - \frac{\nu}{r.r1}(r\Omega) = -\frac{rQ}{rD} \;\ldots\ldots\ldots \quad (3.45)$$

and (3.41b): $$\psi'' + C3\psi' - C4\psi - \frac{\nu}{r.r1}(rQ)_L = -\frac{C}{r}(r\Omega) + \text{loading terms}$$

and
$$\left\{\begin{aligned} C1 &= \frac{\cos\phi_o}{r} + \frac{3}{t}\,\frac{dt}{ds} \\ C2 &= \left(\frac{\cos\phi_o}{r}\right)^2 - \nu\left(\frac{\cos}{r}\right)\,\frac{3}{t}\,\frac{dt}{ds} \\ C3 &= \frac{\cos\phi_o}{r} - \frac{1}{t}\,\frac{dt}{ds} \\ C4 &= \frac{\cos\phi_o}{r} - \nu\,\frac{\cos\phi_o}{r}\,\frac{1}{t}\,\frac{dt}{ds} \end{aligned}\right.$$

Also, Young's Modulus E is assumed constant and r is referred to the original shell. If we were actually distinguishing between the deformed and undeformed shell, as in the case of ϕ, the radial distance would be expressed as r and r_o, respectively.

Considering (3.41a),

on the left hand side

$$-\frac{\nu}{r.r1}(r\Omega) = -\frac{\nu}{r.r1} - (\cos\phi - \cos\phi_o)$$

$$= \frac{\nu}{r.r1}\left(\cos(\beta + \phi_o) - \cos\phi_o\right)$$

on the right hand side

$$-\frac{rQ}{rD} = -\left(\frac{-\psi\cos(\beta+\phi_o) + (rV)\sin(\beta+\phi_o)}{rD}\right)$$

Normally we would expand the trigonometric functions and make the appropriate approximations for β being very small, but in the non-linear analysis β is not very small. As demonstrated earlier by $\beta = \beta_o + \delta\beta$,

therefore $\frac{\nu}{r.rl}(\cos(\beta_o + \delta\beta + \phi_o) - \cos\phi_o)$

$$= \frac{\nu}{r.rl}(\cos(\beta_o+\phi_o)\cos\delta\beta - \sin(\beta_o+\phi_o)\sin\delta\beta - \cos\phi_o)$$

β_o is now a known parameter like ϕ_o or r

$$= \frac{\nu}{r.rl}(\cos(\beta_o+\phi_o) - \cos\phi_o) - \sin(\beta_o+\phi_o)\delta\beta)$$

Similarly, the right hand side

$$\frac{\psi}{rD}\cos(\beta+\phi_o) - \frac{rV}{rD}\sin(\beta+\phi_o)$$

expands to

$$= \frac{(rV)}{rD}\sin(\beta_o+\phi_o)\delta\beta - \frac{rV}{rD}\cos(\beta_o+\phi_o) + \frac{1}{rD}\left[(\psi_o+\delta\psi)(\sin(\beta_o+\phi_o) + \cos(\beta_o+\phi_o)\delta\beta)\right]$$

$$= \frac{(rV)}{rD}\sin(\beta_o+\phi_o)\delta\beta - \frac{(rV)}{rD}\cos(\beta_o+\phi_o) + \frac{1}{rD}\left[\psi_o\sin(\beta_o+\phi_o) + \psi_o\cos(\beta_o+\phi_o)\delta\beta + \delta\psi\sin(\beta_o+\phi_o)\right]$$

The terms containing $\delta\psi$ and $\delta\beta$ are placed on the left hand side and the others on the right hand side

$$\beta'' + C1\beta' - C2\beta - \delta\beta\left(\sin(\beta_o+\phi_o)\left(\frac{\nu}{r.rl} + \frac{(rV)}{rD}\right) + \frac{\psi_o}{rD}\cos(\beta_o+\phi_o)\right) - \frac{\delta\psi}{rD}\sin(\beta_o+\phi_o)$$

$$= (\cos\phi_o - \cos(\beta_o+\phi_o))\frac{\nu}{r.rl} + \frac{1}{rD}\left(\psi_o\sin(\beta_o+\phi_o) - (rV)\cos(\beta_o+\phi_o)\right)$$

The differentials of β are represented in the same way:

$$a_i(\beta_o+\delta\beta)_{i+1} + b_i(\beta_o+\delta\beta)_i + c_i(\beta_o+\delta\beta)_{i-1}\ \{+ d_i\ \delta\psi_i\}$$

The d_i coefficient is introduced to cope with the shear function term created, but which is not apparent from Eqn. (3.45):

$$a_i = 1 + \frac{C1}{2\Delta S} \quad ; \qquad b_i = -2 - C2(\Delta S)^2$$

$$c_i = 1 - \frac{C1}{2\Delta S} \quad ; \qquad d_i = -\frac{\sin}{rD}(\beta_o + \phi_o)(\Delta S)^2$$

Again, the "knowns" are taken on to the left-hand side, then:

$$a_i\ \delta\beta_{i+1} + \bar{b}_i\ \delta\beta_i + c_i\ \delta\beta_{i-1} + d_i\delta\psi_i = \Gamma_{1i} \quad \ldots\ldots\ldots\ldots \quad (3.43a)$$

where

$$\bar{b}_i = b_i - \left(\sin(\beta_o + \phi_o)\ \left(\frac{\nu}{r.rl} + \frac{(rV)}{rD}\right)_i + \frac{\psi_o}{rD}\cos(\beta_o + \phi_o)\right)_i \Delta S^2$$

$$\Gamma_{1i} = -(a_i\beta_{i+1} + b_i\beta_i + c_i\beta_{i-1}) + \left(\cos\phi_o - \cos(\beta_o + \phi_o)\right)\frac{\nu}{r.rl} + \frac{1}{rD}\left(\psi_o \sin(\beta_o + \phi_o) - (rV)\cos(\beta_o + \phi_o)\right)$$

A similar exercise is performed to obtain the shear function equation in the same programable form.

Convergence and convergence tolerance

In general, the number of iterations a problem takes to converge and the convergence tolerance are directly related. Therefore, a certain amount of consideration must be given to the convergence tolerance, although it remains of arbitrary choice. Studies showed that the rotation was better behaved than the shear function, so it seemed reasonable to assume that if the shear function had converged, i.e. $|\delta\psi_i| \leqslant$ convergence tolerance for all i's, then the rotation had.

The arbitrary value of the tolerance chosen was that every i^{th} value of error be less than 0.1 per cent of the updated value of shear function, i.e.

$$\left|\frac{\delta\psi_i}{\psi_i}\right| \leqslant .001 \quad (\text{for } i = 1, 2 \ldots\ldots N).$$

This was found generally to cause the problem to converge within 2 to 5 iterations, 3 iterations being by far the most common number. Any further tightening on the tolerance was unable to show any noticeable improvement in the results.

Pressure/loading increments

Providing the program was solving a problem which would converge (i.e. not an elastically unstable problem), it would produce a correct solution with any size load increment.

Therefore, the number of steps was only dependent on the amount required to obtain a satisfactory pressure/load deflection curve, the only proviso being that the initial solution was in the approximate linear range.

Computer times

A pressure characteristic containing 20 pressure-deflection points could be solved in one second on a C.D.C. 7600 computer. This time can again be compared with a non-linear model developed by F. Abdullah, ref. (19), which used his linear model as a starting point and proceeded with a shooting method and optimisation at each subsequent pressure point; this took approximately 24 seconds to solve. The speed of solution for the finite difference approach is therefore many times faster than the direct integration method, although not quite as accurate, because in the F. Abdullah model strain is taken into consideration at each pressure point.

3.3.3 Model comparison and performance tests

F. Abdullah tested his non-linear model qualitatively by using a fictitious flat plate with a centre boss: Young's Modulus was set to 100 and the plate thickness = 0.1, the overall dimensions being shown on Figure 3.26. The characteristic for this flat plate came from Andreeva, ref. (10), Eqn. (3.30). The results for the model were superimposed on the curve (Figure 3.26).

There was a slight error introduced here, which was that the Andreeva equation did not have a centre boss, but the effect of this was expected to be small. Nevertheless, the agreement was good. Implementing the Billington equations and using the same flat plate parameters, produced the characteristic shown by the x's on Figure 3.26. These results were slightly lower than was expected so, as a further test, the non-linear Reissner equations were also programmed (Eqns. (3.40a) and 3.40b)). The reason for this was because the equations of Abdullah, ref. (19), although they were in state variable form, were also Reissner's basic equations. These are shown by ⊡ symbols in Figure 3.26, and it can be seen that the finite difference results fall either side of the ref. (19) values. The actual values and percentage differences are shown in Table 3.2.

Pressure	Billington	Reissner	% Difference
0.005	.01	.009885	1.1633
0.01	.0197	.01963	0.35659
0.02	.0371	.03773	-1.6953
0.03	.0518	.05344	-3.0688
0.04	.0644	.06686	-3.679
0.05	.0748	.07245	-4.652
0.06	.084	.08862	-5.213
0.07	.0921	.09769	-5.722
0.08	.0994	.1059	-6.1378
0.09	.1061	.1134	-6.437
0.1	.1123	.1203	-6.65
0.11	.118	.1267	-6.866
0.12	.1233	.1327	-7.0836
0.13	.1283	.1383	-7.2306

Table 3.2

The results show that, initially, Billington's deflections are very slightly higher than Reissner's deflection, but the situation is reversed and the Reissner equations give an increasingly higher deflection. The difference values are quite numerically significant and would indicate that the Billington equations are the better to use because, as they contain no allowance for strain, one would expect the results to be on the "stiff" side, i.e. for a given pressure not so much displacement, and also they are nearer the F. Abdullah result. Comparison using a plate could be misleading owing to the very large non-linearity involved, and from a more practical point of view, a flat plate has a very limited application to pressure measurement. Therefore, considering the two sets of equations (Billington's and Reissner's), a comparison between the two was made when applied to a diaphragm shape of four convolutions. The problem is a realistic one: the diaphragm shape simulated is one-half a production capsule 0.006" (0.1524 mm) thick. The table below shows the deflections for equal pressure steps for both sets of equations.

The point to note is that the results presented in the table are not so radically different as for the flat plate case, varying from (0.5 per cent) up to(0.62 per cent). The maximum non-linearities are very similar and occur at the same point in the pressure range.

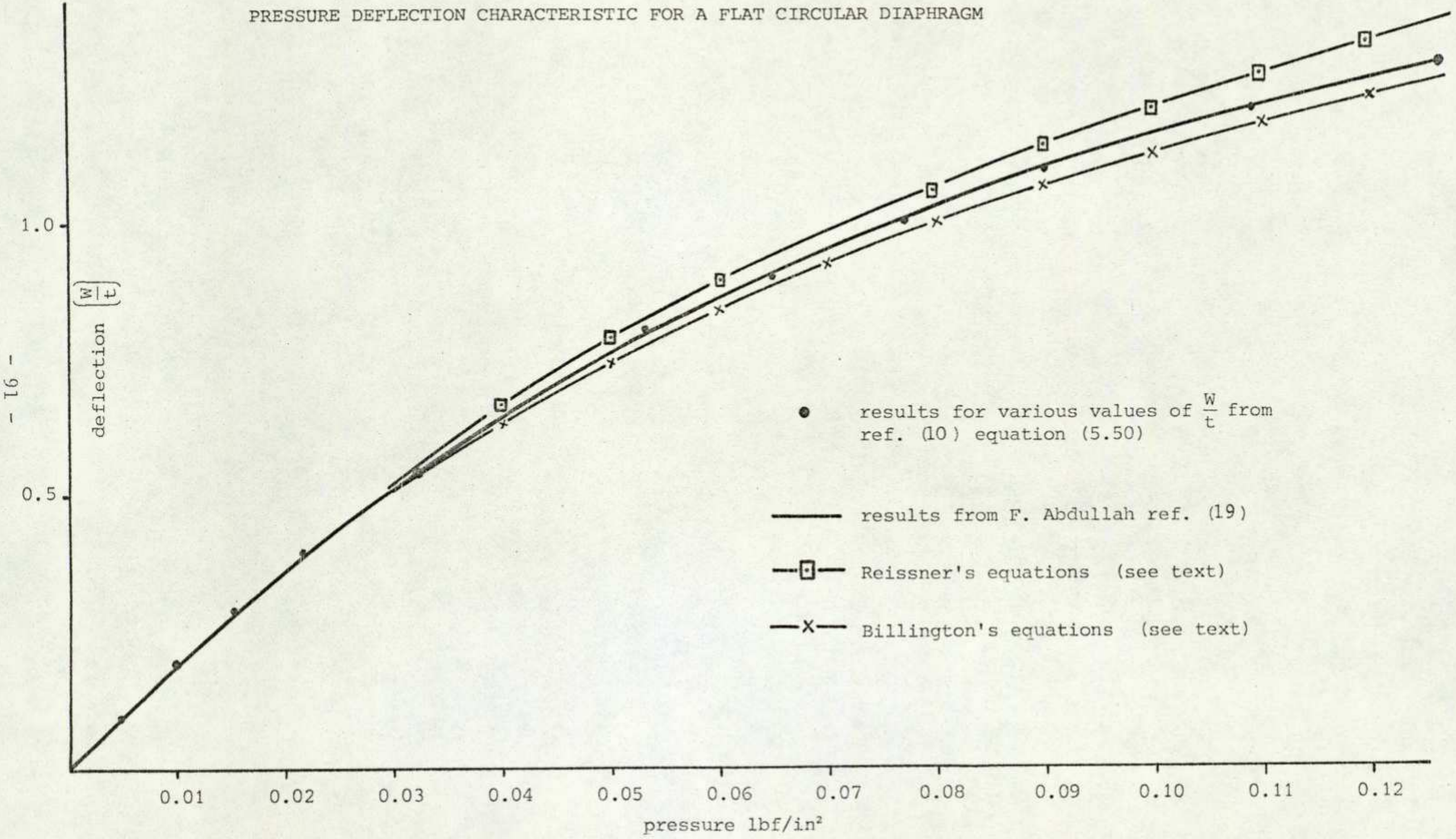
PRESSURE DEFLECTION CHARACTERISTIC FOR A FLAT CIRCULAR DIAPHRAGM

Figure 3.26

Billington	Reissner	% Difference
0.33167	0.33333	.5
0.65416	0.65766	
0.9676	0.97316	
1.2726	1.2800	
1.5693	1.5785	
1.85833	1.8683	.535
2.13833	2.1516	
2.41167	2.4266	
2.6783	2.6950	
2.9383	2.9566	.62
3.4 per cent	3.37 per cent	maximum predicted non-linearity

Table 3.3

Any validation of the models presented so far can only be realistically made when compared with experimental results, and these will be given in a later chapter.

3.3.4 Elastic instability

Convergence of the non-linear problem dependent variable β and ψ may be studied along with the problem of elastic instability. Confining ourselves to the study of pressure elements, elastic instability is utilised in so-called "snap-through" action diaphragms, where, at a certain predetermined pressure, the diaphragm becomes unstable and a slight increase in pressure will cause a large displacement, leading to a more stable position. This action is also known as "oil-canning" when it is an undesirable effect. The snap action operation is used for pressure switches where the accuracy is not highly critical: this is because of associated dead bands. Diaphragms which do utilise the snap action are generally of a conical or spherical profile pressurised from the convex side (Figure 3.27).

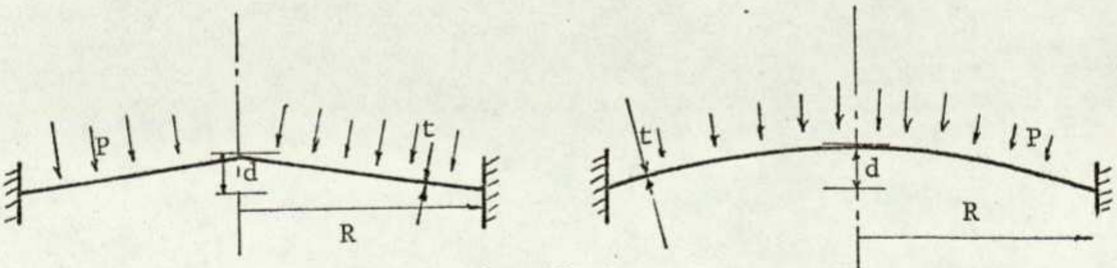

Figure 3.27: Snap-action diaphragms

The manner in which a convex diaphragm operates can now be examined more closely. When it is loaded by a pressure P, the deflection W on the initial section OA of the characteristic (Figure 3.28) increases smoothly.

When the pressure reaches a certain critical value, P_{cr_1}, the diaphragm loses its stability and changes its deflection by a jump, passing to the characteristics section DC. From that point on, the deflections again increase gradually with pressure. When the diaphragm is unloaded, it again returns to the branch OA in a jump, but pressure P_{cr_2} at which this jump occurs is lower than the pressure P_{cr_1}.

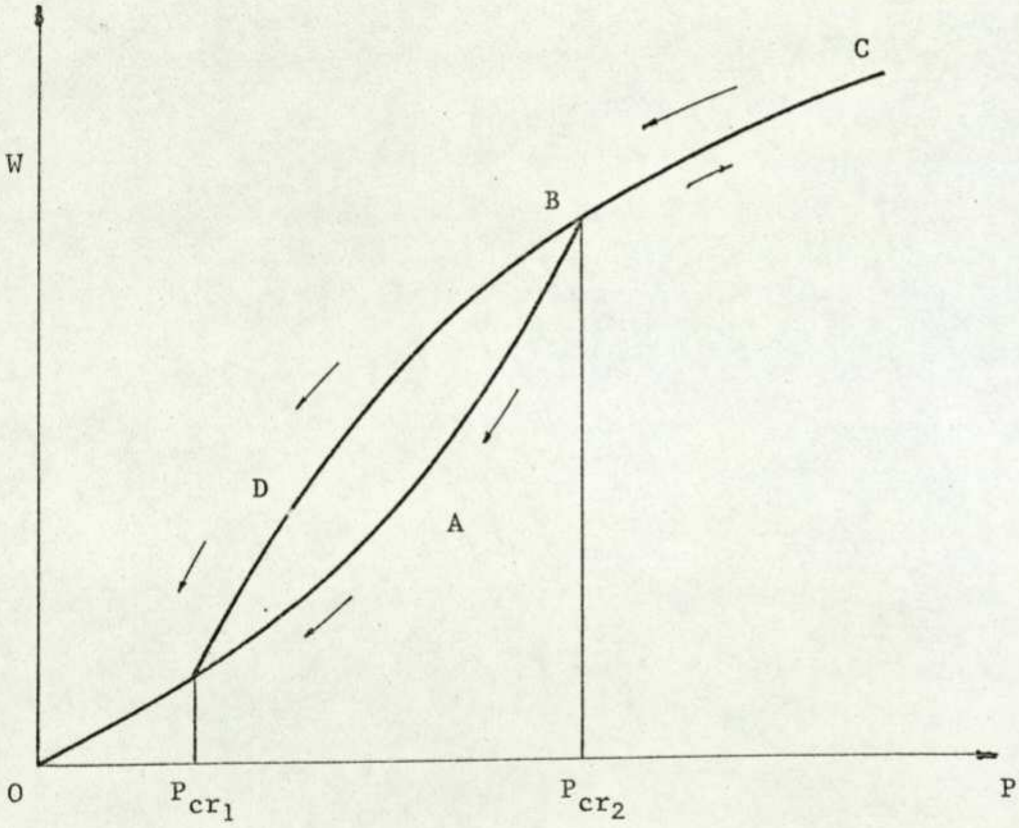

Figure 3.28: Snap action

Andreeva, ref. (10) derives an approximate equation for the pressure deflection curve which is adequate for deflections up to 2-3 thicknesses. The equation is very similar to the ordinary diaphragm equation, but with the inclusion of a squared term:

$$\frac{PR^4}{Et^4} = \alpha \frac{W}{t} \pm \gamma \left(\frac{W}{t}\right)^2 + \beta \left(\frac{W}{t}\right)^3$$

The plus sign of the squared term corresponds to pressure loading from the concave side, and the minus sign to loading from the convex side. Therefore, for conical diaphragms of $\frac{d}{t}$ ratios of 0, 1, 2 and 3, the non-dimensional plots take the following form:

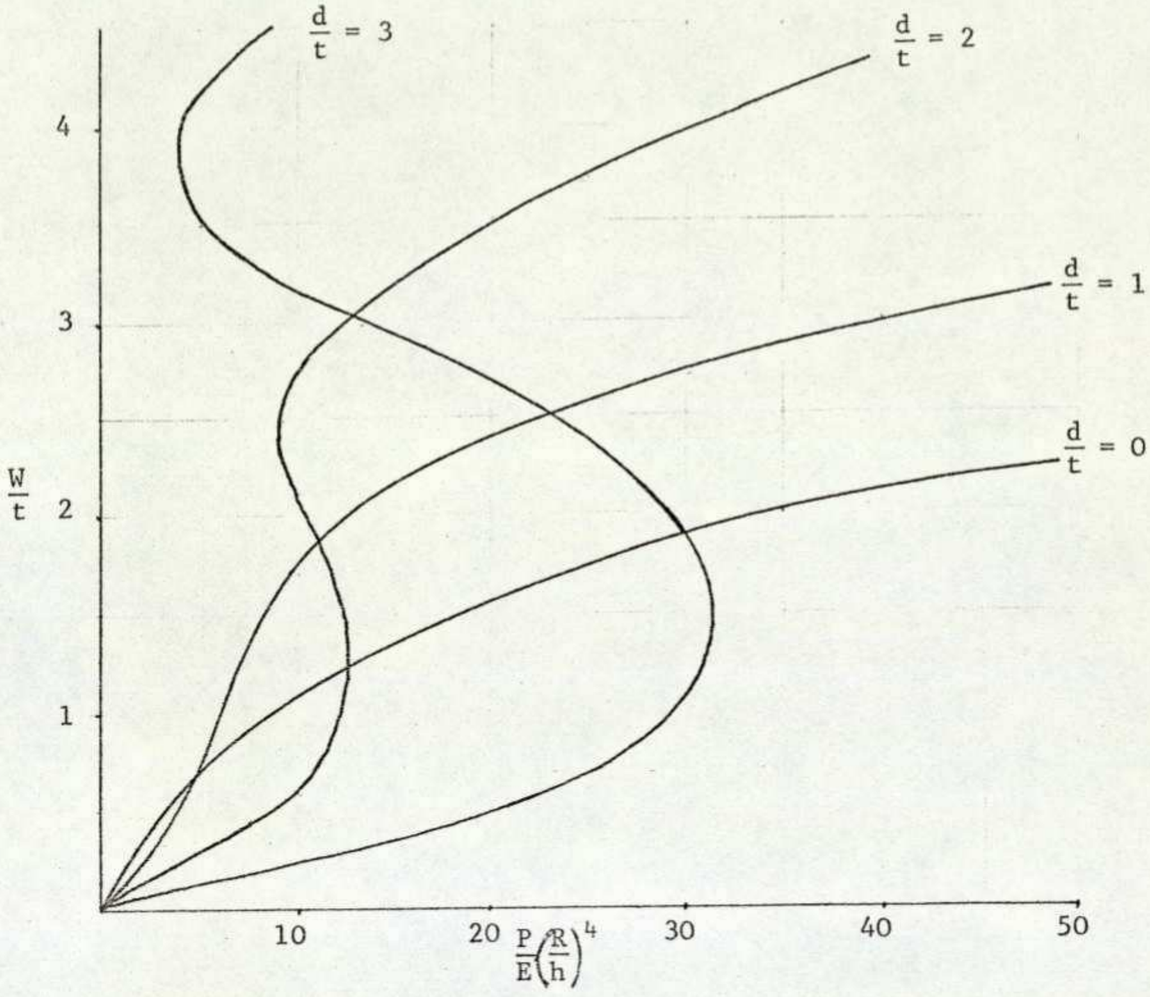

Figure 3.29: Snap-action Andreeva

Computer study of "snap" action

The diaphragm profile programmed is shown below:

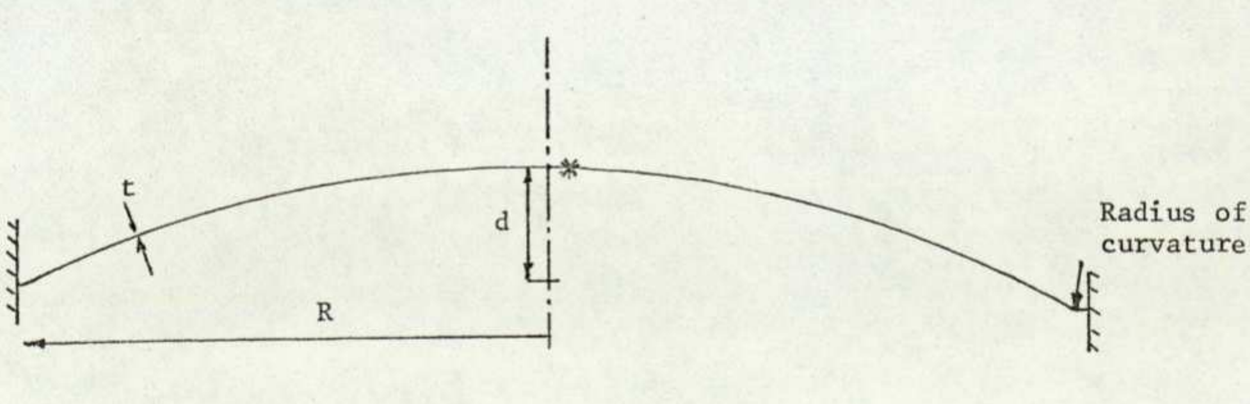

Figure 3.30: Computer snap action diaphragm

The dome-shaped diaphragm had the pressure applied from the convex side:

the dimensions and other input data were:

$R = 2.0$ inches
$t = 0.006$ inches
$d = 1.5t$
$E = 29 \times 10^6$ lbf/in^2 (199×10^6 MN/m^2)
Radius of curvature very small

therefore

$$\frac{P}{E}\left(\frac{R}{t}\right)^4 = (42571)P$$

The values of β and ψ were observed at the second mesh point out from the centre line, indicated by *. This particular shape, with a $(\frac{d}{t})$ ratio of 1.5, was just enough to show "snap through" action without the iteration process breaking down, i.e. $\delta\psi$ and $\delta\beta$ not tending to zero would cause breakdown. The initial pressure was set at 0.005 lbf/in^2 $\left(\frac{P}{E}\left(\frac{R}{t}\right)^4 = 2.128\right)$, and from the values given by the linear model the non-linear model converges within 3 iterations. $\beta_2 = (0.6903$ to 0.8215×10^{-5} and $\psi_2 = (-0.5435$ to $-0.5740) \times 10^{-2}$, the negative value of shear function, indicates a compressive load. Both β_2 and ψ_2 rise to their new values fast (within 3 iterations) and in a steady fashion, i.e. no overshoot.

A pattern which continues up to a pressure of 0.015 lbf/in^2,

$$\frac{P}{E}\left(\frac{R}{t}\right)^4 = 6.386 \qquad \text{when} \qquad \begin{cases} \beta_2 = 0.4707 \times 10^{-4} \\ \psi_2 = -0.20124 \times 10^{-1} \text{ lbs-f} \end{cases}$$

Then, when pressure was subsequently increased to 0.02 lbf/in^2 $\left(\frac{P}{E}\left(\frac{R}{t}\right)^4 = 8.54\right)$, convergence took 9 iterations and the rotation finally settled at 1.4083×10^{-4}, an increase of almost 200 per cent on the previous value. The centre deflection had increased by approximately 190 per cent, but the shear had decreased to -0.15487×10^{-1} lbs-f; the compressive load was reduced. As the pressure was increased, the shear function became less negative and passed through zero and at 0.03 lbf/in^2 $\left(\frac{P}{E}\left(\frac{R}{t}\right)^4 = 12.771\right)$ and had a positive value, indicating that near the centre the diaphragm was now in tension. From the pressure at 0.03 lbf/in^2, the iteration procedure converged once more within 3 iterations. A closer look at what happens at these pressures might reveal why convergence occasionally breaks down. Figure 3.31 is a plot of β_2 against the number of iterations at the pressure 0.02 lbf/in^2. It starts at iteration zero, which is the value of β_2 at the previous

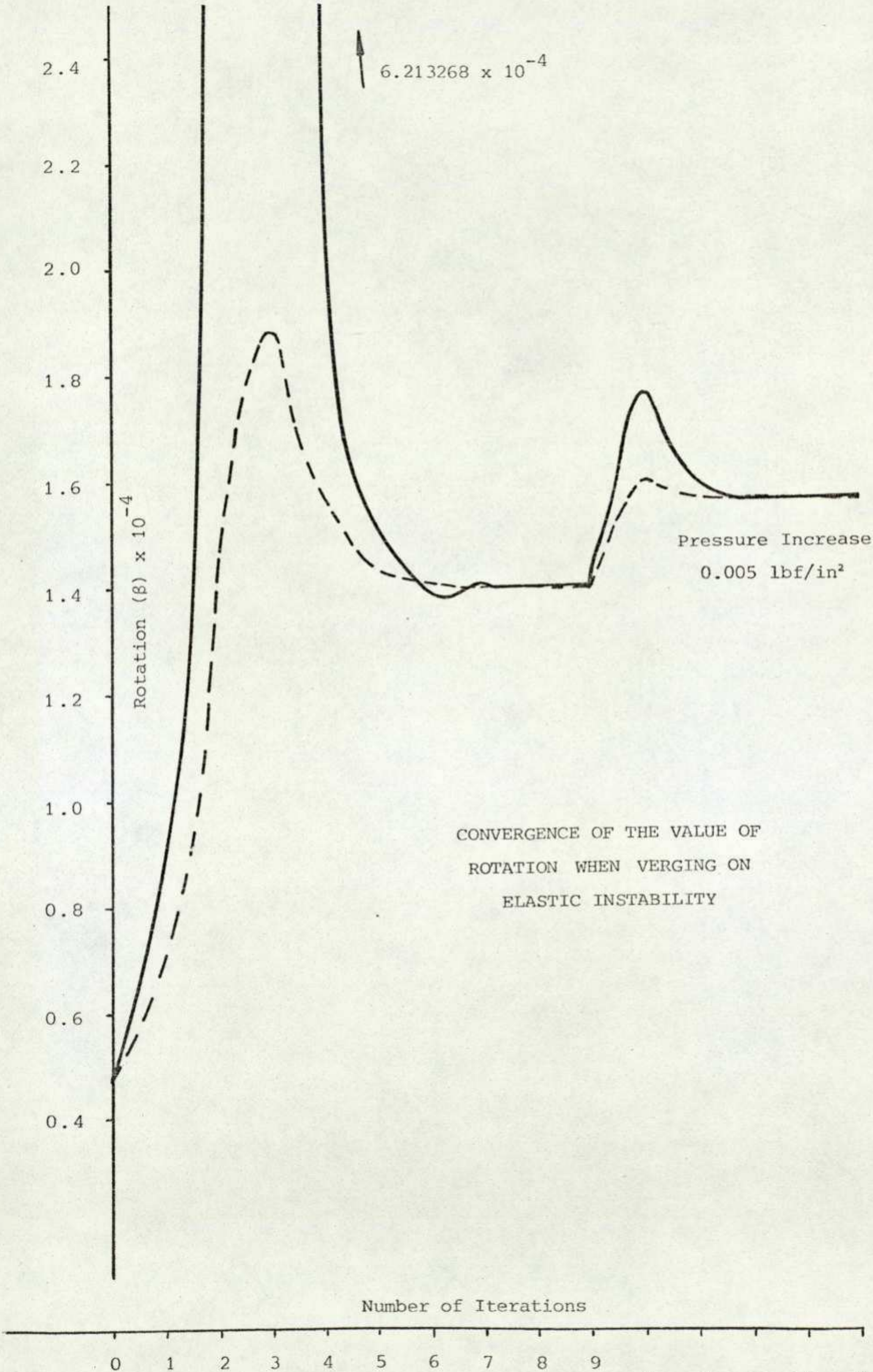

CONVERGENCE OF THE VALUE OF
ROTATION WHEN VERGING ON
ELASTIC INSTABILITY

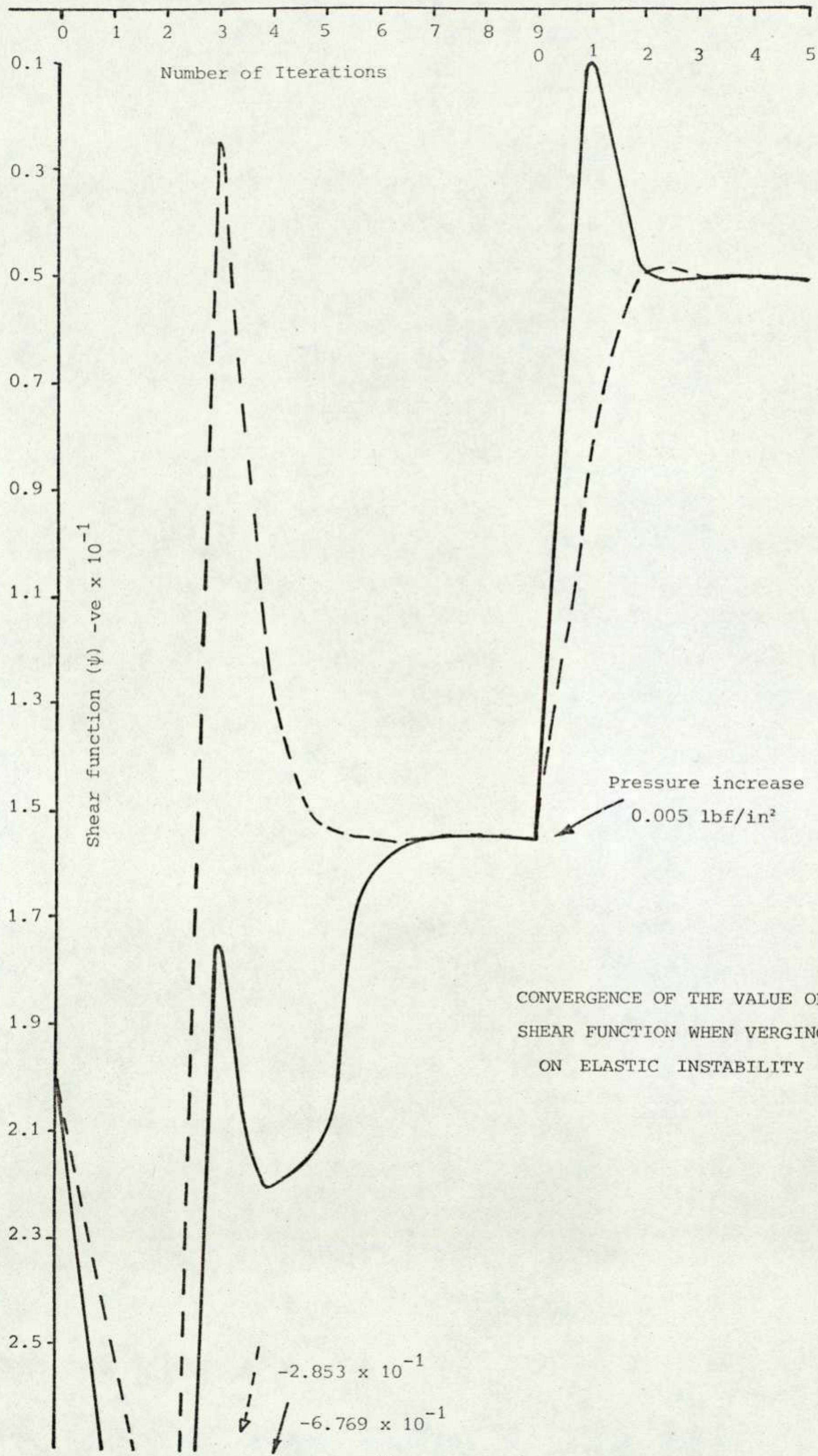

CONVERGENCE OF THE VALUE OF SHEAR FUNCTION WHEN VERGING ON ELASTIC INSTABILITY pressure ($0.4707 \times 10^{-4} = \beta_{o,2}$); this value is increased after one cycle to 0.9886092×10^{-4} and, after two cycles, has risen to a very high value of 6.21326×10^{-4}. It returns and under-shoots the "steady state" value of 1.408346×10^{-4} to 1.396050×10^{-4} after 6 iterations, finally settling after 9 iterations. The point to note about the rotation is that the value does initially move towards the final value.

The shear function ψ_2 (Figure 3.32) initially moves in the opposite direction and becomes very negative after 2 iterations: after 3 iterations the value comes back up, but it oscillates about a value which is not the final value, and then moves into the final value very quickly after the sixth iteration. On Figures 3.31 and 3.32 the iterations are shown for the next pressure point: the rotation β_2 over-shoots and comes back to the final value within 5 iterations, as does the ψ_2 value. Owing to the cross-dependence of the two simultaneous equations, the rotation must affect the shear function and vice-versa; therefore, because the ψ_2 value behaves badly before the rotation, it is probable that the shear function causes the normally well-behaved rotation to exhibit bad stability. An improvement was attempted, aimed at simple proportional control of the error on the first iteration, by reducing it by one-half, i.e.

$$\beta = \beta_o + \frac{\delta\beta}{2}$$

$$\psi = \psi_o + \frac{\delta\psi}{2}$$

This is curve 2 on Figures 3.31 and 3.32. The effect was to reduce the maximum over-shoot and produce a convergence in 8 iterations instead of 9, and 4 instead of 5 for the next pressure up. Generally, the improvement slowed the program down because it overdamped the well-behaved pressure points (Figure 3.33).

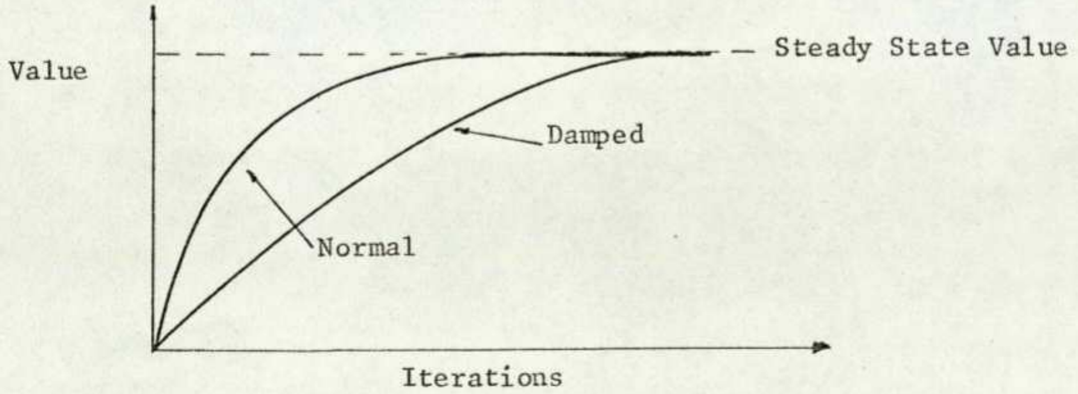

Figure 3.33: Normal operation

In conclusion, a study of elastic instability with these equations appears to be adequate - that is, they do predict the "snap through" action, but the method of solution is not a good one. If the two equations could be further reduced so that the dependent variable was only the rotation, then the solution could possibly be more stable. It was not the intention of the work to predict elastic instability and, therefore, no modification of the equations was thought necessary as convergence was generally very fast. As stated before, a convex shape of greater curvature than that caused by a $(\frac{d}{t})$ ratio of 1.5 caused a convergence failure. To overcome this problem and look at profiles up to $(\frac{d}{t}) = 3$, the following modification was written into the non-linear program:

Consider a point on the surface of the diaphragm before and after "snap through" action (Figure 3.34).

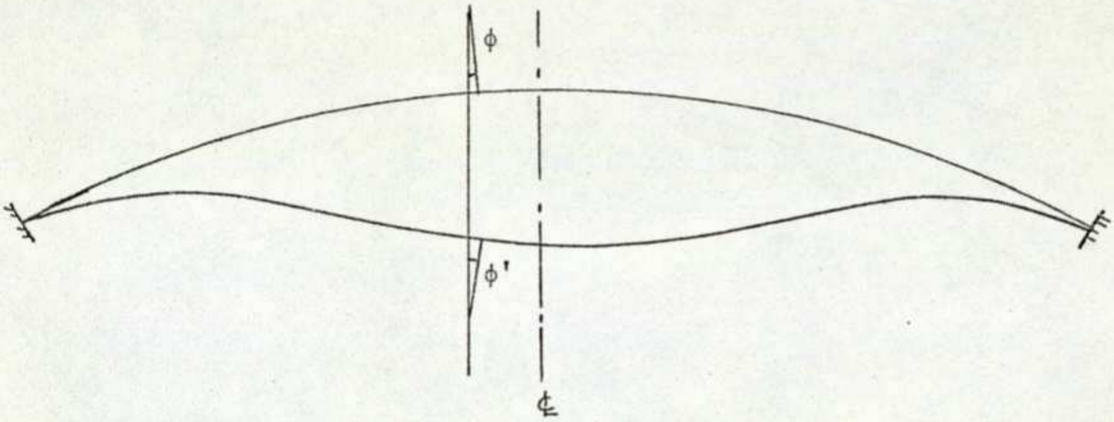

Figure 3.34: A diaphragm snapped through

The angle of the normal drawn through the point to the vertical is the basic geometric parameter ϕ, and after "snap" action the angle is, to a good approximation, the same angle but negative, hence the rotation of the mesh point appears to be 2ϕ. Therefore, when the iteration procedure breaks down, the diaphragm is assumed to have "snapped across" and at that pressure point the problem is re-solved with an initial value of $\beta_{oi} = 2\phi_{oi}$, and the shear function changed from compressive load to tensile, i.e. ψ_{oi} becomes $-\psi_{oi}$ $(i = 2 \ldots\ldots N-1)$.

Problems with $(\frac{d}{t}) = 2$ and 3 were then solved, as shown in Figure 3.35; with $(\frac{d}{t}) = 3$ having solved with increasing pressure, the problem was worked back down the characteristic until it snapped through to its original shape, thus giving the two critical pressures, P_{cr_1} and P_{cr_2}, and the associated dead band.

GRAPH OF "SNAP THROUGH" ACTION CONVEX DIAPHRAGMS

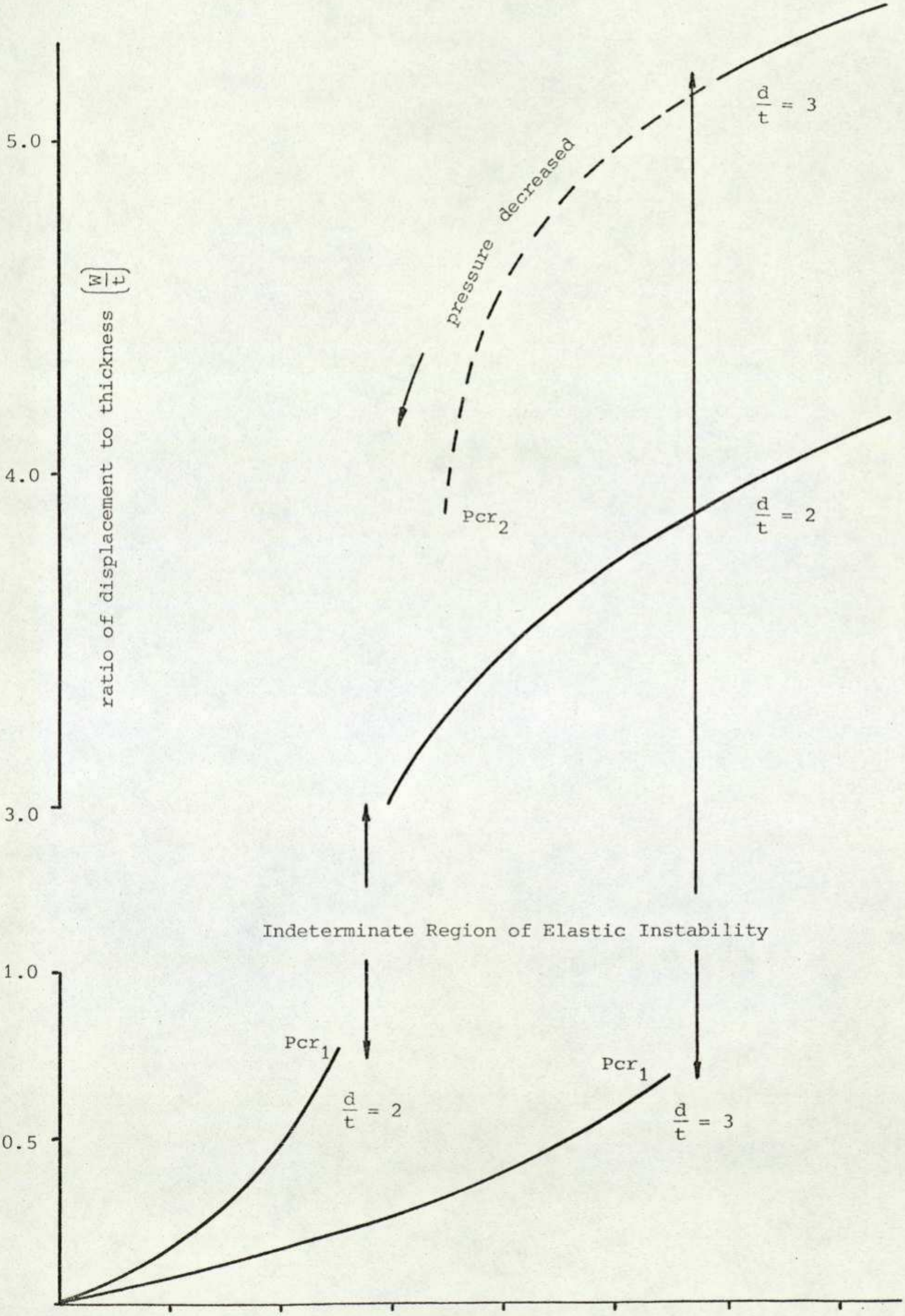

3.4 Capsules

The design of a diaphragm assembly is considerably simplified if two diaphragms are connected along their outer flanges to form a diaphragm box or capsule, the advantage being that the deflection of such a box under a given pressure is, to a good approximation, twice as large as that of a single diaphragm. Additionally, the installation of a capsule in an instrument is much simpler than the installation of a single diaphragm. Several capsules may be connected in series to increase the deflections.

A capsule may be of two basic types (Figure 3.36): the non-collapsible aneroid capsule and the collapsible overload protected capsule, which has the added advantage that it can be used at high static pressures and withstand an overload many times larger than its working pressure.

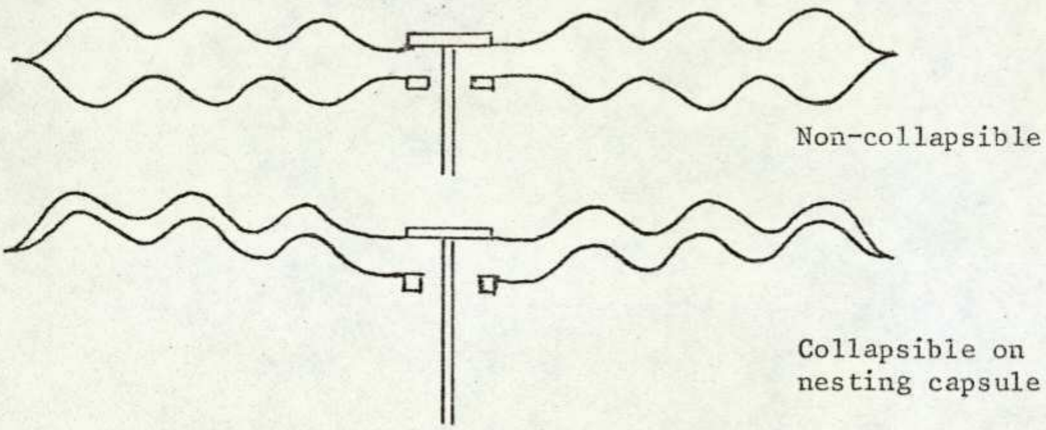

Figure 3.36: The two types of capsule

3.4.1 Linear analysis of capsules

As with the non-linear diaphragm model, the utilisation of the linear diaphragm model and its numerical procedure was considered the best approach to solving the problem. The main difficulty lay in the mode of fixing at the outer edge flange, and two possibilities were considered:

(a) Treating the capsule as two separate diaphragms and matching the boundary conditions to suit at the outer edge;

(b) Treating the capsule as a complete shell which had a very tight fold at the outer edge.

These are illustrated in Figure 3.37 for both types of capsule.

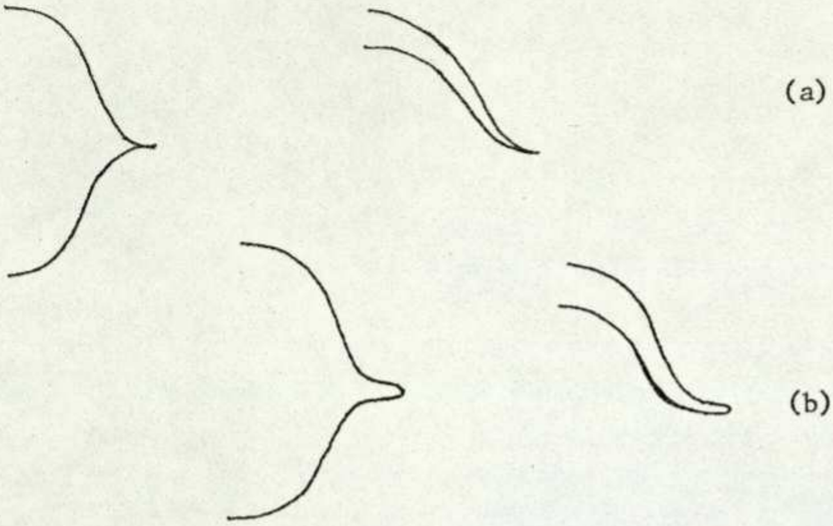

Figure 3.37: Two possible capsule simulations

[N.B. In all cases the lines shown are the neutral axis, and the effect of thickness has been neglected.]

Practical considerations led to the choice of method (a). Investigation of actual production capsules which had been sectioned gave a clear indication that method (a) was a better approximation when the capsule had been electron beam welded. No soldered capsules were available for inspection but this is a less common form of fixing. Figure 3.39b is a 0.025" (0.635 mm) thick production capsule, sectioned along a diameter and magnified 25 times. Also, any attempt to simulate a tight radius would be a poor approximation. Therefore method(a) was adopted.

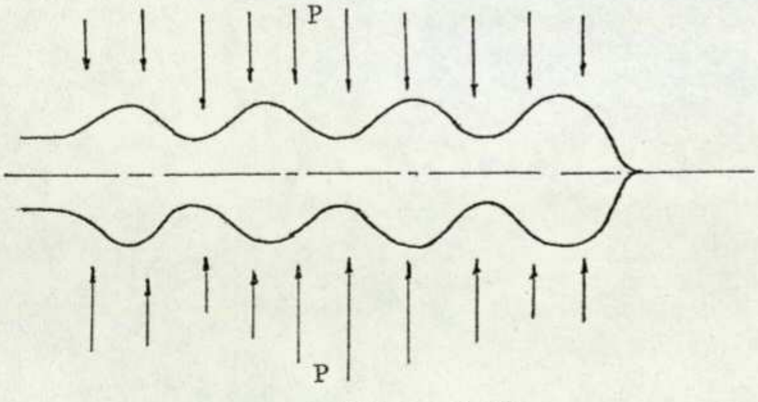

Figure 3.38a

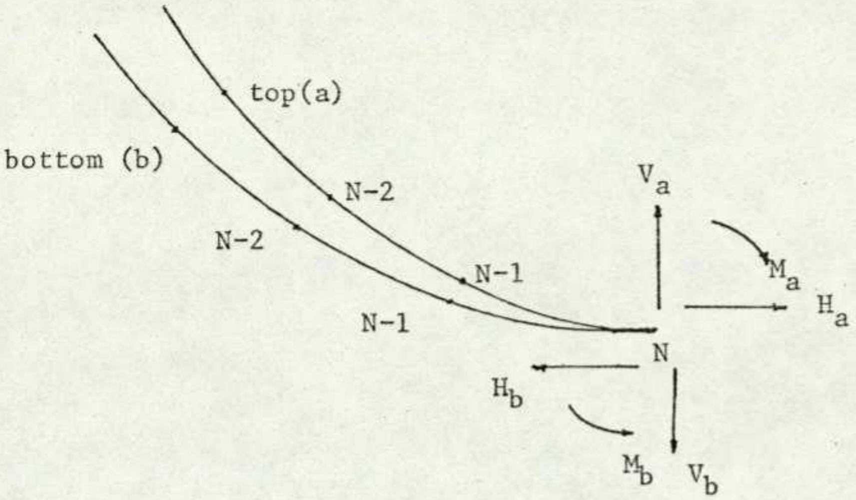

Figure 3.38b

Figure 3.38: Pressure loading on a capsule

Consider the capsule shown in Figure 3.38a as two separate diaphragms. The top diaphragm will always experience a pressure loading equal and opposite to the bottom, i.e. if the top diaphragm is loaded by a pressure (P), then the bottom diaphragm is subjected to a (-P) pressure loading: this will be the case of a compressive pressure on a capsule. Figure 3.38b shows, schematically, the end of a capsule connected at the N^{th} point. As all forces, loads, etc. are referred to the neutral axis, the capsule is assumed connected at the neutral axis. Consideration of the stresses at the end point will give the required relationships between values shown in Figure 3.38b. The stresses are assumed to be linearly distributed through the thickness of the shell, hence, for the top diaphragm in compression (P), the total stress on the top face in the ξ direction will be $\frac{N_\xi}{t} + \frac{6M_\xi}{t^2}$, therefore the bottom face where it is joined has a total stress in the same direction of $\frac{N_\xi}{t} - \frac{6M_\xi}{t^2}$. Because of the reversal in sign of the pressure applied to the bottom diaphragm, the total stress on the top face is equal to $\frac{N_\xi}{t} - \frac{6M_\xi}{t^2}$. Hence, for equilibrium the stresses must be equal and opposite for the joining surfaces, and at the N^{th} point:

$$N_\xi\Big|_a = -N_\xi\Big|_b$$

and $$M_\xi\Big|_a = -M_\xi\Big|_b$$

It then follows from the static equilibrium that the internal forces for the top and bottom must balance at the N^{th} point.

$$H_N^a = -H_N^b \qquad \text{.................................} \quad (3.46)$$
$$V_N^a = -V_N^b$$

$(Vr)_i$, although being an internal force, is derived from the pressure loading and for the compressive case mentioned:

$$(Vr)^a_N = -\frac{Pr_N^2}{2} \quad ; \quad (Vr)^b_N = \frac{Pr_N^2}{2}$$

Compatability leads to the other three conditions and, as the N^{th} point is assumed rigidly joined, the displacements must be equal:

$$\begin{aligned} \beta^a_N &= \beta^b_N \\ U^a_N &= U^b_n \qquad \ldots\ldots\ldots\ldots\ldots\ldots\ldots\ldots\ldots\ldots \quad (3.46) \\ W^a_N &= W^b_N \end{aligned}$$

This concludes the basic ideas on capsules when, to a first approximation, the thickness is neglected. In the analysis that follows the thickness of both diaphragms is assumed the same: from a practical point of view this is a reasonable assumption.

3.4.2 Numerical procedure (linear)

In keeping with the linear diaphragm model, the geometry and equations were set up in the same fashion.

In the solution for ψ_i and β_i $(i = 2 \;.....\; N-1)$, the start of the backward substitution involving equations (3.31) would need to be modified, as β_N and ψ_N are assumed known, as well as the constants BC, BB, etc. For the diaphragm model β_N is known explicitly, and ψ_N is derived from ψ_{N-1} because U_N is known explicitly.

For the capsule no actual values are known, only their dependence one upon another, therefore the rotation and shear function at the N^{th} point are found as functions of the rotation and shear at other points, namely the $N-1^{th}$ if a simple approximation to the first derivative is used,

i.e. $\beta_N = f_1\left(\beta^a_{N-1}, \beta^b_{N-1}\right); \quad \psi_N = f_2\left(\psi^a_{N-1}, \psi^b_{N-1}\right)$

(Again, (a) refers to the top diaphragm and (b) the bottom.)

Then from $M^a_N = -M^b_N$; $M_\xi = D\left[\beta' + \nu \frac{\cos\phi}{r}\beta\right]$ see Eqn. (3.12c)

$$D\left[\beta' + \nu\,\frac{\cos\phi}{r}\,\beta\right]^a = -D\left[\beta' + \nu\,\frac{\cos\phi}{r}\,\beta\right]^b$$

cancel the bending stiffness if the thickness is the same ..... (3.47)

$$\frac{\beta_N - \beta^a_{N-1}}{\Delta S_a} + \nu\,\frac{\cos\phi^a_N\,\beta_N}{r^a_N} = -\,\frac{\beta_N - \beta^b_{N-1}}{\Delta S_b} - \nu\,\frac{\cos\phi^b_N\,\beta_N}{r^b_N}$$

$$\beta_N\left(\frac{1}{\Delta S_a} + \nu\,\frac{\cos\phi^a_N}{r_N} + \frac{1}{\Delta S_b} + \nu\,\frac{\cos\phi^b_N}{r_N}\right) = \frac{\beta^a_{N-1}}{\Delta S_a} + \frac{\beta^b_{N-1}}{\Delta S_b}$$

(It is reasonable to assume at the N^{th} point that $\phi^b = \phi^a$ ..... (3.48)
$r^b = r^a$

$$\beta_N\left(\frac{1}{\Delta S_a} + \frac{1}{\Delta S_b} + 2\nu\,\frac{\cos\phi_N}{r_N}\right) = \left(\Delta S_b\beta^a_{N-1} + \Delta S_a\beta^b_{N-1}\right)\Big/\Delta S_a\Delta S_b$$

$$\beta_N = \frac{1}{\Delta S_b + \Delta S_a + 2\nu\Delta S_a\Delta S_b\cos\phi_N/r_N}\left(\Delta S_b\,\beta^a_{N-1} + \Delta S_a\,\beta^b_{N-1}\right)$$

or $\beta_N = k'_a\,\beta^a_{N-1} + k'_b\,\beta^b_{N-1}$

Now, from Eqn. (3.8b),

$$U = \frac{r}{C}\,(N_\theta - \nu\,N_\xi),$$

then $\dfrac{CU}{r} = \psi' + r\,P_H - \nu\left(\psi\,\dfrac{\cos\phi}{r} + (rV)\,\dfrac{\sin\phi}{r}\right)$

therefore

$$\frac{Et\,U^a_N}{r} = \psi'^a_N + (r\,P_H)^a_N - \nu\left(\psi^a_N\,\frac{\cos\phi}{r} + (rV)^a_N\,\frac{\sin\phi}{r}\right) \quad ..... (3.49)$$

and similarly for b.

Again assuming (3.47) and (3.48) and equating the two ($U^a_N = U^b_N$)

$$\psi'^a_N + r\,P_H - \nu\left(\psi_N\,\frac{\cos\phi}{r} + (rV)_N\,\frac{\sin\phi}{r}\right) = \psi'^b_N + r\,P_H + \nu\left(\psi_N\,\frac{\cos\phi}{r} + (rV)\,\frac{\sin\phi}{r}\right)$$

The ($r\,P_H$) term will cancel out and the (+ve) sign on the right-hand side indicates that ψ_N and $(rV)_N$ are equal but opposite.

$$\psi_N'^{a} - \nu\left(\psi_N \frac{\cos\phi}{r} + (rV)_N \frac{\sin\phi}{r}\right) = \psi_N'^{b} + \nu\left(\psi_N \frac{\cos\phi}{r} + (rV)_N \frac{\sin\phi}{r}\right)$$

$$\frac{\psi_N^a - \psi_{N-1}^a}{\Delta S_a} - \left(\frac{\psi_N^b - \psi_{N-1}^b}{\Delta S_b}\right) = 2\nu\left(\psi_N \frac{\cos\phi}{r} + (rV)_N \frac{\sin\phi}{r}\right)$$

$$\frac{\psi_N}{\Delta S_a} - \frac{\psi_N}{\Delta S_b} - 2\nu\left(\psi_N \frac{\cos\phi}{r} + (rV)_N \frac{\sin\phi}{r}\right) = \frac{\psi_{N-1}^a}{\Delta S_a} - \frac{\psi_{N-1}^b}{\Delta S_b}$$

Hence,

$$\psi_N = \frac{\Delta S_b\ \psi_{N-1}^a - \Delta S_a\ \psi_{N-1}^b + \Delta S_a\ \Delta S_b (rV)_N\ 2\nu\ \sin\phi/r}{(\Delta S_b + \Delta S_a - 2\nu\ \Delta S_a\ \Delta S_b\ \cos\phi/r)}$$

$$\psi_N = k_a\ \psi_{N-1}^a - k_b\ \psi_{N-1}^b + k_c \quad (k_c \text{ is very small and may be neglected})$$

We wish now to form these relationships:

$$\beta_{N-1}^a = BC_{N-1}^a + BB_{N-1}^a \beta_N + BH_{N-1}^a\ \psi_N$$

$$\psi_{N-1}^a = HC_{N-1}^a + HB_{N-1}^a\ \beta_N + HH_{N-1}^a\ \psi_N$$

$$\beta_{N-1}^b = BC_{N-1}^b + BB_{N-1}^b\ \beta_N - BH_{N-1}^b\ \psi_N$$

$$\psi_{N-1}^b = HC_{N-1}^b + HB_{N-1}^b\ \beta_N - HH_{N-1}^b\ \psi_N$$

$$\beta_{N-1}^a = BC_{N-1}^a + BB_{N-1}^a(k_a'\ \beta_{N-1}^a + k_b'\ \beta_{N-1}^b) + BH_{N-1}^a(k_a\ \psi_{N-1}^a - k_b\ \psi_{N-1}^b)$$

$$\psi_{N-1}^a = HC_{N-1}^a + HB_{N-1}^a(k_a'\ \beta_{N-1}^a + k_b'\ \beta_{N-1}^b) + HH_{N-1}^a(k_a\ \psi_{N-1}^a - k_b\ \psi_{N-1}^b)$$

$$\beta_{N-1}^b = BC_{N-1}^b + BB_{N-1}^b(k_a'\ \beta_{N-1}^a + k_b'\ \beta_{N-1}^b) - BH_{N-1}^b(k_a\ \psi_{N-1}^a - k_b\ \psi_{N-1}^b)$$

$$\psi_{N-1}^b = HC_{N-1}^b + HB_{N-1}^b(k_a'\ \beta_{N-1}^a + k_b'\ \beta_{N-1}^b) - HH_{N-1}^b(k_a\ \psi_{N-1}^a - k_b\ \psi_{N-1}^b)$$

This can then be reduced into a convert matrix form, $\bar{A}x = b$

$$\begin{bmatrix} (1 - BB^{a}_{N-1}\, k'_{a}) & (- BH^{a}_{N-1}\, k_{a}) & (- BB^{a}_{N-1}\, k'_{b}) & (BH^{a}_{N-1}\, k_{b}) \\ (- HB^{a}_{N-1}\, k'_{a}) & (1 - HH^{a}_{N-1}\, k_{a}) & (- HB^{a}_{N-1}\, k'_{b}) & (HH^{a}_{N-1}\, k_{b}) \\ (- BB^{b}_{N-1}\, k'_{a}) & (BH^{b}_{N-1}\, k_{a}) & (1 - BB^{b}_{N-1}\, k'_{b}) & (- BH^{b}_{N-1}\, k_{b}) \\ (- HB^{b}_{N-1}\, k'_{a}) & (- HH^{b}_{N-1}\, k_{a}) & (- HB^{b}_{N-1}\, k'_{b}) & (1 - HH^{b}_{N-1}\, k_{b}) \end{bmatrix} = \begin{bmatrix} A \end{bmatrix}$$

$$\begin{bmatrix} BC^{a}_{N-1} \\ HC^{a}_{N-1} \\ BC^{b}_{N-1} \\ HC^{b}_{N-1} \end{bmatrix} = \begin{bmatrix} B \end{bmatrix} \qquad \begin{bmatrix} \beta^{a}_{N-1} \\ \psi^{a}_{N-1} \\ \beta^{b}_{N-1} \\ \psi^{b}_{N-1} \end{bmatrix} = \begin{bmatrix} X \end{bmatrix}$$

Solving for $\begin{bmatrix} X \end{bmatrix}$ enables:

$$\beta_j = BC_j + BB_j\, \beta_{j+1} + BH_j\, \psi_{j+1}$$

$$\psi_j = HC_j + HB_j\, \beta_{j+1} + HH_j\, \psi_{j+1}$$

for (a) and (b) to be solved from $j = \Big((N-2)\ \ldots\ldots\ 2\Big)$

All the forces and displacements were solved as for each separate diaphragm except the vertical displacement W. The solution was started at the inner edge of the bottom diaphragm, where $W\big|_{i=1}$ = zero. This was progressed to the N^{th} point by

$$W_{i+1} = \frac{\left(W_i + W_{i-1}\right)}{2} + \frac{3}{2}\ \Delta S_b \left(\frac{dW}{ds}\right)_i .$$

To remove the slight instability which occurred initially, the $N + 1^{th}$ vertical deflection point was found by

$$W_{N+1} = W_{N-1} + 2\beta_N (\Delta S_a - \Delta S_b)$$

Then the final vertical deflection was found by integrating back along the top diaphragm with

$$W_{i+1} = \left(\frac{W_i + W_{i-1}}{2}\right) - \frac{3}{2} \Delta S_a \left(\frac{dW}{ds}\right)_i$$

3.4.3 Program testing

The program was tested by making a capsule of the nesting type by placing two identical diaphragms together and applying a load. Practically, of course, this is not possible in compression because the diaphragms are unable physically to pass through one another, but in the program no such restriction applies, and some form of "stop" to investigate nesting would have to be built in additionally.

The effect of applying a pressure gave a vertical centre displacement of 6.790517×10^{-2} units and a periphery displacement of 3.395316×10^{-2} units: twice this figure is 6.790632×10^{-2} units. With this test one would expect the outer displacement to be exactly one-half the centre displacement, which it is for all practical purposes. Also, it would be expected that the horizontal displacement at the outer edge be zero: in fact, it came to -3.465×10^{-16} (virtually zero).

Testing the program with an actual modelled nesting capsule, to compare the capsule deflection with the sum of the individual diaphragm, gave the following results:

Top diaphragm separately = 0.033672
Bottom diaphragm separately = 0.0404603
Sum = 0.0741327

As a capsule = 0.07543682

This shows an increase of 1.73 per cent on deflection if the diaphragms are assembled in a nesting capsule as compared to the sum of the diaphragm individually.

This is consistent with the results presented in the second chapter on the experimental observations of capsules, which states that: "The deflection of the capsule was about 3 per cent greater than the sum of the separate diaphragm deflections", but in that case the capsule was formed into a non-nesting type, which will allow more horizontal deflection at the outer edge, whereas the nesting type will tend to cancel out the horizontal deflection. Hence the result of the previous example.

The deflection then obtained from a non-nesting type would be expected to be more than the nesting type, assuming the same conditions - hence the greater percentage difference.

It must be emphasized that these test runs do not verify the model - this is discussed in the chapter on experimental validation - but they indicate that it behaves as expected.

3.4.4 Non-linear capsule model theory

Basically, the non-linear capsule model is a combination of the non-linear diaphragm model and the linear capsule model. Small additions are made to the boundary conditions at the outer edge to accommodate the non-linear equations and the effect of thickness.

Consider the outer edge of the capsule and the associated material thickness (Figure 3.39a):

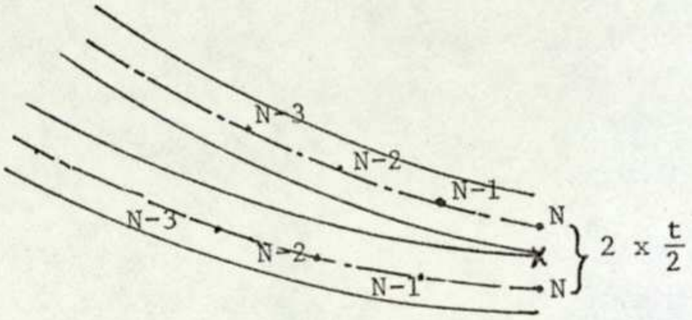

Figure 3.39a

The end points are separated by two half thicknesses and the top diaphragm only touches the bottom at point X; generally, the end point will undergo a vertical displacement W, horizontal displacement U, and rotation β (Figure 3.40).

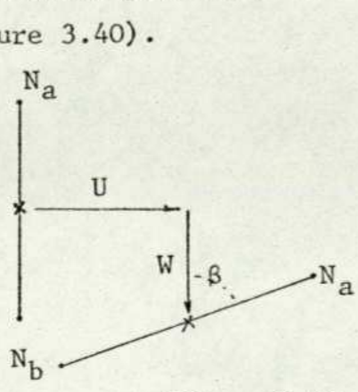

Figure 3.40

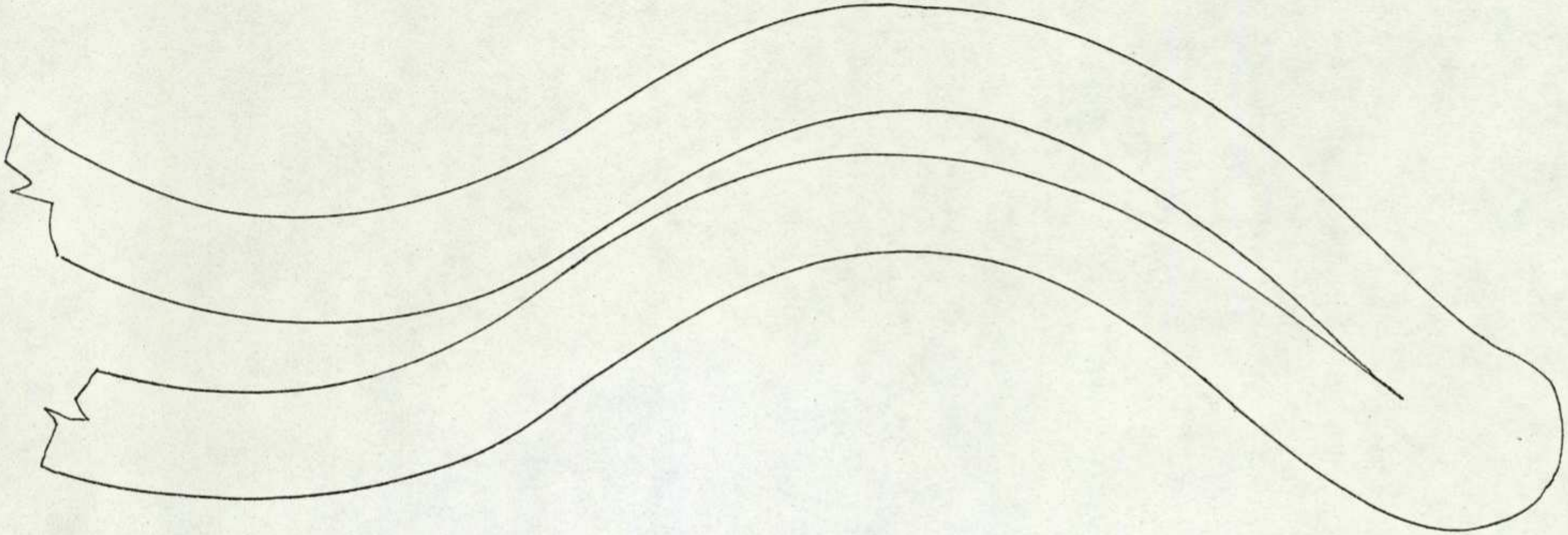

Figure 3.39a: An actual Production Capsule 25 times full size sectioned along a diameter

If β is small, the horizontal displacement of the top diaphragm (a) $= U + \frac{\beta t}{2}$, and the bottom (b) $= U - \frac{\beta t}{2}$.

Referring back to Eqn. (3.4), we have:

$$\frac{Et}{r_a}\left(U + \frac{\beta t}{2}\right) = \psi_N'^{a} + r\,P_H - \nu\left(\psi_N^a \frac{\cos\phi}{r} + (Vr)_N^a \frac{\sin\phi}{r}\right)$$

$$\frac{Et}{r_b}\left(U + \frac{\beta t}{2}\right) = \psi_N'^{a} + r\,P_H - \nu\left(\psi_N^b \frac{\cos\phi}{r} + (Vr)_N^b \frac{\sin\phi}{r}\right)$$

So

$$\psi_N'^{a} - \nu\left(\psi_N \frac{\cos\phi}{r} + (Vr)_N \frac{\sin\phi}{r}\right) - \frac{Et^2\beta_N}{2r} = \psi_N'^{b} + \nu\left(\psi_N \frac{\cos\phi}{r} + (Vr)_N \frac{\sin\phi}{r}\right) + \frac{Et^2\beta_N}{2r}$$

which reduces to:

$$\psi_N = \frac{\Delta S_b\,\psi_{N-1}^a - \Delta S_a\,\psi_{N-1}^b + \Delta S_a\,\Delta S_b\left((rV)2\nu\,\sin\phi/r + Et^2\beta_N/r\right)}{\left(\Delta S_b + \Delta S_a - 2\nu\,\Delta S_a\,\Delta S_b\,\cos\phi/r\right)} \tag{3.50}$$

This last term, i.e. $\frac{Et^2\beta_N}{r}$, can be seen to have an increasingly large effect as the material thickness increases.

Therefore,

$$\psi_N = k_a\,\psi_{N-1}^a - k_b\,\psi_{N-1}^b + k_{bb}\,\beta_N,$$

the penultimate term being neglected as before. The $\left[A\right]$ then takes the following form:

$$\begin{bmatrix}
\left\{1 - k_a'\left(BB_{N-1}^a - k_{bb}BH_{N-1}^a\right)\right\} & \left(-BH_{N-1}^a k_a\right) & \left\{-k_b'\left(BB_{N-1}^a - k_{bb}BH_{N-1}^a\right)\right\} & \left(BH_{N-1}^a k_b\right) \\
\left\{-k_a'\left(HB_{N-1}^a - k_{bb}HH_{N-1}^a\right)\right\} & \left(1 - HH_{N-1}^a k_a\right) & \left\{-k_b'\left(HB_{N-1}^a - k_{bb}HH_{N-1}^a\right)\right\} & \left(HH_{N-1}^a k_b\right) \\
\left\{-k_a'\left(BB_{N-1}^b - k_{bb}BH_{N-1}^b\right)\right\} & \left(BH_{N-1}^b k_a\right) & \left\{1 - k_b'\left(BB_{N-1}^b - k_{bb}HB_{N-1}^b\right)\right\} & \left(-BH_{N-1}^b k_b\right) \\
\left\{-k_a'\left(HB_{N-1}^b - k_{bb}HH_{N-1}^b\right)\right\} & \left(HH_{N-1}^b k_a\right) & \left\{-k_b'\left(HB_{N-1}^b - k_{bb}HH_{N-1}^b\right)\right\} & \left(1 - HH_{N-1}^b k_b\right)
\end{bmatrix}$$

3.4.5 Numerical procedure (Non-linear)

The program flow chart is shown on the next sheet.

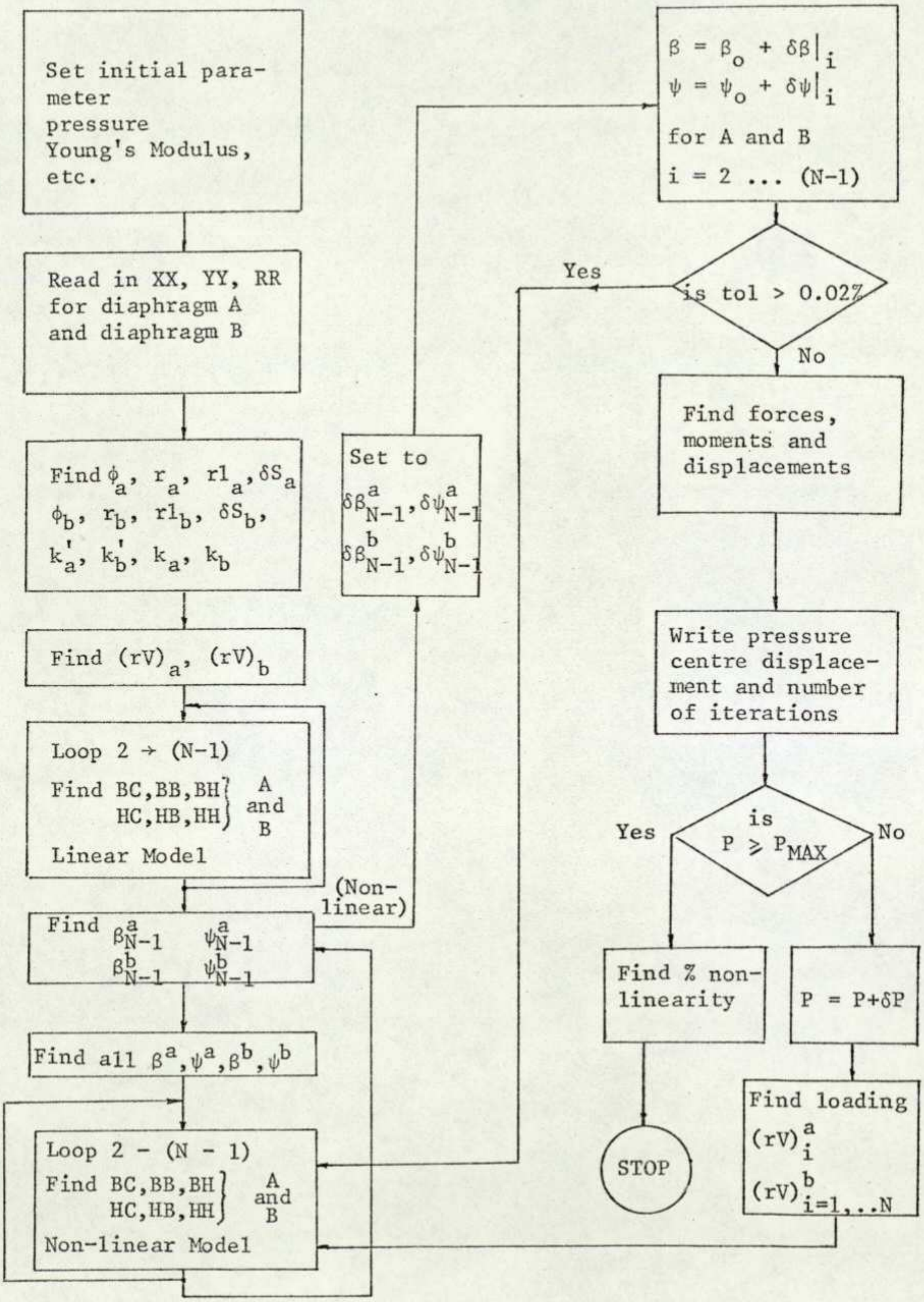

Figure 3.41: Non-linear capsule flow chart

The program structure is made a lot simpler by having subroutines and having a large amount of the variables carried across in common blocks. The routine which finds the values at the (N-1) mesh point finds either the actual values or the error, depending which part the program has reached. Program space is saved by only having two values of each of the following variables: $\delta\beta^a$, $\delta\psi^a$, $\delta\beta^b$, $\delta\psi^b$, the computed, and the present value, which was the previous value updated.

In the non-linear diaphragm model there are as many values of error as mesh points, and in this program the extra store would have amounted to about 2 K words.

This is achieved by setting the error at the $(N-1)^{th}$ point to the second of the two values, then updating the actual values, i.e.

$$\begin{aligned}
\beta^a_{N-1} &= \beta^a_{oN-1} + \delta\beta^a_{(2)} \\
\psi^a_{N-1} &= \psi^a_{oN-1} + \delta\psi^a_{(2)} \\
\beta^b_{N-1} &= \beta^b_{oN-1} + \delta\beta^b_{(2)} \qquad \text{error at } N-1^{th} \text{ mesh point} \\
\psi^b_{N-1} &= \psi^b_{oN-1} + \delta\psi^b_{(2)}
\end{aligned}$$

Then

$$\begin{aligned}
\delta\beta^a_{(1)} &= BC^a_{N-2} + BB^a_{N-2}\,\delta\beta^a_{(2)} + BH^a_{N-2}\,\delta\psi^a_{(2)} \\
\delta\psi^a_{(1)} &= HC^a_{N-2} \quad HB^a_{N-2}\,\delta\beta^a_{(2)} \quad HH^a_{N-2}\,\delta\psi^a_{(2)} \\
\delta\beta^b_{(1)} &= BC^b_{N-2} \quad BB^b_{N-2}\,\delta\beta^b_{(2)} \quad BH^b_{N-2}\,\delta\psi^b_{(2)} \\
\delta\psi^b_{(1)} &= HC^b_{N-2} \quad HB^b_{N-2}\,\delta\beta^b_{(2)} \quad HH^b_{N-2}\,\delta\psi^b_{(2)}
\end{aligned} \tag{3.51}$$

$$\begin{aligned}
\beta^a_{N-2} &= \beta^a_{oN-2} + \delta\beta^a_{(1)} \\
\psi^a_{N-2} &= \psi^a_{oN-2} + \delta\psi^a_{(1)} \\
\beta^b_{N-2} &= \beta^b_{oN-2} + \delta\beta^b_{(1)} \\
\psi^b_{N-2} &= \psi^b_{oN-2} + \delta\psi^b_{(1)}
\end{aligned}$$

after which the second values are overwritten:

$$\delta\beta^{a}_{(2)} = \delta\beta^{a}_{(1)}$$
$$\delta\psi^{a}_{(2)} = \delta\psi^{a}_{(1)}$$
$$\delta\beta^{b}_{(2)} = \delta\beta^{b}_{(1)}$$
$$\delta\psi^{b}_{(2)} = \delta\psi^{b}_{(1)}$$

The procedure is then iterative returning to (3.51) and working on the N-3 point. The routine stops at the second point.

3.4.6 Non-linearity algorithm

Before the non-linearity has any meaning it has to be adequately defined. Consider the following curve (Figure 3.42):

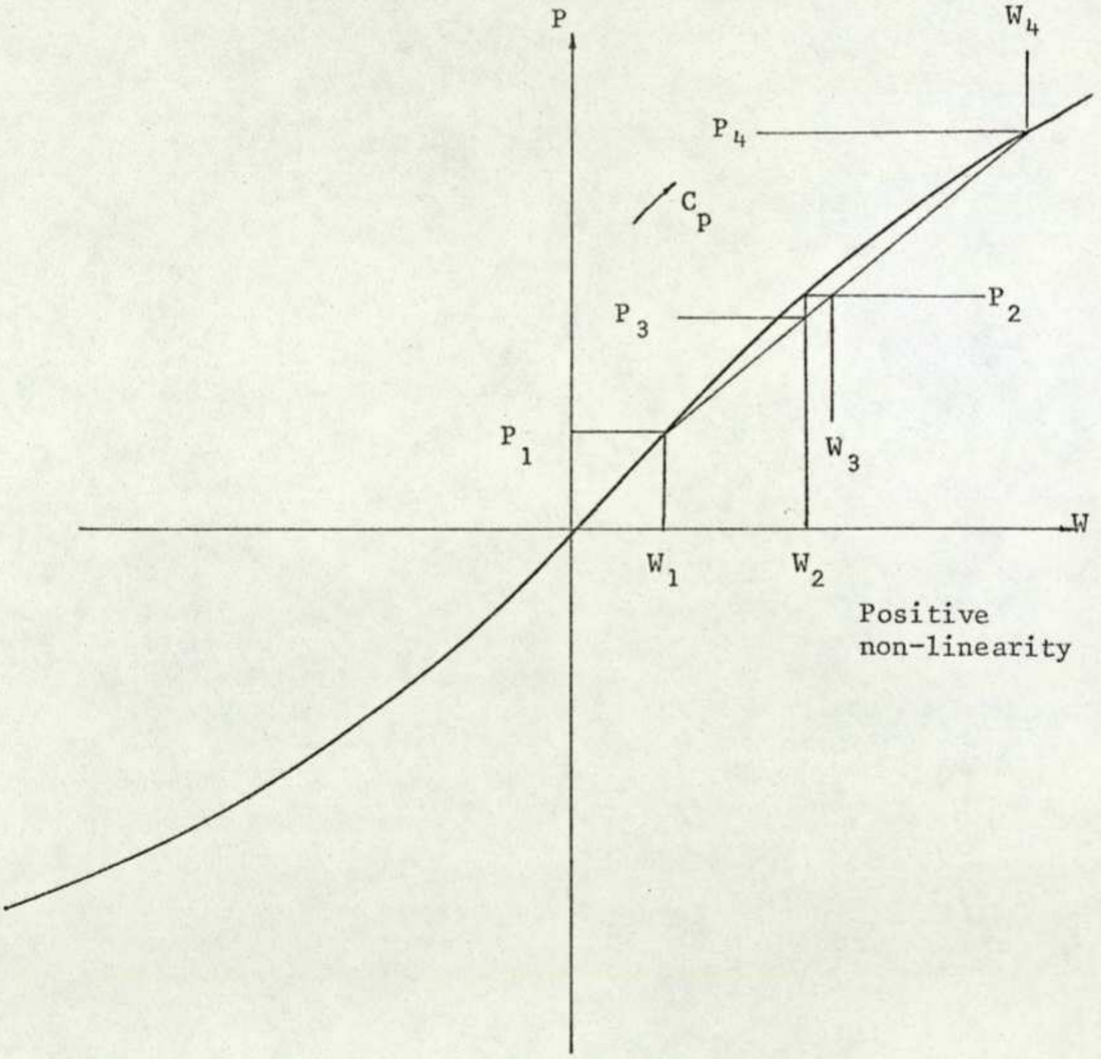

Figure 3.42: General non-linearity

It is generally more convenient to measure the deflections corresponding to specified pressures. If the non-linearity is to be computed at a specified pressure P_2 in a cycle whose minimum pressure and deflection are P_1 and W_1, and maximum P_4 and W_4, then the non-linearity, in per cent of the deflection span $(W_4 - W_1)$ is Z_W, which is equal to

$$100 \times (W_2 - W_3)/(W_4 - W_1) \quad \ldots\ldots\ldots\ldots\ldots\ldots\ldots\ldots\ldots \quad (3.52)$$

Where W_2 is the deflection corresponding to the specified pressure P_2, and W_3 is the linear deflection corresponding to the same pressure, the value of W_3 can be computed from the straight line equation:

$$W_3 = W_1 + (W_4 - W_1).(P_2 - P_1)/(P_4 - P_1) \quad \ldots\ldots\ldots\ldots\ldots \quad (3.53)$$

The non-linearity is then positive when the pressure constant C_p (which is equal to $\frac{P_i}{W_i}$) increases as the pressure increases. If the pressures corresponding to specified deflections are measured, the non-linearity as a percentage of the pressure span $(P_4 - P_1)$ is Z_p, which is equal to $100 \times \frac{(P_3 - P_2)}{(P_4 - P_1)}$. Where the pressure P_2 corresponds to a specified deflection W_2, and P_3 is the linear pressure corresponding to the same deflection, the value of P_3 is computed in a manner similar to that above. This makes the non-linearity positive when the pressure constant increases as the pressure increases. When the non-linearities are to be determined for several points in the cycle and the ends of the span are two of the equally spaced values of the independent quantity, the values of the dependent quantity for points on a straight line can be easily computed by dividing the span of the dependent quantity by the required number of points and adding that value repeatedly to the dependent quantity in the low end of the span.

With the program we are computing deflections for a specific input pressure, therefore over the range considered the values of pressure and deflection are stored - for the beginning of the range designated P_1 and W_1, respectively, and hence for the end of the range, P_4 and W_4.

The actual values from the curve P_2 and W_2 from Figure 3.42 become the general values P_i and W_i ($i = 1 \ldots\ldots N$), at which the non-linearity over the range $P_1 - P_4$ is required.

From (3.52),

$$Z_W = \frac{(W_i - W_3)}{(W_N - W_1)} \times 100\%$$

Substituting (3.53),

$$Z_W\Big|_i = \left[\frac{W_i}{(W_N - W_1)} - \frac{W_1(P_N - P_1) + (W_N - W_1)(P_i - P_1)}{(P_N - P_1)(W_N - W_1)} \right] \times 100\%$$

if we start conveniently at the origin, then $W_1 = P_1 = 0$, and the non-linearity at the i^{th} pressure point reduces to

$$Z_W\Big|_i = \frac{W_i}{W_N} - \frac{P_i}{P_N} \times 100\%$$

The above non-linearity calculation was a useful addition to both the capsule and diaphragm models, for experimental evaluation and design.

3.4.7 Program check

To test the non-linear capsule model, a flat plate capsule with a rigid centre boss was simulated, the flat plate capsule being a non-realisable capsule in practice as the two plates cannot pass through one another. The results are shown in Figure 3.43, and it can be seen that the deflection at the outer edge is one-half the centre deflection to within 1.7 per cent of the centre deflection.

To see how the model performed for the two cases of nesting and non-nesting capsules, two runs were carried out and the results for the same pressure range are shown in Table 3.4. Again, the nesting capsule was a fictitious concept because the same profile was used for the top and bottom diaphragm; as these results are, the two pass through one another. The non-nesting capsule, which is the same profile, could make a practical capsule, both in compression and extension. The deflections are quoted as $(\frac{W}{t})$, where t = 0.006" (.1524 mm).

The results are mainly as expected, i.e. the deflections are both of the same order, with the horizontal deflection for the non-nesting case many times that of the nesting case and positive, which indicates that it moves outwards, as expected, when in compression. The nesting capsule horizontal displacement is virtually zero. It is interesting to note that the non-linearity over the range is a lot less in magnitude for the nesting capsule, and presumably it would make a better pressure-sensing element: this seems to be borne out by industrial practice.

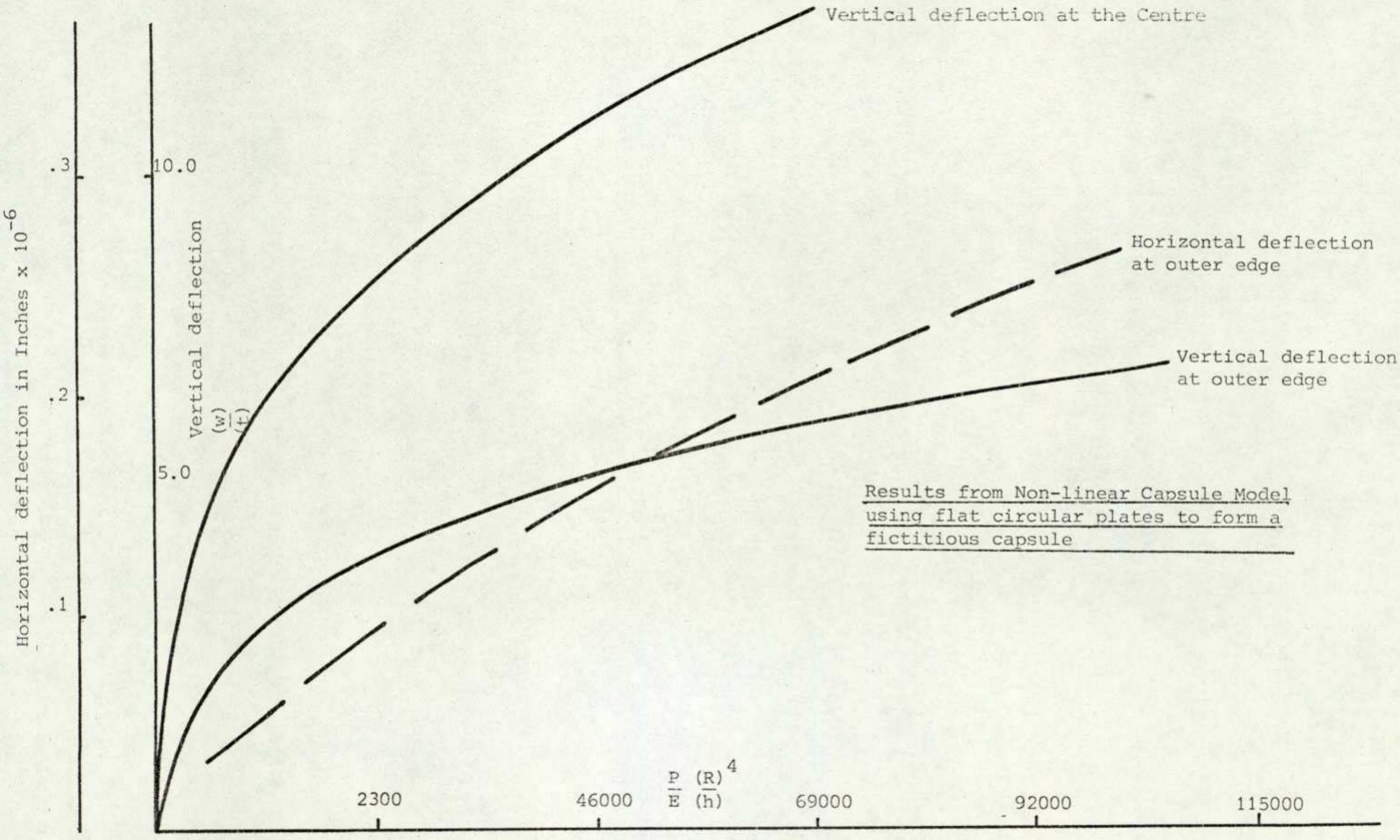

Results from Non-linear Capsule Model using flat circular plates to form a fictitious capsule

Figure 3.43

Pressure lbf/in^2 (compression)	Non-nesting capsule ($^W/t$)	η%	Nesting capsule ($^W/t$)	η%
0.1	2.2329	0.08	0.2261	-0.0034
0.6	1.3911	0.42	1.3565	-0.0202
1.1	2.54	0.653	2.4872	-0.03512
1.6	3.68	0.793	3.6182	-0.046
2.1	4.812	0.832	4.7495	-0.053
3.6	8.1482	0.358	8.148	-0.027
4.1	9.2422	0	9.2825	0
$(\frac{U}{t})$	(.0936)		(-.0013675)	

Table 3.4

Typical computer times on the C.D.C. 7600 machine are about 0.2 seconds per pressure point for the non-linear capsule model, which gives a reasonable characteristic in both directions in approximately 8 seconds.

4.0 Model Validations

The proposed models have previously been shown to behave satisfactorily for limiting soluble cases. However, comparing model prediction with actual experimental observation is essential. An investigation of this type into a subject which proposes to solve a general problem is inherently limited, therefore the experimental work carried out by the author is also backed up by comparison with results presented by other experimental investigations.

The main purpose of the work, as presented in this chapter, must be to substantiate whether the various models are adequate and what we mean by the term adequate. Ultimately, the models will be required for design purposes and to these ends they must be accurate to within a suitable tolerance. The tolerances placed will depend upon a large number of contributing factors, e.g. the number of mesh points along the generator; but in the main part of this chapter, the physical causes of uncertainties are examined, and related directly to the model.

The first section, 4.1, compares the results of two papers with the work presented in Chapter 3, one a direct comparison of computational work in which internal forces, stresses and displacements can be compared, and the second which compares the results of actual diaphragms with the numerical predictions of the same diaphragm profiles.

The second section deals with the results, observations and experimental detail of the validation actually performed by the author. The last section covers additions made to the model by way of improvements, building in strain and investigating whether the geometry description can be improved.

4.1 Comparison of reported work

This deals firstly with application to the linear model, followed by a non-linear analysis, both applied to diaphragms only.

4.1.1 Computational

Wildhack, Lloyd and Dressler, ref. (11), with their linear model of the Grover-Bell diaphragm, Figure 2.1, produced a number of graphs relating the outputs, i.e. displacements, stress resultants, and stresses from a particular loading, measured out from the axis of symmetry. This work was further extended by Dressler, ref. (12), who simulated three diaphragms based on the Grover-Bell shape: his medium case was the same as used in ref. (11) and the other two were fictitious being a third as thick and three times as thick. These plots are shown as Figure 4.1 (Figures 5, 6, 7, 12 and 13 from the original Dressler paper); the values on the y axis have been non-dimensionalised.

As the stress resultants, N_ξ, M_ξ, N_θ, etc., are implicit in the stresses, only plots of vertical displacement, Figure 5, horizontal displacement, Figure 6, normal shear force, Figure 7, and total stresses (top and bottom), Figures 12 and 13, are shown. The thin, medium and thick cases shown refer to thicknesses of 0.002332" (0.059258 mm), 0.007" (0.1778 mm) and 0.021" (0.5334 mm), respectively, as described in Chapter 2.

These thickness values were programmed along with the "Grover-Bell" profile and a handbook value of Young's modulus of 17.6 lbf/in^2 (12.13 GN/m^2) for Beryllium Copper. The results of the author's simulation are shown as Figures 4.2, 4.3 and 4.4. The only numerical comparison between the two is performed for what is considered the most significant quantity, namely the vertical displacement and the stresses on both surfaces. In both papers the displacements have the dimensionless form defined by:

$$\bar{W} = \frac{EW}{(1 - \nu^2)Zd}$$

where W = actual displacement
$\bar{W}$ = normalised displacement
Z = pressure
d = active diameter.

The actual values of vertical displacement found from the author's predictions are, for the three cases starting with the thinnest:

0.3982657" (10.116 mm)
0.046555" (1.1825 mm)
0.0071913" (0.182659 mm)

When these are normalised they become:

241,432
28,227
4,360

The values may then be compared with the plots of vertical deflection from the Dressler plots, Figure 5, and can be seen to agree very well.

A comparison of stress values can be made by picking a maximum from the two sets of Dressler graphs, Figures 12 and 13; the normalising

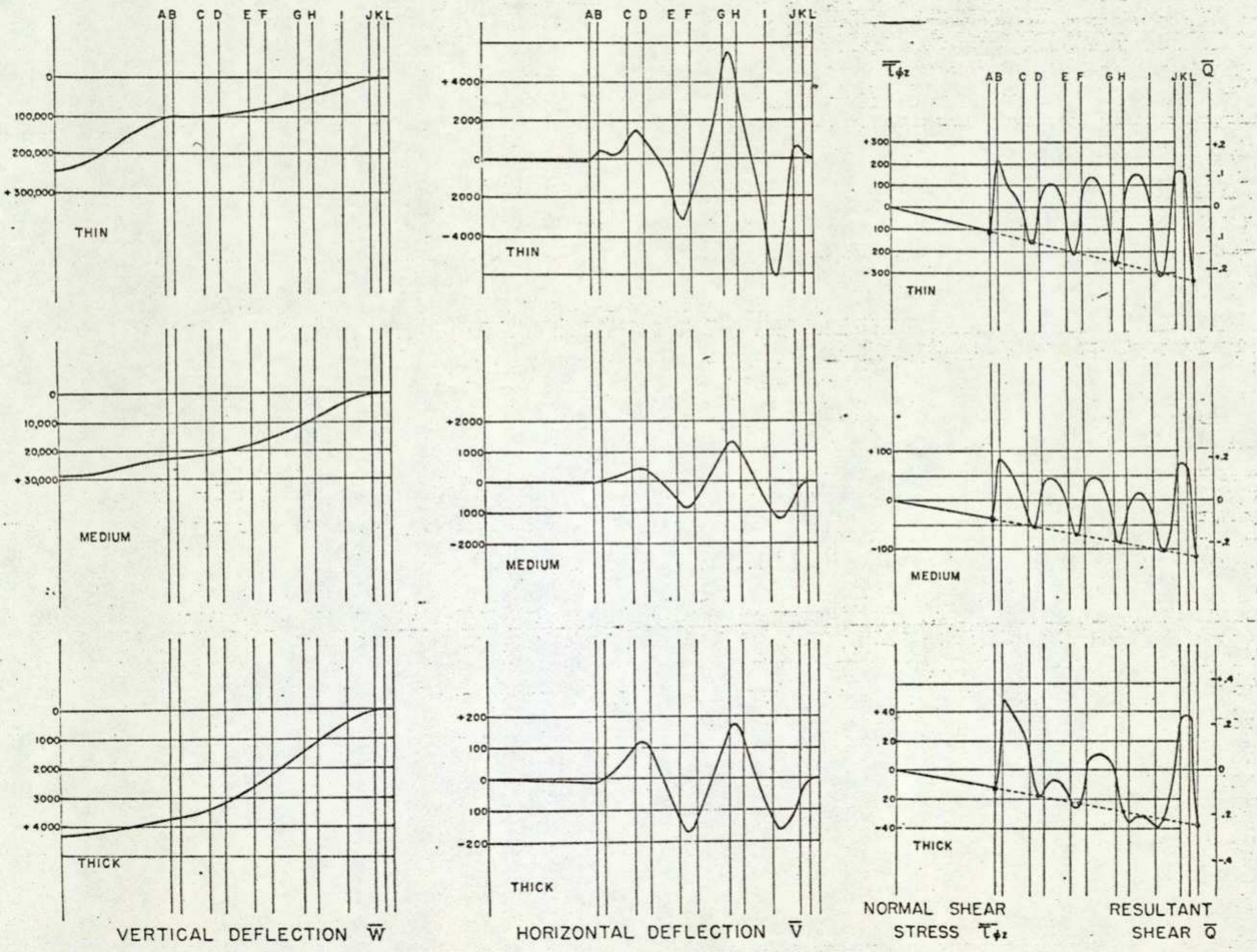

Figs. 5 and 6 Vertical and horizontal deflection components

Fig. 7 The shear stress and resultant

Figure (4.1)

Computer generated plots from Dressler ref. (12) showing horizontal and vertical displacements and normal shear force, for the three cases mentioned in the text.

Figure (4.1)

Computer generated plots from Dressler ref. (12) showing the total stress on the top and bottom faces, for the meridional (radial) and Circumferential directions (σ_ξ and σ_θ)

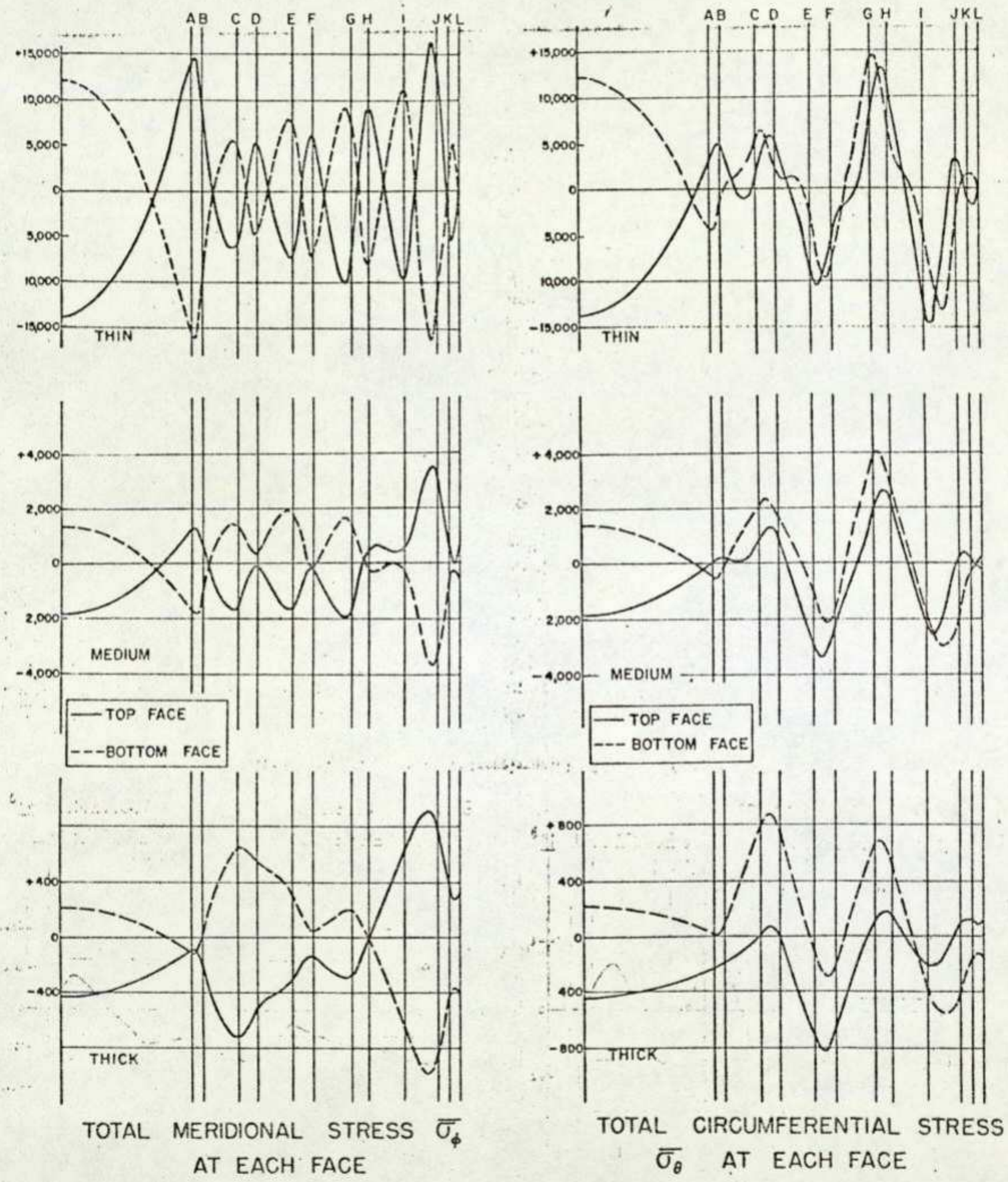

TOTAL MERIDIONAL STRESS $\overline{\sigma_\phi}$ AT EACH FACE

TOTAL CIRCUMFERENTIAL STRESS $\overline{\sigma_\theta}$ AT EACH FACE

Figs. 12 and 13 Total stresses at each face

The Thin case of the Grover-Bell diaphragm programmed by the Author for comparison with Dressler's results (the dotted lines show the effect of having a 'free' outer edge).

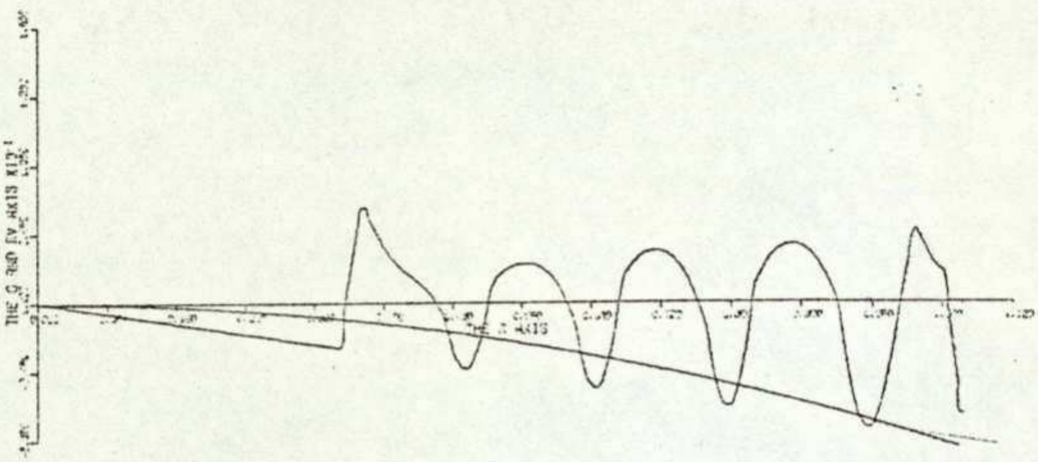

Normal shear force and (rV) loading

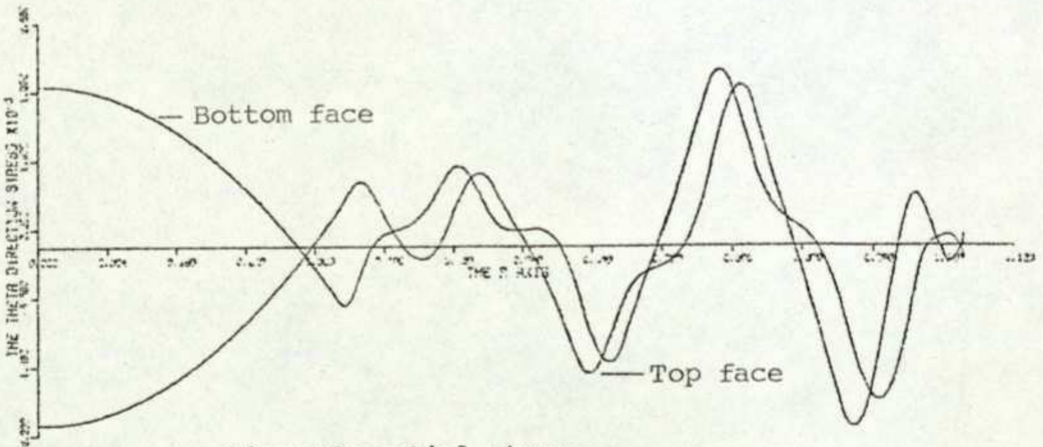

Circumferential stress

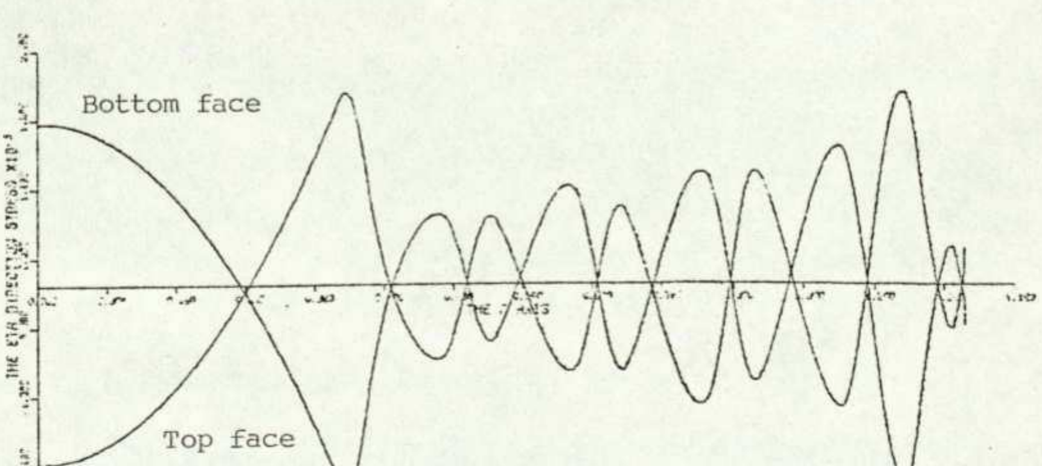

Radial stress

fig. con't

Figure 4.2

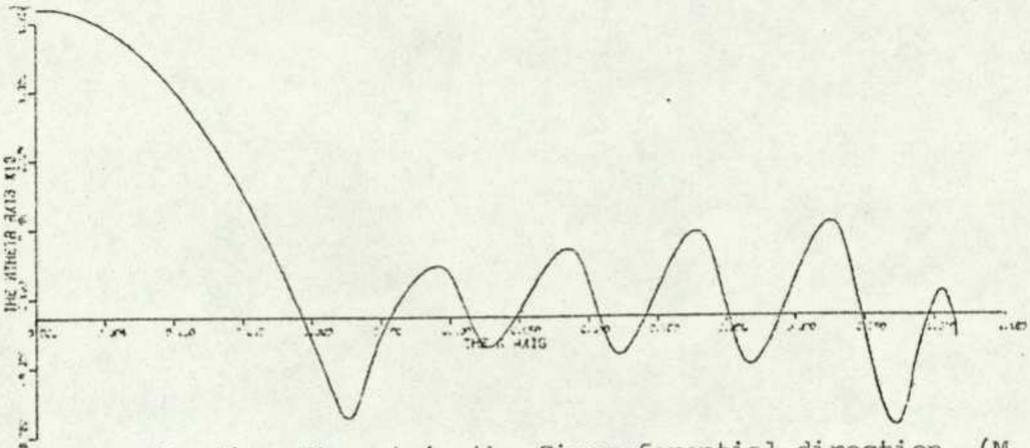

Bending Moment in the Circumferential direction (M_θ)

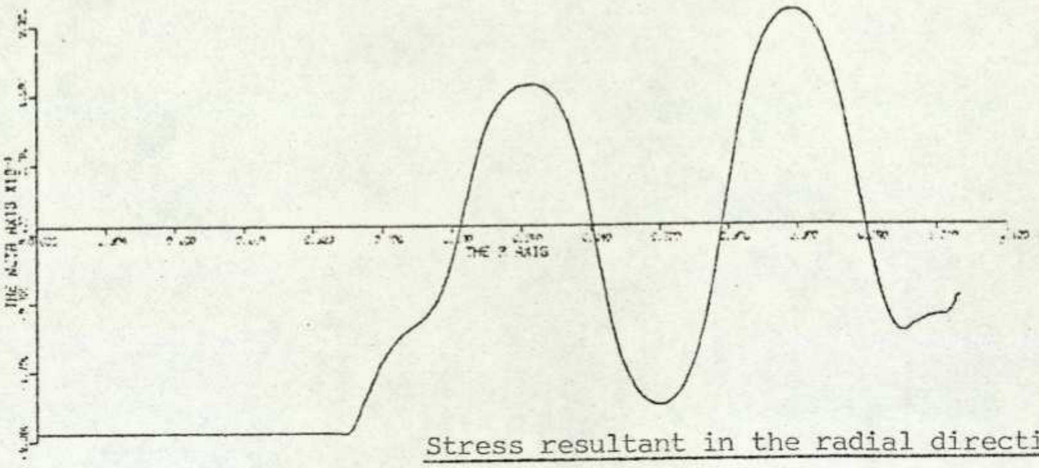

Stress resultant in the radial direction $(N_\xi$

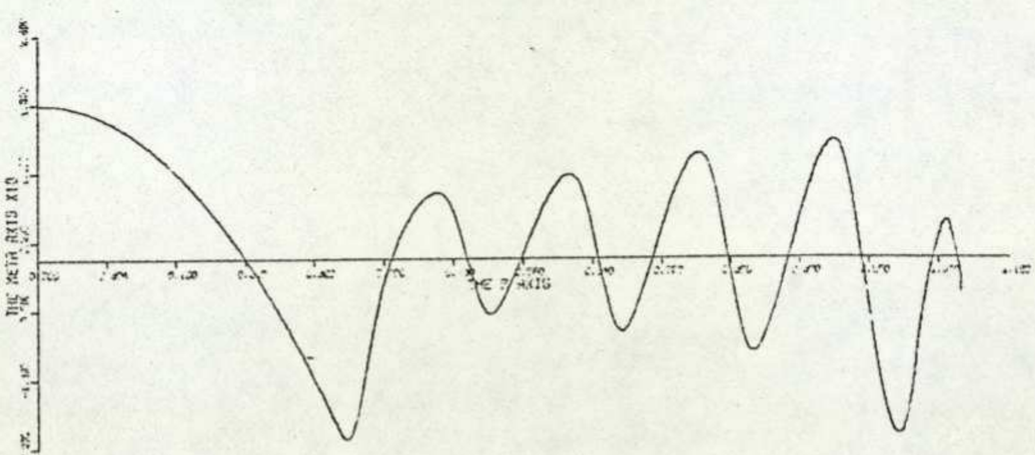

Bending Moment in the radial direction (M_ξ)

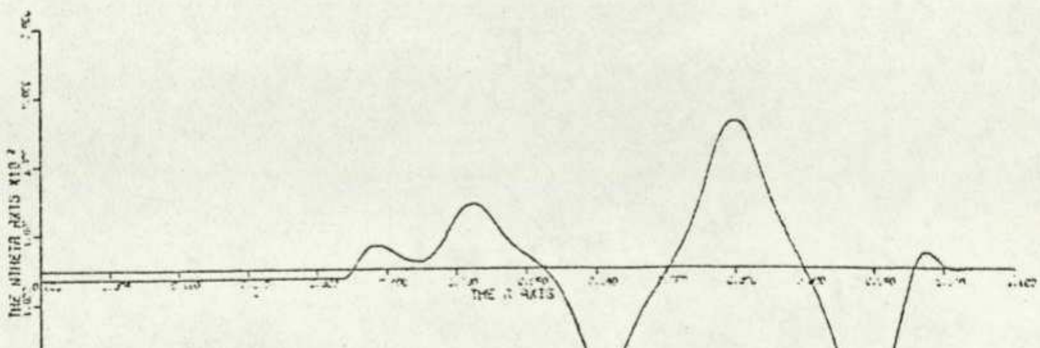

Stress resultant in the circumferential direction (N_θ)

fig. con't

Figure 4.2

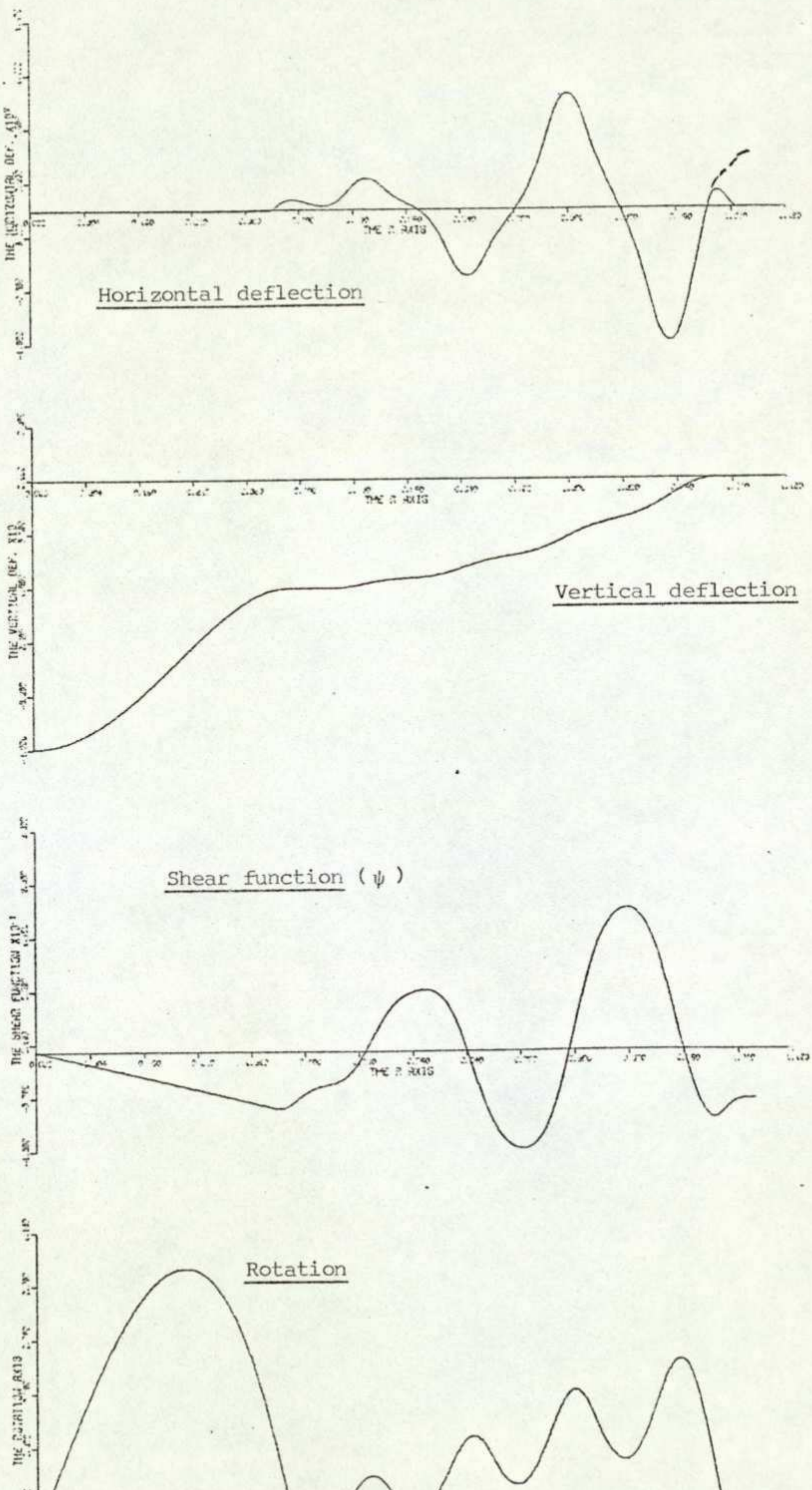

Horizontal deflection

Vertical deflection

Shear function (ψ)

Rotation

The Medium case of the 'Grover-Bell' diaphragm programmed by the Author for comparison with Dressler's results (the dotted lines show the effect of having a 'free' outer edge).

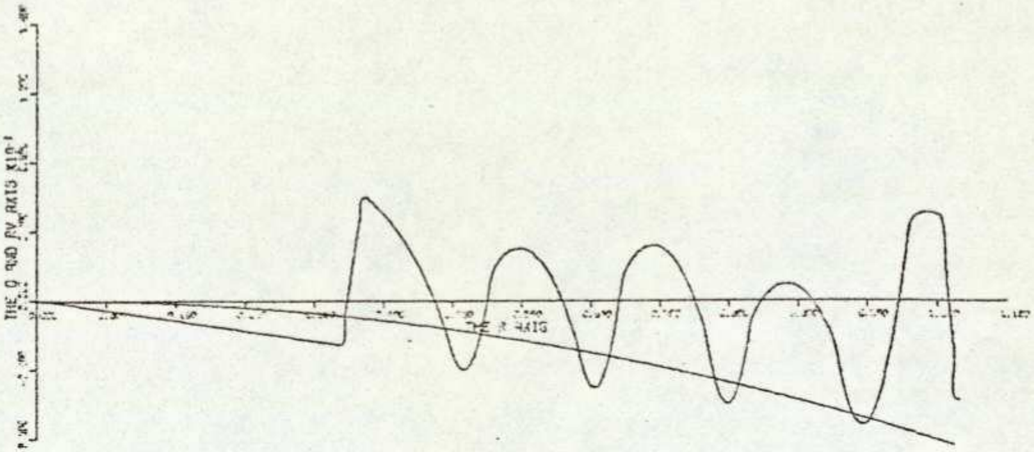

Normal shear force and (rV) loading

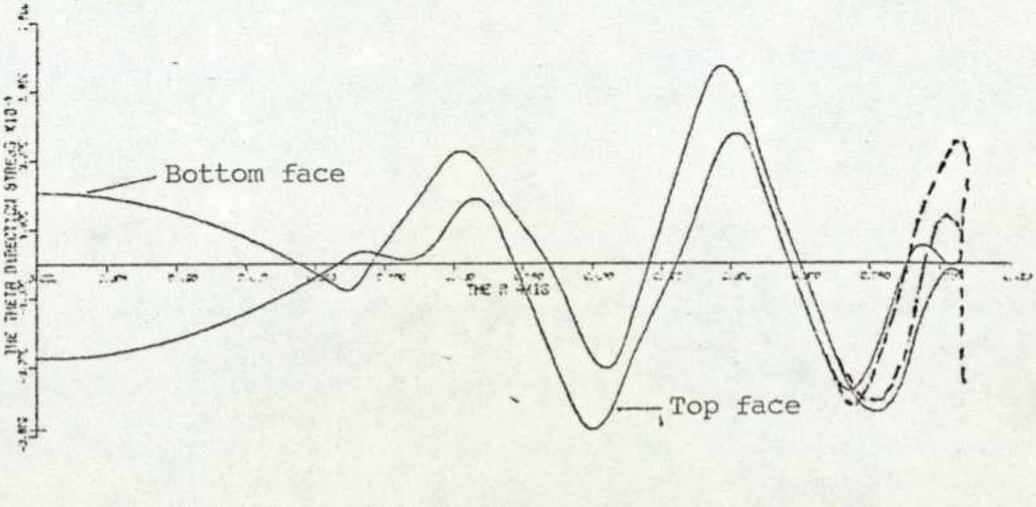

Circumferential stress

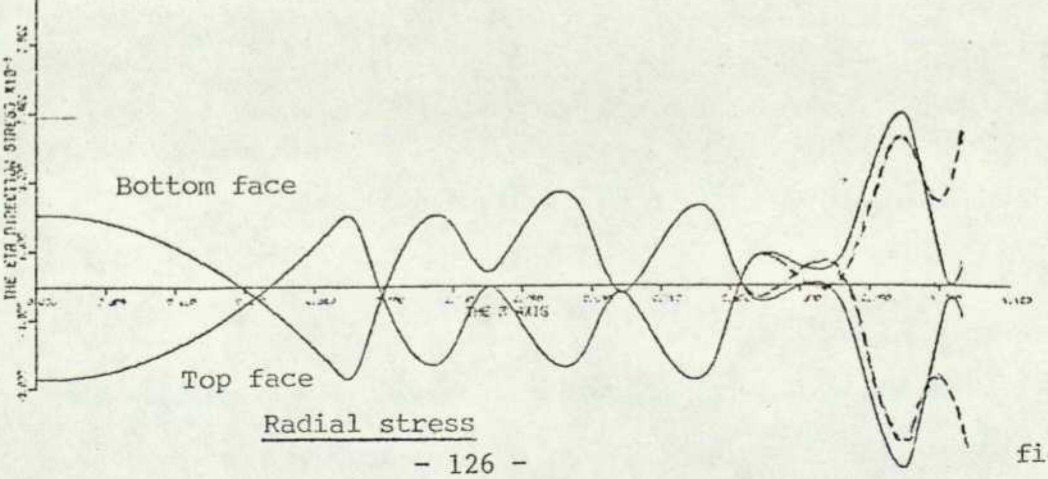

Radial stress

fig. con't

Figure 4.3

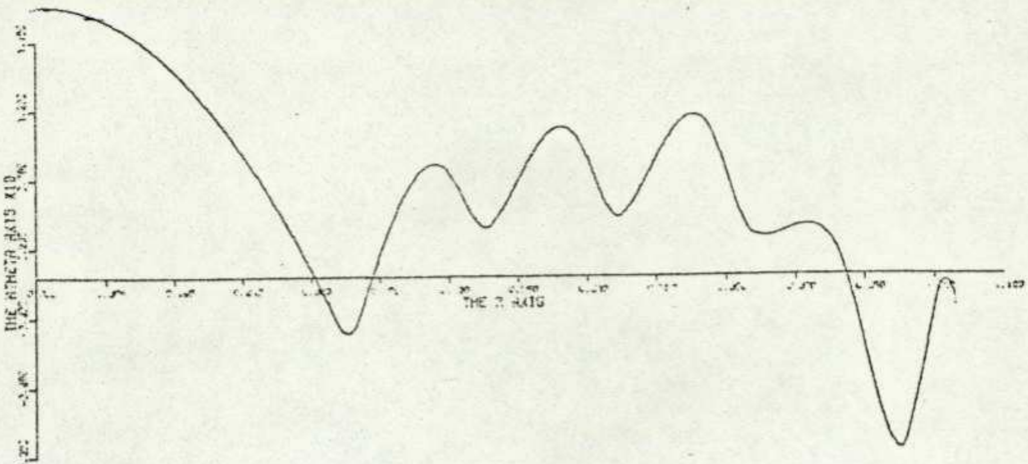

Bending Moment in the Circumferential direction (M_θ)

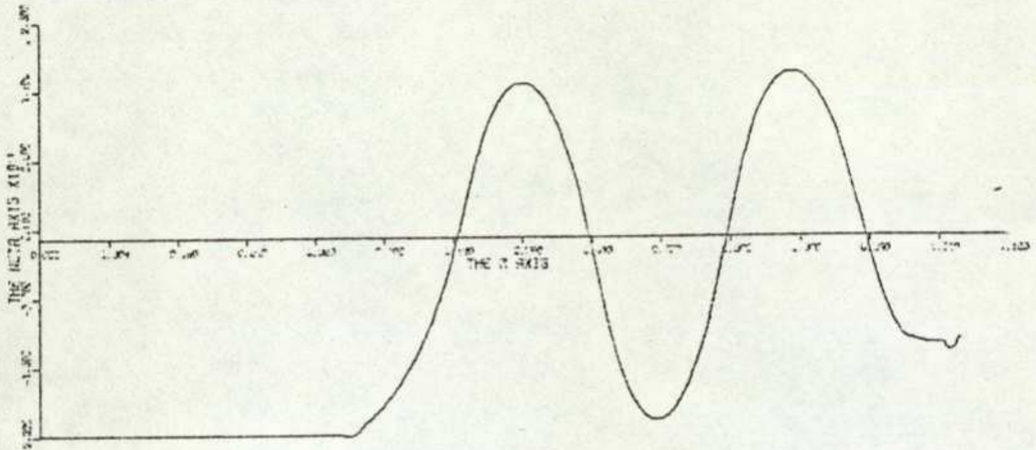

Stress resultant in the radial direction (N_ξ)

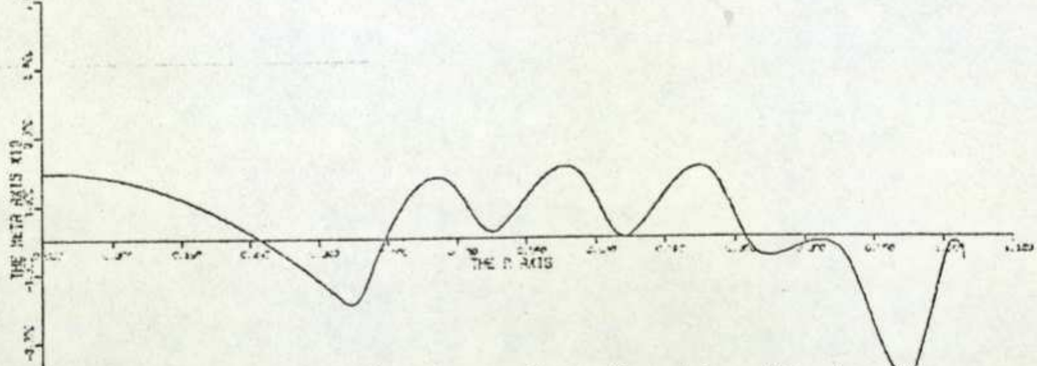

Bending Moment in the radial direction (M_ξ)

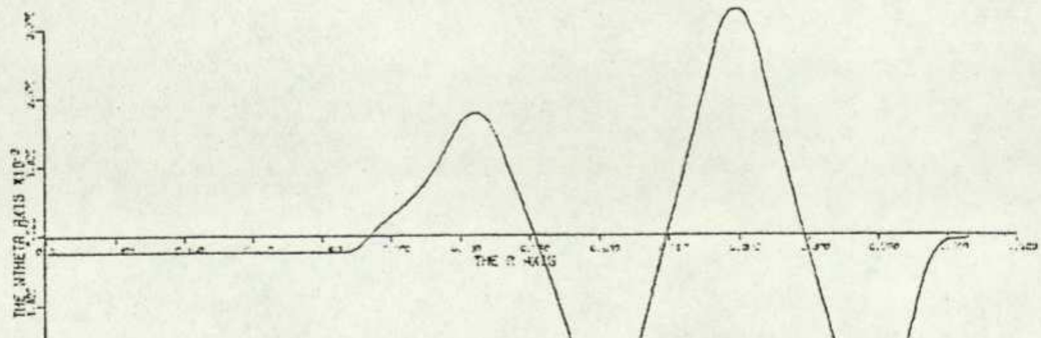

Stress resultant in the circumferential direction (N_θ)

fig. con't

Figure 4.3

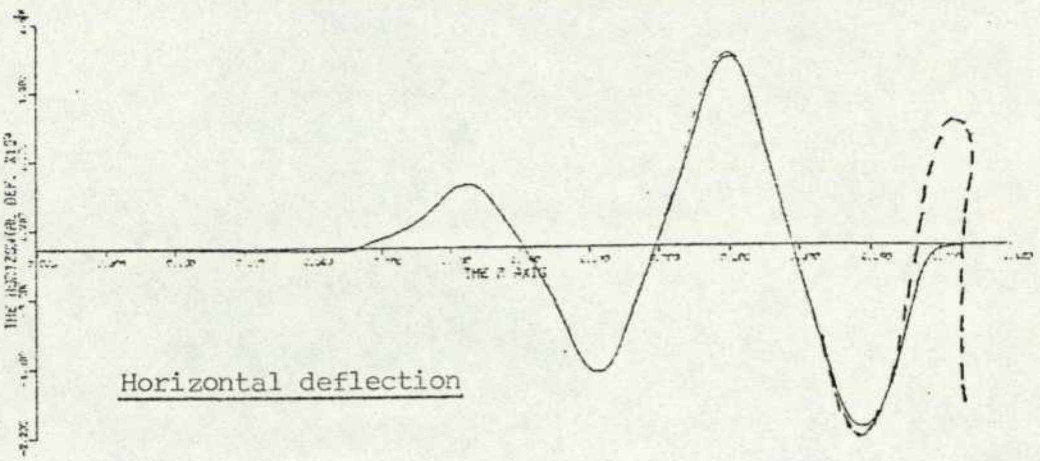
Horizontal deflection

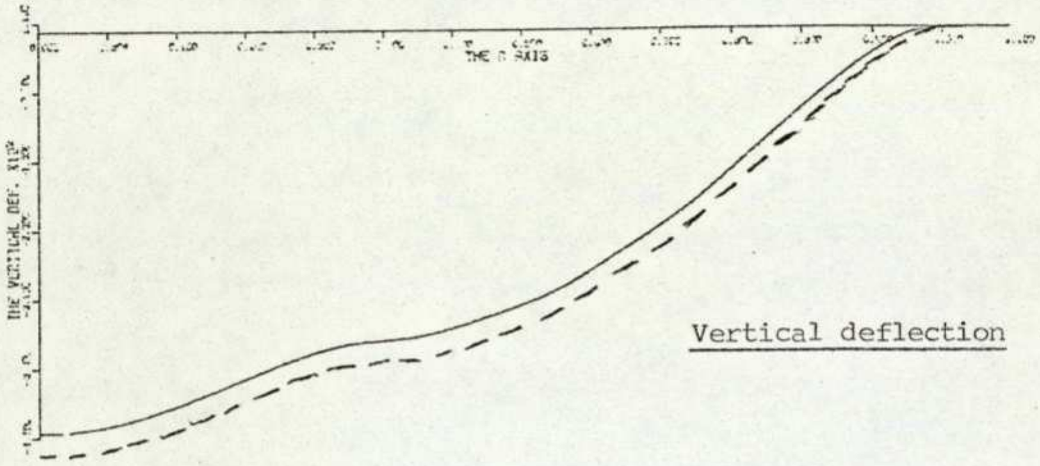
Vertical deflection

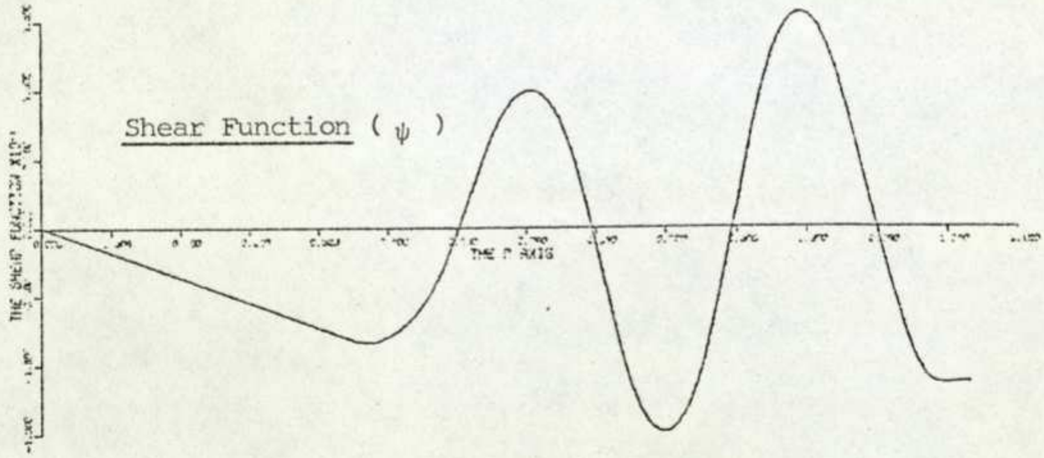
Shear Function (ψ)

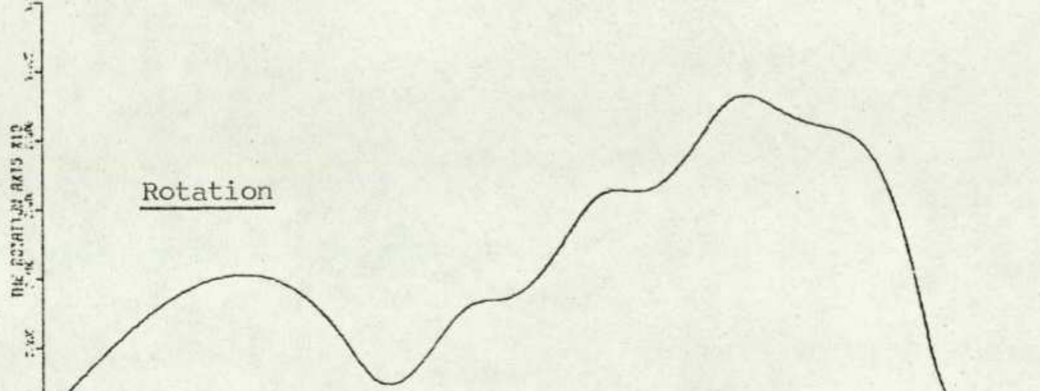
Rotation

The Thick case of the Grover-Bell diaphragm programmed by the Author for comparison with Dressler's results (the dotted lines show the effect of having a 'free' outer edge).

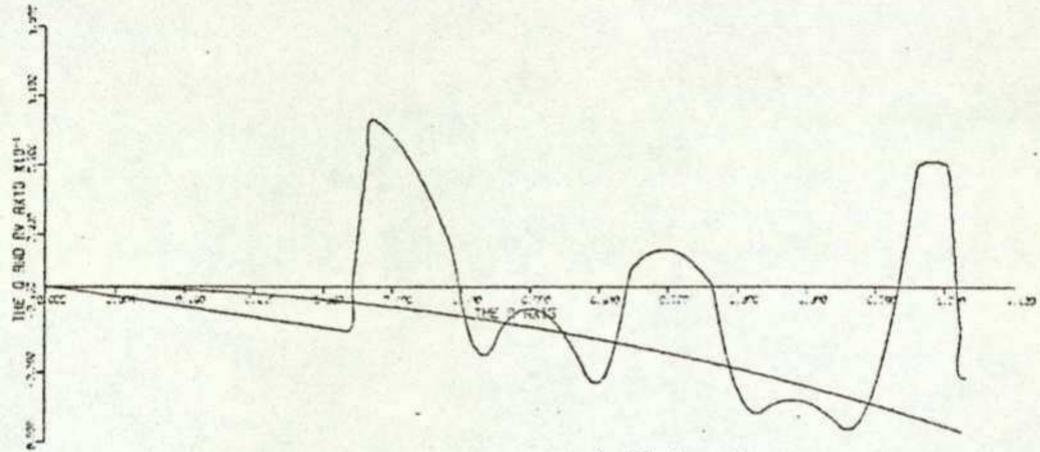

Normal shear force and (rV) loading

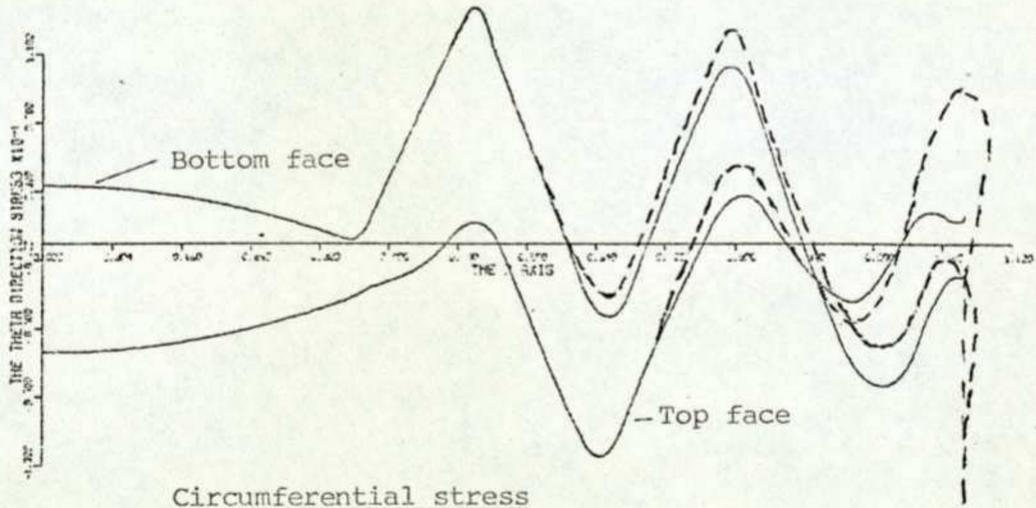

Circumferential stress

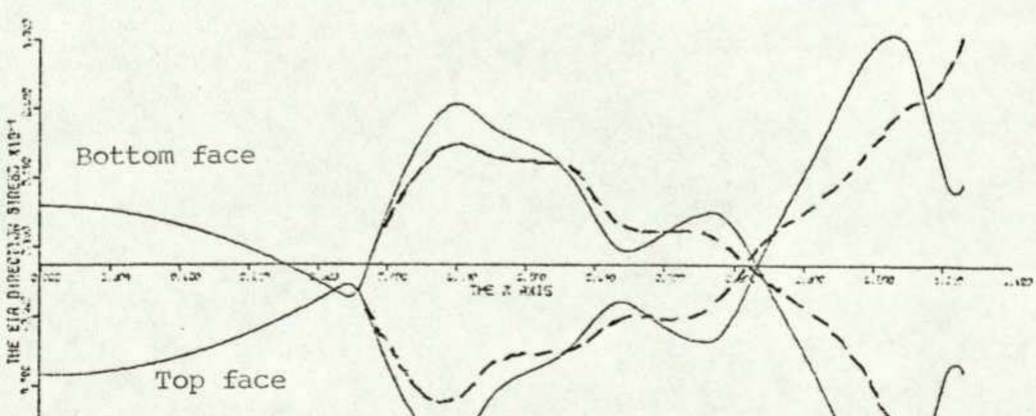

Radial stress

fig. con't

Figure 4.4

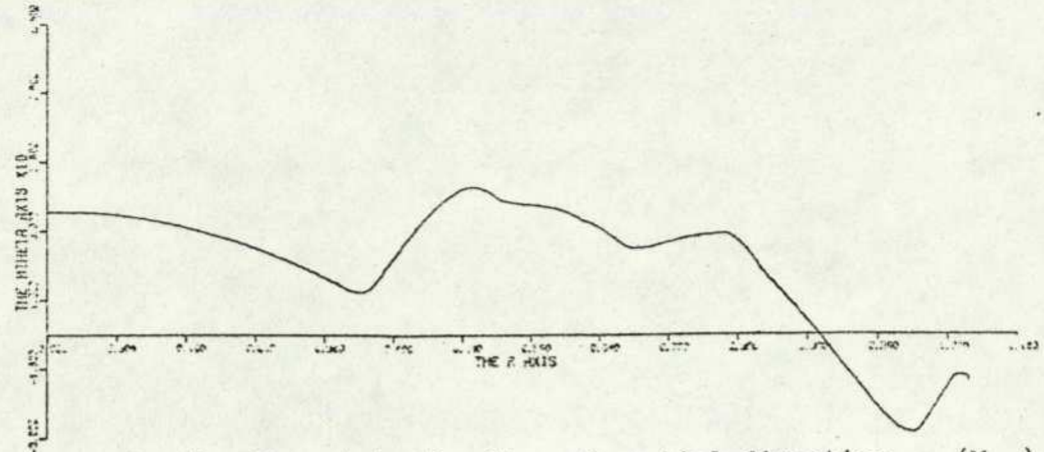

Bending Moment in the Circumferential direction (M_{θ})

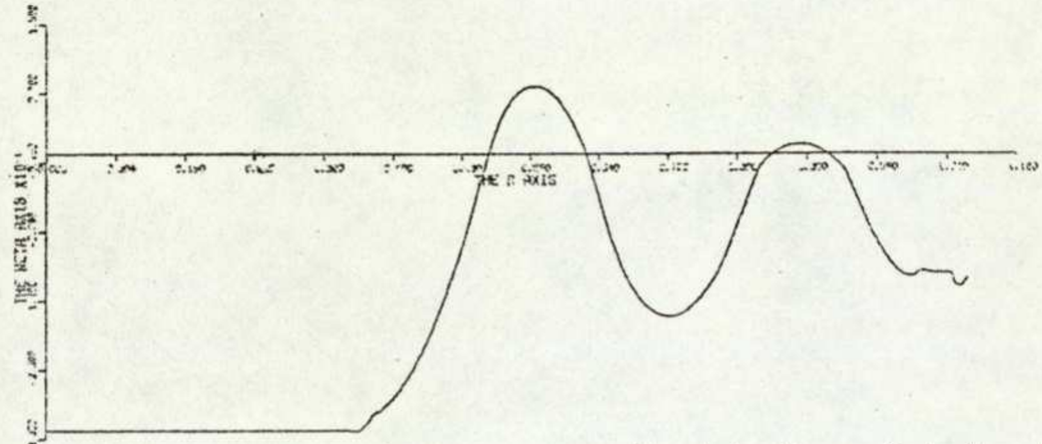

Stress resultant in the radial direction (N_{ξ}

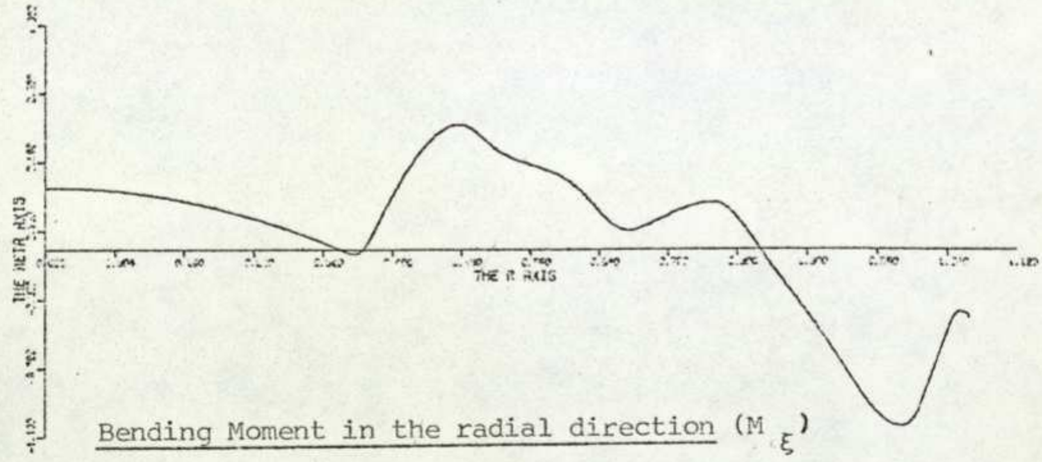

Bending Moment in the radial direction (M_{ξ})

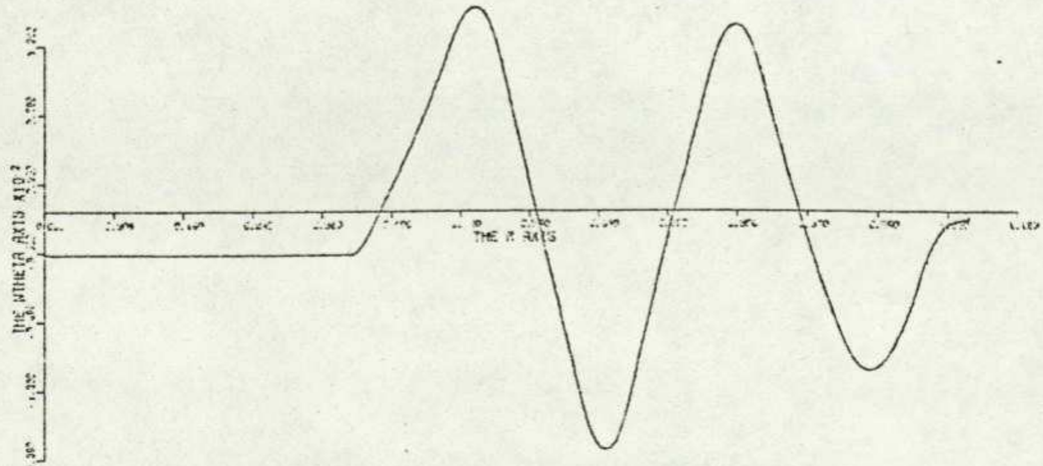

Stress resultant in the circumferential direction (N_{θ})

fig. con'

Figure 4.4

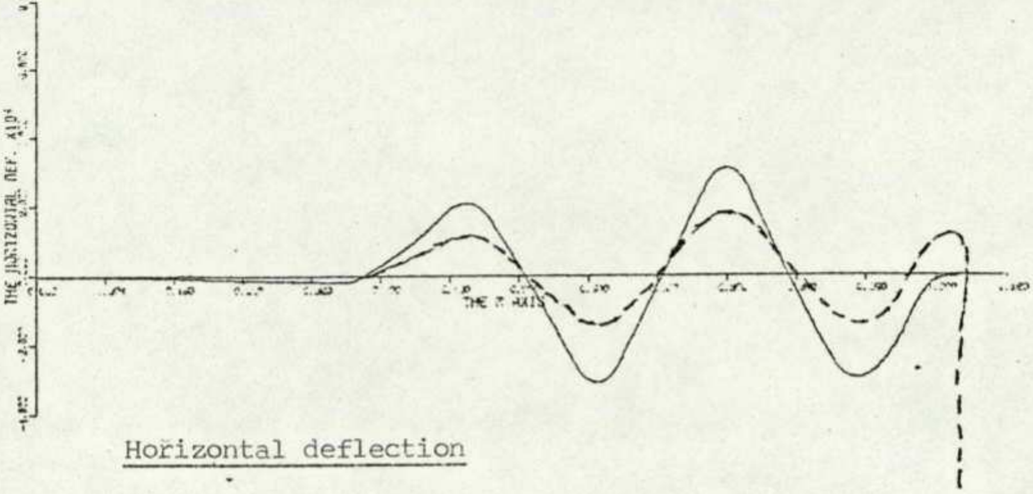

Horizontal deflection

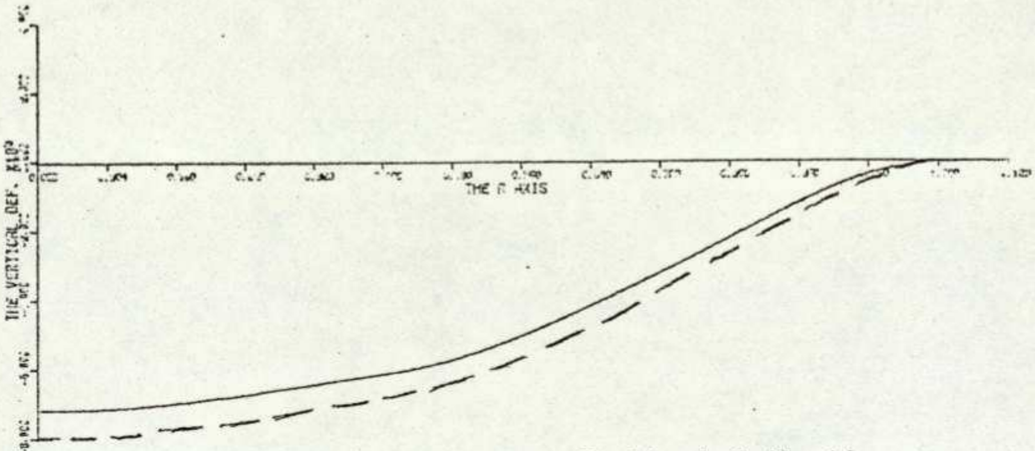

Vertical deflection

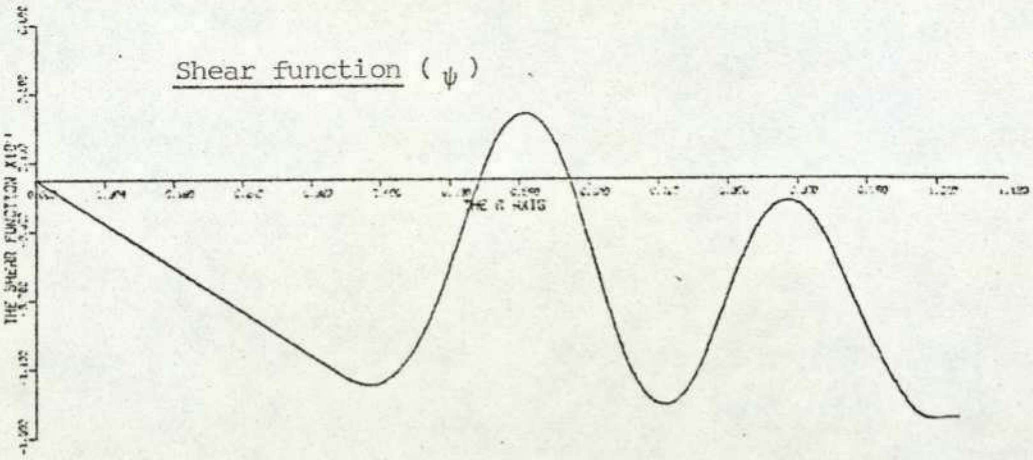

Shear function (ψ)

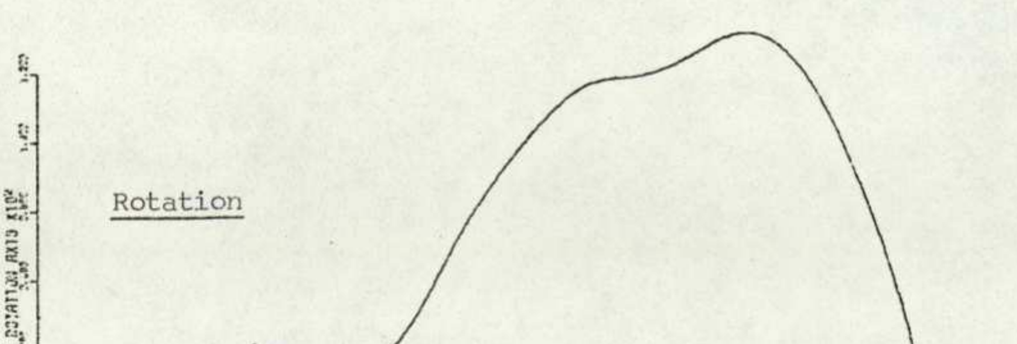

Rotation

factor for stress is $\bar{\sigma} = \frac{\sigma}{Z}$. Again, to within the accuracy of reading from the small graphs, the agreement is very good, as an example Dressler's maximum stress for the medium case, in the circumferential direction and on the bottom face comes out to be approximately 60,000 lbf/in^2 (414 MN/m^2). For the same maximum point on Figure 4.3, the value is about 58,000 lbf/in^2 (400 MN/m^2).

Also shown in dotted lines are the characteristics for the "free-end" situation, as defined in Chapter 3. A comparison of the "free" and "clamped" conditions can be made from the earlier paper by Wildhack "et al". With these, as with all the other curves, a qualitative comparison can be made and in most cases the shapes of the curves are very similar.

4.1.2 Experimental

In the report for the National Bureau of Standars, A. V. Kankel and D. C. Whitten, ref. (5), tested a number of phosphor bronze diaphragms 0.0044" (0.11176 mm) thick. The profiles were reported to be of the shape shown in Figure 4.5, where each corrugation consists of two identical circular arcs made tangential to each other.

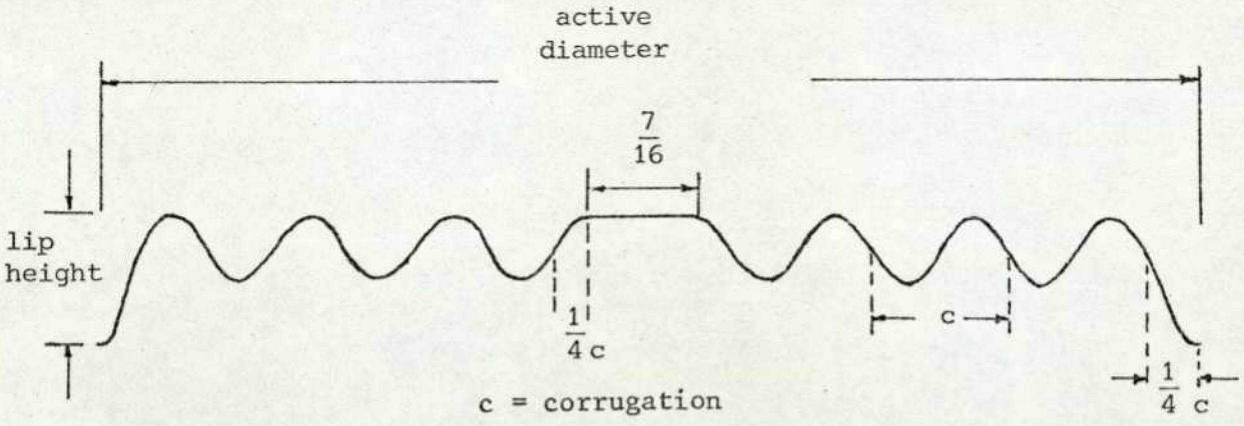

Figure 4.5: Diaphragm tested at the National Bureau of Standards, ref. (5)

The space for each corrugation is thus determined when the number of corrugations and the diameter are known. The depth of each corrugation was determined by the arc angle θ, therefore only four parameters were required to specify the diaphragm profile, i.e. the active diameter d, the number of convolutions N, the lip height L, and the angle θ. From these four parameters a subroutine was written to produce the X, Y, R1 coordinates needed for the model. Table 1 of the report, which shows the diaphragm parameters and deflections in inches, when pressurised (to 30

Die No.	Effective diameter	N	L x 10^{-3}	θ^{o}	Deflection in inches x 10^{-3}		Non-linearity η%	
					@ 30" wg	@ 80" wg	@ 30" wg	@ 80" wg
1	3.1"	7	16	80	46	96	3.6	11.3
2	3.1"	7	53	80	57	108	6.5	10.6
3	3.1"	7	90	80	58	114	4.5	13.6
4	3.1"	5	21	80	37	89	0.3	4.3
5	3.1"	9	13	80	53	99	6.4	15.4
7	3.1"	5	90	80	35	90	0.0	2.4
10	3.1"	5	90	60	51	106	2.6	11.0
11	3.1"	5	90	100	24	66	0.0	-0.4

Table 4.1: Die profiles and summary of deflections characteristics

and 80 inches of water gauge), is reproduced as Table 4.1. Because of the method of fixing, pressure was applied only from the underside, and, unfortunately, some of the dies used to produce diaphragms are not included owing to other variations not allowed for in the program.

The results of the Computer Simulation of the die shapes (Table 4.1) are shown in Table 4.2. The pressure was taken up to 80" wg (2.8 lbf/in^2) (19.9 KPa) in steps of 5" wg, and the deviation from linearity quoted ($\eta\%$) is that for 80" wg only.

The results are varied, with very good agreement for dies 1 and 5, where the agreement is within about 1 per cent. Except for die 1 at 30" wg, which is out by 5.76 per cent, the rest of the die shapes show discrepancies of up to 25 per cent which is quite unacceptable when compared with results achieved in the following section. The reason for the generally poor comparison is probably due to the fact that the profiles given, and hence programmed, were of the actual die profiles, not the diaphragms, and therefore spring-back has not been allowed for. On a thin material, i.e. 0.0044" (.11176 mm) this will be quite considerable. Hence, the diaphragm shapes will be quite different. Bearing this in mind, the results do indicate three main factors: firstly the values are not wildly out, both in sensitivity and non-linearity predictions; secondly all the values are less than the experimentally quoted ones; it is shown later that a decrease in the corrugation height causes an increase in sensitivity and, as spring-back would cause a decrease in the height of corrugation, the actual diaphragms will be more sensitive. Finally, the best result is that of die No. 5, which has nine corrugations indicating that the model appears capable of handling a "large" number of convolutions, "large" being a relative term, but diaphragms tested in the following sections only have a maximum of four corrugations, indicating the usefulness of the above result.

Die No.	Predicted			Experimental		
	30"	80"	$\eta\%\|_{80}$	Test 30"	Test 80"	$\eta\%\|_{80}$
1	0.04335	0.0924	9.76	0.046	0.096	11.3
2	0.042	0.0905	9.15	0.057	0.108	10.6
3	0.0423	0.0912	8.91	0.058	0.114	13.6
4	0.283	0.0737	1.21	0.037	0.089	4.3
5	0.0526	0.09735	16.56	0.053	0.099	15.4
7	0.026861	0.0709	0.54	0.035	0.09	2.4
10				0.051	0.106	11.0
11	0.01745	0.04718	-0.518	0.024	0.066	-0.4

Table 4.2

4.2 Experimental validation performed in this study

The validation consisted of pressure-deflection tests on diaphragms which were either the top or bottom of a nesting capsule and on complete capsules. KDG Instruments, Ltd. manufactured and supplied the diaphragms and capsules, which were made from a highly alloyed material of mainly Nickel and Chromium, Inconel X-750. From earlier work performed by Schricker, ref. (13), the uncertainty of material constants was put forward as a possible cause for the discrepancy between his own model and experimental tests. The value of Young's Modulus (E) is simply related to deflection, therefore it is a critical parameter affecting the accuracy of a model. A highly alloyed material makes the determination of material properties difficult because of the variation afforded to the constituents. Hence it was necessary for the author to attempt to assess the value of (E) for Inconel, as the values given in the handbook, ref. (30), were not conclusive for the sizes of material used to manufacture diaphragms. This was done before conducting any pressure-deflection tests.

The actual experimental pressure-deflection tests for diaphragms were performed by the author and the tests on capsules by the staff at KDG Instruments, Ltd.

The test on capsules is part of the production procedure, as the characteristics of every capsule stack are recorded. The method of test, being a production procedure, is carried out on a specially designed "test-bed" and is automated as much as possible. The capsule stack is placed in a pressure chamber and "ranged-in": this means the full working pressure is applied and its total displacement measured in compression, the displacement is recorded and set as one hundred per cent on an X-Y plotter, then the pressure is re-applied slowly and the deviation as a percentage between the linear prediction and the actual displacement is plotted. The procedure is then repeated for the capsule in extension and the resulting plot from the X-Y plotter is as Figure 4.20. The equipment gives a result which is better than 0.05%, i.e. if a typical deviation is plotted as 0.5%, then the result is between 0.45% and 0.55%.

4.2.1 Practical stress-strain relationships for elastic materials

The mechanical properties of materials can efficiently be characterised by the stress-strain diagram obtained from a tension test, Figure 4.6.

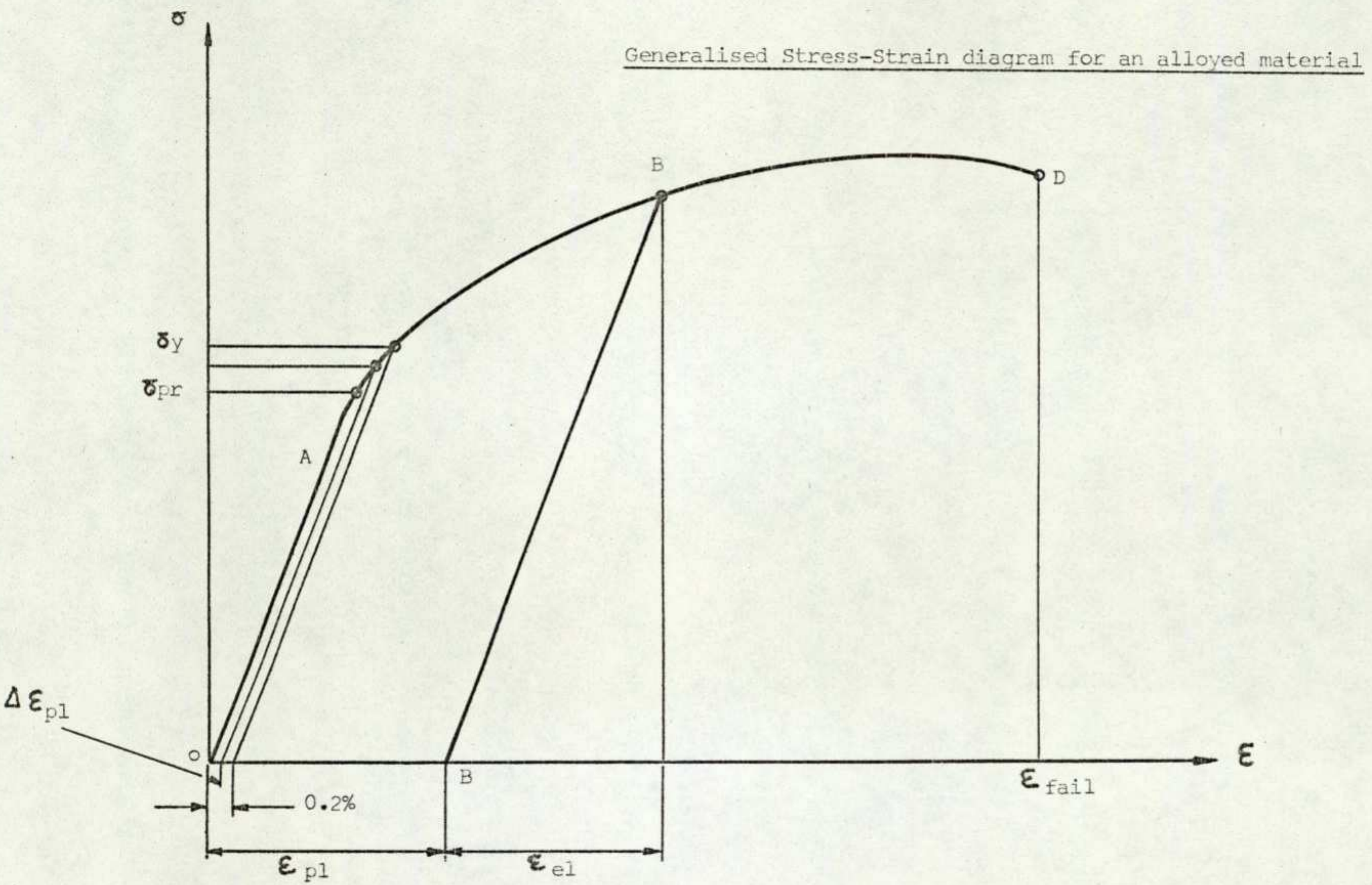

Generalised Stress-Strain diagram for an alloyed material

Figure 4.6.

The diagram represents the stress $\sigma = \frac{T}{A_o} = \frac{\text{(tensile force)}}{\text{(original cross-section)}}$

as a function of strain $\frac{\Delta \ell}{\ell_o} = \frac{\text{(elongation)}}{\text{(gauge length)}}$

The linear stress-strain relationship is expressed by Hooke's law which, for the monoaxial stressed state, is written as:

$$\sigma = E\varepsilon$$

where the all-important constant of proportionality is E (Young's Modulus).

The maximum stress δ_{pr} for which Hooke's law is still valid is called the proportional limit. Determination of the proportional limit is somewhat arbitrary, since it depends, as will be shown later, on the value of the deviation of the curve from a straight line which is chosen as the limit. The proportional limit is usually defined as that point on the curve at which the tangent deviates substantially from the tangent at the origin.

As loading (and deformation) continues, plastic deformation occurs in the specimen, rigidity decreases, and the deformation increases with further load at a higher rate than in the initial section OA. Next, the specimen necks down at its weakest section and fails when the deformation reaches the limiting value ε_{fail}. The highest point on the stress-strain diagram corresponds to the tensile strength of the material, which is defined as the maximum stress, divided by the original cross-sectional area. If the test specimen is loaded until a plastic deformation occurs and the load is then completely removed, the variation of the stress and strain during unloading will follow Hooke's law, and the line CB will be a straight line parallel to Section OA.

The strain ε at point C can be represented as the sum of the elastic and plastic strains $\varepsilon = \varepsilon_{el} + \varepsilon_{pl}$. The elastic strain ε_{el} disappears after unloading, while the plastic strain ε_{pl} remains.

The definition of yield strength σ_y is also somewhat arbitrary, being the stress at which plastic deformation reaches 0.1 or 0.2 per cent. The stresses set up in an elastic element in operation must not exceed the yield strength, since the appearance of residual deformations will distort its shape and disturb its correct functioning. Strictly speaking, the operating stresses in an elastic element must be below the elastic limit σ_{el} defined as the maximum stress at which only negligible residual deformation occurs. Just as in the case of the yield strength, the elastic limit is determined from a residual-deformation allowance

$\Delta\varepsilon_{pl}$, but while this allowance was 0.2 per cent for the yield point, it is much smaller for the elastic limit (of the order of 0.001, 0.003 per cent, etc.)

4.2.2 Inconel and its reported properties

The chemical composition of Inconel is given in Table 4.3 to illustrate the high alloyed nature of the material.

Nickel (plus Cobalt)	70.00
Chromium	14.00 - 17.00
Iron	5.00 - 9.00
Titanium	2.25 - 2.75
Aluminium	0.40 - 1.00
Columbium (plus Tantalum)	0.70 - 1.20
Manganese	1.00 maximum
Silicon	.50 maximum
Sulphur	.01 maximum
Copper	.50 maximum
Carbon	.08 maximum
Cobalt	1.00 maximum

Table 4.3: Limiting chemical composition percentage, ref. (30)

From the handbook Inconel X-750 is quoted generally as having a value of Young's Modulus in tension of 31.0 x 10^6 lbf/in^2 (213.7 GNm^{-2}) and a Poisson's ratio of 0.29 at 26°C, and this value decreases as the temperature increases. For strip material under 0.010" (0.234 mm) thick the tensile strength is quoted as 140,000 lbf/in^2 (965.3 MNm^{-2}) in the annealed condition and 150,000 lbf/in^2 after heat treatment. For sheet material 0.062" (1.5748 mm) thick, cold rolled annealed, the tensile strength is quoted as 110,000 lbf/in^2 (758.4 MNm^{-2}) with a yield of 46,500 lbf/in^2 (320.6 MNm^{-2}) (0.2 per cent offset). The handbook does not mention a Young's Modulus for strip or sheet material, so presumably it is the same as the value given initially. Also the book is vague in the difference between strip and sheet material. Tensile properties in different directions of roll for sheet of two thicknesses are presented in Table 4.4.

Thickness	Orientation	Tensile strength lbf/in^2	Yield strength (0.2% offset) lbf/in^2	Elongation %	Modulus elasticity 10^6 lbf/in^2
0.062"	Longitudinal	170,500	116,000	26.5	28.4
	Transverse	166,000	116,000	28.0	30.4
0.125"	Longitudinal	179,500	124,000	26.0	32.8
	Transverse	180,000	129,000	26.0	30.7

Table 4.4

Here the variation of Young's Modulus is given, but whether any meaningful result can be extrapolated, for the thicknesses used in diaphragms (0.003" - 0.025"), is very doubtful.

4.2.3 Apparatus and method of tensile test

Having defined certain terms, actual Young's Modulus tests were made. It was thought that E might be different in perpendicular directions of roll, and, indeed, the manufacturers of pressure capsules reduce this uncertainty, to some extent, by ensuring that two diaphragms made from the same sheet are set 90° to each other.

A number of tests were carried out on specimens made to British Standard Specification No. 18 (for sheet metal); the actual material was supplied by the manufacturers of the diaphragms.

Initially, four identically sized test specimens were produced, two along the direction of roll and two across it, to look for any measurable difference in material properties. The metal was 0.495" (12.573 mm) wide and 0.0077" (0.1956 mm) thick, making it possible for strain gauges to reinforce the material and give false readings, so for the first tests a mechanical extensometer, the Huggenberger, was used. Two gauges were clamped across the width of the specimen and the average reading of strain recorded. This cancels out the initial effect of a slight off centre loading which will inevitably occur. Strain of 8×10^{-6} could be read directly with this type of extensometer. The operation of the Huggenberger extensometer is adequately described in the standard book on structures by H. Ryder, "Strength of Materials", ref. (31).

To obtain values of yield strength and check the consistency of these results, tensometer tests were made on the above specimens using electrical resistance strain gauges. These were yield point gauges which allow strains in the plastic region to be measured without going open circuit.

Huggenberger extensometers are difficult to use, even in the hands of experienced experimenters and especially so on very thin material. The results obtained from the first test pieces had a large variation in Young's Modulus and therefore it was decided to repeat the experiments using very small strain gauges which would not reinforce the material.

Again, two gauges were bonded to the specimen, one on each face, so that the average would cancel out any uneven pull on the test piece. Three tests were carried out: one 0.006" (0.1524 mm) thick specimen and two 0.004" (0.1016 mm) thick, all 0.5" (12.7 mm) wide.

4.2.4 Discussion of results for Young's Modulus measurements

Values of Young's Modulus found for the first specimens, for both directions of roll, were consistently higher than in ref. (13), the range varying from 29.5 - 34.5 x 10^6 lbf/in^2 (203.4 - 237.8 GNm^{-2}), the average being about 10 per cent higher than ref. (13).

Whether any significance may be attached to the slight difference in readings in both directions is doubtful, for two reasons:

(a) The difference is only of the order of 1 per cent and an estimation of accumulative error (human and machine error) is higher.

(b) Range: the Huggenberger Extensometer was only able to work effectively up to a load with these test pieces of 500 N, yet the noticeable yield strength was much higher than this value.

Computed values of Young's Modulus made at high loadings, i.e. using strain gauges, gave lower results than those at lower load ranges, i.e. using the Huggenberger, indicating that, although the elastic range appears a straight line, when plotted, it is a very slight curve. This will make Young's Modulus difficult to assess accurately. The only difference between the two directions of roll was that the transverse direction extended over 40 per cent more before breaking, the fracture point in both cases showing no localised necking and only a very small reduction in cross-sectional area over the gauge length, under 2 per cent.

The results using smaller strain gauges on the second specimens lead to the conclusion that an accurate value of Young's Modulus (better than ± 5 per cent), for a highly alloyed material such as Inconel is not possible using these techniques. An average value would have to be used in the model. Table 4.5 is one of 0.004" specimens tested to 500 N. The output is converted to Imperial units to show E in Imperial units.

Stress x 10^3 lbf/in^2	Strain gauge 1 x 10^{-6}	Strain gauge 2 x 10^{-2}	Average	E x 10^6 lbf/in^2
4.51	0	0	0	–
10.54	181	190	185.5	32.5
14.7	320	322	32.1	31.8
19.55	476	479	477.5	31.5
24.8	656	644	650	31.2
30.4	846	844	845	30.6
36.05	1034	1033	1033.4	30.4
41.0	1232	1215	1223.5	29.8
45.0	1388	1364	137.5	29.4

Table 4.5

If the value of E is computed at each loading it can be seen to decrease, suggesting that the stress-strain curve has no straight section where stress can be directly related to strain. This same pattern occurs when the 0.004" (0.1016 mm) specimen was loaded with the same number of increments but only up to 200 N; the value of E was slightly higher than the above table (4.5). The test using the 0.006" (0.1524 mm) specimen loaded to 500 N did not have this tendency to curve, but gave a value of E only 29.6 lbf/in^2 (200.6 GNm^{-2}).

The slight curvature effect noted with the 0.004" (0.1016 mm) specimen does not show up on a test taken to destruction.

Figure 4.7 shows one of the first test pieces actually taken to destruction with a straight portion up to 1950 N, a slight bend after yield, then a lot of straining with only small increases in load. The value of yield strength computed at 1950 N is 115,010 lbf/in^2, which is in very good agreement with values quoted in the manufacturers' handbook for (0.010" - 0.025") (0.254 mm - 0.635 mm) thick material at 0.2 per cent offset.

Bearing in mind the uncertain nature of the value of Young's Modulus, an average value of 30 x 10^6 lbf/in^2 (206.9 GNm^{-2}) was taken for Computational Work.

4.2.5 Apparatus and method of pressure-deflection tests for diaphragms

A series of pressure-deflection tests was carried out on four diaphragms using two thicknesses, 0.004" (0.1016 mm) and 0.006" (0.1524 mm). Two different tool dies were used to produce the diaphragms and these

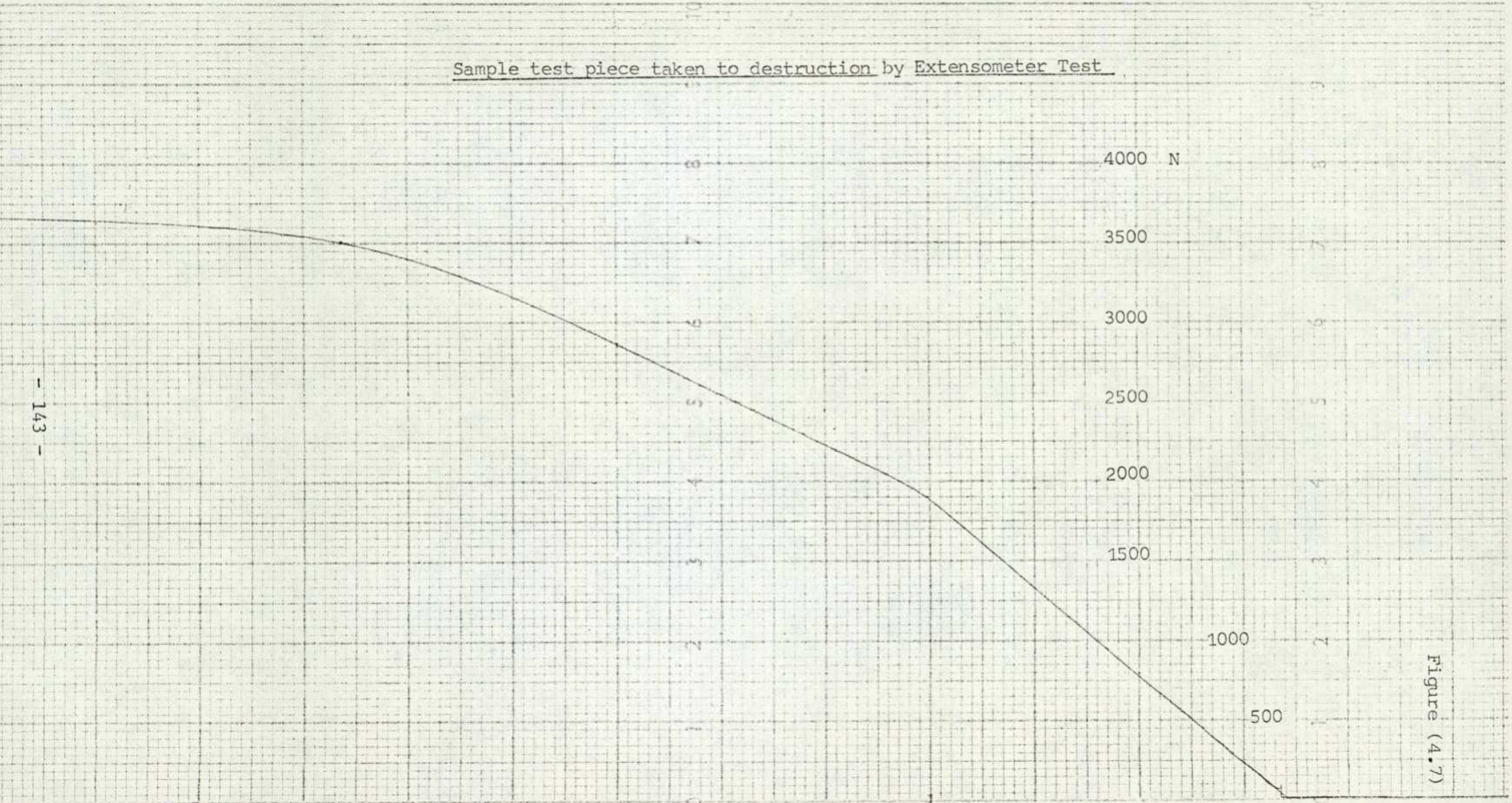

Sample test piece taken to destruction by Extensometer Test

Figure (4.7)

will be denoted by the numbers 6 and 7, being the top and bottom, respectively, of a nesting production capsule. The original flat sheets were fully annealed when supplied and then given the appropriate heat treatment after forming; this will minimise the presence of internal stresses caused by the forming process.

The diaphragms were electron beam welded to a rigid cylindrical base, which had the same thermal coefficient of expansion as the diaphragm material, thus minimising the build-up of internal stresses caused by differential expansion during welding.

The active radius of the diaphragm is dependent on the weld penetration, but, fortunately, this has been reported by Schricker, ref. (13), as small, on average 0.008" (0.203 mm), and a small lip around the outer edge of the diaphragm is allowed for the weld.

With the diaphragm welded into position, the cylindrical base could then be screwed into a solid rigid stand, which had a bench micrometer positioned vertically above the centre of the diaphragm. The micrometer was capable of reading to 0.0001" (.00254 mm) (Figure 4.8). The deflections were observed with the aid of an optical lever arrangement: when the micrometer tip touched the centre of the diaphragm, an electrical circuit was formed indicating contact, and thus a micrometer reading could be made. Compressed air was applied through the pipe (e) and measured by two methods:

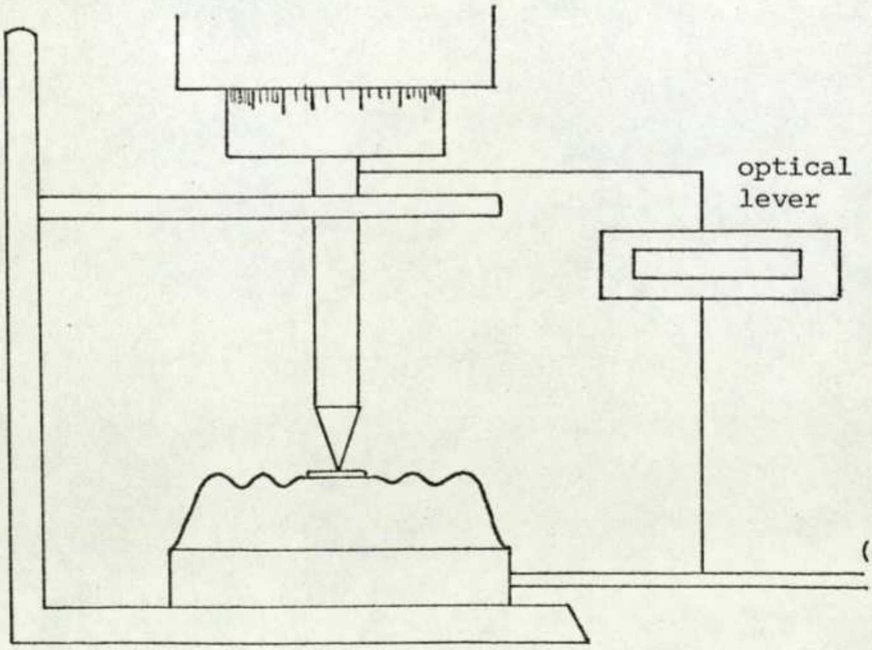

Figure 4.8: Diagram of test apparatus for diaphragms

(a) Texas precision pressure gauge manufactured by Texas Instruments, Ltd.

(b) A dead-weight tester.

The two methods were used because the first method, although easier to operate, did not have the required range. This method of testing does ensure that the diaphragms are perfectly clamped at the outer boundary, but does have the disadvantage that each time the diaphragm needs to be changed, it must be machined off the base and hence destroyed. Owing to the inevitable "spring-back", it was necessary to section diaphragms across a diameter to examine the profile. The sectioning of the diaphragms was performed in three ways:

(1) Potting in transparent acrulite for embedment: this protects the geometry from distortion caused in the cutting process, after which the acrulite is removed.

(2) Electron spark erosion: this method is quicker than the first, although the edge must be cleaned after cutting.

(3) Cutting with a high speed grindstone wheel: this is the simplest method, but initially it was not available.

The sectioned diaphragm is now examined under a shadow-graph with a magnification of 50 times; a tracing of the profile is produced and the X, Y, R1 co-ordinates found are mentioned more fully in Chapter 3.

4.2.6 Discussion of results for linear diaphragm model

A preliminary test was carried out for the linear model using the No. 6 diaphragm tool, 0.006" (.1524 mm) thick. This was tested up to 20 lbf/in^2 (137.87 KPa) in 1 lbf/in^2 (6.894 KPa) steps. Other than knowing the material to be Inconel X-750, the actual batch specification was unknown. Young's Modulus was taken to be 30×10^6 lbf/in^2 (206.9 GNm^{-2}); Poisson's ratio was taken from the manufacturers' handbook as 0.29. The predicted deflection was 2.5 per cent lower than the experimental value (the shape of the graph at the origin). This accuracy was better than expected, and well within the tolerances which can be placed on the physical properties of the material and geometric description of the profile. If Young's Modulus was as high as 34×10^6 lbf/in^2 (234.5 GNm^{-2}), the predicted deflection would be 15.85 per cent below the experimental value; within the linear range the deflection is inversely proportional to Young's Modulus (Figure 4.10). Taking the nominal thickness of 0.006" (vi), the deflection if $E = 28 \times 10^6$ lbf/in^2 is .0348" and if

34×10^6 lbf/in^2 (234.5 GNm^{-2}), only 0.0287".

Diaphragm thickness is quoted as the thickness of the sheet it was formed from, and because of the stretching involved in the forming, the thickness will vary along the generator. On average, the thickness will be less than the original thickness. Schricker, ref. (13), made measurements of thickness at several points along the diaphragm generator and took the average. The following results are quoted from his work:

Original thickness	Average thickness
0.004" (0.1016 mm)	0.0038" (0.09652 mm)
0.006" (0.1524 mm)	0.0057" (0.14478 mm)
0.008" (0.2032 mm)	0.0077" (0.19558 mm)

The predicted deflection using 0.0057" as the constant thickness gave a deflection which was 2.0 per cent above the experimental value. The actual situation, of course, is more complex: the thickness varies along the generator in a fashion which is dependent on the geometry of the diaphragm.

Some attempt has been made to simulate the variation, first by noting the actual trend and then trying to approximate a curve to the variation. What appears to happen is that in the forming process a rubber pad grips the initially flat blank and pushes it into the female tool form; the material is held by the pad on the bottom of the corrugations and stretched up into the required shape causing a slight thinning effect down the sides and at the peak of the corrugations (Figure 4.9).

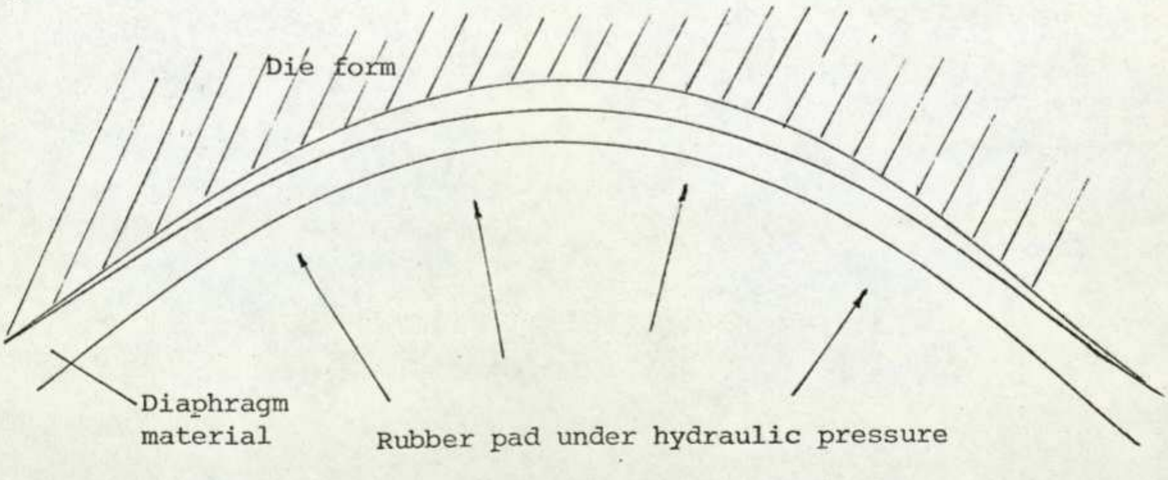

Figure 4.9: Diaphragm forming showing thinning down of material

Figure 4.10

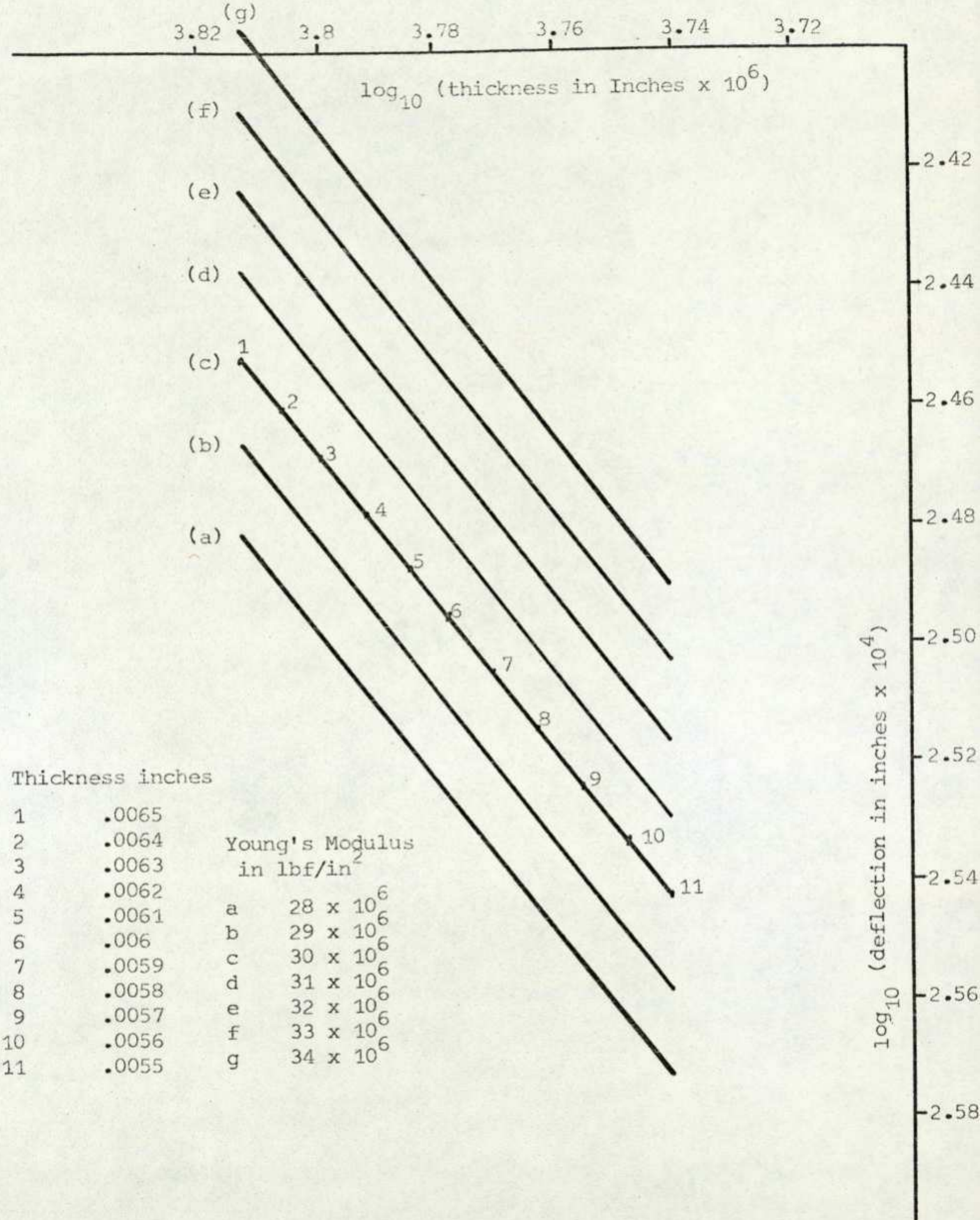

Graph showing the effect varying both the thickness and Young's Modulus has upon the deflection, based upon a single profile

A section of diaphragm form tool No. 6, .006" (0.1524 mm) thick, was mounted, etched, and polished as for a metallurgical specimen, and examined under a travelling microscope which was able to measure the thickness of the material in a number of places along the profile. The effect when programmed gave a 4.2 per cent increase in deflection over the constant original blank thickness. The sensitivity of the diaphragm model to variations in thickness (constant) is also shown in Figure 4.10. This slope of lines of constant E on the logarithmic axis indicates that thickness is related to displacement directly by some power law: this is indeed so and will be discussed fully in a later chapter.

4.2.7 Discussion of results for non-linear diaphragm model

Figure 4.14 shows the non-linear predicted curves superimposed on the experimental curves for all four diaphragms tested. The 0.004" (.1016 mm) and 0.006" (.1524 mm) No. 6 diaphragms were tested before the No. 7 specimens and, unfortunately, not pressurised as much as the No. 7 diaphragms. Looking at Figures 4.11, 4.12 and 4.13, all curves initially indicate a firstderivative increasing characteristic, which can be seen on the No. 7 diaphragms to become first derivative decreasing as the pressure is further increased.

All the diaphragms have been pressurised well above the actual operating pressure (the 0.006" diaphragms are used up to a pressure of approximately 3.617 lbf/in^2 (25 KPa). Figures 4.12 and 4.13 have had the pressure removed in equal steps to show the amount of plastic deformation that has occurred in the testing, and in this region the assumptions of the thin shell theory do not hold, i.e. Hooke's law is not valid. With the relatively crude apparatus used to test the diaphragms, the overall deflections could be assessed accurately, but the computation of small non-linearities (less than about 2 per cent) is difficult. It can be seen that the gross-non-linearity associated with the tested diaphragms is most probably plastic not geometric non-linearity.

Referring back to Figures 3.13, 3.14, etc., which are plots of the theoretically predicted stress distribution along the generator from the top and bottom surface in the radial and circumferential directions, as the stress is assumed to vary linearly through the thickness, the maximum absolute values will be at the surfaces. Both sets of curves show a very rapid variation of stress over short sections of the diaphragm. To determine which section of the diaphragm goes beyond the yield point first, a yield criterion will have to be applied: a suitable one chosen was the

Experimental pressure - deflection characteristic - tool 6
0.004" and 0.006" diaphragms

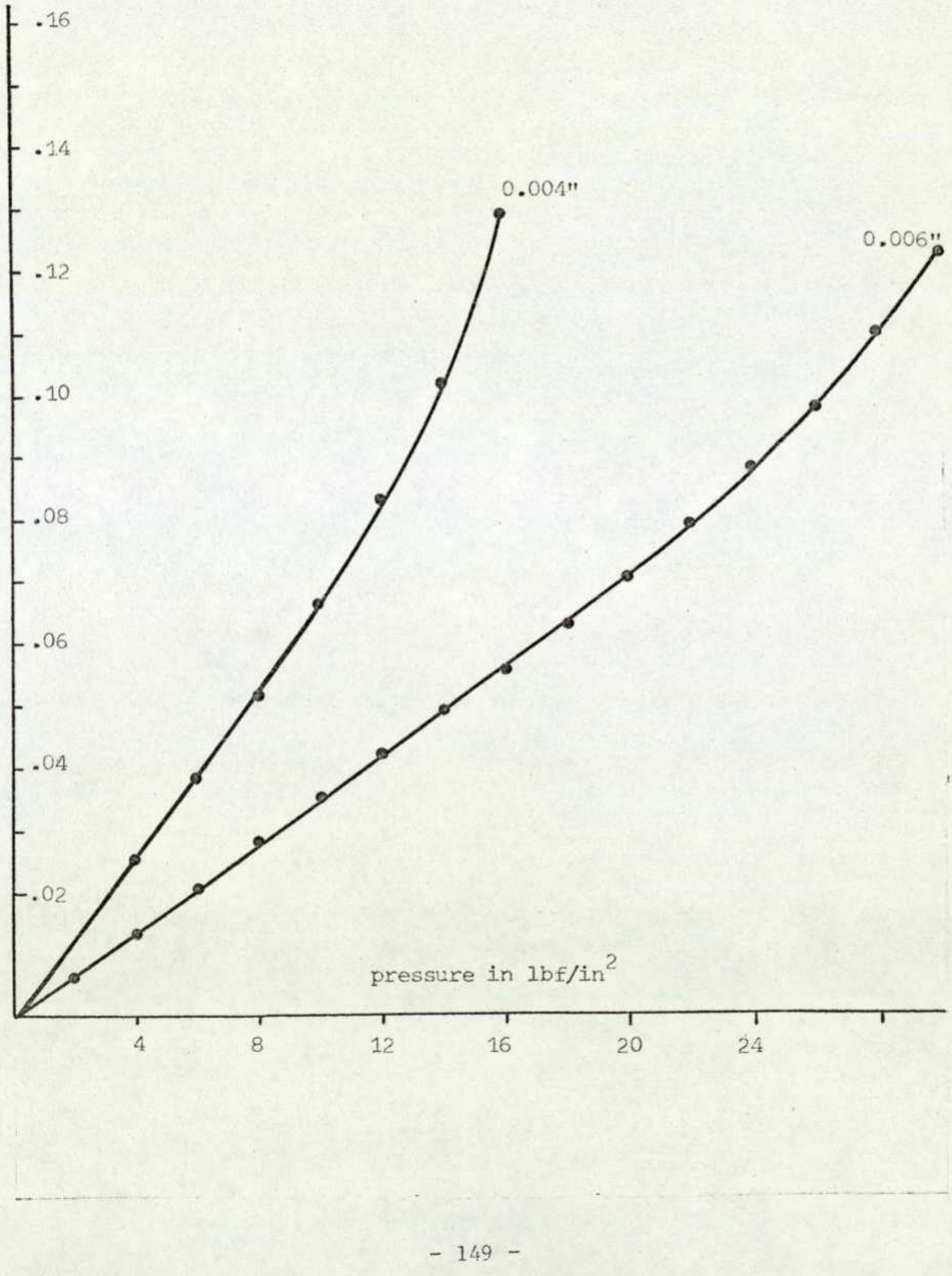

Figure (4.12)

Experimental pressure - deflection characteristic - tool 7
0.004" diaphragm

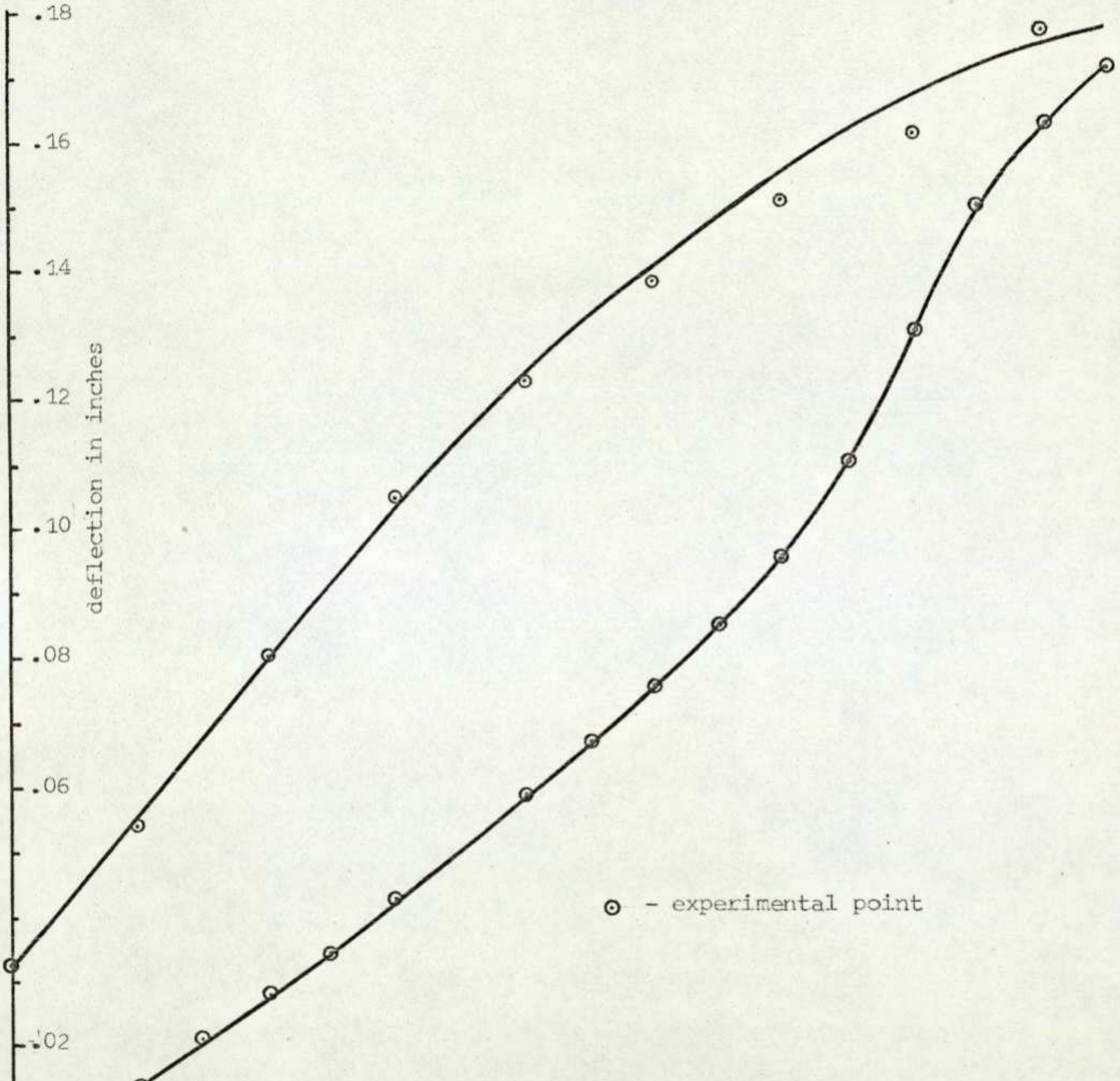

Experimental pressure - deflection characteristic - tool 7 0.006" diaphragm

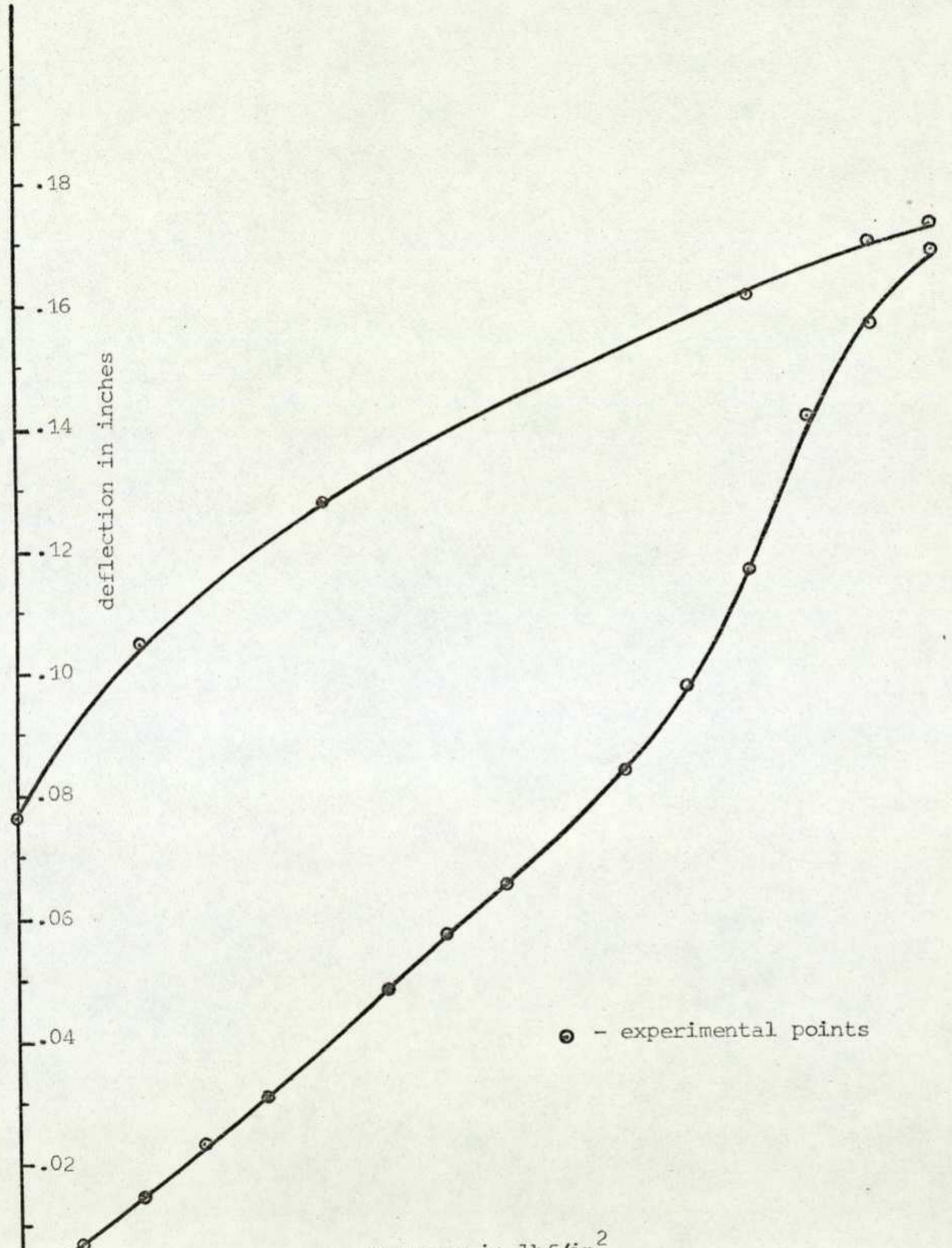

Figure (4.14)

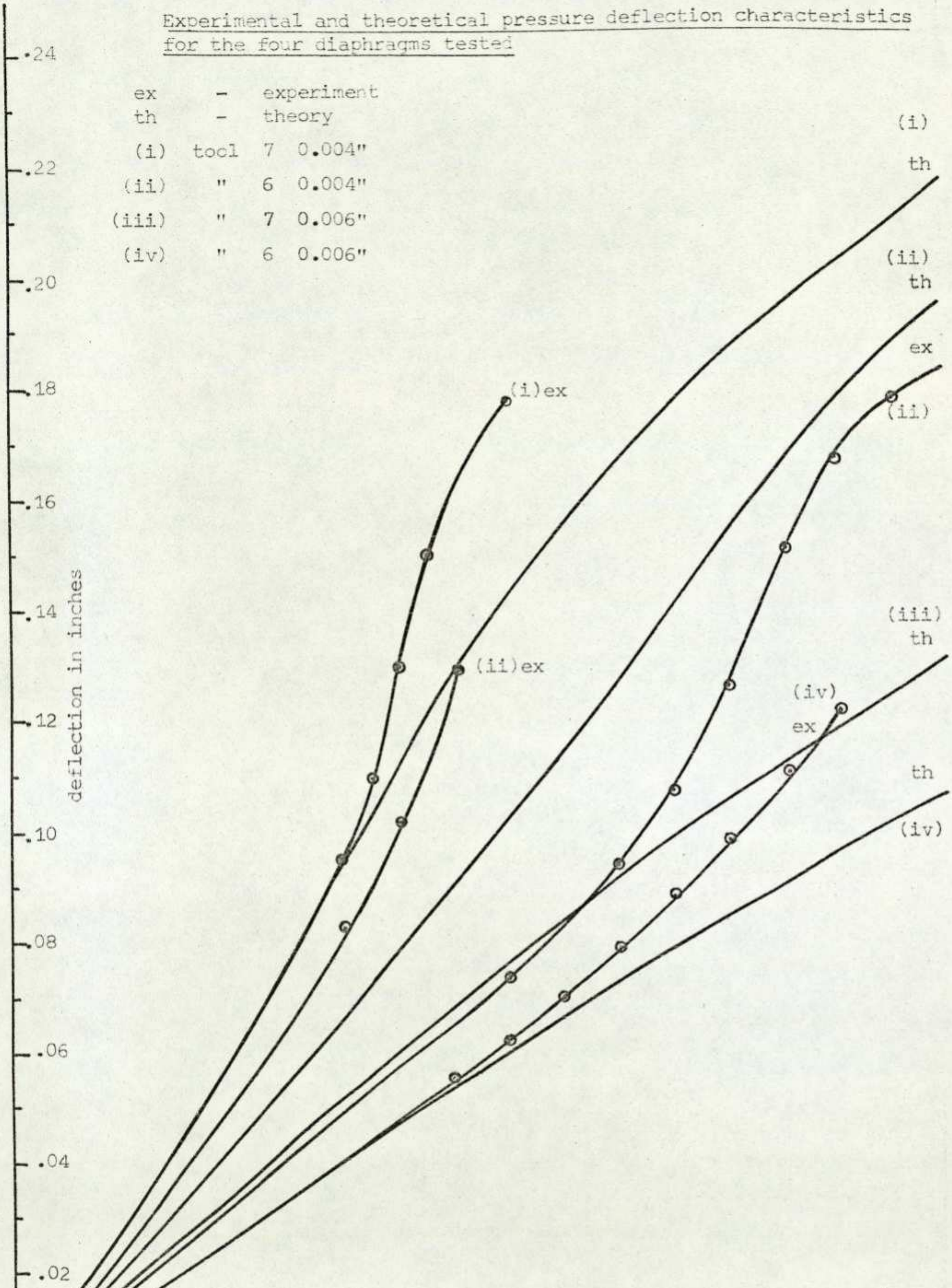

Experimental and theoretical pressure deflection characteristics for the four diaphragms tested

Von-Mise's criterion:

$$\sigma_y = \sqrt{\sigma_\xi^{\ 2} + \sigma_\theta^{\ 2} - \sigma_\xi \sigma_\theta} \qquad \text{where } \sigma_y = \text{yield stress.}$$

For a two-dimensional stress pattern, when computing the values of stress for each point along the generator, this criterion can be applied to test whether the diaphragm material has yielded at that point.

An attempt was made to simulate a plastic state to show that the experimental curves are the result of passing the yield point of the material. Inconel X-750 has a stress-strain relationship which has no really sharp discontinuities and could be represented fairly simply:

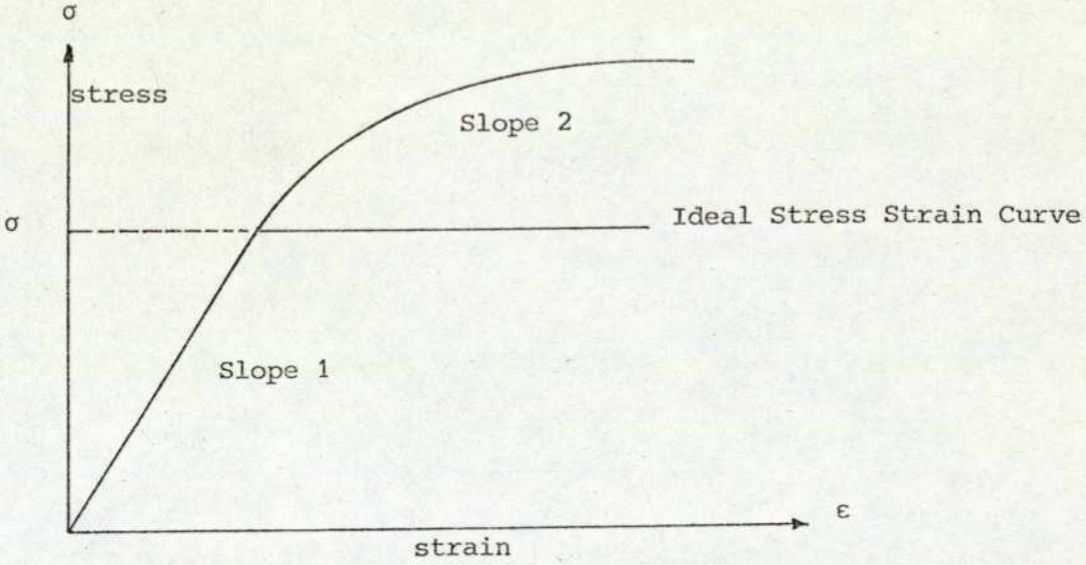

Figure 4.15: Showing simple representation of stress-strain curve

Initially, the yield criterion was calculated at each mesh point, and if it had been exceeded the value of E was adjusted according to the extent to which the stress had exceeded the yield stress. The results for the No. 6 tool, 0.004" (.1016 mm) thick, diaphragm are shown in Figure 4.16. The work was further refined by modifying the differential equations to include the variation of E along the generator; previously E had been assumed constant, e.g. terms in the equations such as $\frac{(rD)'}{rD}$ now reduce to:

$$\frac{1}{E}\frac{dE}{ds} + \frac{\cos\,\phi}{r} + \frac{3}{t}\frac{dt}{ds}\ , \text{ etc.,}$$

but this had noticeably little effect.

Various approximations to the plastic variation of Young's Modulus were programmed $\left(\text{with } \sigma_y \text{ (yield stress)} = 115{,}000 \text{ lbf/in}^2 \text{ (793 MNm}^{-2}\text{)}\right)$

Figure (4.16)

First attempt to approximate the Non-linear behaviour due to plasticity

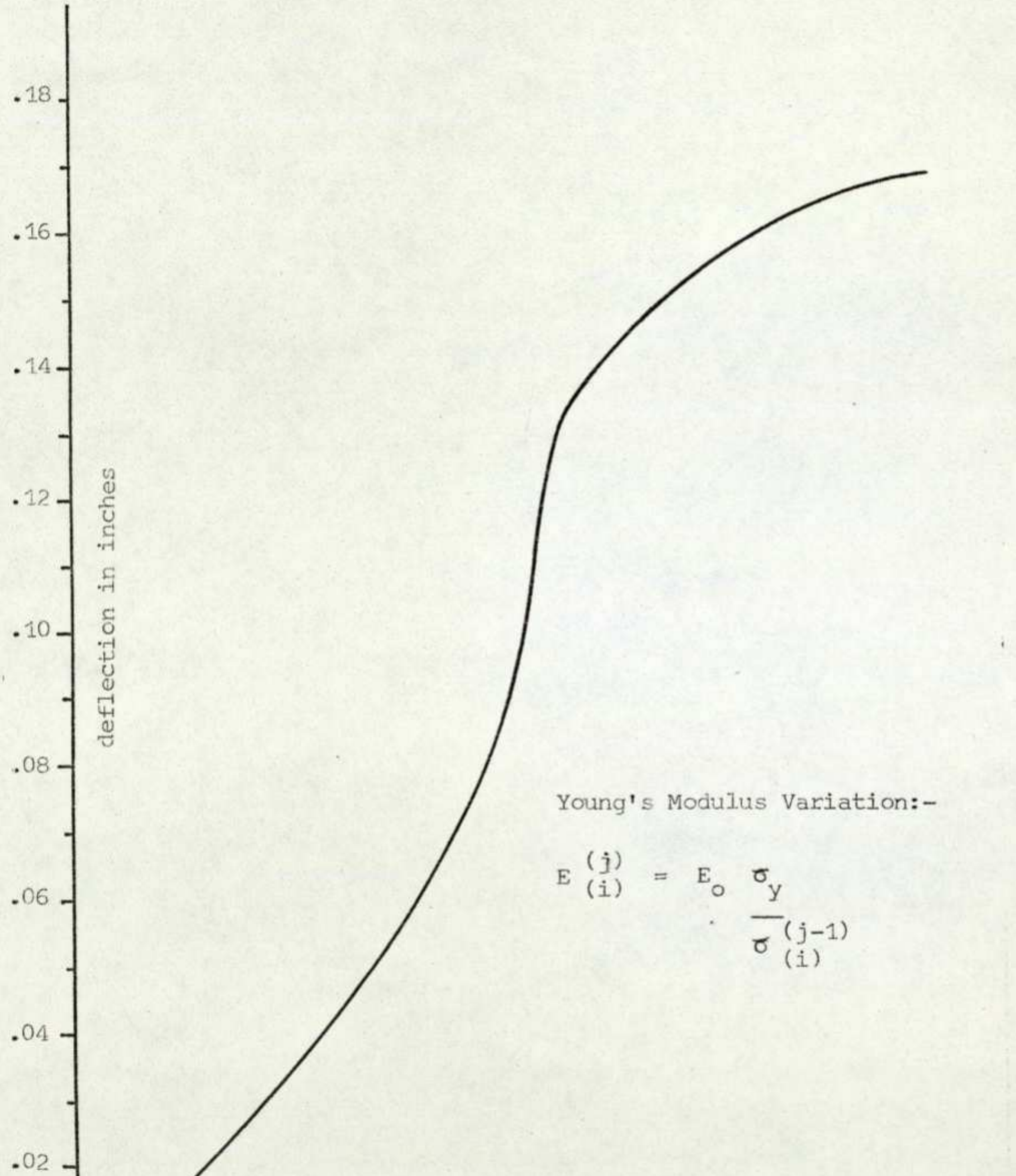

Young's Modulus Variation:-

$$E_{(i)}^{(j)} = E_o \frac{\sigma_y}{\sigma_{(i)}^{(j-1)}}$$

(a) $E_i^{(j)} = \frac{E_o \, \sigma_y}{\sigma_i^{(j-1)}}$

(b) $E_i^{(j)} = E_i^{(j-1)} \, \frac{\sigma_y^{(j-1)}}{\sigma_i}$

(c) third degree polynomial curve fit to the stress-strain curve to obtain:

$$E = \frac{d\sigma}{d\varepsilon}$$

(d) second degree polynomial curve fit (with matching of end slopes, i.e. slope 1 and slope 2)

E_o = linear value of E

E_i, σ_i = value at i^{th} mesh point

(the superscript refers to the j^{th} pressure iteration)

An approximation from (c) for E_i was found by taking an actual stress-strain curve for Inconel and using a third-degree least squares polynomial curve fitting routine, finding the equation

$$\varepsilon = a_1 + a_2\sigma + a_3\sigma^2 + a_4\sigma^3$$

differentiating

$$\frac{d\varepsilon}{d\sigma} = a_2 + 2\,a_3\,\sigma + 3\,a_4\,\sigma^2$$

and inverting

$$\frac{1}{\frac{d\varepsilon}{d\sigma}} = \frac{d\sigma}{d\varepsilon} = E = \frac{1}{a_2 + 2\,a_3\,\sigma + 3\,a_4\,\sigma^2}$$

An approximation from (d) for E may be formed analytically by taking the same stress-strain curve and finding the initial and final slopes S_1 and S_2 and their co-ordinates σ_1, ε_1 and σ_2, ε_2

$$\varepsilon = a_1 + a_2\,\sigma + a_3\,\sigma^2$$

$$\frac{d\varepsilon}{d\sigma} = a_2 + 2\,a_3\,\sigma \qquad \text{therefore} \qquad \frac{d\sigma}{d\varepsilon} = \frac{1}{a_2 + 2\,a_3\,\sigma}$$

$$S_1 = \frac{1}{a_2 + 2\,a_3\,\sigma} \qquad S_2 = \frac{1}{a_2 + 2\,a_3\,\sigma_2}$$

The above two equations are solved to obtain a_2 and a_3 and then

$$E = \frac{1}{a_2 + 2\,a_3\,\sigma}$$

Figure (4.17)

Various attempts to approximate the Non-linear behaviour due to plasticity

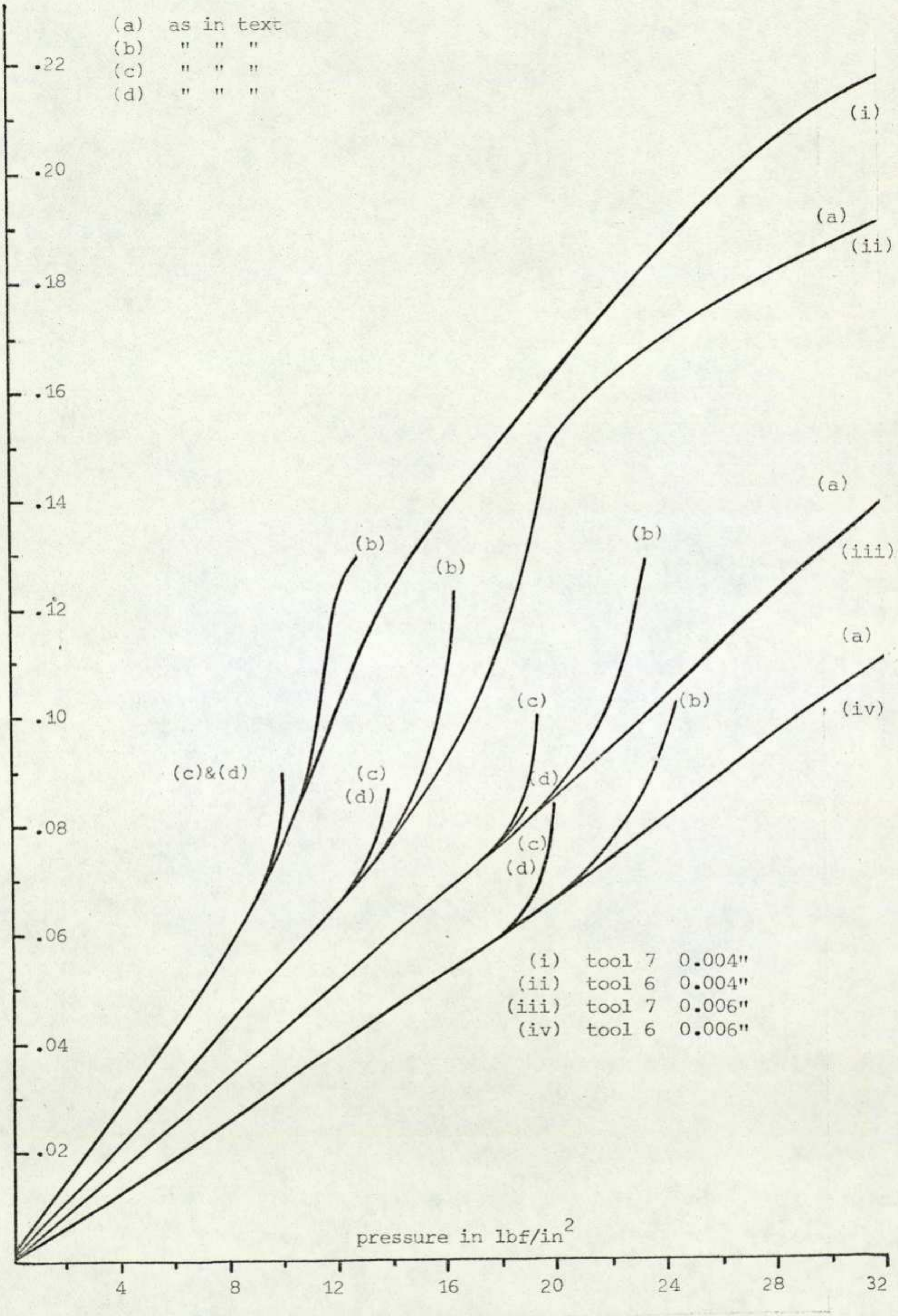

The above four approximations for E were programmed and the results plotted on Figure 4.17. For all approximations except (a), the iterative process failed to converge to a sensible result soon after the curve deviated from the linear region. These points of deviation agree reasonably with experiments (see Table 4.5).

Die No.	Material thickness		Theory lbf/in^2	Experiment lbf/in^2
	inches	mm		
6	0.006	0.1524	22.0	25
7	0.006	0.1524	21.2	20.0
6	0.004	0.1016	13.4	8.5
7	0.004	0.1016	9.5	9.5

Table 4.5: Comparisons of diaphragm theory and experiments for the pressure at which a 5 per cent deviation from linearity occurs

It was noticed that, if the value of E is reduced by an amount, this will reduce by the same amount the values of bending and tensile stiffness, which reduce the stress level that depends upon these stiffnesses. In a real situation this is known as working hardening, i.e. if the stress level drops, after the yield point σ_{y_0} has been exceeded the curve takes the same slope as the initial value of E; if the stress is increased again the yield σ_{y_1} is at the higher position on the curve (Figure 4.18).

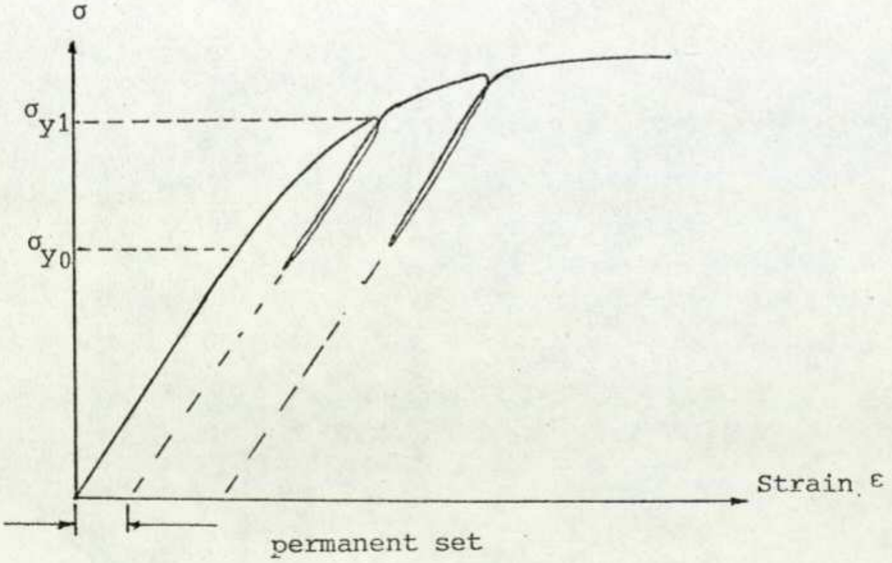

Figure 4.18: Showing work hardening effect

Owing to the fact that the program is only able to apply the pressure in an iterative fashion, this work hardening type of phenomenon was programmed, causing obviously incorrect results in the pressure deflection characteristic. This is because the assumption of thin shell theory neglects strain, even in a geometric non-linear model. Here the amount of strain, and hence permanent "set", is very large and ought not to be neglected. Any permanent deformation would show up as an offset at the centre.

Any attempt to include large plastic strains would require a major re-modelling of the shell theory. This major modification was not considered as it deviates too far from the aims of the present work, although in section 4.3.1 finite elastic strains are built into the model to indicate that it does have slight improvements to the results but with the resulting cost in increased complexity.

4.2.8 Capsules

4.2.8.1 Discussion of results for linear capsule model: Experimental tests of production capsules conducted by staff at KDG Instruments, Ltd., during routine production tests at their laboratories at Rustington, have been compared with theory. The capsules were made from diaphragms formed on tool dies Nos. 6 and 7. The individual diaphragms have already been tested against theory (see section 4.2.4). Two such capsules are stacked together (termed a "two-stack capsule") and this is used in one chamber of a differential pressure cell: a matched two-stack capsule is used in the other chamber. Experimental pressure tests were made on several capsule stacks and the results are shown in Table 4.7.

Thickness Inches	(mm)	Pressure Wg	(KPa)	Average deflection inches	(mm)	Theory inches	(mm)
0.004	(.1016)	45	(11.188)	0.0456	(1.158)	.0400	(1.016)
0.006	(.1524)	100	(24.864)	0.0546	(1.386)	.0544	(1.3817)

Table 4.7

The results for the 0.006" capsule stacks are very good and are well within the tolerances that can be placed on the geometrical and physical parameter used in the capsule model. With regard to the 0.004" capsule results, the computer model showed that the deflection of the capsule was equal (to within 3 per cent) to the sum of the deflections of the two constitutive diaphragms clamped at their periphery. On this basis we can explain the discrepancy between the theoretical and experimental results for the 0.004" capsule stack as being due to the inadequacy of the diaphragm model results for the 0.004" diaphragm formed on die tool No. 6 (see Figure 4.14). If we take the experimental results for this diaphragm, we find that the total deflection for the capsule stack is 0.046", in close agreement with the experimental result of 0.0456".

It now remains to explain why the results for the 0.004" diaphragm are in disagreement with experiment. There appear to be two possible causes:

(a) On examining the sectioned diaphragm from which profile measurements were made, it was discovered that the diaphragm had not been sectioned along a diameter. This led to a somewhat faulty profile being used in the computer model.

(b) Taking the above profile, the effect of a slight error in thickness was investigated. Reducing the thickness from 0.004" to 0.0038" (.09652 mm) increased the deflection by 13.5 per cent, bringing it almost exactly in line with the experimental results. The diaphragm was formed from a 0.004" blank and it is expected that there would be some reduction in thickness along the length of the diaphragm generator (particularly for this diaphragm because it is the top of the capsule and is therefore formed deeper). The actual variation of thickness is very difficult to assess theoretically.

<u>4.2.8.2 Validation of the non-linear capsule model</u>: After the initial experimental validation of the linear, non-linear and linear capsule models, where some anomalies had been brought to light, a much more extensive validation of the model was performed using the non-linear capsule model. The program was applied to the range of capsules used by KDG Instruments, Ltd. in their 4000 Series differential pressure transmitters; Figure 4.19 shows a typical capsule, sectioned and mounted, reproduced from a KDG Instrument Manual. The range examined is not the complete range as used in the differential pressure transmitters, but the thickness range (i.e. 0.003" - 0.025" (0.076 - 0.635 mm) is adequately covered. The capsules investigated cover a pressure range 0 - 10 to 0 - 1400 inches Wg (0 - 2.5 KPa to 0 - 349 KPa). Table 4.8 shows the number of capsules in each stack and the actual thickness of the material used for each range.

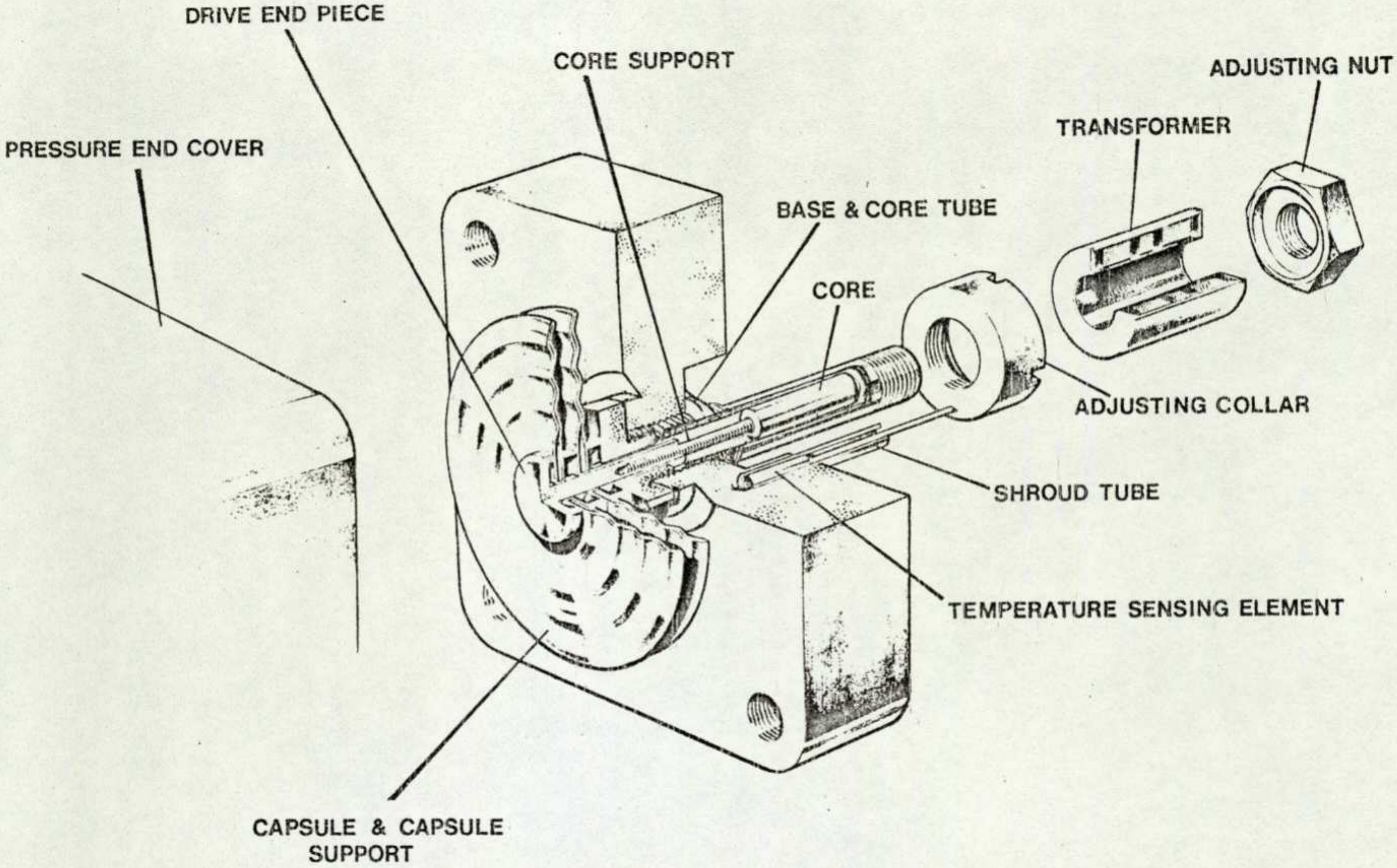

Figure 4.19

Sensor assembly

Range Wg	(KPa)	Thickness inches	(mm)	No. of capsules in the stack
0 - 10	(2.49)	0.003	(.0762)	3
0 - 100	(24.92)	0.006	(.1524)	2
0 - 150	(37.38)	0.008	(.2032)	2
0 - 325	(80.99)	0.012	(.3048)	2
0 - 800	(199.36)	0.020	(.508)	2
0 - 1400	(348.89)	0.025	(.635)	2

Table 4.8: Range of capsule examined

Every capsule stack which is assembled into an instrument is catalogued and a record kept of its displacement, both in compression and extension, as well as a graphical deviation from linearity over its entire working range. It is therefore easy to make a statistical comparison between experiment and theory instead of the "one off" tests applied to diaphragms. The constituent diaphragms for each capsule range were examined, as previously described, and traced out on to plastic film; from this the X and Y co-ordinates of the peaks and troughs were measured and also the "best fit" radius of curvature. The results were fed into a computer program, along with the particular thickness of the material, and a working drawing 50 times full size was constructed using the measured data. Comparing with the original shape, minor adjustments (mainly in radius of curvature) could be made, so that the simulated diaphragm was as near as possible a copy of the original. Any errors at this stage were fortunately multiplied by 50. The non-linear capsule model was supplied with the relevant thickness and pressure range, and the displacement and non-linearities in both directions (compression and extension) were printed out. Table 4.9 shows the results of overall centre deflection for the mean of a number of experiment results, compared with the predicted result multiplied by the number of capsules in that particular stack.

Thickness	Experiment		Predicted	
	Compression	Extension	Compression	Extension
0.003"	.04016"	.041"	.04392"	.042081"
0.006"	.05123"	.0506"	.051788"	.050296"
0.008"	.03896"	.0392"	.040707"	.040008"
0.012"	.045075"	.0447"	.045796"	.04464"
0.020"	.0466"	.04655"	.043472"	.042112"
0.025"	.0528"	.0575"	.04916"	.0439"

Table 4.9: Comparison between experiment and theory

The deviation on the experimental mean was small, generally less than 0.002" (0.051 mm). If these results are plotted out (Figure 4.21) against increasing thickness, an interesting trend may be observed. For the lesser thickness, notably 0.003" and 0.008", the predicted deflections are both larger than the means and for the larger thickness, i.e. 0.020" and 0.025",the predictions are both smaller. Predicted deflections in compression are also greater for both 0.006" and 0.012", but these results are particularly good anyway, the largest deviation between experiment and theory being about 1.6 per cent. The non-linearity of each capsule is plotted as a continuous curve over the working range in both directions, and generally the curves are opposite in sign (see Figure 4.20).

The opposing signs in compression and extension enable the matching of capsules in the manufacture of differential pressure cells. From a number of these plots for one particular range a mean of maximum non-linearity in each direction could be found along with the standard deviation. These were plotted on a graph (Figure 4.22) for the range of thicknesses. Again, an interesting point arises; purely from the experimental results, two straight lines can be drawn approximately through the areas shown as one standard deviation of non-linearity, compression being a much better example than extension. These lines not only cross, but the sign of the non-linearity is reversed as the thickness increases. This has the effect of giving the 0.012" (.3048 mm) capsule a very small non-linearity in both directions; only the 0.008" (.2032 mm) capsule does not have opposite sign non-linearities. The predicted maximums are shown as ⓧ for extension and X for compression. These, it will be noted, do not change sign as the thickness increases, i.e. for compression a negative non-linearity is always predicted and positive for extension.

Figure 4.20

Example of Capsule Non-linearity plot

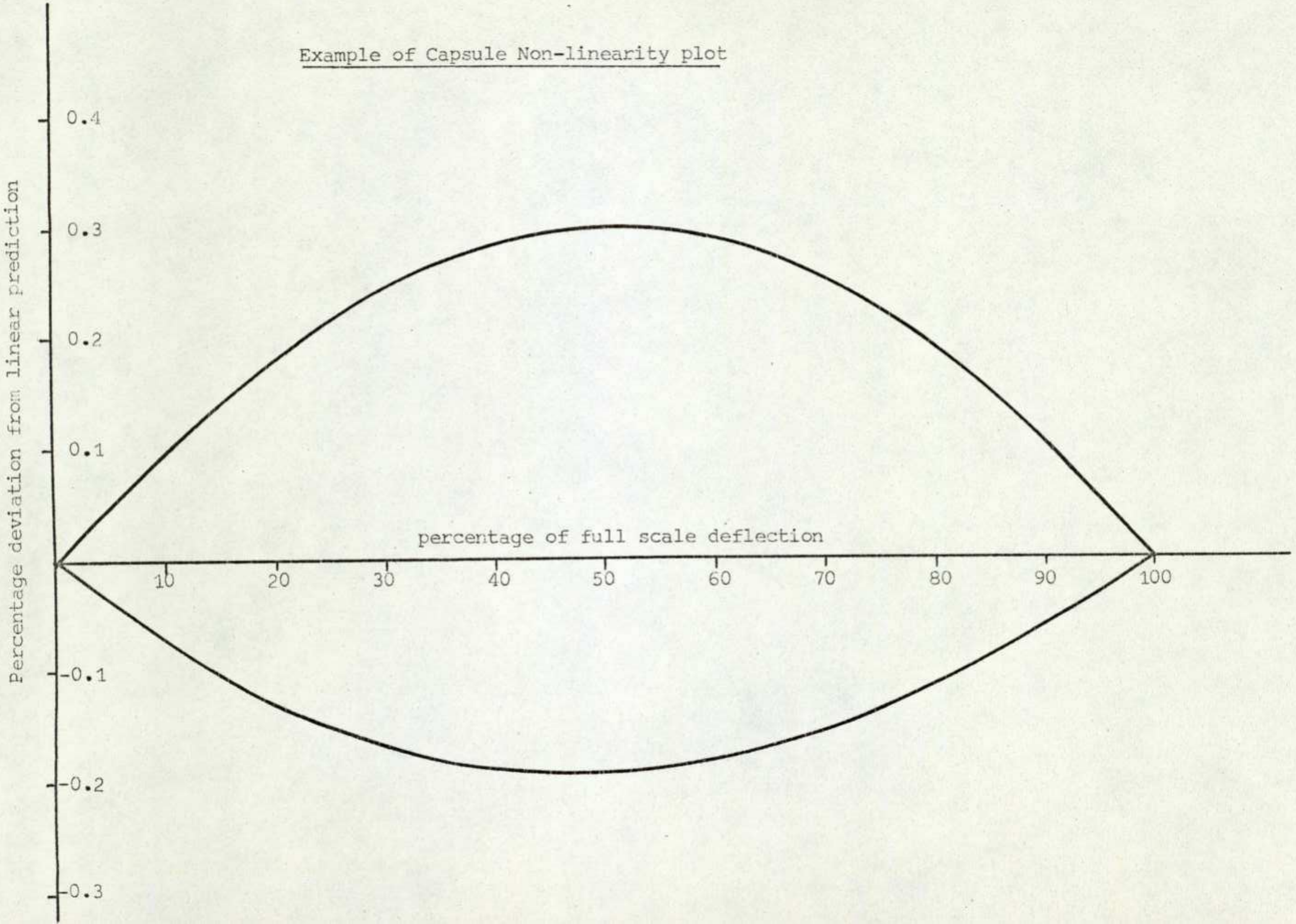

Figure 4.21 a

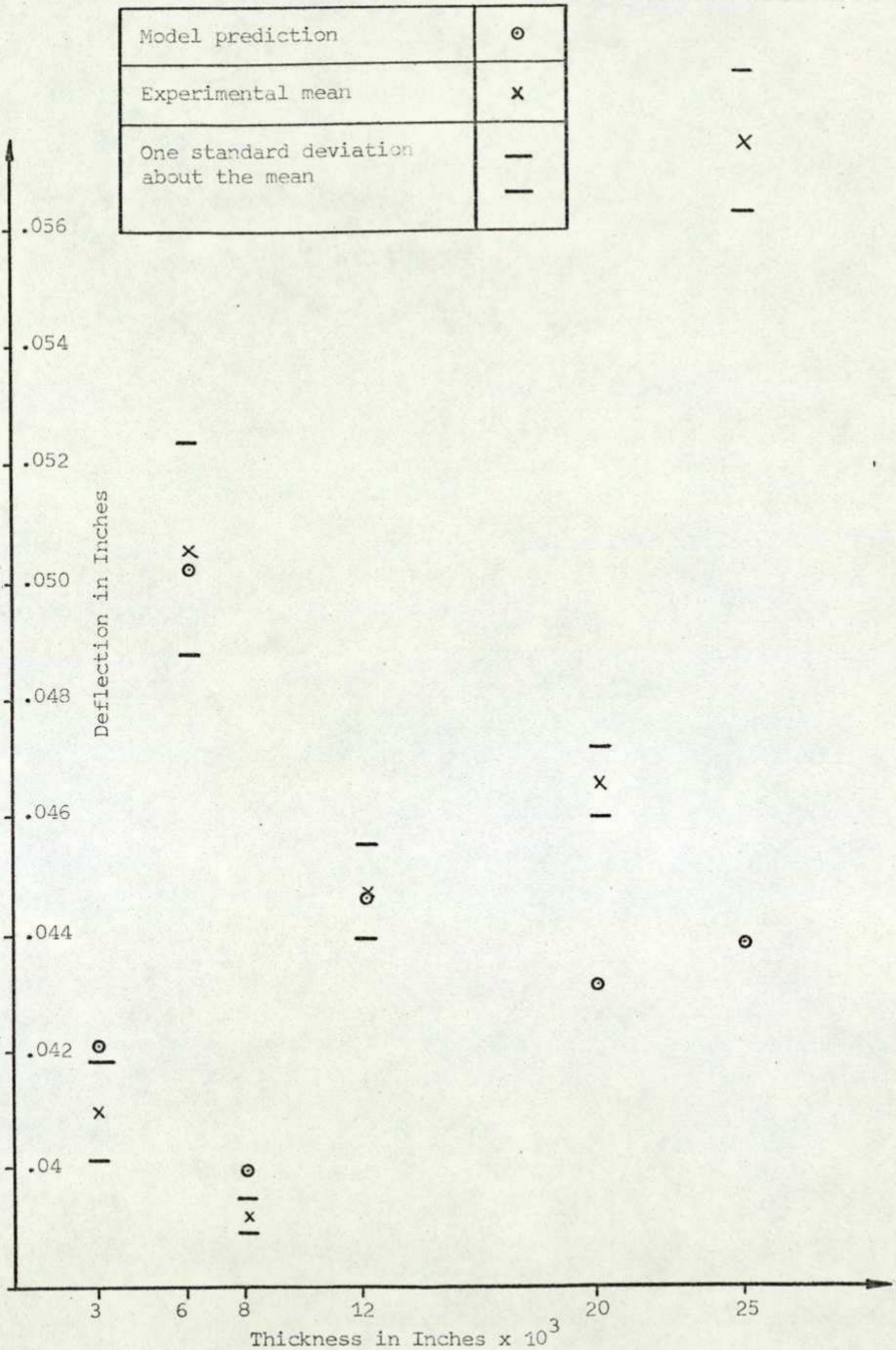

Model predictions against Experimental results for Capsule deflections used in Extension Only.

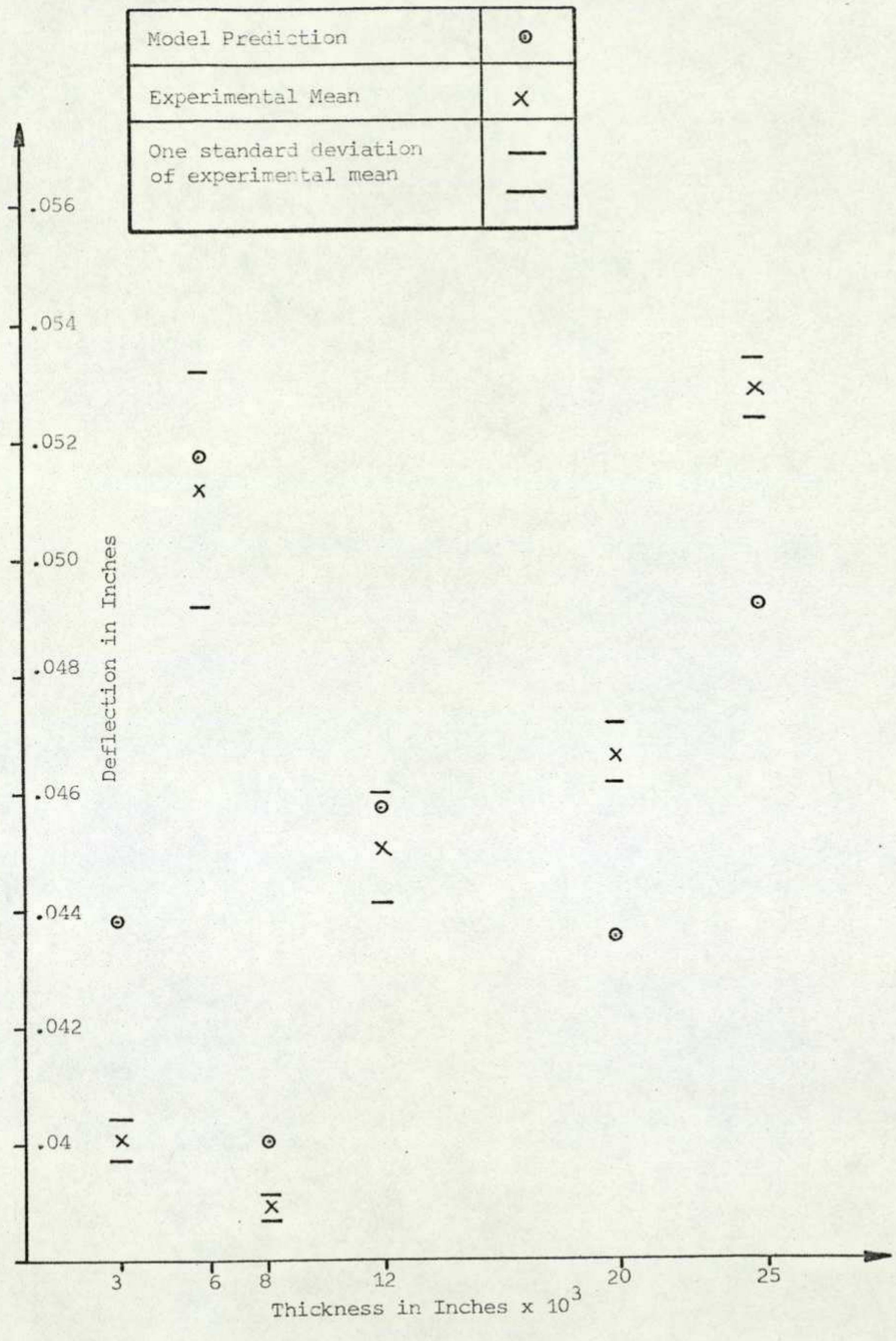

Model predictions against Experimental results for Capsule deflections used in Compression Only.

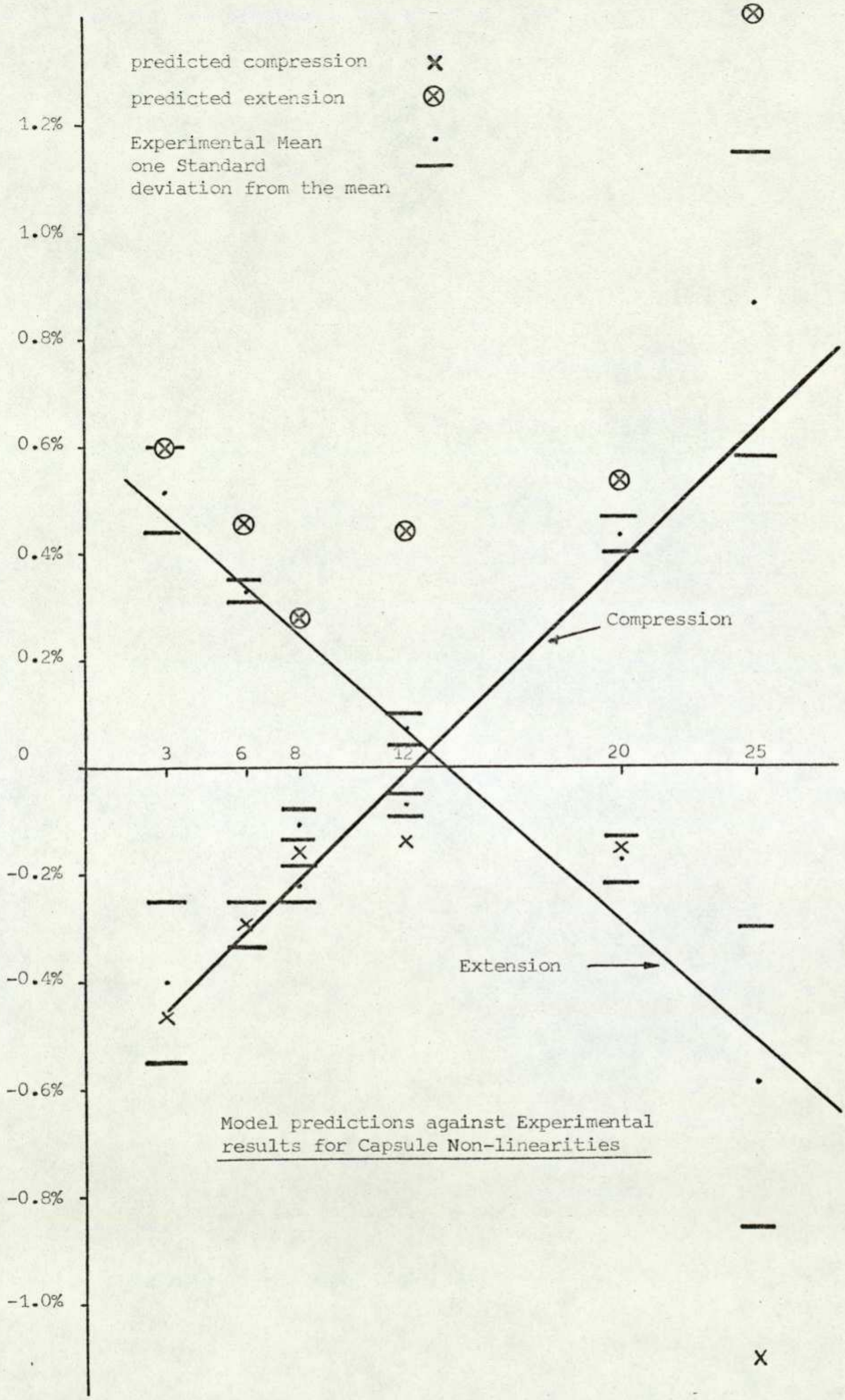

Model predictions against Experimental results for Capsule Non-linearities

4.2.8.3 Discussion of results for non-linear capsule model:

From previous discussions on the value of Young's Modulus and the variations in thickness of material along the generator, the accuracy expected must take into account the tolerances of the above parameters. From the percentage deviations of the centre deflections shown in Table 4.10, most of the comparisons give very good agreement, and some much better than could be hoped for. Assuming the profile to be accurately modelled, the very good agreement possibly arises from the trade off in choosing a slightly low value for Young's Modulus, and a higher value of thickness; as the deflection in the linear region is inversely proportional to deflection, the result would be on the high side, but as a constant value of thickness is used (that of the original blank), the actual thickness must be something less owing to stretching. As the deflection is approximately inversely proportional to deflection, the actual relationship is discussed later; the prediction is then lower, the two unpredictable effects tending to cancel one another out.

Thickness inches	(mm)	Variation of centre deflection per cent	
0.003	(.0762)	Ext.	-2.636
		Comp.	-9.3625
0.006	(.1524)	Ext.	0.6004
		Comp.	-1.077
0.008	(.2032)	Ext.	-2.0612
		Comp.	-4.486
0.012	(.3049)	Ext.	0.1344
		Comp.	-1.578
0.020	(.508)	Ext.	9.534
		Comp.	6.712
0.025	(.635)	Ext.	23.652
		Comp.	6.894

Table 4.10: Percentage deviation of predicted centre deflections of capsules

Table 4.10 is the error between predicted (W_p) and experimental (W_e) deflections based upon $\frac{(W_e - W_p)}{W_e}$ x 100 per cent.

Overall, the deflections compare very well with the theory, with the exception of the 0.025" (.625 mm) in extension, and possibly the 0.003" (0.0762 mm) in compression. The result of the 0.003" capsule is known to be in error owing to the practical problem of premature "nesting", the capsule shutting down before the end of working range. The discrepancy on the 0.025" capsule is most probably due to a breaking down of the actual theory, i.e. the shell considered is not any longer a thin shell by the assumptions stated in Chapter 3. This idea is again reinforced by the non-linearity results of Figure 4.22, although this is a much finer comparison; any appreciable difference first appears in the 0.008" predictions and gets worse as the thickness increases, owing to the sign reversal at about 0.012" and the predictions always give the same sign of maximum non-linearity in one particular direction, irrespective of the thickness.

The magnitudes of non-linearity are of the same order for experiment and theory and are therefore not entirely useless for additional work such as design. Assuming again that the reason for the non-reversal of sign is that of the breaking down of the thin shell theory, the question arises - when does a thin shell become thick?, and how is this applied to diaphragms and capsules? Referring back to Chapter 3, the terms neglected because the shell was thin were $\frac{Z}{R_\xi}$ and $\frac{Z}{R_\theta}$; being small compared to unity, the curvature term $\frac{Z}{R_\xi}$ always dominates $\frac{Z}{R_\theta}$ which can be neglected from this consideration, because the radial distance is usually much larger than half the thickness, when a practical sized centre boss is taken into account.

If we take a somewhat arbitrary figure of $\frac{Z}{R_\xi} < 0.1$ as the upper limit for thin shell theory to apply, this would make $\frac{t}{R_\xi} < 0.2$. Now listing the minimum and maximum values of $\frac{t}{R_\xi}$ for the diaphragms of the six capsules considered (Table 4.11), it can be seen that the maximum value of the $\frac{t}{R_\xi}$ ratio first goes above 0.2 for the 0.008" capsule where, in fact, the theory initially appears to break down.

	0.003"	0.006"	0.008"	0.012"	0.020"	0.025"
$t/R_\xi\vert_{max}$	0.086206	0.174	0.2777	0.348	0.617	0.584
$t/R_\xi\vert_{min}$	0.0239	0.071	0.0523	0.102	0.165	0.177

Table 4.11: Values of the maximum and minimum $\frac{t}{R_\xi}$ ratios for the capsules considered

As would be expected, these ratios increase as the thickness increases, the only exception being in the minimum value going from the 0.006" capsule to 0.008". This is simply explained because 0.003" and 0.006" capsules are made from four convolution diaphragms and the rest three convolutions. Therefore, the radius of corrugation will be larger because there are less convolutions.

When considering flat plate the curvature criterion cannot apply, so the more obvious choice of the ratio $\frac{d}{t}$ is used (the diameter to thickness ratio). For a corrugated diaphragm, strictly both criteria must be applied, although it has been stated that the $\frac{Z}{R_\theta}$ ratio may be neglected.

Again, no definite value may be put on this ratio to say when a thin diaphragm becomes a thick diaphragm, but Neuburt, ref. (32), states subjectively, "a $\frac{d}{t}$ ratio of 20 is a thick diaphragm, and a thin diaphragm will probably have a $\frac{d}{t}$ ratio in the neighbourhood of 200." It is therefore pertinent to look at the $\frac{d}{t}$ ratios for the six capsules:

Thickness inches	(mm)	$\frac{d}{t}$
0.003	(.0762)	827
0.006	(.1524)	413.5
0.008	(.2054)	310.125
0.012	(.3048)	206.75
0.020	(.508)	124.05
0.025	(.635)	99.24

It is interesting to note that the last two are below the 200 limit, but not as low as 20. Then, from the above results and observations, it may be postulated that:

(i) The curvature/thickness, affects the non-linearity measurements

(ii) The diameter/thickness, affects the overall deflection

If this is the case for (ii), the $\frac{d}{t}$ ratio for thin shell theory still to be appropriate would appear to be lower than the 200 region, because it seems that the 0.025" capsule is just about the limit. Hence, practical limits may be set on the application of the models.

4.3 Attempted model additions and improvements

From a study of the previous chapters it becomes evident that certain assumptions and approximations, made at the time for ease, of formulation and clarification may not be justified when looking for a model of high integrity. To these ends, three areas of improvement are looked at:

4.3.1: The building in to the basic thin shell equations an allowance for sharp curvature of the diaphragm (or capsule) profile. This is a particular problem when the diaphragm material thickness is increased and the diaphragm profile is not, thus increasing the pressure range.

4.3.2: Generally, the levels of strain are very small and can be neglected in comparison with unity, but in comparing two models, certain discrepancies appeared, albeit at high stress levels, which could be explained by including some form of strain update.

4.3.3: The geometric description of the diaphragm profile can be adequately described by circles and straight lines, but mathematically this is not continuous in the first and second deviations and a different formulation is used to investigate the inadequacy.

4.3.1 Attempted curvature modification

From the foregoing experimental study of capsules, it appears that an improvement to the model could be achieved by programming in an allowance for curvature, i.e. by not neglecting the $\frac{Z}{R_\xi}$ and $\frac{Z}{R_\theta}$ in the terms $\left(1 - \frac{Z}{R_\xi}\right)$ and $\left(1 - \frac{Z}{R_\theta}\right)$.

Referring back to equations (3.9) as the strain expressions used for forming the stresses and not (3.10), we have:

$$\sigma_\xi = \frac{E}{(1-\nu^2)}\left(\frac{\varepsilon_1}{1 - Z/R_\xi} - \frac{Z}{1 - Z/R_\xi}\chi_\xi + \frac{\nu\,\varepsilon_2}{1 - Z/R_\theta} - \frac{\nu\,Z}{1 - Z/R_\theta}\chi_\theta\right) \ldots\ldots \quad (4.1)$$

$$\sigma_\theta = \frac{E}{(1-\nu^2)}\left(\frac{\varepsilon_2}{1 - Z/R_\theta} + \frac{\nu\,\varepsilon_1}{1 - Z/R_\xi} - Z\left(\frac{\chi_\theta}{1 - Z/R_\theta} + \frac{\nu\,\chi_\xi}{1 - Z/R_\xi}\right)\right) \ldots\ldots \quad (4.2)$$

Substituting into equations (3.7):

$$N_\xi = \int_{-t/2}^{t/2} \frac{E}{1-\nu^2}\left[\frac{(1 - Z/R_\theta)}{(1 - Z/R_\xi)}(\varepsilon_1 - Z\chi_\xi) + \nu(\varepsilon_2 - Z\chi_\theta)\right] dZ \ldots\ldots \quad (4.3a)$$

$$N_\theta = \int_{-t/2}^{t/2} \frac{E}{1-\nu^2}\left[\frac{(1-Z/R_\xi)}{(1-Z/R_\theta)}\,(\varepsilon_2 - Z\chi_\theta) + \nu(\varepsilon_1 - Z\chi_\xi)\right] dZ \;\ldots\; (4.3b)$$

$$M_\xi = \int_{-t/2}^{t/2} \frac{E}{1-\nu^2}\left[\frac{(1-Z/R_\theta)}{(1-Z/R_\xi)}\,(\varepsilon_1 - Z\chi_\xi) + \nu(\varepsilon_2 - Z\chi_\theta)\right] ZdZ \;..\; (4.3c)$$

$$M_\theta = \int_{-t/2}^{t/2} \frac{E}{1-\nu^2}\left[\frac{(1-Z/R_\xi)}{(1-Z/R_\theta)}\,(\varepsilon_2 - Z\chi_\theta) + \nu(\varepsilon_1 - Z\chi_\xi)\right] ZdZ \;..\; (4.3d)$$

The integrations indicated in the foregoing expressions are extremely cumbersome to perform, thus it is appropriate at this point to make the assumption that $\frac{Z}{R_{\xi,\theta}}$ is less than unity, so that an expansion of the type

$$\left(1 - \frac{Z}{R}\right)^{-1} = 1 + \frac{Z}{R} - \left(\frac{Z}{R}\right)^2 + \;\ldots\ldots\ldots\ldots$$

may be carried out. We rejected the fourth term and high order terms: this is not so restrictive on the ratio $\frac{Z}{R_{\xi,\theta}}$ as was Love's thinness assumption.

Performing the integrations gives:

$$N_\xi = \frac{Et}{1-\nu^2}\left[\varepsilon_1 + \nu\varepsilon_2 + \frac{t^2}{12}\left(\frac{1}{R_\xi} - \frac{1}{R_\theta}\right)\left(\chi_\xi - \frac{\varepsilon_1}{R_\xi}\right)\right] \;\ldots\ldots\ldots\; (4.4a)$$

$$N_\theta = \frac{Et}{1-\nu^2}\left[\varepsilon_2 + \nu\varepsilon_1 - \frac{t^2}{12}\left(\frac{1}{R_\xi} - \frac{1}{R_\theta}\right)\left(\chi_\theta - \frac{\varepsilon_2}{R_\theta}\right)\right] \;\ldots\ldots\ldots\; (4.4b)$$

$$M_\xi = D\left[\chi_\xi + \nu\chi_\theta + \left(\frac{1}{R_\xi} - \frac{1}{R_\theta}\right)\varepsilon_1\right] \;\ldots\ldots\ldots\ldots\ldots\ldots\ldots\ldots\ldots\; (4.4c)$$

$$M_\theta = D\left[\chi_\theta + \nu\chi_\xi - \left(\frac{1}{R_\xi} - \frac{1}{R_\theta}\right)\varepsilon_2\right] \;\ldots\ldots\ldots\ldots\ldots\ldots\ldots\ldots\ldots\; (4.4d)$$

The notation can now be "tidied up" in the same way as (3.13) and also replace $\frac{1}{R_\xi} - \frac{1}{R_\theta}$ by τ, i.e.

$$M_\xi = D\left[\chi_\xi + \nu\chi_\theta + \tau\ \varepsilon_{\xi m}\right] \quad \text{(4.5a)}$$

$$M_\theta = D\left[\chi_\theta + \nu\chi_\xi - \tau\ \varepsilon_{\theta m}\right] \quad \text{(4.5b)}$$

The strains $\varepsilon_{\xi m}$ and $\varepsilon_{\theta m}$ can now be expressed in terms of N_ξ, N_θ, M_ξ, M_θ, etc.

$$\varepsilon_{\xi m} = \frac{K_1}{Et}\left[W_2 N_\xi - \nu N_\theta - D\tau(W_2\chi_\xi + \nu\chi_\theta)\right] \quad \text{(4.6a)}$$

$$\varepsilon_{\theta m} = \frac{K_1}{Et}\left[W_1 N_\theta - \nu N_\xi - D\tau(W_1\chi_\theta + \nu\chi_\xi)\right] \quad \text{(4.6b)}$$

where

$$K_1 = \frac{(1 - \nu^2)}{\left(1 - \frac{t^2\tau^2}{12} - \nu^2\right)} ; \quad W_2 = 1 + \frac{t^2\tau}{12R_\theta} ; \quad W_1 = 1 - \frac{t^2\tau}{12R_\xi}$$

In the attempt to formulate two simultaneous differential equations by substituting these above expressions (4.5 a,b) and 4.6 a,b) into the equations of equilibrium and compatability, extreme difficulty is found owing to the "cross dependence", i.e. bending and direct strain appear in the bending resultant and vice-versa. This would result in shear function and rotation having both first and second deviations on the left-hand side of each equation. A new solution Algorithm would, therefore, be required to solve the set of equations: at this point it was decided to try to make approximations to the complete solution, but any attempt at this approach caused a breakdown in the iterative procedure and the problem failed to converge.

4.3.2 Strain update

Figure 4.23 shows the comparison of F. Abdullah's (see Chapter 2) model for a non-linear diaphragm with the programmed equations of Billington's, ref. (27). To a certain extent the problem is academic because the pressures which are being applied to the diaphragm would take it well into the plastic region. But bearing this in mind it does illustrate the large difference between the two predictions at these high

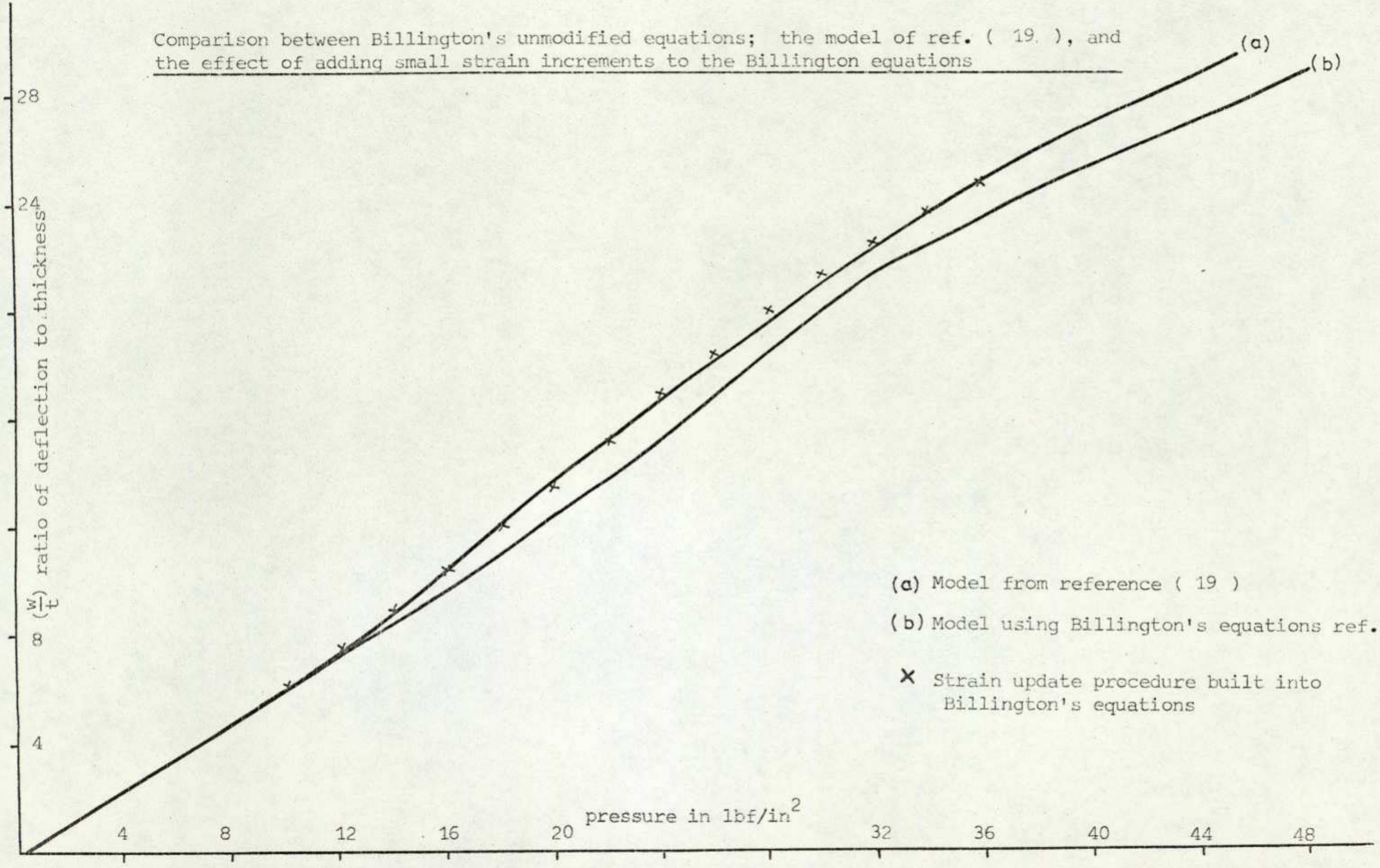

Comparison between Billington's unmodified equations; the model of ref. (19), and the effect of adding small strain increments to the Billington equations

Figure 4.23

pressures. It was therefore decided to attempt to build a strain update routine into the finite difference program to see if this was the reason for the discrepancies.

This work took the form of continually making minor strain adjustments to the program until its performance was somewhere close to the F. Abdullah curve. It is not proposed to go through and catalogue the whole development, but just to describe the final resulting program, how it works, and the numerical changes.

Referring back to the equations of Chapter 3, section 3.3, α is no longer assumed constant and unity, but is updated by $\alpha = \alpha_o(1 + \varepsilon_\xi)$; also the radial distance $r = r_o(1 + \varepsilon_o)$.

Working through the program the initial values of α_i and r_i and ϕ_i are all set equal to undeformed shell:

$$\alpha_i = \alpha_{oi} = 1; \quad r_i = r_{oi}; \quad \phi_i = \phi_{oi}.$$

Then the original step length ds, or now more correctly $d\xi$, is stored and the working step length at any i^{th} point $ds = \alpha_i d\xi$. The constants C1, C2, C3 and C4 at the i^{th} point now become:

$$C1 = \frac{\text{Cos }\phi}{r} + \frac{3}{t}\frac{dt}{ds} + \frac{1}{\alpha}\frac{d\alpha}{ds}$$

$$C2 = \left(\frac{\text{Cos }\phi}{r}\right)^2 - \nu\left(\frac{\text{Cos }\phi}{r}\frac{3}{t}\frac{dt}{ds} - \frac{\text{Sin }\phi}{r\,r1} - \frac{\text{Cos }\phi}{r}\frac{d\alpha}{\alpha\, ds}\right)$$

$$C3 = \left(\frac{\text{Cos }\phi}{r} - \frac{1}{t}\frac{dt}{ds} - \frac{1}{\alpha}\frac{d\alpha}{ds}\right)$$

$$C4 = \left(\left(\frac{\text{Cos }\phi}{r}\right)^2 - \nu\left(\frac{\text{Sin }\phi}{r.r1} + \frac{\text{Cos }\phi}{r}\frac{1}{t}\frac{dt}{ds} + \frac{\text{Cos }\phi}{r}\frac{1}{\alpha}\frac{d\alpha}{ds}\right)\right)$$

$$\text{where} \quad \left(\frac{d\alpha}{ds}\right)_i = \frac{\alpha_{i+1} - \alpha_{i-1}}{2\alpha_i d\xi}$$

and if the other terms where α appears, and does not cancel out, then it must be taken into account.

The strain update is achieved by adjusting the values of r_i, ϕ_i and α_i accordingly from the calculation of the stress resultants and displacements, hence the updated values really apply to the pressure of the previous iteration, therefore for this method to be of much use the pressure steps must be kept small. After the values of shear function and rotation are found, ϕ is updated by:

$$\phi_i = (\phi_o + \beta)_i .$$

Then N_θ and N_ξ are found with

$$N_\xi\Big|_i = \frac{\text{Cos } \phi}{r} \psi_i + \frac{\text{Sin } \phi}{r} (rV)_i .$$

This is not the same as Equation (3.), which is an approximation caused by expanding Cos ϕ and Sin ϕ. The two mid-surfacal strains are then found ($\varepsilon_{\xi m}$ and $\varepsilon_{\theta m}$), from which the horizontal displacement is simply given by $\{r_o \; \varepsilon_{\theta m}\}$ and $\alpha_i = 1 + \varepsilon_{\xi m}$

$$r_i = (r_o + u)_i$$

The pressure is then increased and the iteration process re-started. The main problems arise when numerically implementing this update; irrespective of the size of the pressure step the iteration of $\delta\psi$ and $\delta\beta$ would not converge, i.e. tend to zero except for very small pressures. From reference to elastic instability, the shear function is the cause of any inability as the rotation is generally well behaved.

Therefore, a "boot-strap" type model was proposed where the rotation only was reduced to a guess value and an error, the shear function was solved for directly as in the linear model and modified at each iteration by the changing values of β. This modification was generally able to overcome the breakdown of convergence criterion, and was also fairly easy to introduce, owing to the use of subroutines where only the formal parameters are changed.

The example plotted in Figure 23 and shown in Table 4.12 shows how each pressure point converged with three iterations using this method; the values of β, $\delta\beta$ and ψ are for an arbitrary point along the diaphragm.

β	(Exponent)	δβ	(Exponent)	ψ	(Exponent)	Pressure lbf/in^2	W/t
0.4006	(-1)	0.4848	(-2)	-0.1487	(1)	7.0	4.36
0.4006	(-1)	0.2022	(-4)	-0.1477	(1)		
0.4008	(-1)	0.1809	(-8)	-0.1477	(1)		
0.4489	(-1)	0.4813	(-2)	-0.1703	(1)	8.0	5.00
0.4491	(-1)	0.2144	(-4)	-0.1693	(1)		
0.4969	(-1)	0.4778	(-2)	-0.1927	(1)	9.0	5.64
0.4971	(-1)	0.2283	(-4)	-0.1916	(1)		
0.4971	(-1)	0.2259	(-8)	-0.1916	(1)		
0.5446	(-1)	0.4744	(-2)	-0.2159	(1)	10.0	6.3
0.5448	(-1)	0.2442	(-4)	-0.2148	(1)		
0.5448	(-1)	0.2553	(-8)	-0.2148	(1)		

Table 4.12

With such an update the geometry is effectively being altered by changing r and ϕ, therefore the step length is being changed along the generator by the addition of radial strain. Therefore the general finite difference assumptions:

$$\frac{dy}{dx} = \frac{Y_{i+1} - Y_{i-1}}{2\Delta X} \quad \ldots\ldots\ldots\ldots\ldots\ldots\ldots\ldots\ldots \quad (4.10a)$$

$$\frac{d^2y}{dx^2} = \frac{Y_{i+1} - 2Y_i + Y_{i-1}}{\Delta X^2} \quad \ldots\ldots\ldots\ldots\ldots\ldots\ldots\ldots \quad (4.10b)$$

are not valid because the step length (in this case ΔX) is not constant. To allow for changes in step-length, the general deviation of finite differences must be applied which takes into consideration unequal intervals between the mesh points.

Finite derivation for equal intervals

Consider a curve where the step length between the (i-1)th and ith points is ΔX_1 and between the ith and i+1th point is ΔX_2 (Figure 4.24):

$$\text{Let } \Delta X = \Delta X_1 \qquad \text{where } j = \frac{\Delta X_2}{\Delta X_1}$$
$$\text{then } j\Delta X = \Delta X_2$$

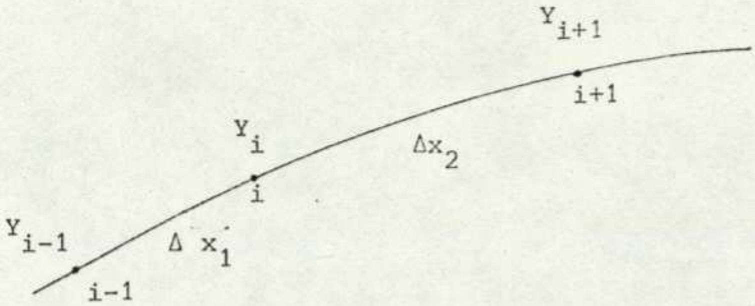

Figure 4.24: Unequal step lengths

Now, expanding the Y_{i+1} and Y_{i-1} values as two Taylor expansions,

$$Y_{i+1} = Y(X + j\,\Delta X) = Y_i + j\,\Delta X Y'_i + \frac{j^2}{2}(\Delta X)^2 Y''_i + \frac{j^3}{6}(\Delta X)^3 Y'''_i \quad \ldots\ldots$$

$$Y_{i-1} = Y(X - \Delta X) = Y_i - \Delta X Y'_i + \frac{(\Delta X)^2}{2} Y''_i - \frac{(\Delta X)^3}{6} Y'''_i \quad \ldots\ldots\ldots\ldots$$

To obtain the first derivative we could easily subtract Y_{i-1} from Y_{i+1} which would then simply express $\frac{dy}{dx}$ as:

$$\frac{dy}{dx} = \frac{Y_{i+1} - Y_{i-1}}{(1+j)\Delta X}$$

but this would have an error term associated with the 2nd derivative. It is therefore better to eliminate Y_i by multiplying Y_{i-1} by j^2 and subtracting:

$$Y_{i+1} = Y_i + j\,\Delta X\, Y'_i + \frac{j^2}{2}\Delta X^2\, Y''_i + \frac{j^3}{6}\Delta X^2\, Y'''_i + \ldots\ldots$$

$$j^2\, Y_{i-1} = j^2\, Y_i - j^2\,\Delta X\, Y'_i + \frac{j^2}{2}\frac{\Delta X^2}{2}\, Y''_i - \frac{j^2}{6}\,\Delta X^3\, Y'''_i - \ldots\ldots$$

$$Y_{i+1} - j^2\, Y_{i+1} = (1-j^2)Y_i + j\,\Delta X(1+j)Y_i + j^2\,\frac{\Delta X^3}{6}\,(1+j)Y_i$$

therefore,

$$Y'_i = \frac{Y_{i-1} - j^2\, Y_{i-1} - (1-j^2)Y_i}{j(1+j)\Delta X} - \frac{\Delta X\, j}{6}\, Y'''_i$$

where

$$-\frac{\Delta X\, j}{6}\, Y'''_i + \text{higher order terms} = \text{error}$$

and $$\frac{dy}{dx} \doteq \frac{1}{j(1+j)} \left[\frac{Y_{i+1} - j^2 Y_{i-1} - (1-j^2)Y_i}{\Delta X}\right] \quad \ldots\ldots\ldots\ldots\ldots \quad (4.11)$$

Similarly, to find the 2nd derivative, Y'_i is eliminated by multiplying Y_{i-1} by j and adding:

$$Y_{i+1} + j\, Y_{i+1} = Y_i(1+j) + \frac{j}{2}(j+1)(\Delta X)^2\, Y''_i + \frac{j}{6}(j^2+1)Y'''_i \quad (\Delta X)^3$$

$$Y''_i = \frac{Y_{i+1} - (j+1)Y_i + j\, Y_{i+1}}{\Delta X^2}\left(\frac{2}{j(j+1)}\right) - \left(\frac{j-1}{3}\right)\Delta X\, Y'''_i$$

where

$$-\frac{(j-1)}{3}\,\Delta X\, Y'''_i = \text{error}$$

therefore

$$\frac{d^2y}{dx^2} \doteq \left[\frac{Y_{i+1} - (j+1)Y_i + j\, Y_{i-1}}{\Delta X^2}\right]\frac{2}{j(j+1)} \quad \ldots\ldots\ldots\ldots\ldots \quad (4.12)$$

For a one-to-one step length correspondence, i.e. $j = 1$, the expressions equal Equations (4.10a) and (4.10b).

Returning to the problem where in the general form the first equation =

$$\beta'' + C1\,\beta' + C2\,\beta + C3\,\psi = C4$$

then in finite difference from:

$$a_i\,\beta_{i+1} + b_i\,\beta_i + C_i\,\beta_{i-1} + d_i\,\psi_i = K_i$$

where the coefficients are given by Equations (3.30b).

If the expressions (4.11) and (4.12) are used instead of (4.10a) and (4.10b), then

$$a_i = \left[\frac{2}{(j+1)j} + \frac{C1\ ds}{j(1+j)}\right]$$

$$b_i = \left[ds\ C2 - \frac{2}{j\ ds} - \frac{C1(1-j^2)}{j(1+j)}\right]$$

$$c_i = \left[\frac{2}{1+j} - \frac{C1\ j\ ds}{(1+j)}\right]$$

d_i and K_i are unchanged.

A similar expression may be derived for the shear function equation. In the actual program the j parameter at each i^{th} point is obtained from $\left({}^{\alpha_{i+1}}\!\!\diagup_{\alpha_i}\right)$.

Iteration still breaks down at 38 lbf/in^2, well above any particular application.

4.3.3 Cornu spiral

In Chapter 3 the geometric construction of the general corrugated diaphragm profile was taken to be a piece-wise continuous curve of circular arcs and straight lines. The best reason for choosing this method was that it described, simply and adequately, the actual example diaphragms examined. The flexibility of the approach was the main advantage for the circle and straight method, but another important reason is the consideration of the dependent variable, in this case S, the general distance along the curve. For an analytic function in which $y = f(r)$, the distance along the curve is given by

$$S = \int_o^r \left(1 + \left(\frac{dy}{dr}\right)^2\right) dr \quad \ldots\ldots\ldots\ldots\ldots\ldots\ldots \quad (4.13)$$

and, in general, for any configuration other than circles and straight lines, this Integration (4.13) is not possible except by numerical means. From S the step length ds is then derived: this has been shown to be a very sensitive parameter and any possible discrepancy at this early stage needs to be avoided if possible. An added complexity arises with a $y = f(r)$ formulation, that is, in expressing the curvature (k) (or the radius of curvature $R_\xi = 1/k$).

Where $k = \dfrac{\dfrac{dy^2}{dr^2}}{\left(1 + \left(\dfrac{dy}{dr}\right)^2\right)^{3/2}}$, this expression may need to be numerically solved. Therefore it appears that the piece-wise description, using circles and straight lines, is an ideal choice, but from the mathematical point of view the description is not a good one, even if it can be shown numerically to be adequate.

The reason for this is the sharp discontinuities in the curvature along the generator of the diaphragm, both in magnitude and sign, as illustrated in Figure 4.25.

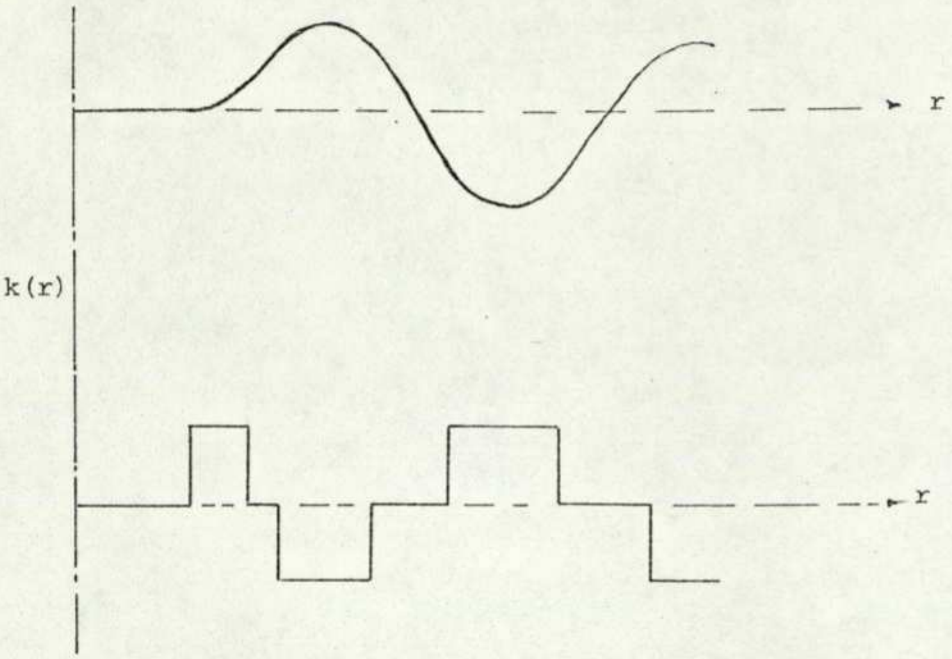

Figure 4.25: Variation of curvature for a diaphragm profile based upon circles and straight lines

No attempt was made to smooth out these abrupt changes in curvature, as it did not appear necessary, although smoothing functions are used by Wildhack, Lloyd and Dressler, ref. (11).

To investigate the possibility of any adverse effects caused by the discontinuities in curvature, a completely different formulation of profile was used. This method makes the discontinuities slightly less sharp, by using a straight line curvature variation instead of a constant value, giving a variation from the maximum value at the peaks to zero where the sign change occurs.

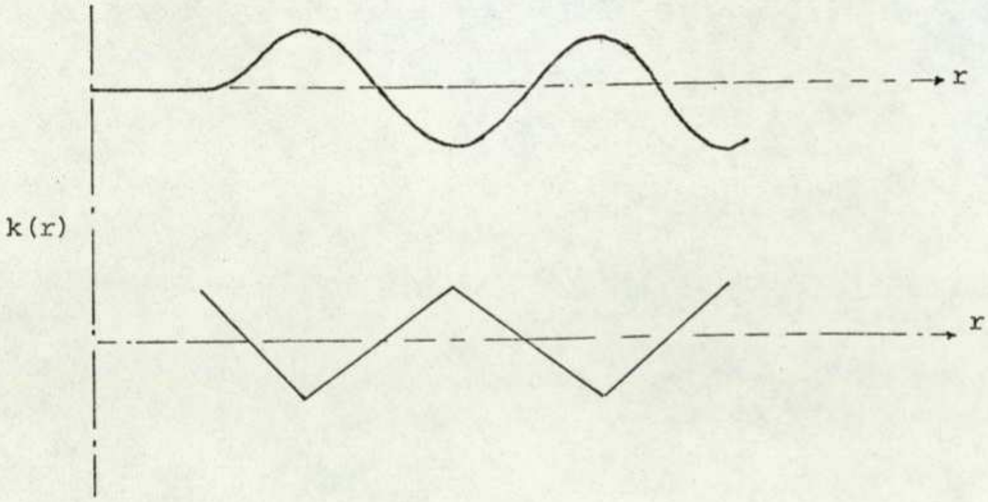

Figure 4.26: Variation of curvature for a diaphragm profile based upon a Cornu Spiral

An abrupt change of direction does occur at the peaks, but the general shape is less severe than the first case.

The problem with the ordinary approach is that the variation of curvature has been shown to vary with the actual curve if the first and second derivations are known!

What is required is a formula with x and y on the left-hand side and some function of k on the right-hand side. A formula has been established by the computer-aided design research group at Cambridge, ref. (33). This involves a point moving in two-dimension space and considering its velocity at any particular time.

The position of x and y as functions of time may be stated as:

$$x(t) = x_o + \int_o^t V(\sigma)\,\mathrm{Cos}\left[\theta_o + \int_o^\sigma V(t)k(t)dt\right]d\sigma \quad \dots\dots\dots\dots \quad (4.14a)$$

$$y(t) = y_o + \int_o^t V(\sigma)\,\mathrm{Sin}\left[\theta_o + \int_o^\sigma V(t)k(t)dt\right]d\sigma \quad \dots\dots\dots\dots \quad (4.14b)$$

where x_o, y_o = Starting co-ordinates

$x(t)$, $y(t)$ = Co-ordinates after a period time

$V(t)$ = Linear velocity

$k(t)$ = Curvature as a function of time

θ_o = Initial angle between the tangent to the curve and the X axis

σ = Dummy variable

For the situation of a plain curve, the time variable is unnecessary; also it is useful to substitute the variable $\omega(t) = V(t)k(t)$ and keep the velocity V constant V_o.

As an example which can be solved analytically, consider a point moving with constant angular velocity $\omega(t) = \omega_o$.

Then

$$x(t) = x_o + V_o \int_o^t \mathrm{Cos}\left[\theta_o + \int_o^\sigma \omega_o\, dt\right]d\sigma$$

$$y(t) = y_o + V_o \int_o^t \mathrm{Sin}\left[\theta_o + \int_o^\sigma \omega_o\, dt\right]d\sigma$$

becomes

$$x(t) = x_o + V_o \int_o^t \text{Cos }(\theta_o + \omega_o\sigma)d\sigma$$

$$y(t) = y_o + V_o \int_o^t \text{Sin }(\theta_o + \omega_o\sigma)d\sigma$$

$$\frac{x - x_o}{V_o} = \frac{1}{\omega_o}\left[\text{Sin }(\theta_o + \omega_o t) - \text{Sin }\theta_o\right]$$

$$\frac{y - y_o}{V_o} = -\frac{1}{\omega_o}\left[\text{Cos }(\theta_o + \omega_o t) - \text{Cos }\theta_o\right]$$

These two equations may be put in the form:

$$\left[x - \left(x_o - \frac{V_o}{\omega_o}\text{ Sin }\theta_o\right)\right]^2 + \left[y - \left(y_o + \frac{V_o}{\omega_o}\text{ Cos }\theta_o\right)\right]^2 = \left(\frac{V_o}{\omega_o}\right)^2$$

in which it is convenient to put $V_o = 1$ giving a circle of radius $R = \frac{1}{\omega_o}\left(\frac{1}{k_o}\right)$ centred on $x_o = R \text{ Sin } \theta_o$, $y + R \text{ Cos } \theta_o$.

The other simple case which could have been studied was $\omega(t) = 0$: this would have resulted in a straight line, i.e. infinite radius of curvature.

If these two examples, $\omega(t) = \omega_o$ (constant and $\omega(t) = 0$, are combined, it is possible to construct the curvature pattern of Figure 4.25. Now taking the work a step further and considering a constant value of $\omega(t)$ superimposed with a linearity varying value in the time domain, i.e.

$\omega(t) = \omega_o + mt$, (cf. $y = mx + C$)

gives a straight line of gradient m on the curvature graph (Figure 4.26).

Substituting in expressions (4.14a) and (4.14b) gives:

$$\frac{x - x_o}{V_o} = \int_o^t \text{Cos}\left(\theta_o + \omega_o\sigma + \frac{m\,\sigma^2}{2}\right)d\sigma \quad \ldots\ldots\ldots\ldots\ldots\ldots \quad (4.15a)$$

$$\frac{y - y_o}{V_o} = \int_o^t \text{Sin}\left(\theta_o + \omega_o\sigma + \frac{m\,\sigma^2}{2}\right)d\sigma \quad \ldots\ldots\ldots\ldots\ldots\ldots \quad (4.15b)$$

These equations can be solved analytically but are very complex, involve Fresnel integrals and are probably best solved numerically. This straight line curvature profile (Figure 4.27) when integrated out gives a curve known as a Cornu Spiral.

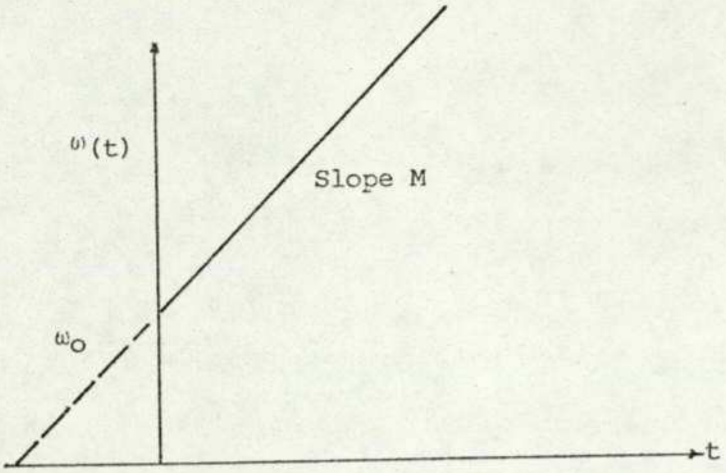

Figure 4.27: Curvature derivation of a Cornu Spiral

Thus the problem of providing a curve given the starting point and radius of curvature, knowing its variation (linear), would appear to be solved, but this is not so - the end point is a variable and therefore must be controlled.

Basically, a diaphragm profile constructed using Cornu Spirals can be made in a piece-wise fashion going from a peak to a trough, starting and finishing horizontally (hence θ_o = zero) with the same absolute value of radius of curvature.

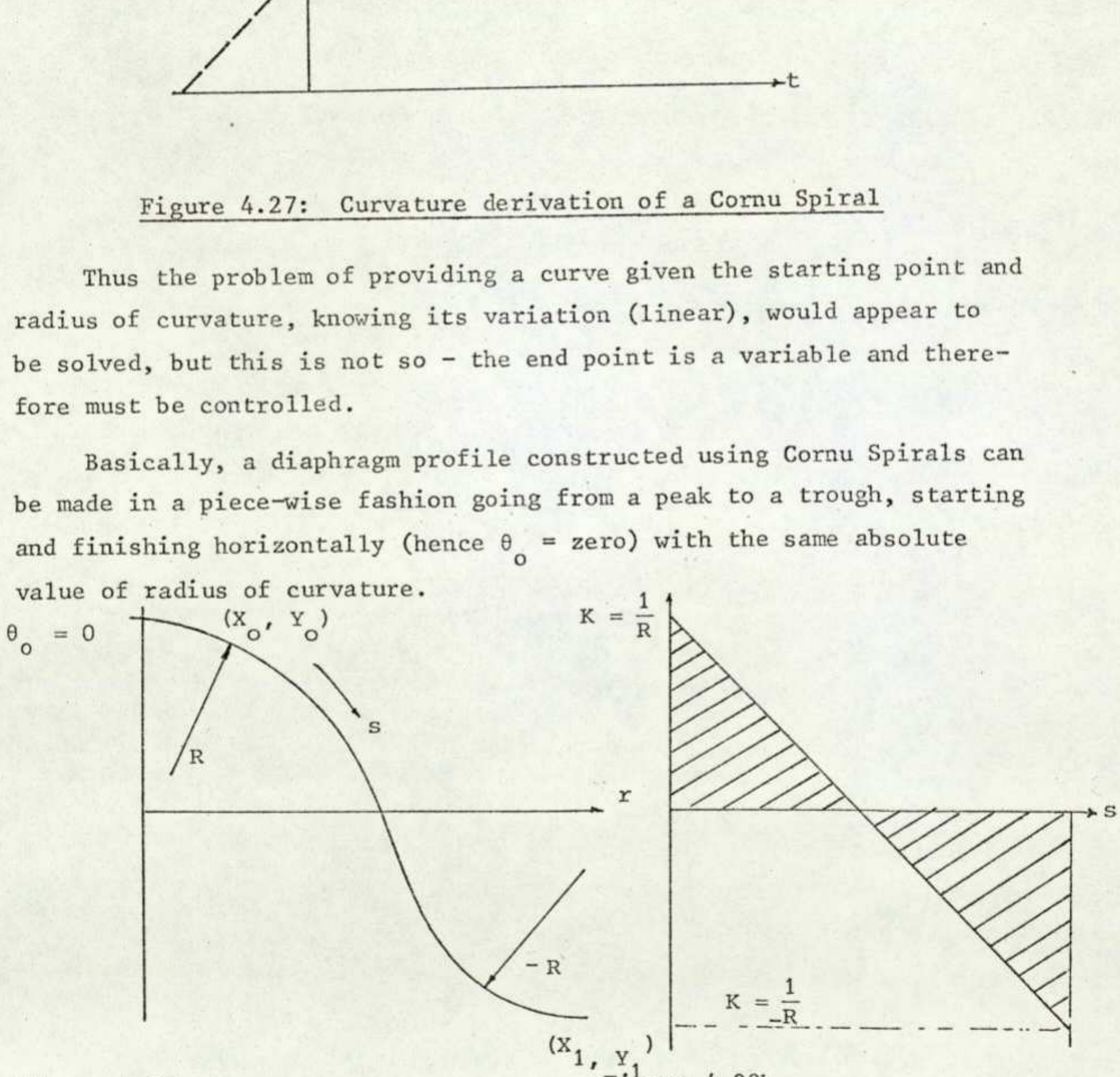

Figure 4.28a

Figure 4.28b

Figure 4.28: Computational representation of the Cornu Spiral

It can be shown that: "The angle the tangent turns through in tracing out the curve (x_o, y_o) to (x_1, y_1) is the area under the $\omega(t)$ profile between these two points". Thus, if the curve starts with θ_o = zero, the triangles must be equal in area in Figure 4.28b for the curve's tangent to end horizontal, therefore requiring the same radius of curvature at peak and trough; this is a limitation of the method, in this form. The time variable is replaced by the distance travelled along the curve, which becomes the horizontal axis of the curvature plot, Figure 4.28b.

The controllable variables which are adjusted so that the curve ends up at x_1, y_1 are then R and S (the total distance). Therefore another limitation is added to this formula; the actual radius of curvature cannot be stated, only the starting points (x_o, y_o) and (x_1, y_1). This is achieved by putting $\omega_o = 1/R$ and $m = \frac{2/R}{S_T}$ and using an optimisation routine based upon ratios to find the desired values of R and S_T.

A diaphragm profile may then be specified by only three parameters, namely, the height of corrugation and wavelength giving (x_o, y_o) and (x_1, y_1) and the number of corrugations. This produces a very limited but complete diaphragm profile which finds its own radius of curvature at the peaks and troughs, which is, of course, only the minimum value which varies linearly to infinite and then back to a minimum negative value.

A diaphragm was modelled using the linear model with the following dimensions: height of corrugation = 0.05" (1.27 mm)
wavelength = 0.24" (6.096 mm)
number of corrugation = 4.

Material thickness = 0.007" (0.1778 mm), and by the Cornu Spiral method the minimum value of radius of corrugation came out as 0.055826" (1.418 mm). The sensitivity of this particular diaphragm came to 3.375×10^{-3} inches/ lbf/in^2 (1.244×10^{-2} mm/KPa). The profile and its deflected shape is shown in Figure 4.29a. A similar profile was simulated using the original method of circles and straight lines, using 0.055826" as the radius of curvature, all other parameters and dimensions being identical. The profile is shown in Figure 4.29b and had a sensitivity of 3.53×10^{-3} inches/ lbf/in^2 (1.302×10^{-2} mm/KPa) about a 4 to 5 per cent difference. The result is consistent with Andreeva, ref. (10), which states that saw-tooth profiles of the same overall dimensions as a sinusoidal profile are more sensitive but have a higher non-linearity. Other than centre deflection, the differences in the stresses induced and horizontal

Figure 4.29

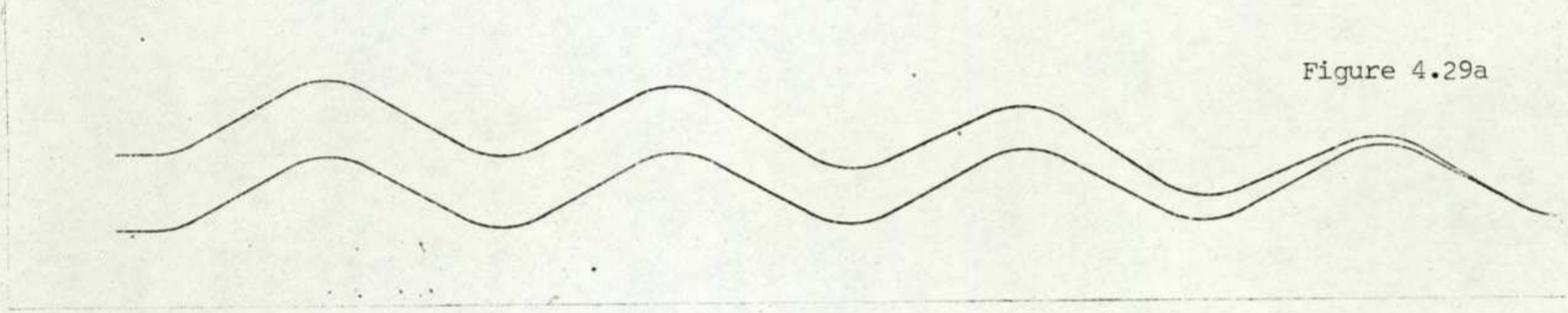

Figure 4.29a

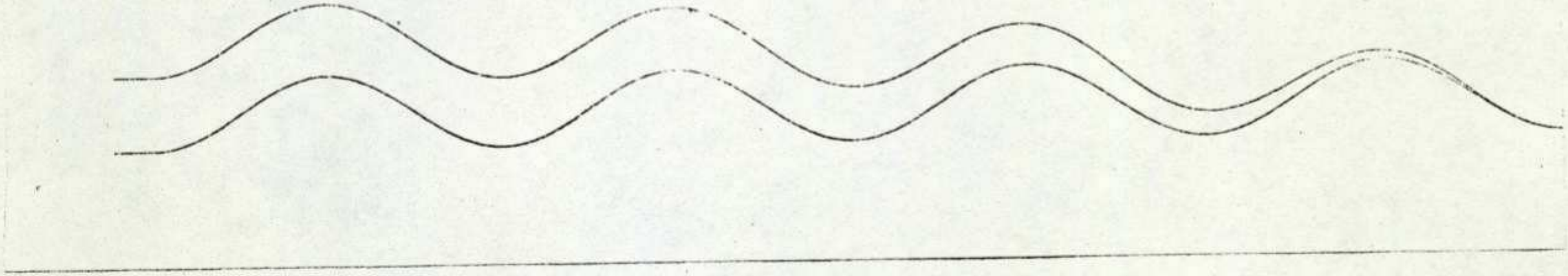

Figure 4.29b

Two diaphragm profiles constructed by (a) circles joined by straight lines and (b) Cornu Spiral, both using the same input data.
(The bottom curve in each case is the diaphragm, the top curve is the deflected position when pressurized).

Stress levels on the top and bottom faces in Circumferential direction for two diaphragm profiles, one constructed from circles and straight lines the other using a Cornu Spiral.

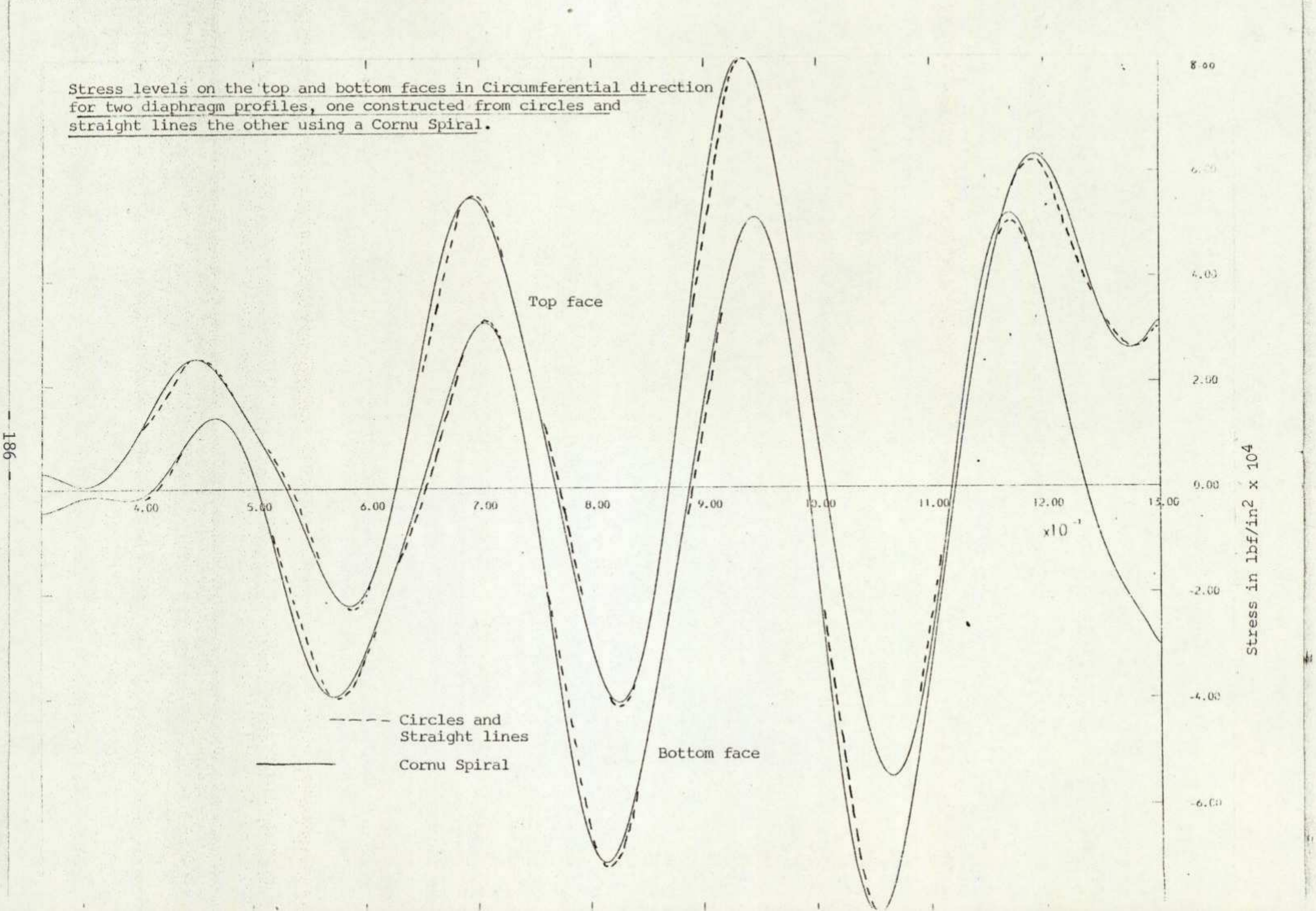

Figure 4.30

Stress levels on the top and bottom faces in Radial direction for two diaphragm profiles, one constructed from circles and straight lines the other using a Cornu Spiral.

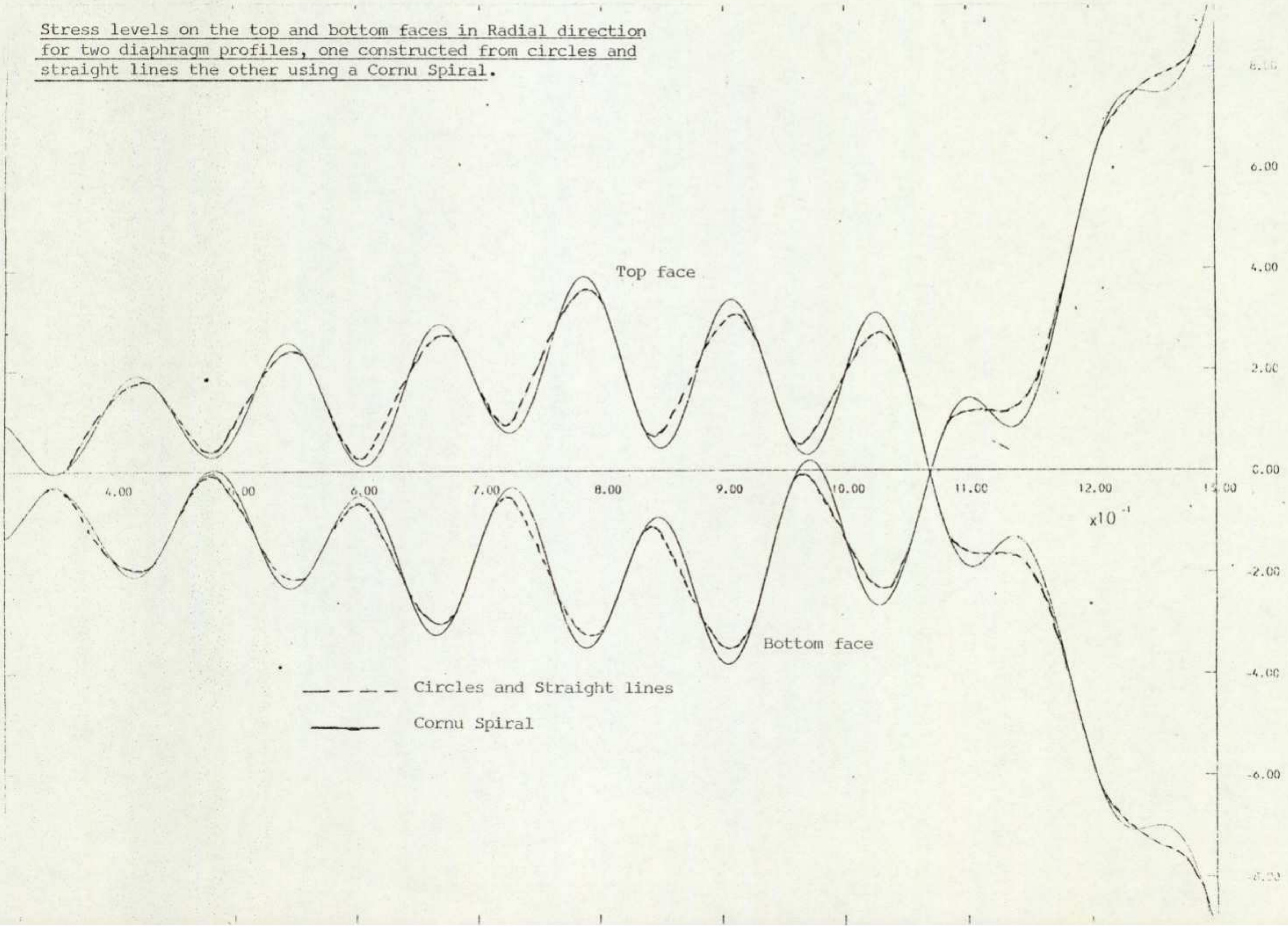

Figure 4.31

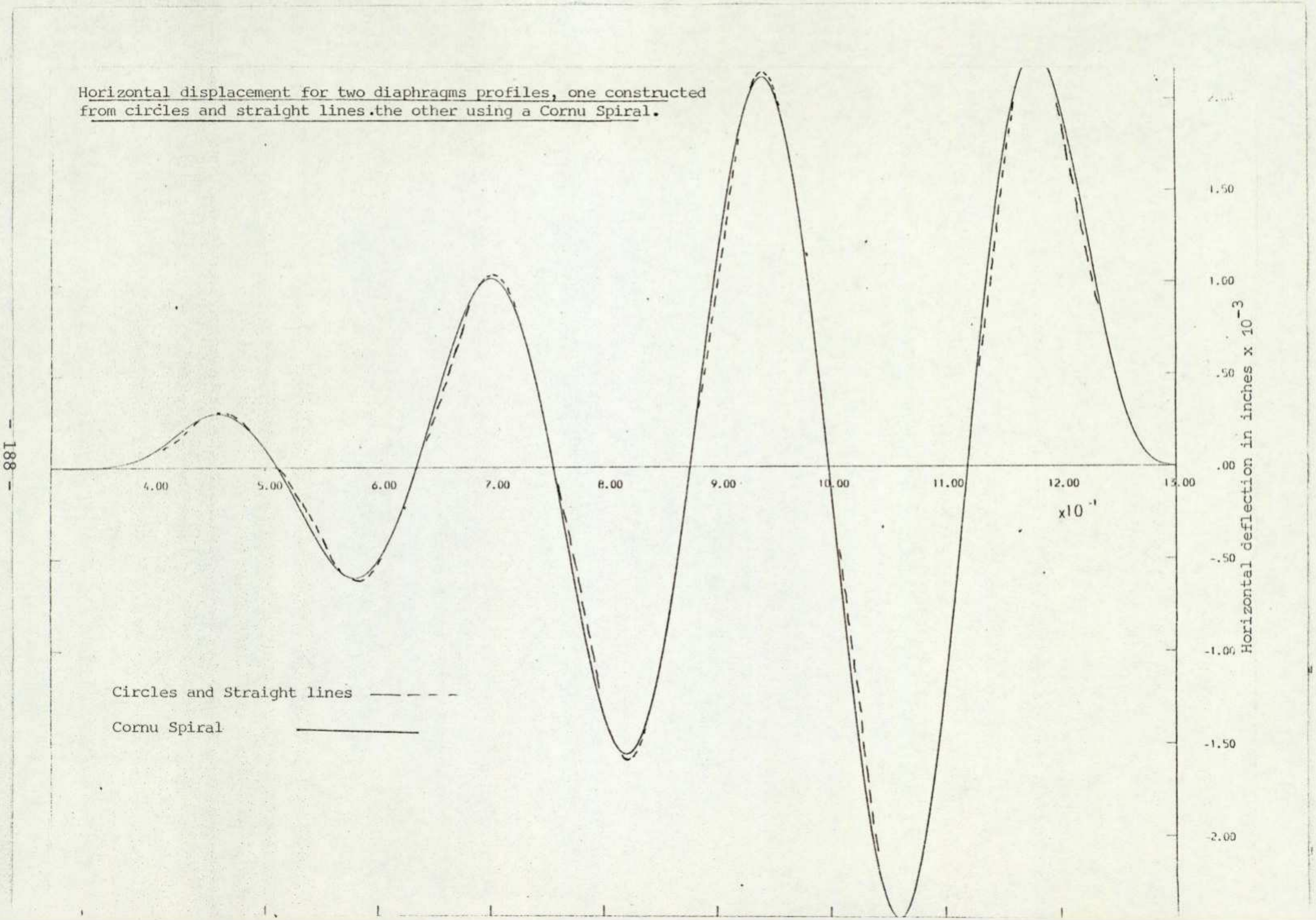

Horizontal displacement for two diaphragms profiles, one constructed from circles and straight lines.the other using a Cornu Spiral.

Figure 4.32

deflection are very small (Figures 4.30, 4.31 and 4.32); generally, curves of the output N_ξ N_θ M_ξ, etc., are very similar, both in shape and magnitude, and nothing seems to be gained, either numerically or practically, from using a complex but mathematically more correct method of simulating a diaphragm profile.

4.4 Conclusions

Taking an overall view of the details presented in this chapter, section by section, has shown:

The comparison of the model with the one developed by Wildhack "et al" is very good indeed, as would be expected, as the same equations are used but solved with a different numerical technique. Testing the model against reported experimental work gives a generally poor comparison, but this is in no way conclusive because of the unknowns associated with the experimental profile.

Experimental comparisons made by the author, assuming an average value of Young's Modulus, are good. The prediction of gross non-linearities (approximately 10 to 20 per cent) has been difficult because the diaphragms are shown to be entering the plastic region. Non-linearities which would concern an instrument designer (up to a maximum of 1 per cent) are shown to be predicted well, so long as the assumptions of thin shell theory are adhered to. Sensitivity is also well predicted for the case of small non-linearities, and an overall figure of 5 per cent may be placed on sensitivity predictions. Better than 5 per cent would be fortuitous, as this is less than the accumulative tolerance placed on the physical and geometric properties.

As has been shown, the limitations of the models are governed by the assumptions of thin shell theory, and attempts to extend the model applicability, i.e. reduce the restriction on the thickness to curvature ratio are shown to be very complicated.

The addition of small strains into the model can be achieved by modifying both the equations and techniques for numerical solution, although the actual improvement is not justified: firstly for practical problems (small non-linearities) the improvement is very slight, and, secondly, for gross non-linearities there is an increased possibility of numerical instability.

The last section which deals with the Cornu Spiral is seen more as a method of showing that the simple straight line and circle method for constructing geometry is adequate rather than an improvement. The increased restriction and complexity of the method again do not justify any marginal improvement made.

5.0 Dynamics of Corrugated Diaphragms and Capsules

The models developed in the previous chapters predict the static behaviour of diaphragms and capsules. In certain applications (e.g. diaphragms/capsules used as a simple spring), dynamic behaviour is of direct importance. In other situations, such as operation in a vibration-prone environment, the dynamic response, particularly any resonance frequencies, would be useful.

In its fundamental mode of vibration the system (diaphragm or capsule) may be represented as a second order system. If damping is assumed negligible, then energy is conserved in the system. For such a system the well-known Rayleigh's energy method can be used to predict the system dynamic response. In this chapter the basic Rayleigh method is applied and its use justified by showing that the damping is very small.

5.1 Rayleigh's energy method applied to diaphragms and capsules

The Rayleigh energy method utilises the static deflection curve as an approximation for the dynamic deflections during vibration. Since the models already described enable prediction of the static deflection curve, it appeared to be the most convenient method for determining the fundamental natural frequency of a diaphragm. Besides, previous work with various structures has shown this method to be accurate for practical purposes.

The problem could have been treated as a distributed mass system approximating to a continuous system, in which "n" point masses would be joined by massless springs, where n would be large ($\doteqdot 200$). This would have resulted in the eigenvalue solution of a large matrix equation of the form $\bar{x} = \lambda \left[A\right] \bar{x}$, where λ is either equal to $\omega_n{}^2$ or $1/\omega_n{}^2$, depending upon the formulation of $\left[A\right]$. The complete eigenvalue solutions will yield all the system frequencies, but an iterative solution using the deflection curve would give the fundamental, and hence this process would have involved a large programming effort.

The method was initially applied to diaphragms by Alalasundaram ref. (35), and Franklin, ref. (36), and has been further refined and applied to capsules by the author.

5.1.1 Theory of Rayleigh's method for diaphragms

For a single degree of freedom, the well-known differential equation of motion of a Second Order System subjected to forced vibrations of sinusoidal nature is:

$$M\overset{''}{x} + C\overset{'}{x} + Kx = F_o \text{ Sin } \omega t$$

and its steady state solution has amplitude

$$x = \frac{Fo/K}{\left(\left(1 - \frac{\omega^2}{\omega_n^2}\right) + \left(2 \zeta \frac{\omega}{\omega_n}\right)^2\right)^{\frac{1}{2}}}$$

where ζ is the damping ratio $\zeta = \frac{C}{2\sqrt{KM}}$.

For the damped case, the resonance occurs at

$$\omega = \omega_n \sqrt{1 - 2\zeta^2}$$

whereas for the undamped case ($\zeta = 0$), a condition of resonance exists at $\omega = \omega_n$ (termed the undamped natural frequency).

In this investigation, damping is assumed to be negligible, e.g. $\zeta < 0.1$ (which corresponds to a deviation from undamped natural frequency of < 1%). If a corrugated diaphragm is modelled as a single degree of freedom Second Order System, without damping, the first natural frequency is given by:

$$f_n = \frac{1}{2\pi} \sqrt{\frac{K}{M}} \text{ Hz},$$

where K and M are the equivalent stiffness and mass of the diaphragm.

Rayleigh's energy method finds an approximation to the first natural frequency of an elastic element which executes simple harmonic motion in the fundamental mode. When the deflection is a maximum, all parts of the body are motionless and the kinetic energy (K.E.) is zero, all energy is potential and stored as strain energy. When the body passes through its equilibrium position all the energy is kinetic. In a conservative system these two computed energies must be equal and solutions can be found for equivalent mass, stiffness, and natural frequency. It is convenient to realise a vibrating diaphragm as a large number of finite elements, each having its own elemental mass and deflection, each element being a finite difference station from the static solution model.

5.1.1.1 Kinetic Energy (KE): The element may have both translation and rotational KE, but the latter was shown to be negligible. The program gives the vertical (W) and horizontal (U) deflections for each element; the actual path from equilibrium to maximum deflection for the linear case is a straight line:

$$W_d^2 = W^2 + U^2.$$

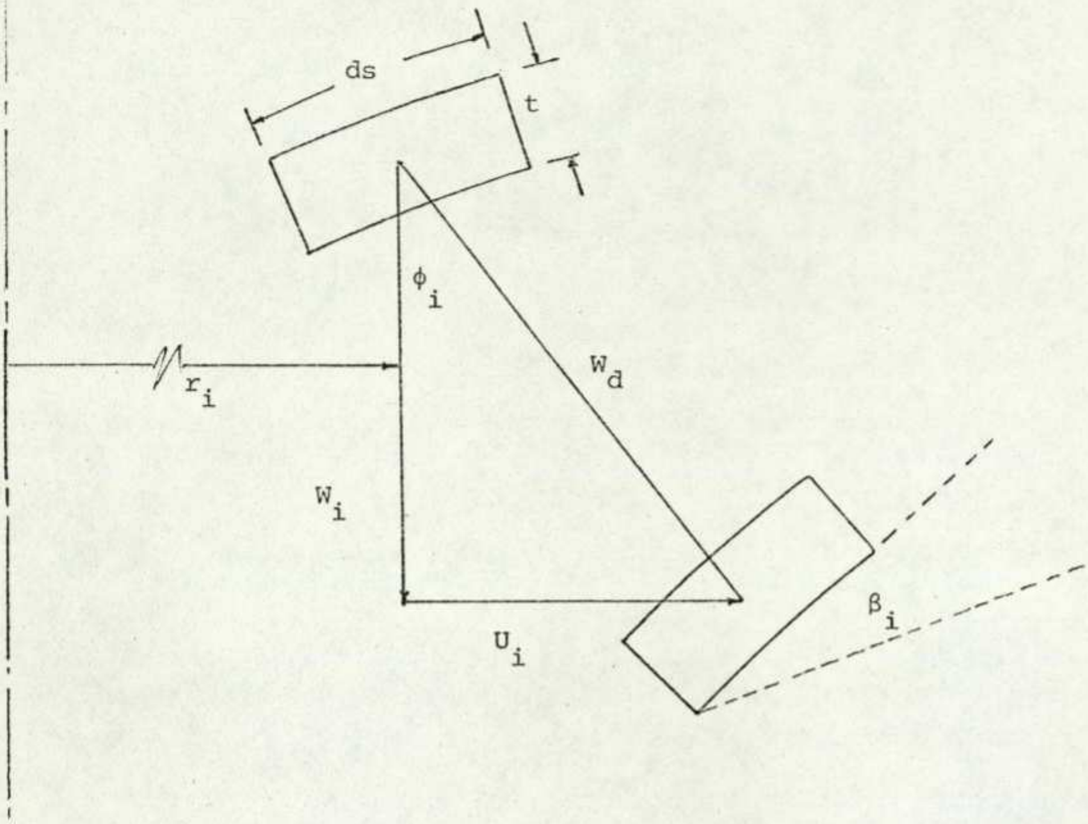

Figure 5.1: Elemental diaphragm section showing displacement

At equilibrium position the element has maximum velocity V_{max}

$V_{max} = \omega W_d$.

Hence KE of translation $= \frac{1}{2} mV^2\Big|_i = \frac{1}{2} m\omega^2 W_d^2\Big|_i = \frac{m}{2}\omega^2(U^2 + W^2)\Big|_i$

at the i^{th} element.

If ds and t are small, then the mass of an elemental ring of diaphragm = $2\pi r_i \, ds \, t\rho$,

therefore, KE of ring = $2\pi r_i \frac{ds}{2} t\rho \, \omega^2 (U_i^2 + W_i^2)$.

If ds is a constant step length, then the total translational KE

$$= \omega^2 \pi t\rho \, ds \sum_{i=1}^{i=N} r_i (W_i^2 + U_i^2),$$ where N = number of elements,

rotational KE $= \frac{1}{2} I \dot{\beta}^2$

$\dot{\beta} = \omega$

I = moment of inertia through the centroid of element, cf

$$I = \frac{m}{12}(a^2 + b^2) = \frac{m}{12}(ds^2 + t^2),$$

therefore, moment of inertia of ring $= 2\pi r_i \, t \frac{ds \, \rho}{12}(ds^2 + h^2)$

and total KE of rotation $= \frac{ds^2 + t^2}{12} \pi\, t\, ds\, \rho\, \omega^2\, \Sigma\, r_i\, \beta_i^2$.

This value was about 0.003% of the translational KE. The total KE of an equivalent mass spring system $= \frac{1}{2} mV^2$, where V = velocity of its mass which is equivalent to $\omega^2 W_T^2$. Thus the system equivalent mass (M_{eq})

$$M_{eq} = \frac{2\pi\, t\rho\, ds}{W_T^2} \sum_{i=1}^{i=N} r_i\, (W_i^2 + U_i^2)$$

5.1.1.2 Potential energy (PE): Strain energy in a linear spring $= \frac{1}{2} Fx_o$, where F = force producing deflection x_o. The force to cause an axi-symmetric deflection in a diaphragm can be either a uniform pressure or load applied at the centre, or both. For a centre load the equation is the same as above. For a pressure the load is considered for an elemental ring at the i^{th} point and summed over the diaphragm; as the pressure acts normal to the surface the maximum deflection normal to the surface is used, i.e. $x_i = (W_i \cos\phi_i + U_i \sin\phi_i)$. Then the elemental force $dF_i = P\, 2\pi\, r_i\, ds$.

Hence, $\frac{1}{2}\, dF_i x_i = \frac{1}{2} P\, ds\, 2\pi r_i (W_i \cos\phi_i + U_i \sin\phi_i)$,

therefore, the total PE $= P\, ds\, \pi \sum_{i=1}^{i=N} r_i (W_i \cos\phi_i + U_i \sin\phi_i)$ ... (5.1)

5.1.1.3 Equivalent stiffness:

If the total PE $= \frac{1}{2}$. (Equivalent force) . W_o

equivalent force $= K_{eq} . W_o$, where K_{eq} = equivalent stiffness,

therefore, total PE $= \frac{1}{2} K_{eq}\, W_o^2$ .... (5.2)

Hence, equating Eqns. (5.1) and (5.2),

$$K_{eq} = \frac{2\, ds\, P\, \pi}{W_o^2} \sum_{i=1}^{i=N} r_i (W_i \cos\phi_i + U_i \sin\phi_i)$$

Note: For the digital simulation of the actual experiment the stiffness and mass of the moving parts of the vibrator were added into the value of M_{eq} and K_{eq}.

5.1.2 Rayleigh's method applied to capsules

Using an extension of the foregoing theory, there are possibly two ways of modelling a capsule to find the natural frequency. Looking generally at the problem, a diaphragm clamped at the edge has its distributed mass assumed to act at the centre, this being the maximum displacement.

A capsule shown sectioned in Figure 5.2 has a bottom diaphragm clamped at the centre with its maximum displacement at (b), whilst the top diaphragm has its maximum displacement at the centre (c): the displacement (b) for the top diaphragm is just an overall "DC" shift. This could be modelled as shown in Figure 5.3:

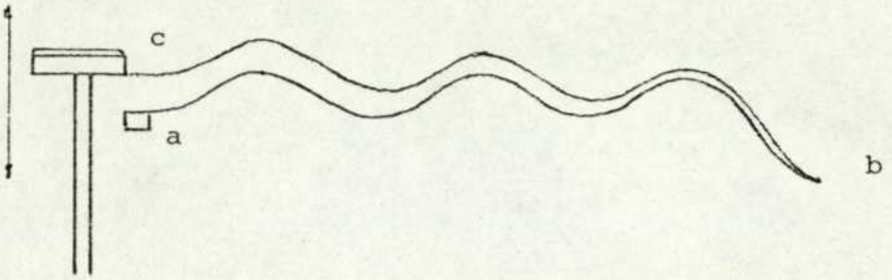

Figure 5.2: Capsule sectioned

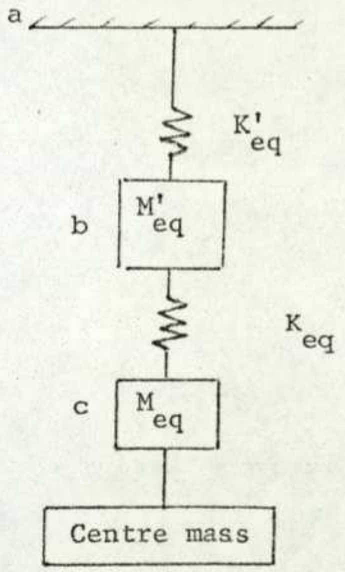

where M'_{eq} and M_{eq} represent equivalent masses of single diaphragms;

K'_{eq} and K_{eq} represent equivalent stiffness of single diaphragms

Figure 5.3: Equivalent capsule

OR the second method, the whole capsule, i.e. the two diaphragms could be treated as a single spring with an equivalent mass acting at the centre similar to a single diaphragm (Figure 5.4):

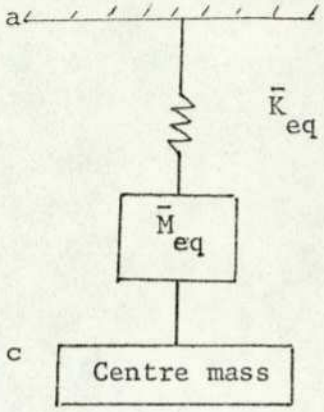

where $\bar{K}_{eq}$ = equivalent stiffness of capsule stack

$\bar{M}_{eq}$ = equivalent mass of capsule stack

Figure 5.4: Simplified equivalent capsule

The second method would be the simpler to program, especially when considering capsule stacks, because of the decrease in degree of freedom of the system. The first method was assumed inconsistent with a lumped parameter model, and the visualised anti-phase movement of the two diaphragms would probably be a second mode vibration for the second method.

To check the computer simulation, comparison was made with the soluble case of a flat plate capsule. The flat plate capsule is a fictitious concept that could never work in practice, but, for the purpose of this work, it is assumed that each plate can pass through the other and hence displace in a manner similar to a more usual capsule. The complete analysis is shown in Appendix 3, and the main results are summarised below. The left-hand side shows the results for K_{eq}, M_{eq} and f_n for an ordinary flat plate which may be compared to the same desired quantities for a capsule.

$$K_{eq} = \frac{\pi}{3} C_p r_T^2 \qquad\qquad K_{eq} = \frac{\pi}{6} C_p r_T^2$$

$$M_{eq} = \frac{M}{5} \qquad\qquad M_{eq} = \frac{3}{10}(2m)*$$

$$f_n = \frac{1}{2\pi}\sqrt{\frac{K_{eq}}{M_{eq}}} = \bar{K}\sqrt{\frac{5}{3}} \qquad f_n = \frac{1}{2\pi}\sqrt{\frac{K_{eq}}{M_{eq}}} = \bar{K}\frac{1}{3}\sqrt{\frac{5}{2}}$$

* Because a capsule is being considered, and everything is referred to a single diaphragm, the mass is doubled.

$C_p = \frac{P}{W_T}$; M = total mass of diaphragm; $\bar{K} = \frac{1}{2\pi}\sqrt{\frac{\pi C_p r_T^2}{M}}$

The analytical results on the right-hand side were tested against results obtained from a computer prediction using a flat plate capsule, of the following geometric and material values:

$$E = 30 \times 10^6 \text{ lbf/in}^2 \ (207 \text{ GNm}^{-2})$$

$$\nu = 0.29$$

$$r_T = 1.0'' \ (25.4 \text{ mm})$$

$$t = 0.005'' \ (0.127 \text{ mm})$$

$$\rho = 0.307 \text{ lbf/in}^3 \ (8.5 \text{ gms/cm}^3)$$

To obtain an analytical value for (f_n) of a flat plate capsule the result must be inferred from the expressions above and by obtaining a C_p (pressure constant) from the linear prediction of a flat plate:

$$\frac{P}{E}\left(\frac{R}{t}\right)^4 = \frac{3}{16}(1 - \nu^2)\frac{W_T}{t} .$$

This gives the fundamental frequency of a single flat plate, from the formula above, as: 481.536 Hz,

then $\bar{K} = 372.997$

And substituting in $f_n = \bar{K}\frac{1}{3}\sqrt{\frac{5}{2}}$

gives $f_n = \underline{196.58 \text{ Hz}}$.

The table below shows the numerical results for a flat plate capsule against a computer program prediction of the same flat plate capsule:

	Analytic	Program
Natural frequency	196.58 Hz	195.522 Hz
K_{eq}	11.506 lbf/in (2.006 N/mm)	11.2968 lbf/in (1.970 N/mm)
Mass ratio	0.3	0.299645

This result shows good agreement and gives confidence in the computer program. The validation of the computer model requires comparison with experiment.

5.2 Capsule stacks as multi-degree of freedom systems

Typical pressure instruments usually have more than a one-capsule stack: two is much more common and occasionally, on low pressure ranges, three stacks are used. For the experimental apparatus a two-stack capsule was used, each stack being identical; so as to be consistent this configuration would have to be simulated as well as the vibrating equipment. This was rigidly attached to the "drive end piece" shown schematically in Figure 5.5a.

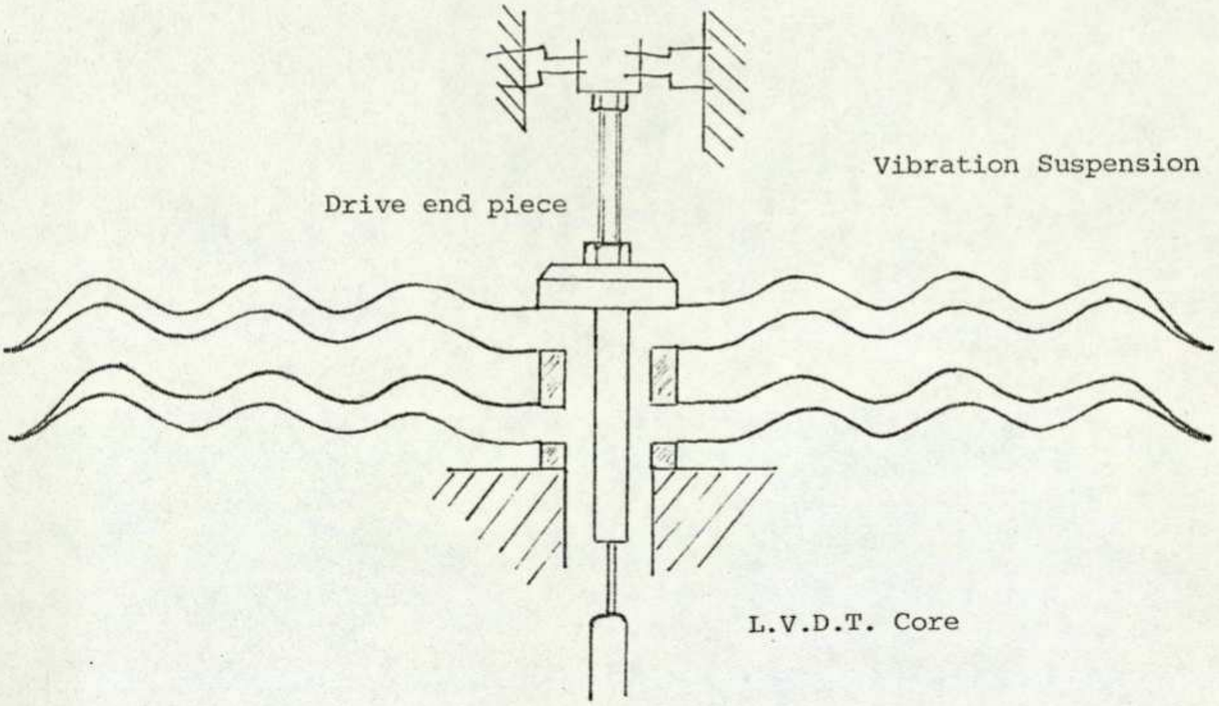

Figure 5.5a

The two-stack capsule and vibrator is then analogous to:

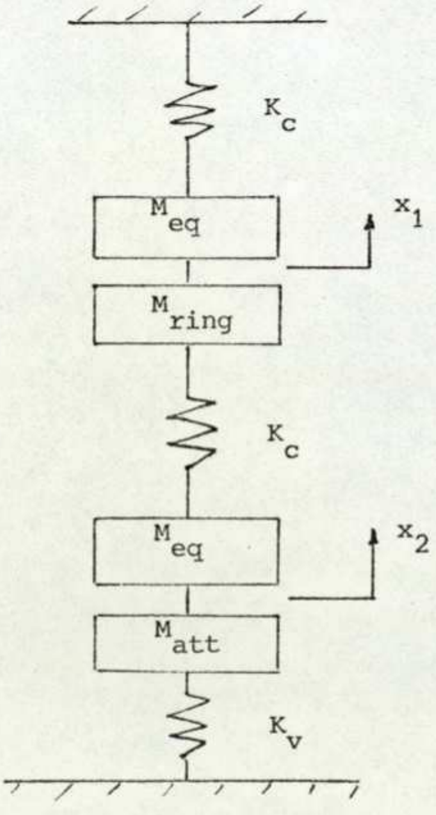

Figure 5.5b

Figure 5.5: A two-stack capsule plus attachments

where

K_c = equivalent stiffness of one-capsule stack
M_{eq} = equivalent mass of one-capsule stack
K_v = stiffness of vibrator
M_{ring} = mass of annular ring between the two-capsule stacks
M_{att} = mass of all the attached parts (drive and piece, L.V.D.T. core, vibrator moving parts, etc.)

This configuration can be analysed as a two degrees of freedom system which will yield two natural frequencies.

Let $M_1 = M_{eq} + M_{ring}$ and $M_2 = M_{eq} + M_{att}$

$$\text{Then } M_1\ddot{x}_1 = - K_c x_1 + K_c(x_2 - x_1)$$

$$M_2\ddot{x}_2 = - K_v x_2 - K_c(x_2 - x_1) + F_o \text{ Sin } \omega t$$

in matrix form

$$\begin{bmatrix} M_1 & 0 \\ 0 & M_2 \end{bmatrix} \begin{bmatrix} \ddot{X}_1 \\ \ddot{X}_2 \end{bmatrix} + \begin{bmatrix} 2K_c & - K_c \\ -K_c & (K_c + K_v) \end{bmatrix} \begin{bmatrix} X_1 \\ X_2 \end{bmatrix} = \begin{bmatrix} 0 \\ F_o \text{ Sin } \omega t \end{bmatrix}$$

assuming no damping and sinusoidal motion by the masses

$$x_1 = X_1 \text{ Sin } \omega t \qquad \ddot{x} = - X_1 \omega^2 \text{ Sin } \omega t$$

$$x_2 = X_2 \text{ Sin } \omega t \qquad \ddot{x}_2 = - X_2 \omega^2 \text{ Sin } \omega t$$

and dividing by Sin ωt

$$\begin{bmatrix} 2 K_c - M_1\omega^2 & - K_c \\ - K_c & K_c + K_v - M_2\omega^2 \end{bmatrix} \begin{bmatrix} X_1 \\ X_2 \end{bmatrix} = \begin{bmatrix} 0 \\ F_o \end{bmatrix}$$

it can be seen that this will lead to the natural frequency of the above system; to find the natural frequency of just the capsule stacks and L.V.D.T. core, M_{att} is somewhat smaller and $K_v = 0.0$.

The Eigenvalue solution will give the natural frequencies when the determinant is zero.

$$(2K_c - M_1\omega^2)\left((K_c + K_v) - M_2\omega^2\right) - K_c^2 = 0$$

$$M_1 M_2(\omega^2)^2 - \left(M_1(K_c + K_v) + 2 K_c M_2\right)\omega^2 + K_c^2 + 2K_c K_v = 0$$

Hence, a quadratic with two solutions for ω^2, i.e. the two natural frequencies of the system. With a knowledge of M_1, M_2, K_c and K_v the two ω_n's can easily be found.

5.3 Experimental apparatus for testing diaphragms and capsules

The apparatus and experimental procedure for diaphragms is adequately described by Franklin, ref. (36), and it is proposed not to repeat this work here, only to refer to it. The experimental apparatus for the testing of capsules required more complex instrumentation, but the principle involved was the same. The vibrator was set up in the manner shown in Figure 5.6, reproduced from ref. (36) but with the capsule stack (Figure 5.5a) replacing the diaphragm.

Also, it was possible to use the L.V.D.T. without a sleeve as it is shown in Figure 5.6. This was an advantage because the output is more linear without it when used at high frequencies. The instrument is normally operated at 600 Hz and at this frequency the linearity is unaffected, but in the experiment it was excited at 2k Hz and is subject to eddy current effects, ref. (34) (Graph 1).

It was decided to look at the electromechanical coupling of the vibrator and capsule, and carry out an electrical-impedance analysis on the overall configuration and extract the natural frequency from the vector impedance plot. To undertake this, the oscilloscope was dispensed with, except for checking waveforms and a transfer function analyser (T.F.A.) was used to make the most of the measurement. The T.F.A. was used to measure the voltage at the vibrator terminals; the current was inferred by measuring the voltage across a standard 1 ohm resistance in series with the vibrator. To receive the L.V.D.T. output voltage proportional to displacement, the T.F.A. had to have the carrier frequency, i.e. 2k Hz removed from the signal. Figure 5.7 shows the schematic rectification circuit.

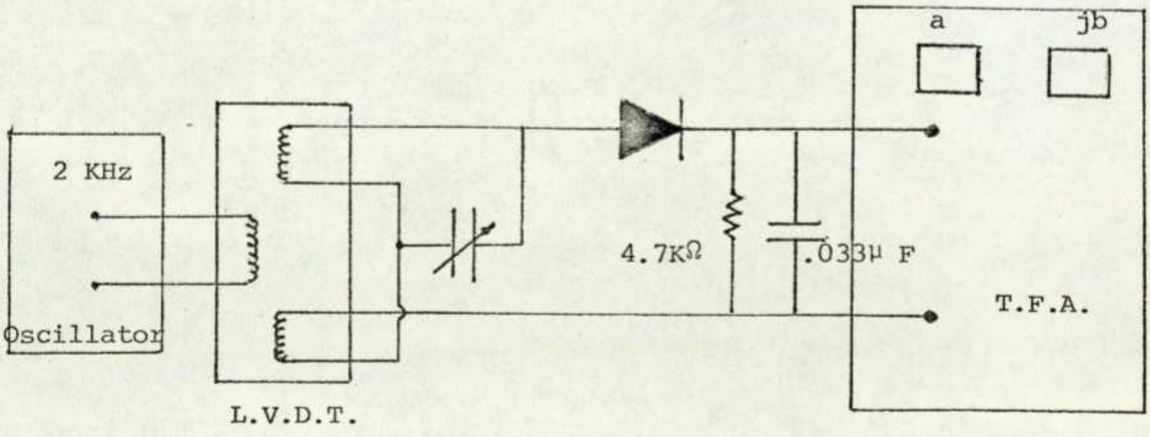

Figure 5.7: Rectification circuit for the L.V.D.T.

Figure 5.6

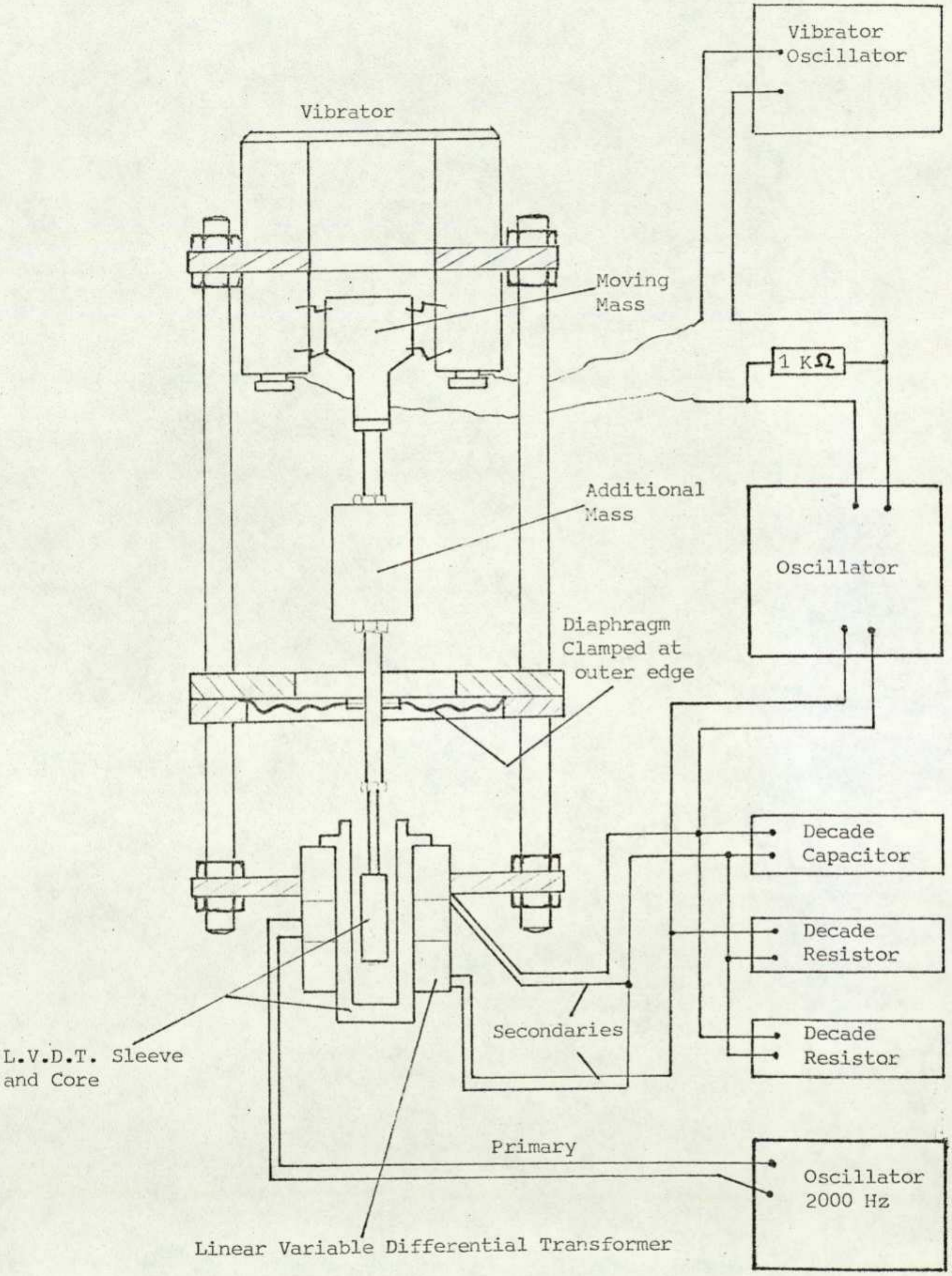

Test Rig and Measuring System for Diaphragms

The adjustable capacitor enables a near zero to be obtained when the L.V.D.T. armature has been adjusted mechanically to the central position, or as near as possible. The read-out was in a digital a + j b form.

The supply to the vibrator was taken from the T.F.A. in the form $V = V_o \sin \omega t$ (0 - 450 Hz); this, unfortunately, had to be amplified so that it could drive the vibrator (Figure 5.8).

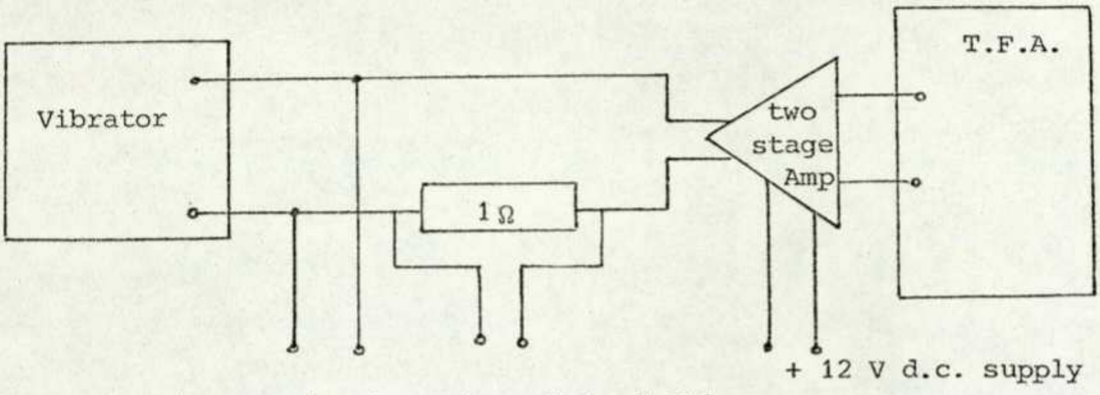

I/P Volts/IP Current read for T.F.A.

Figure 5.8: Vibrator drive circuit

Over the frequency range 1.0 - 450 Hz, readings of both input voltage and current to the vibrator and output voltage from the L.V.D.T. were taken for the capsule vibrating in situ as shown in Figure 5.5a. The amplitude of vibration was chosen so that the capsule did not nest and give a non-linear stiffness curve; this meant the output from the L.V.D.T. was very small and on some tests was amplified 100:1 before being rectified, a higher number of readings being taken around the observed natural frequency. With the vibrator blocked up so that it could not move, the input voltage and current were measured over the same frequency range: this would give the blocked electrical impedance. The first experiment was then repeated using the capsule plus an additional mass in the form of a brass weight which was vibrated through the axis of the capsule stack.

The sensitivity of the L.V.D.T. was found using a micrometer plus stand fixture and oscilloscope. With the sensitivity on 0.5V/cm the micrometer moved the trace 5 cm going from 0.161" to 0.167", thus giving a sensitivity of 416.66 millivolts per 0.001". Finally, the attached masses were weighed on a chemical balance.

5.4 System model and experimental results

Two equations will be required to describe the behaviour of the system: one will need to be written in terms of the electrical variable and must include the electrical effects arising from motion in the mechanical system; and one written in terms of the mechanical variables and must include all the mechanical effects arising from currents or voltages in the electrical system. The symbols T_{em} and T_{me} appearing in Figure 5.9 represent "Transduction coefficients".

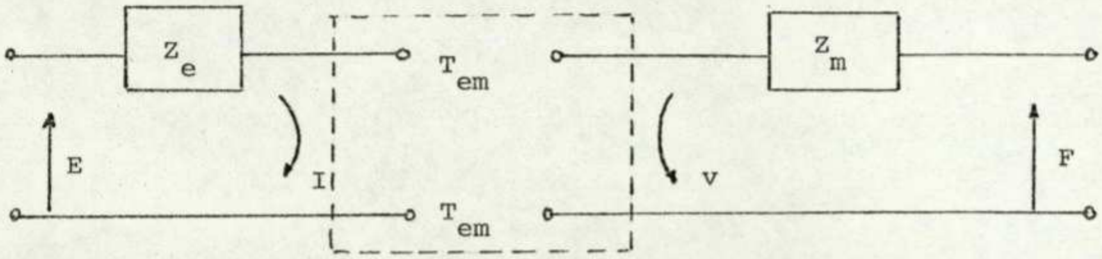

$$E = Z_e I + T_{em} v \quad \ldots\ldots\ldots\ldots\ldots\ldots\ldots \quad (5.3)$$
$$F = T_{me} I + Z_m v \quad \ldots\ldots\ldots\ldots\ldots\ldots\ldots \quad (5.4)$$

Figure 5.9: Transduction coefficients

Note:

The Analogy is Force - Voltage "effort" variable ref. (38)
Velocity - Current "flow" variables

Z_e, T_{em}, T_{me}, Z_m can all be of a complex form,

i.e. $Z_e = K_e + j\omega L_e + \frac{1}{j\omega C_e}$.

In the experiment the transducer is the vibrator, being an electromechanical device converting electrical energy into mechanical energy, and from "a priori" knowledge of its characteristics, the dynamic performance of the capsule stack may be deduced. Referring to the actual experiments performed and Equations (5.3) and (5.4), blocking up the vibrator so that it was not free to move, this would be putting v = 0.0. Then from (5.3),

$$Z_e = \left(\frac{E}{I}\right)_{v=0}$$

Z_e = blocked impedance.

Now if the capsule is removed, this will approximate F = 0.0.

Then $T_{me} I = -Z_m v$ from (5.4),

$$Z_{ee} = \left(\frac{E}{I}\right)_{F=0} = Z_e + \frac{-T_{me}\ T_{em}}{Z_m}$$

Also, $\dfrac{-T_{me}\ T_{em}}{Z_m} = Z_{mot}$, where Z_{ee} = total impedance

Z_{mot} = motion impedance.

Since v is also measured, L.V.D.T. voltage is proportional to displacement to x (say),

then $V = (j\omega)\ x$,

therefore

$$(j\omega)\ \frac{x}{I} = -\frac{T_{me}}{Z_m}$$

The capsule will represent a force = $-v\ Z_L$,

where Z_L = load impedance,

therefore, from (5.3) and (5.4),

$$E = Z_e I + T_{em} v$$

$$-vZ_L = T_{me} I + Z_m v$$

Then $$Z_{ee} = Z_e + \frac{-T_{em}\ T_{me}}{(Z_m + Z_L)} \qquad \text{(5.5)}$$

and $$\frac{(j\omega)x}{I} = \frac{-T_{me}}{(Z_m + Z_L)} \qquad \text{(5.6)}$$

5.4.1 Vector impedance locus

Taking Z_m as a general form equal to $r_m + j\omega\ \frac{1}{m} + \frac{1}{j\omega\ C_m}$, the variation of this impedance with frequency can be exhibited most usefully by representing the impedance as a vector drawn from the origin in the real-imaginary plane. As frequency changes, both the magnitude and the phase angle of the vector will also change and the tip of the vector will trace out a curve. If r_m is constant, the locus will be a vertical straight line (Figure 5.10a).

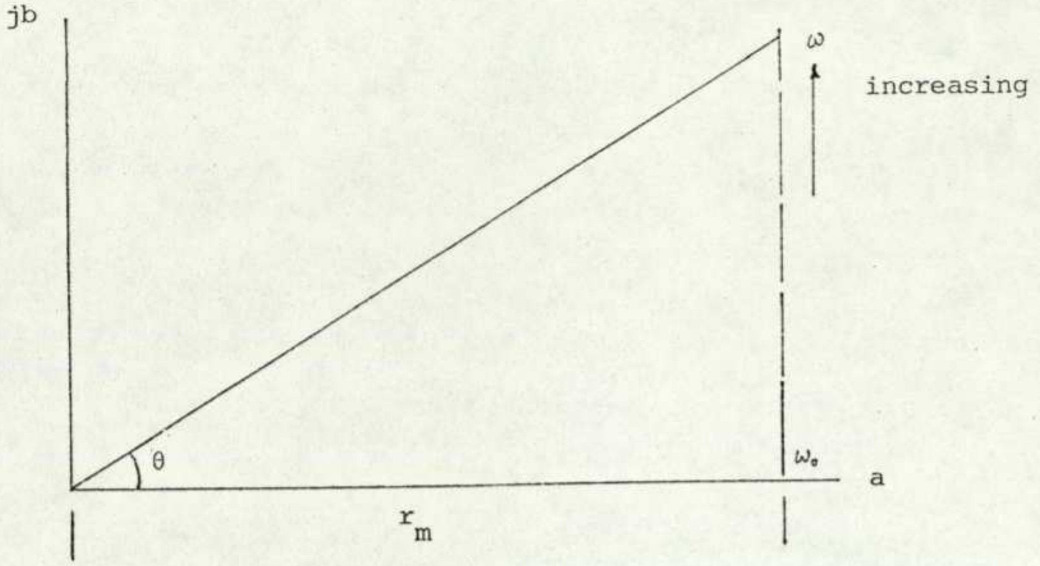

Figure 5.10a

If the mechanical admittance were plotted $Y_m = g_m - j\, h_m = \frac{1}{Z_m}$, this would be a circle figure (5.10b).

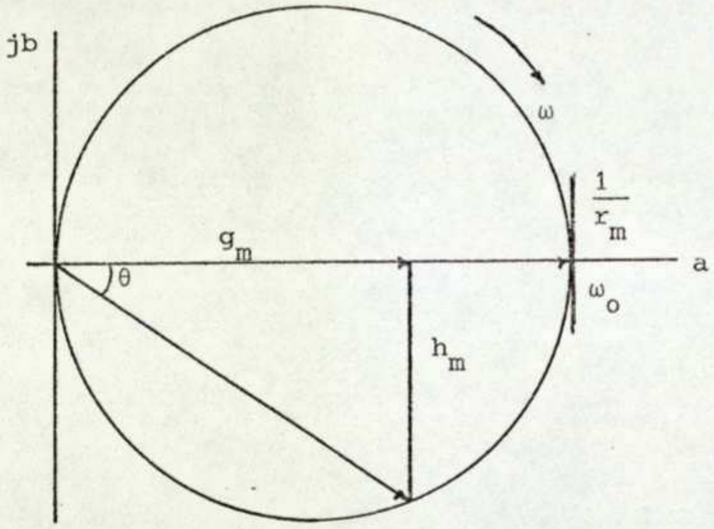

Figure 5.10b

Observation at the electricalterminals is the admittance locus multiplied by the scaling factor ($-T_{em}T_{me}$). This transduction factor must be considered as a vector operator which not only may alter the scale of Figure 5.10, but also may rotate the diameter of the admittance circle about the origin by an angle identified as 2β, but, more important, the transduction factor is a "units" operator having such dimensions as to convert the locus of mechanical admittance into a locus of electrical impedance (Figure 5.10c) (Z_{mot}).

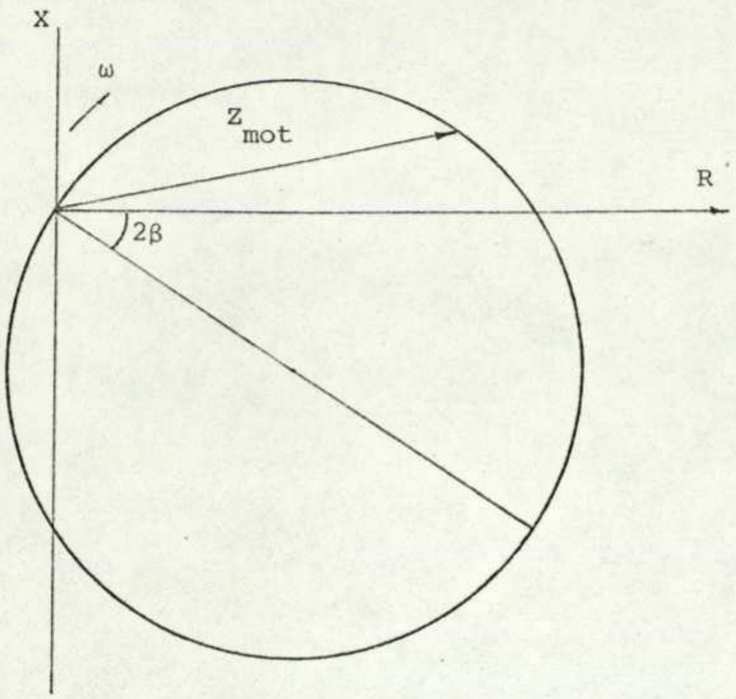

Figure 5.10c

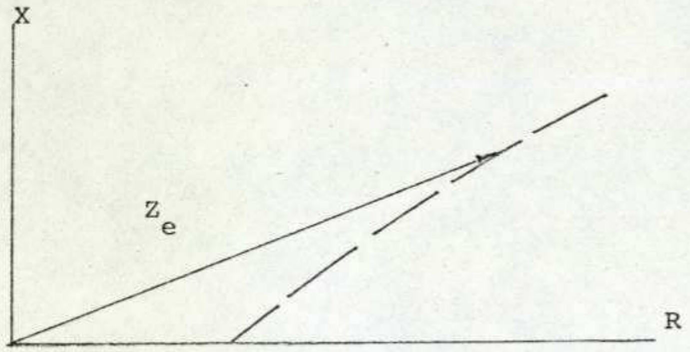

Figure 5.10d

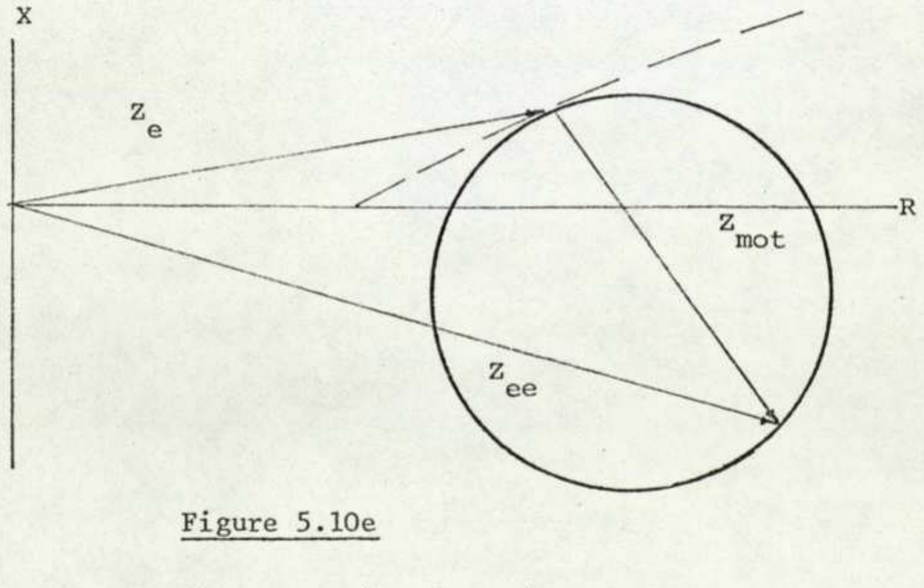

Figure 5.10e

Figure 5.10: The vector impedance locus

Thus, with the addition of the blocked electrical impedance Z_e (Figure 5.10d), the total impedance Z_{ee} will have a general form as shown in Figure 5.10e.

The method used to find the mechanical constants was the added mass method, a brass weight in series with the attached masses of Figure 5.5.

Consider the mechanical impedance Z_m in the general form

$$Z_m = r_m + j\omega\,\ell_m + \frac{1}{j\omega\,C_m}$$

ℓ_m is analogous to mass

$\frac{1}{C_m}$ is analogous to stiffness

$$\text{then } \omega_o = \sqrt{\frac{K}{m}} = \frac{1}{\sqrt{\ell_m C_m}} \qquad \text{......................................} \qquad (5.7)$$

Now if an auxiliary mass $\delta\ell_m$ is attached to the system, a new natural frequency is found:

$$\omega_{om}^2 - + \frac{1}{C_m(\ell_m + \delta\ell_m)} \qquad \text{................................} \qquad (5.8)$$

From (5.7) and (5.8),

$$\ell_m = \delta\ell_m \frac{\omega_{om}^2}{(\omega_o^2 - \omega_{om}^2)} \qquad \text{.................................} \qquad (5.9)$$

and hence C_m from (5.7).

The diameter of the motional impedance circle is simply related to one of the constants of the mechanical system since the mechanical impedance reduces to r_m at resonance.

$$\text{Thus, } D = \left| Z_{mot} \right| = \left| \frac{-T_{me}T_{em}}{r_m} \right| = \frac{A^2}{r_m} \qquad \text{..................} \qquad (5.10)$$

Assuming $\left|T_{me}\right| = \left|T_{em}\right| = A$ (say)

A = absolute value of the product of the transduction coefficient.

There are two methods for the determination of A and r_m. Firstly, by observing the two frequencies for which the real and imaginary parts of the mechanical admittance (or impedance) are equal $(\overset{'}{\omega}, \overset{''}{\omega})$ and for which the associated phase angle is 45°,

$$\text{then } \overset{'}{\omega}\,\overset{''}{\omega} = \omega_o^2$$

$$\text{and } \overset{''}{\omega} - \overset{'}{\omega} = \frac{r_m}{\ell_m} \qquad \text{..} \qquad (5.11)$$

Secondly, by using the "current transformation ratio", previously mentioned,

$$\frac{j\omega\ x}{I} = \frac{Z_{mot}}{T_{em}}$$

Using Equation (5.10),

$$\left| T_{em} \right| = \frac{DI_o}{\omega_o\ x_o} = A \quad \ldots\ldots\ldots\ldots\ldots\ldots\ldots\ldots\ldots\ldots \quad (5.12)$$

5.4.2 Results of capsule tests

Figures 5.11 and 5.12 are magnitude and phase plots of the frequency response to both experiments: Experiment 1 is the normal capsule stack and Experiment 2 is the capsule stack with the added mass.

Figure 5.11 is a magnitude plot of Experiment 1 on a linear frequency base. Figure 5.12 is a Bode plot of Experiment 2. These two graphs are included for two reasons: (a) to illustrate that the response is essentially Second order with very little damping and hence supporting the theory that Rayleigh's energy method can be used to predict natural frequencies, and (b) the observation that: the phase plot does not approach 180^o phase shift asymptotically but has more phase shift; over 200^o this could be due to the system being of a higher order than two but exhibiting mainly a second order response; also on the Bode plot the asymptote slope is -50 db/decade and a second order slope "fall off" would be -40db/decade, indicating again a higher order than two.

The first natural frequencies of the two tests were $\doteqdot$ 139.5 Hz and $\doteqdot$ 103 Hz, respectively. The added mass ($\delta \ell_m$) was 0.0583 lbs (129.2 gms), so from Equation (5.9),

$$\ell_m = 0.0669 \text{ lbs } (147.5 \text{ gms}),$$

and from Equation (5.7),

$$\frac{1}{C_m}\ \frac{1}{g_o} = 134 \text{ lbf/in } (23.47 \text{ N/mm}).$$

Figure 5.13 is a sample motional impedance plot for Experiment 2. There is a certain amount of zero "off-set": this was caused by the difficulty of effectively blocking the vibrator to obtain the blocked electrical impedance. A large scatter of results was discovered when a curve of $\frac{E}{I}\Big|_{F=0.0}$ in the a + jb form was plotted (Figure 5.14). To obtain results values were interpolated between the ends of the range.

The effect of the blocked impedance on the total impedance is shown

Figure 5.11

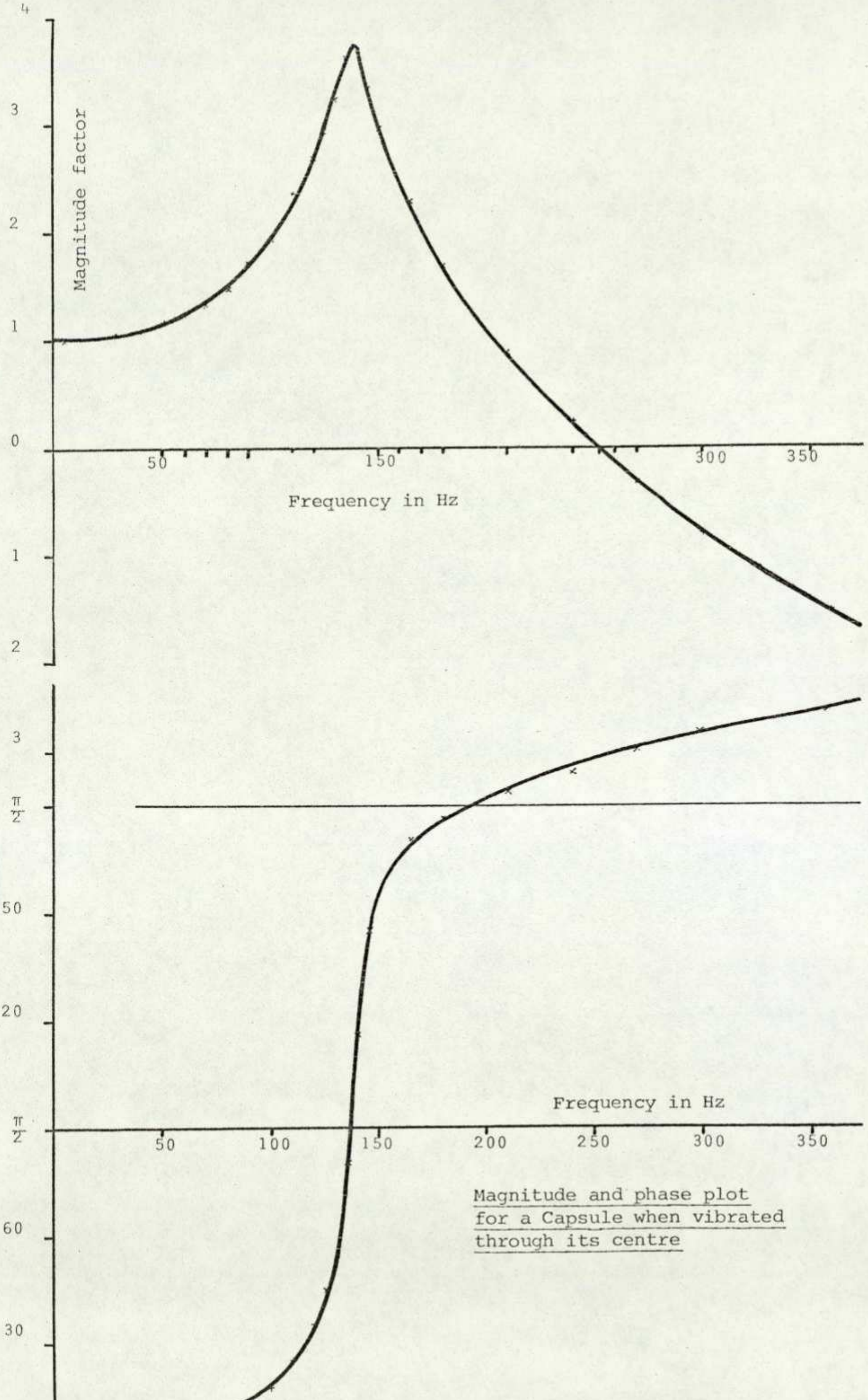

Magnitude and phase plot for a Capsule when vibrated through its centre

Figure 5.12

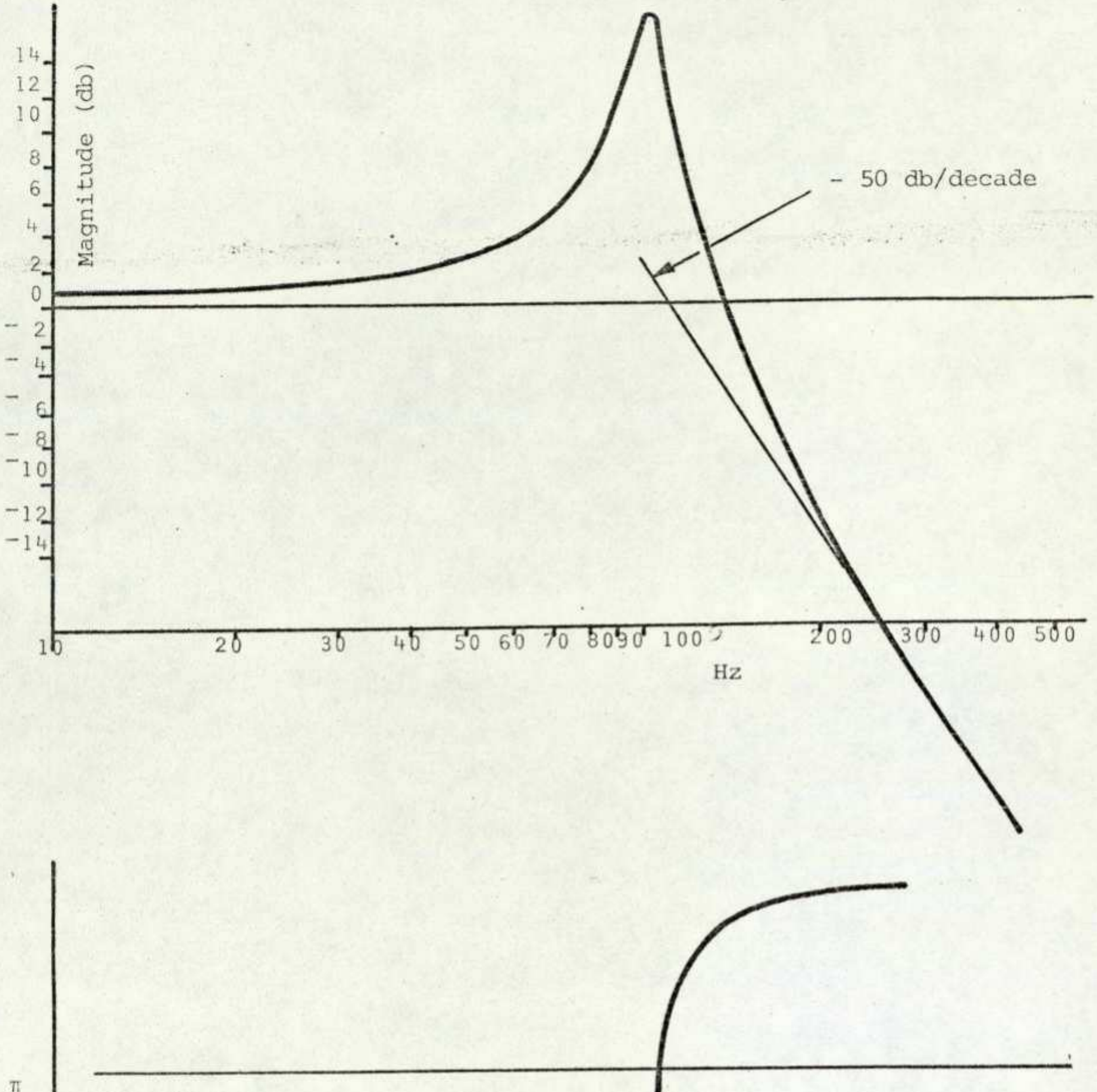

Bode plot for the same Capsule as in Figure 5.11

Figure (5.13)

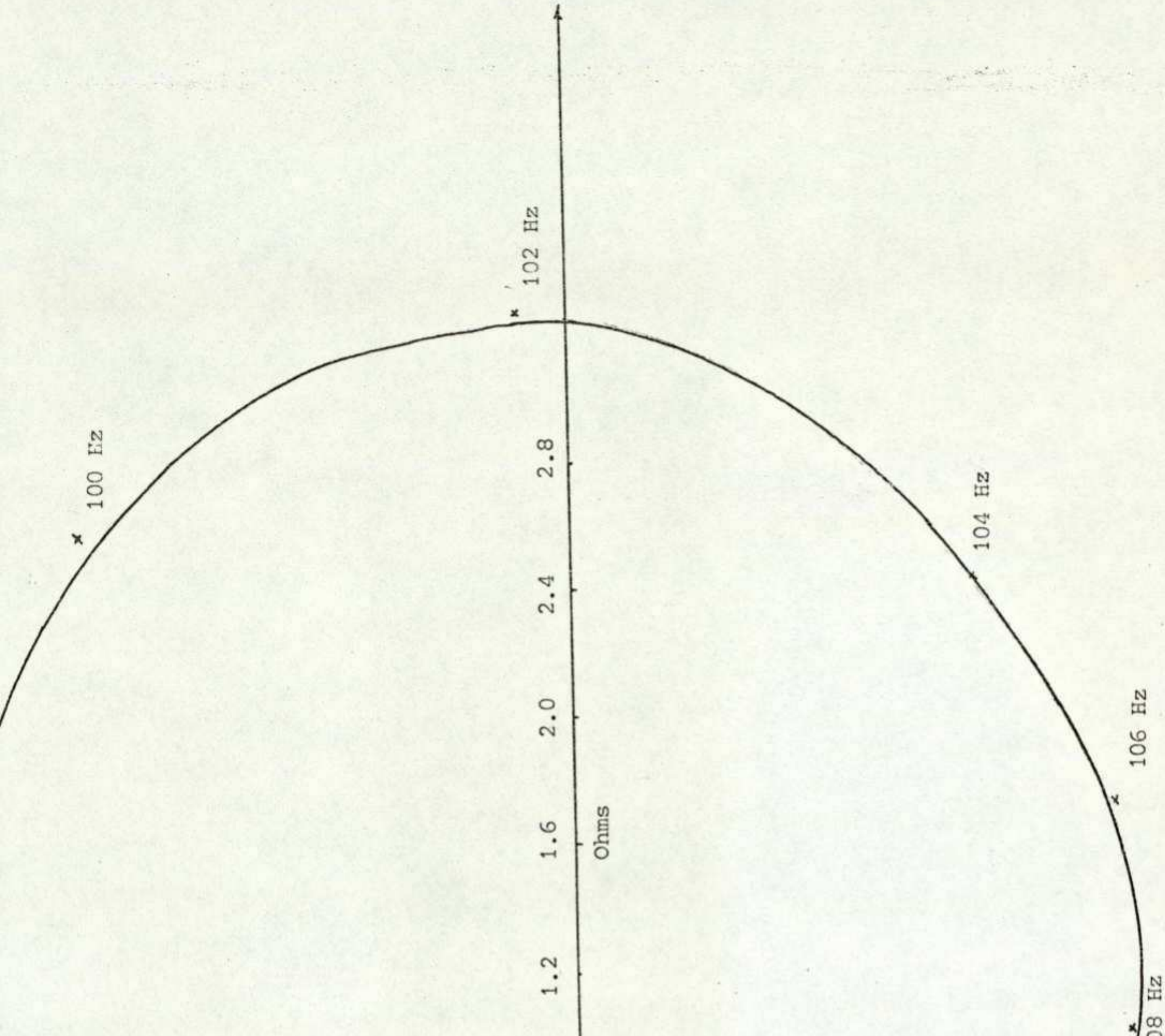

Motional Impedance plot for Experiment 2

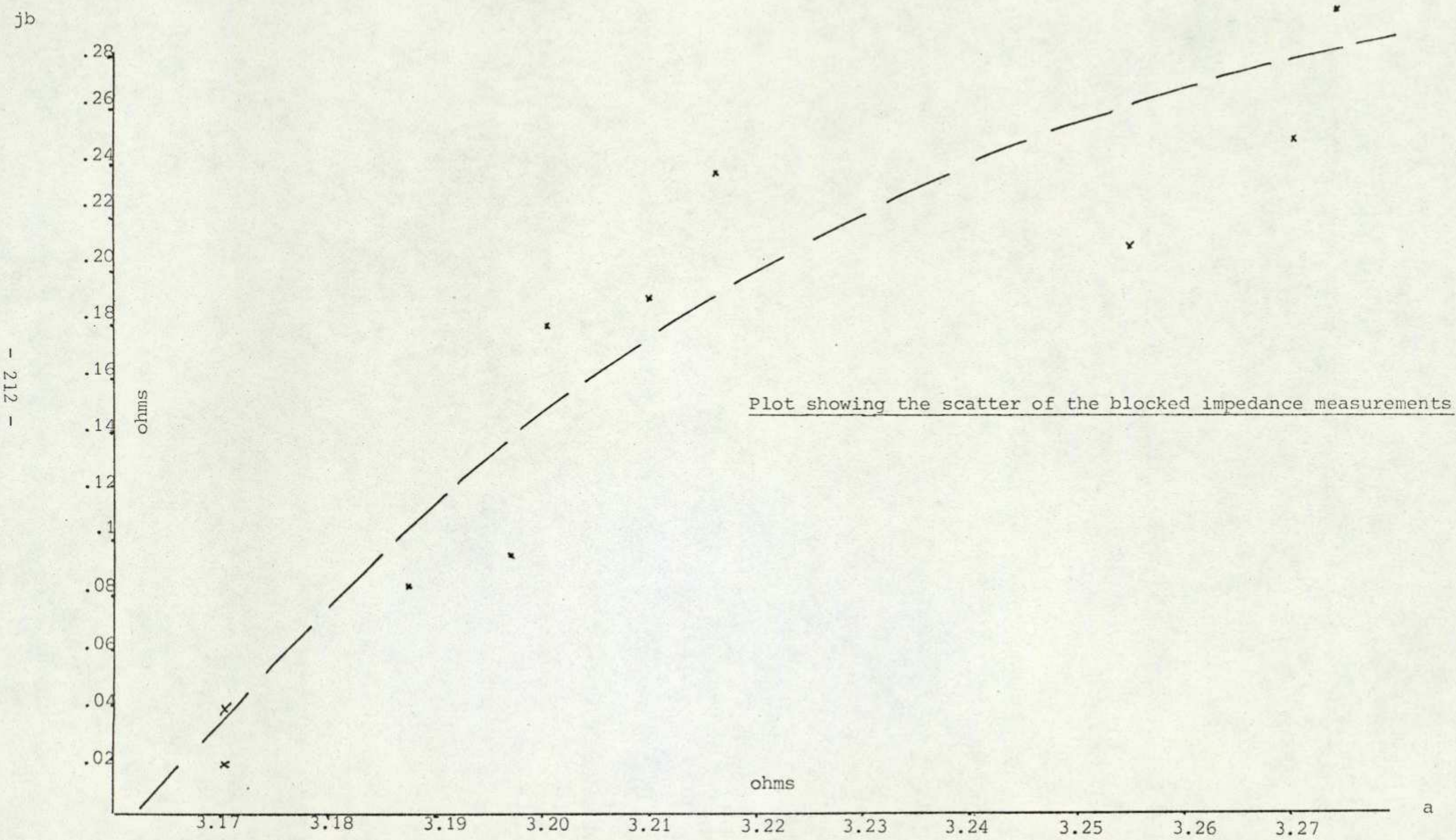

Plot showing the scatter of the blocked impedance measurements

Figure 5.14

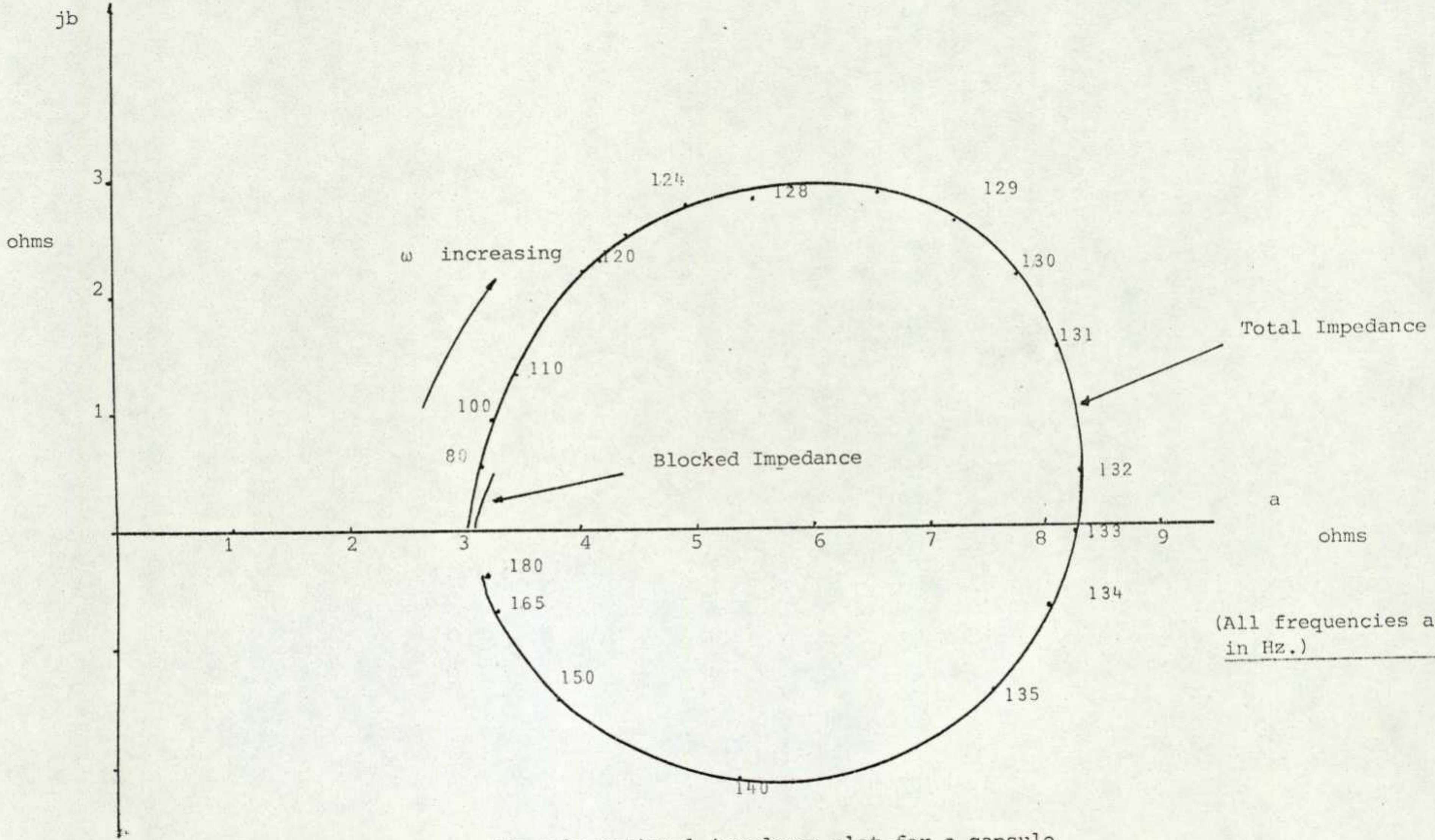

(All frequencies are in Hz.)

Example motional impedance plot for a capsule

Figure 5.15

in Figure 5.15, both curves being plotted over a total range of 180 Hz. This illustrates how a "zero offset", as shown in Figure 5.13, can occur because the motional impedance is just the vector difference of the total and blocked impedances.

To find r_m and A

Method 1 from Equation 5.11: $\omega'' = 143$ Hz

$\omega' = 125$ Hz

$$\text{therefore, } r_m = 0.0669 \cdot 2\pi \cdot (143 - 125) = 7.5662 \text{ lbf/sec} = (33.66 \text{N/sec})$$

Method 2:

$$D = 3.6\Omega$$

$$\omega_o x_o = 7.3 \times 10^{-2}$$

$$I_o = 0.104$$

$$\frac{DI_o}{\omega_o x_o} = 5.1285 \ |A| \text{ (transduction coefficient)}$$

$$r_m = \frac{(5.1285)^2}{3.6} = 7.31 \text{ lbf/sec} \quad (32.5 \text{ N/sec})$$

Now looking at a mass-spring-damped system (Chapter 5.1), the damping ratio $\zeta = \frac{C}{2\sqrt{KM}} = \frac{C}{2\omega_n M}$

Therefore, taking an average value of $r_m = 7.44$ lbf/sec,
the damping ratio $\zeta = 0.073$,
which is very small and gives us justification to neglect damping effects when vibrating a capsule in air.

Hence, the three mechanical constants associated with the impedance (Z_m) can be deduced. Further analysis could be carried out to find the values of T_{em} and T_{me}, but this was thought to detract too much from the main purpose of the chapter - the comparison of the theoretical and experimental prediction of the fundamental frequency of diaphragms and capsules.

5.5 Improvement on basic Rayleigh's method

Whilst Rayleigh's method was thought, and later shown, to be adequate as a prediction for natural frequency from Franklin's work, ref. (36), some anomalies do arise, the main one being that the computer program would give different results for three cases, namely:

(i) pure pressure loading,
(ii) pure point loading,
(iii) point and pressure loading,

the pure pressure loaded case being much higher than (ii) and (iii). This is correct because the program assumes no mass at the centre, and for this reason could not be verified by experiment. The other two cases were tested experimentally and no significant difference could be detected: this was concluded as being due to the experimental apparatus, poor damping, leaks, etc. Also, in ref. (36) a mistake was found in the programming - a fifth of the mass of the diaphragm was unnecessarily added to the attached masses in the computation, giving an artificially low result for natural frequency.

It was therefore decided to attempt to improve Rayleigh's method as well as extend it from diaphragms to capsule stacks, possibly by calculating the actual dynamic deflection curve. This was achieved by an iterative procedure using the static deflection curve as an initial approximation for the final dynamic one. After the first cycle, all the external loading and temperature terms are set to zero and the inertial terms are substituted into the equations of equilibrium. This is consistent with Kraus, ref. (17), pp. 455.

The vertical reaction $(rV)_i = -\int_{r_o}^{r} P_v \cos\phi \, r \, ds = -\frac{Pr_i^2}{2}$

becomes $-\int_{r_o}^{r} \rho t \, \omega_n^2 \, \frac{Wr}{g_o} \, ds = -\frac{ds \, \rho t \, \omega_n^2}{g_o} \sum_{i=1}^{i=N} W_i r_i$

$$(r\,P_V)_i = -\frac{\rho t \, \omega_n^2}{g_o} W_i r_i \qquad (r\,P_H)_i = -\frac{\rho t \, \omega_n^2}{g_o} U_i r_i .$$

These new equations are now solved using the previous value of natural frequency and displacements. A better approximation to the frequency is produced; this is re-substituted and solved until ω converges to a constant value (usually within 2 - 3 iterations). Any masses other than the elemental ring masses of the diaphragm, such as the centre loading, were treated as part of the vibrating system, and not added on after the main calculation, as in the more usual method.

5.5.1 Results for computer predictions; diaphragms

Using the same data as Franklin used in ref. (36), a comparison of the two methods can be made: Method 1 - Rayleigh's energy method; Method 2 - Rayleigh's energy working with the dynamic deflection curve. The diaphragm was an actual production diaphragm 0.006" (.1524 mm) thick of Inconel $\rho = 0.307$ lb/in^3 (8.5×10^3 kgs/m^3), Young's modulus as in Chapter 4.

	Pressure 5 lbf/in^2	Point load (0.2175 N)	Point plus pressure
Method 1	1441.86 Hz	305.32 Hz	339.5 Hz
Method 2	1481.43 Hz	305.25 Hz	305.25 Hz

Table 5.1

These results indicate that for Method 2 there is no change if the diaphragm is point loaded or point plus pressure loaded. Bearing in mind that all the digital simulations are assumed in the linear region, then the "no change" situation would appear sensible because the pressure is directly proportional to displacement and natural frequency is not dependent on the amplitude of the vibration, but it is dependent on the mass of the vibrating system and in this case it includes the applied load, if point loaded at the centre. These results show very close agreement between the two methods for the point loaded case only, but it should be noted that this is only for a particular loading, i.e. 0.0496 lbf (0.2175 N), and the discrepancy between Method 1 and Method 2 for prediction increases as the point loading decreases. This can be seen from the pressure only case where the program "sees" no mass at the centre, therefore the point load is zero.

5.5.2 Comparison of computer and experimental results

Table 5.2 shows the computer predictions for both experimental tests using the capsule: the situation where the capsule has no additional load at the centre is designated case (1), and where it has the additional load, case (2). The first iteration of the program will give the ordinary Rayleigh approximation (Method 1) and this is quoted as a comparison.

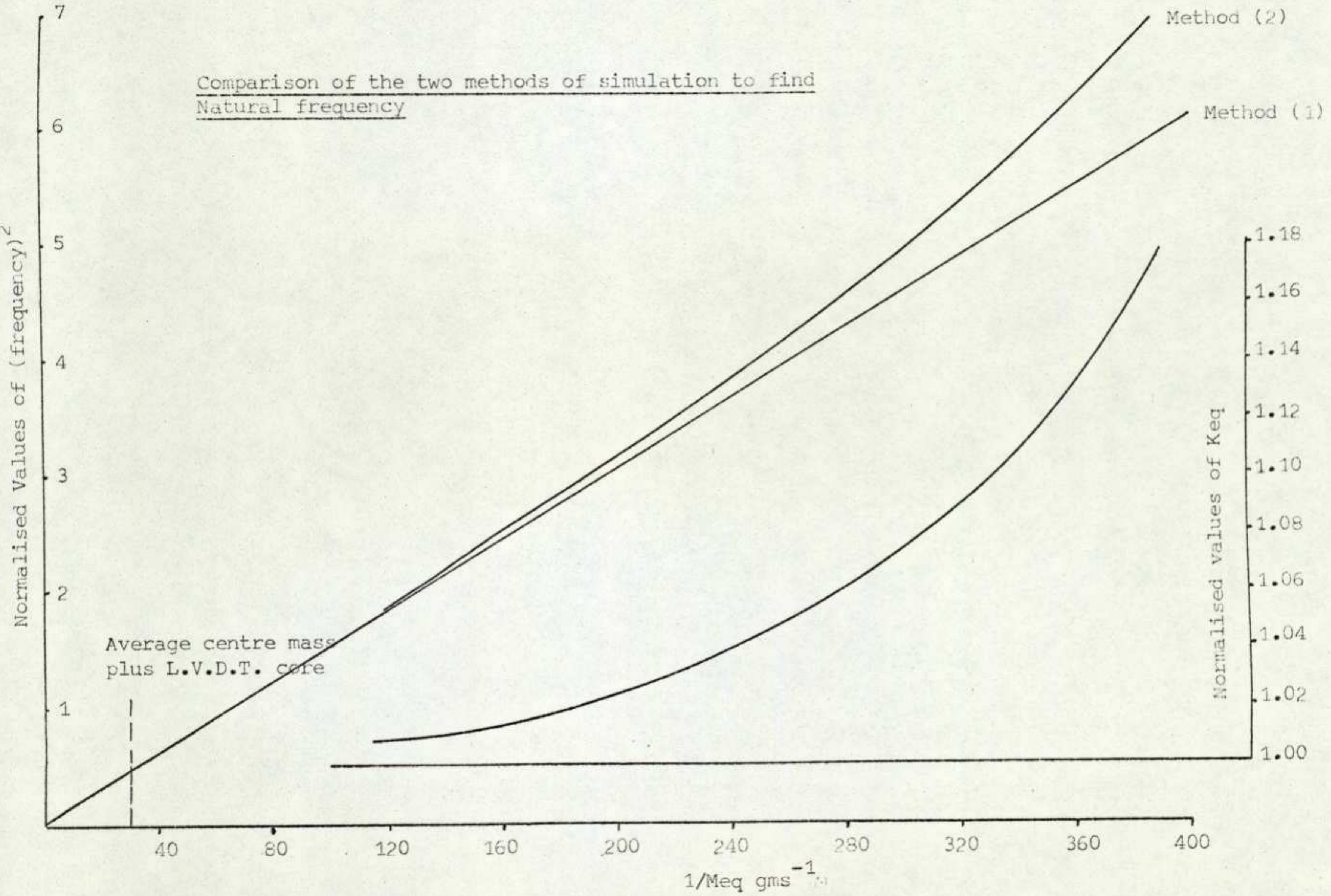
Comparison of the two methods of simulation to find
Natural frequency
Method (2)
Method (1)
Normalised Values of (frequency)^2
1
2
3
4
5
6
7
Normalised values of Keq
1.00
1.02
1.04
1.06
1.08
1.10
1.12
1.14
1.16
1.18
Average centre mass
plus L.V.D.T. core
40
80
120
160
200
240
280
320
360
400
1/Meq gms^{-1}

Figure 5.16

		Case (1)	Case (2)
For single stack combination	M_{eq} lbs (gms)	.05816 (26.4 gm)	.10341 (47 gms)
	K_{eq} lbs/in (N/mm)	276.18 (48.37)	268.022 (46.94)
	f_n (Hz)	215.50	159.21
	Method 1 f_n (Hz)	224.72	162.99
Two stack	Actual mass lbs (gms)	.01724 (7.8 gms)	.01724 (7.8 gms)
	Mass ratio	.3093	.31154
	1st mode f_n (Hz)	143.05	104.84

Table 5.2

We can now compare between the observed natural frequencies and the predicted; for case (1) the experimental result was between 139 - 140 Hz, and for case (2) between 102 - 104 Hz. As can be seen from Table 5.2 this is very good agreement.

All vibration tests had the extra loading of the vibrator attachments and vibrator stiffness, which, of course, were modelled for the computer simulations. The above results give justification for predicting the actual natural frequency of a two stack capsule with just the L.V.D.T. core attached, i.e. as it would be used in a pressure measuring instrument.

To obtain the actual natural frequency refer to Figure 5.5a and put $K_v = 0.0$ and reduce M_{att} by the value of the moving mass of the vibrator in the program. The result for the capsule without the simulated vibrator is shown in Table 5.3, a result which could not be found experimentally with the present apparatus.

Single stack combination	M_{eq} lbs (gms)	=	0.034051 (15.45)
	K_{eq} lb/in (N/mm)	=	290.082 (50.8)
	f_n (Hz)	=	288.64
	Method 1 f_n (Hz)	=	310.184
Two stack	Actual mass lbs (gms)	=	0.01724 (7.8)
	Mass ratio	=	0.3054
	1st mode f_n (Hz)	=	172.51

Table 5.3

5.5.3 Comparison of the two Rayleigh energy methods

A comparison of the two methods presented in this report indicates an expected non-linear relationship. This is shown up if case (2) from Table 5.2 is compared with the result of Table 5.3: using Rayleigh's straightforward energy method, frequencies of 162.99 and 310.184 Hz were found which, when iterated using the dynamic deflection curve, were reduced to 159.21 and 288.64 Hz, respectively. This shows a reduction of 2.325% and 6.945%; the smaller reduction was the case for which a larger mass was attached to the centre.

5.6 Discussion of experimental and computer simulation results

The experimental procedure employed for capsules was more complex than was required simply to find the natural frequency, the purpose being to put the analysis in a generalised form synonymous with systems engineering methods. The mechanical impedance being the quantity of interest is represented by $Z_m = r_m + \ell_m j\omega + \frac{1}{C_m j\omega}$; r_m is the mechanical damping which cannot be found from the process owing to the energy method assumptions, ℓ_m is the mass and $\frac{1}{C_m}$ is the mechanical stiffness. From the experiment ℓ_m worked out to be 0.0669 lbs (0.03035 kgs), and from the computer program the equivalent masses plus the attached masses for case (1), Table 5.2, summed to 0.066536 lbs (0.03018 kgs). The experimental stiffness was 134 lbf/in (23.47 N/mm) for the capsule stack, the equivalent stiffness predicted for a single stack is 276.18 lbf/in (48.37 N/mm), therefore for the two stack arrangement (essentially two springs in series) = 138.09 lbf/in (24.18 N/mm).

This also shows good agreement between experiment and theory, especially when considering the inherent errors within the experimental system. The effective mechanical blocking of the vibrator to find its blocked impedance was done by restraining the moving parts by clamping down the attachment. Electrically, this was poor as the results indicate; the zero "off-set" in Figure 5.13 is because the blocked impedance at low frequencies appears greater than the total impedance which is obviously not correct. Taking readings at different occasions produced impedance readings which differed by 20% for the same input frequency.

Another unavoidable source of error was the actual reading of the input current from the T.F.A., the readout being a "ranged" digital output, i.e. (0-10 mV), (0-100mV), (0-1000 mV), etc. So if the discrimination between readings was good for voltage, it would be poor for the current, approximately $\frac{1}{3}$, because the resistance of the vibrator is 3 ohms; if the current resolution was good the voltage would overload the T.F.A. and a higher range had to be used. A stabilised voltage and frequency source fed the L.V.D.T. and the output was assumed linear, although it was not compensated and had to be rectified. The signal was amplitude modulated and therefore the carrier frequency had to be removed. This was achieved using a basic peak detector circuit, and it was observed on the oscilloscope to give a good rectified waveform for large low frequency vibrations. But, unfortunately, the trace deteriorated for higher frequency vibrations which were accompanied by smaller amplitudes and hence the accuracy must have been lost when the D.C. value was measured on the T.F.A.

The plots of magnitude and phase show mainly a second order system, but with the phase shift being greater than 180^{o} and the asymptotic Bode plot being approximately -50 db/decade, indicates a higher order system. A third order system was not assumed because the first order effects of the vibrator were thought to be insignificant, therefore the effect is probably due to measurement errors. The time constant of the peak detector was 0.1551×10^{-3} seconds and at 450 Hz the period is 2.22×10^{-3} seconds, so the envelope shape would be distorted slightly by the discharge of the rectifying circuit (Figure 5.17)

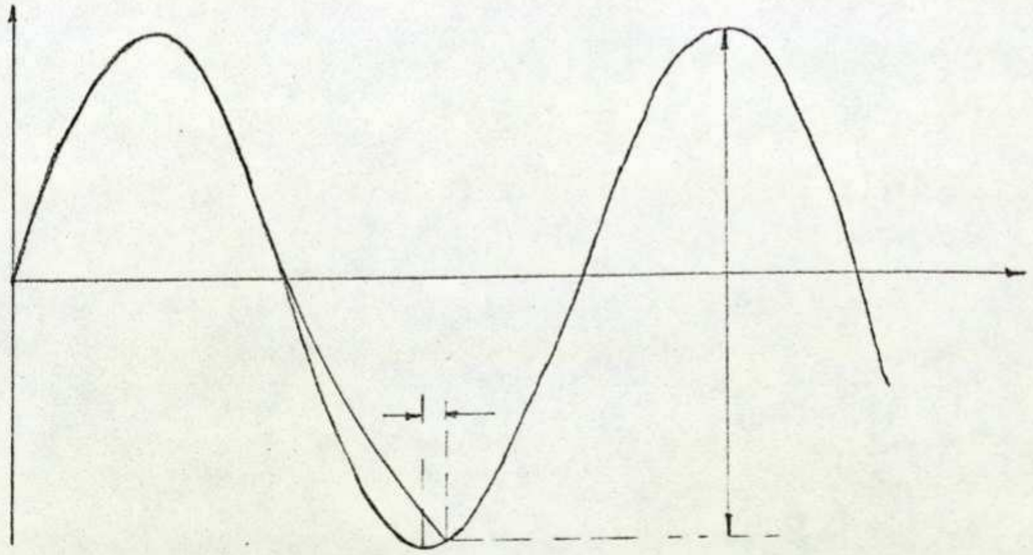

Figure 5.17: The effective change in the phase and amplitude at high frequencies

As the T.F.A. measures the fundamental of the waveform by Fourier series, the result would be different in amplitude as well as phase. This could well account for the third order effects noted in the frequency plots.

5.6.1 Discussion of the two methods of simulating the system

In the comparison of the two methods of computer predictions there is a large percentage difference in the natural frequency as the mass attached at the centre is reduced. This is because it is becoming less like the simplified mass-spring equivalent system which the analysis assumes, and the iterative method exemplifies this, whereas the ordinary Rayleigh's method is linear for ω_n^2 against 1/mass.

This effect is illustrated in Figure 5.16, which is a plot of computer predictions for a 0.006" (0.1524 mm) production diaphragm using the dynamic deflection curve method (Method 2) and varying the attached centre mass from some finite value down to zero; then the equivalent mass (M_{eq}) is just the effective mass of the diaphragm itself. The straight line tangential to the slope at the origin is the ordinary Rayleigh's method prediction (Method 1); this is an explanation for the higher reading in column 1, Table 5.1. Unfortunately, this is not the complete picture because the equivalent stiffness is also not proportional to f_n^2 as M_{eq} is varied (Figure 5.16). The program was able to converge rapidly (2 - 3 iteration), probably because the static deflection curve for the first mode of vibration was similar to the dynamic deflection curve. If a higher mode of vibration were required, this could conceivably be obtained from this program by feeding in an approximation to the deflection shape of the higher mode. This would, for a thin flat circular plate clamped at the edge, be an extension of the Ritz Method, ref. (37), where the deflection curve (x) is assumed to be a Series:

$$x = x_o \left(1 - \left(\frac{r^2}{a}\right)\right)^2 + x_1\left(1 - \left(\frac{r^2}{a}\right)\right)^3 \quad \text{, etc.}$$

and approximations to higher order modes can be found.

The program did predict the two natural fundamental frequencies of the two stack capsule, but the higher one has not been quoted because it fell outside the range of the measuring equipment.

5.7 Conclusions

The experimental tests on capsules performed by the author and the previous studies on diaphragms show that fundamental-mode dynamic behaviour can be adequately predicted by Rayleigh's energy method. Both "Bode type" plots (used in the diaphragm work) and the vector impedance locus plot (used in the present capsule work) show that damping is small enough to justify using Rayleigh's energy method.

The exact dynamic shell equations (without damping) were solved in an iterative method using the Rayleigh method predictions as initial guess values. This resulted in an improved prediction, as well as in removal of some slight anomalies that arose in previous diaphragm work.

With regard to accuracy of predictions when compared to experiment, the present capsule results are exceedingly good:

Experiment (Hz)	Theory (Hz)
139 - 140	143.05
102 - 104	104.84

However, as pointed out in previous chapters, such excellent agreement may be fortuitous. A more realistic assessment, taking into account uncertainties in material properties and in geometrical description, would be that the fundamental mode dynamic characteristics (i.e. equivalent mass, equivalent stiffness and first resonant frequency) can be predicted to within 10%. This is adequate for most practical purposes.

6.0 The Design of Corrugated Diaphragms and Capsules

This present chapter examines some of the ways in which the mathematical model can be used for obtaining design information, and actually designing by computer. A mathematical model, even when it has been validated against experiment, is still only an analysis tool; turning it into a successful design tool is often a formidable task.

The first sections look at the possible utilisation of the models, starting with a simple one-variable sensitivity analysis with the linear model, leading up to applying the non-linear model to an optimisation routine which is fairly complex. Finally, two industrial design problems are tackled, the first abandoned after the feasibility study, and the second culminating in an actual working design being incorporated in an instrument.

6.1 A general statement of the design problem

In the design of a corrugated diaphragm/capsule, a number of considerations must be taken into account. These may be divided into four main groups:

- (a) Material specification
- (b) Method of forming
- (c) Profile geometry
- (d) Method of assembly.

(a), (b) and (d), although necessary considerations, are usually fixed by constraints other than the actual output characteristic from the diaphragm/capsule (e.g. a certain material may be used for its corrosion-resistance abilities in preference to its spring properties). Therefore, the design specification in terms of input-output requirements is met almost entirely by (c) (the diaphragm dimensions and geometry). As can be visualised, the number of different corrugated profiles is infinite and therefore a simple systematic but flexible description of a corrugated profile is required.

In the initial development of the model, the geometry was automated in a way which was hoped useful for future design work. This was done (chapter 2) by specifying the geometry in terms of X, Y and R1 coordinates at peaks and troughs. Thus, the number of geometric variables for a plain sinusoidal-shaped diaphragm then become a function of the number of convolutions. Figure 6.1 is an example of such a four-corrugation diaphragm clamped at the outer edge with an initial flat section attaching it to a rigid centre boss.

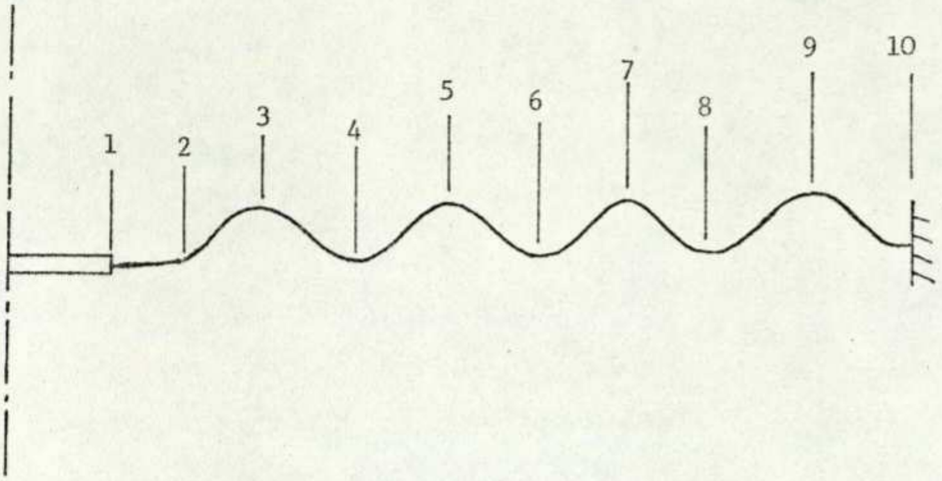

Figure 6.1: Showing input data points

The number of stations needed to describe this shape is ten and, with three variables at each station (X, Y,R1), it makes a possible total of 30, but, in fact, this is only 27 because the first station is generally started at zero for X and Y, with an infinite radius of curvature for R. For a three-convolution diaphragm, the number is eight stations, and for a five-convolution twelve, etc., hence the resulting number of possible design variables is very large. This number can be reduced by making three fairly un-restrictive assumptions:

(1) The height of convolution (except the outer edge) is constant or changing in a linear fashion;

(2) The radius of convolution is constant except at the outer edge;

(3) The wavelength of convolution is constant except at the outer edge.

These assumptions are quite reasonable and afford much more scope to the designer than previous attempts, refs. (8), (9) and (10). The outer edge, sometimes referred to as the end bead, is considered separately because of the likelihood of various methods of clamping used in instrument systems.

Therefore it is then proposed to use the profile shown below for reducing the number of variables in a design situation (Figure 6.2).

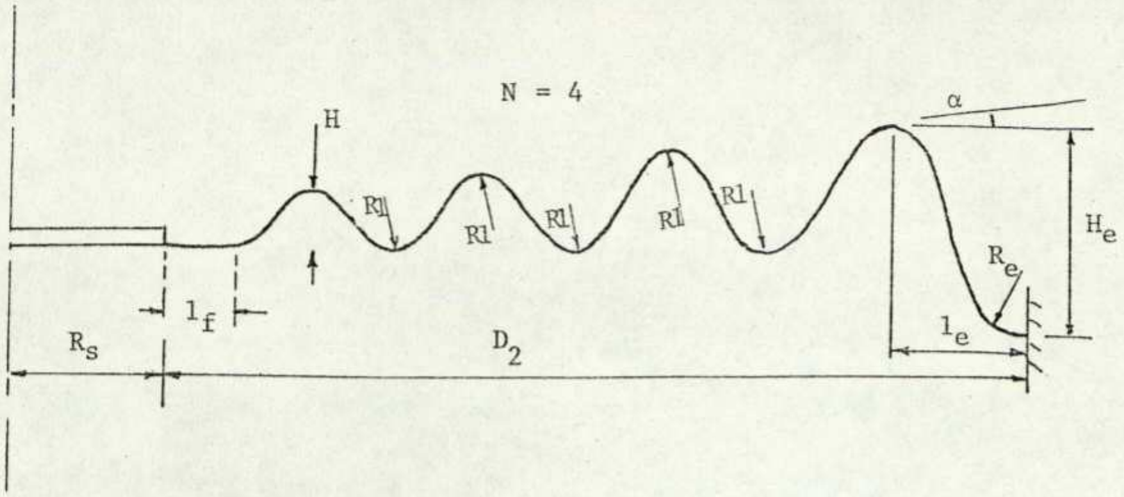

Figure 6.2: Geometric design variables

where (1) D_2 = active radius-centre boss

(2) R_s = centre boss

(3) l_f = initial flat section

(4) H = height of convolution

(5) H_e = height of end convolution

(6) l_e = length of end convolution

(7) R_e = radius of end bead

(8) Rl = radius of corrugation

(9) α = axial pitch

(10) N = number of convolutions

The particular configuration has only ten design variables, which are not dependent on the number of convolutions, as was seen to be the case before. The actual number of variables is twelve, because the material (e) and its thickness have to be considered, but in practice some of the variables will normally be constrained.

6.2 Sensitivity analysis using the linear model

Having therefore proposed the design variables to the model, some form of systematic sensitivity analysis can be undertaken: this is a straightforward operation whereby the chosen profile has one design variable varied, while the others (wherever possible) remain constant; the output displacement is then recorded.

Work along these lines was undertaken as long ago as 1939, ref. (14), where Wildhack and Goerke used the Buckingham Theorem of Dimensional Analysis to study diaphragms and concluded that: "Experimental observations on many diaphragms of a given shape show that the pressure deflection curve is fairly linear over the range of deflection up to $\frac{W}{D}$ = 2 per cent. For this range of deflections and over the range of $\frac{10^3 t}{D}$ from 0.6 - 6.0, the following approximate equation was found to hold for all the diaphragms tested:

$$\frac{W}{D} = \frac{P}{E/(1-\nu^2)} \; 2.25 \times 10^5 \left(\frac{10^3 t}{D}\right)^{-1.52} \quad \ldots\ldots\ldots \quad (6.1)$$

The statement and equation are not as useful as they at first appear: "fairly linear" and "approximate equation" are terms too vague to be applied to modern instrumentation. If there were one index value which was constant for all diaphragms, the design of diaphragms for various pressure ranges would be a trivial matter, but, unfortunately, this is not so and there is a reasonable difference in the index for different profiles. However, the equation:

$$W = kt^{-n}, \text{ where } k = \text{constant} \quad \ldots\ldots\ldots\ldots\ldots\ldots \quad (6.2a)$$

$$\log_e W = -n \log_e t + \log_e k \quad \ldots\ldots\ldots\ldots\ldots\ldots\ldots \quad (6.2b)$$

still holds for a particular profile of differing thicknesses. This was shown previously by Figure 4.2, where the different thicknesses of one diaphragm profile lie along a straight line of slope -n on logarithmic axes. The values of index found by the author for the variation of deflection with thickness averages at -1.35, which is less than that given by Wildhack and Goerke, ref. (14), but the value can vary up to a maximum of -3.0, which is a flat plate operating in the linear region. This can be seen by observation of the equations relating to pressure for a flat circular plate, of active radius R, Eqn. (6.3):

$$\frac{P}{E}\left(\frac{R}{t}\right)^4 = \frac{W}{t}\alpha + \left(\frac{W}{t}\right)^3 \beta \quad \ldots\ldots\ldots\ldots\ldots\ldots\ldots\ldots \quad (6.3)$$

where α and β are constants.

Consider again the flat plate and the functional relationship (for the linear region) of: $W = kR^n$, where n = +4. It would be most useful to be able to extend this type of functional relationship to corrugated diaphragms, but, as was pointed out in Chapter 1, design variables, except thickness, are to some extent inter-related. With a flat plate, the active radius may be altered completely independently of the other variables, but altering the active radius for a corrugated diaphragm would change the profile, e.g. the wavelength would have to be increased to accommodate an increase in active radius without adding in more convolutions. The reason for the wavelength not being quoted on Figure 6.2 is that the profile may be adequately specified without it; by knowing N, R_s, l_f, and D_2, the wavelength of corrugation is known, therefore only the minimum required number of variables is included on Figure 6.2.

The value of the index n has more significance when considering the Bode sensitivity parameter (B_p), which is defined as a factional change in the dependent variable (Y) divided by the factional change in the independent variable (X).

$$B_p = \frac{\delta Y/Y}{\delta X/X} = \frac{\delta Y.X}{\delta X.Y} \quad \ldots\ldots\ldots\ldots\ldots\ldots\ldots\ldots\ldots\ldots \quad (6.4)$$

Now, if generally:

$$W = kx^n,$$

then $$\frac{dW}{dx} = nkx^{n-1}$$

and in the same form as (6.4), but taking the limit:

$$\frac{dW}{dx} \cdot \frac{x}{W} = nkx^{n-1} \cdot \frac{x}{kx^n} = \underline{\underline{n}}$$

It is, therefore, apparent that the index is a direct measure of the sensitivity of the diaphragm to a particular design variable. Some quantities, being more sensitive (i.e. a larger absolute value of n) predominate over other quantities, and the general relationship $W = kx^n$ holds. A good example of this is the height of corrugation which cannot be varied independently of the radius of convolution, but the relationship $W = kH^{-n}$ holds over a large range because the latter dominates the former in sensitivity. This can be seen from Figure 6.3, which shows the relative increase in deflection, of changing the radius of curvature at each convolution peak and trough compared with the same change of height of corrugation. A plot of $\log_e W = -n \log_e H + \log_e k$ over a considerable range of H is seen to be a straight line (Figure 6.4).

Other variables do not exhibit this useful feature so well. To illustrate, consider the axial pitch α: if this is varied the heights of corrugation (H) will increase along the generator and the radius of curvature (R1) will probably have to be reduced to allow for the increase in (H). Figure 6.6 shows the effect of varying this angle between -3^o and 9^o plotted against the centre deflection: although this is a smooth curve there is no single $W = k\alpha^{-n}$ relationship which will fit the entire

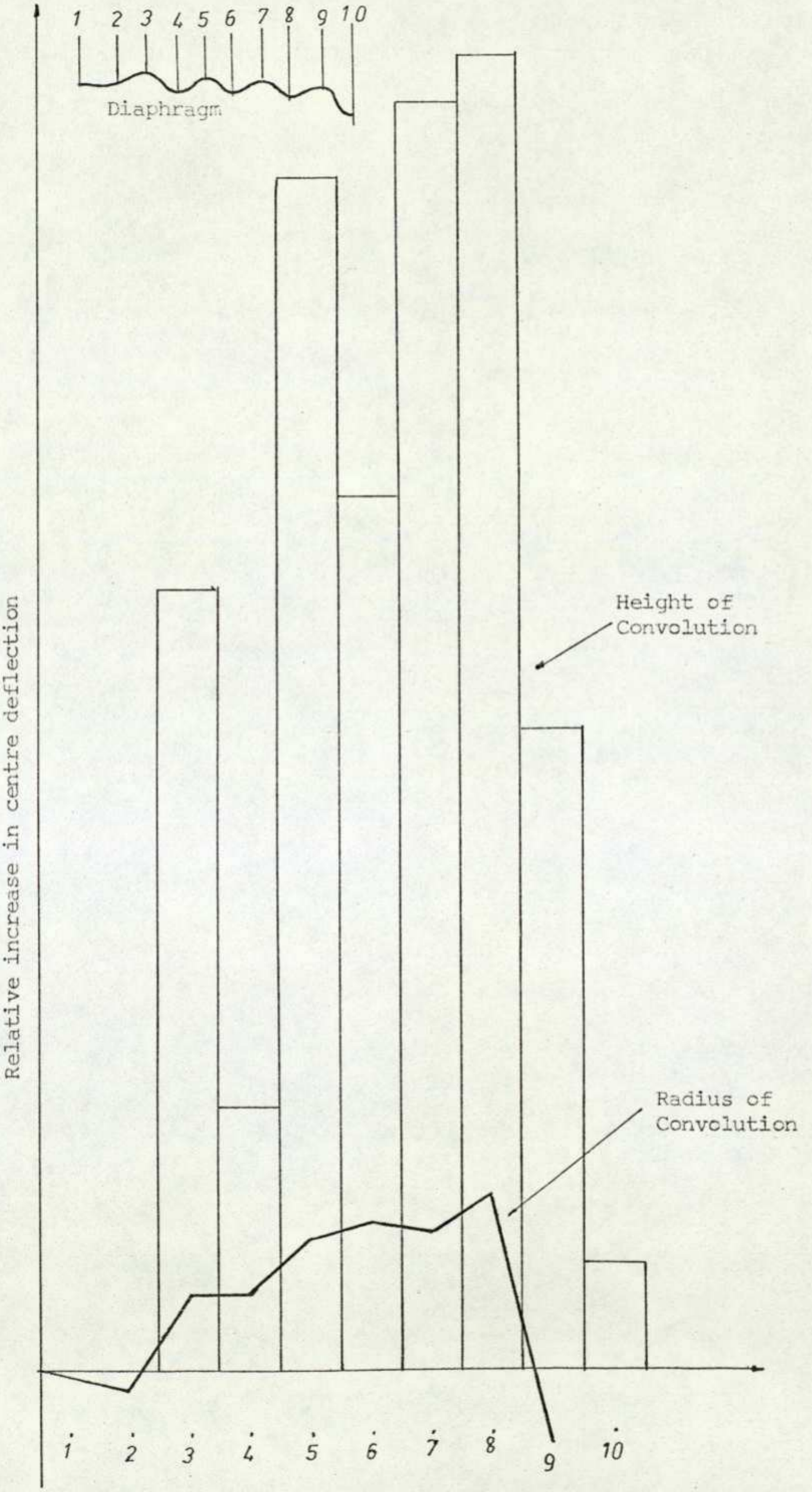

The relative effect on the centre deflection of increasing either the height of convolution or the Radius of Convolution by 10 per cent range, but over shorter ranges, e.g. 2^o to 4^o, a straight line on logarithmic axes of slope -0.344 can be fitted. This "short range" fit appears to be the case with other design variables as well. It is, therefore, proposed to use the general $W = kx^n$ relationship for small "design perturbations" around the original as a direct measure of the sensitivity to a particular profile of its design variables.

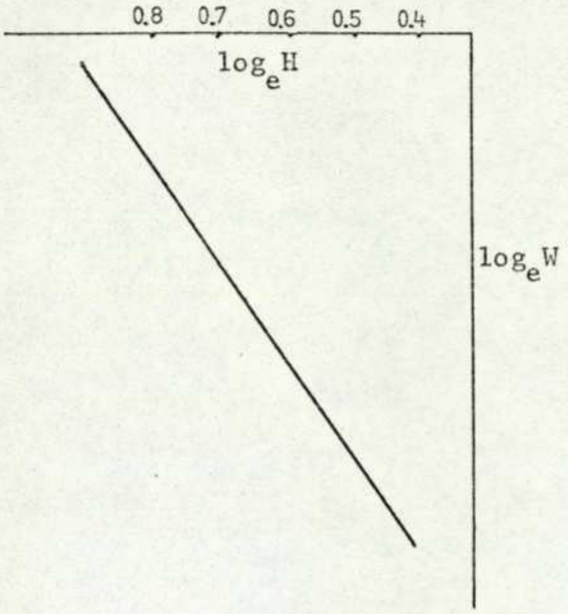

Figure 6.4: Plot of $\log_e H$ against $\log_e W$

So far, discussion has been exclusively on the basic sinusoidal diaphragm shape, whereas the possible number of profile configurations is immense. Andreeva, ref. (10), compared the characteristics of diaphragms of saw tooth, trapezoidal and sinusoidal profile with identical corrugation depth, and number of convolutions (Figure 6.5).

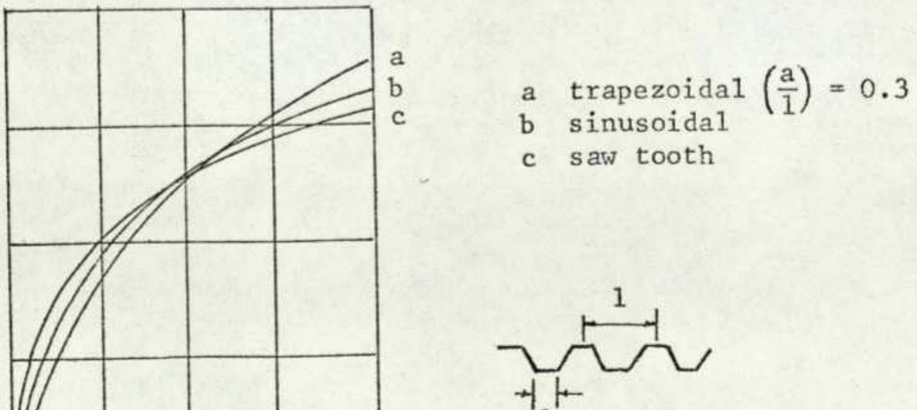

Figure 6.5

Fig. 145 from Andreeva, ref.(10)

Figure 6.6 and 6.7

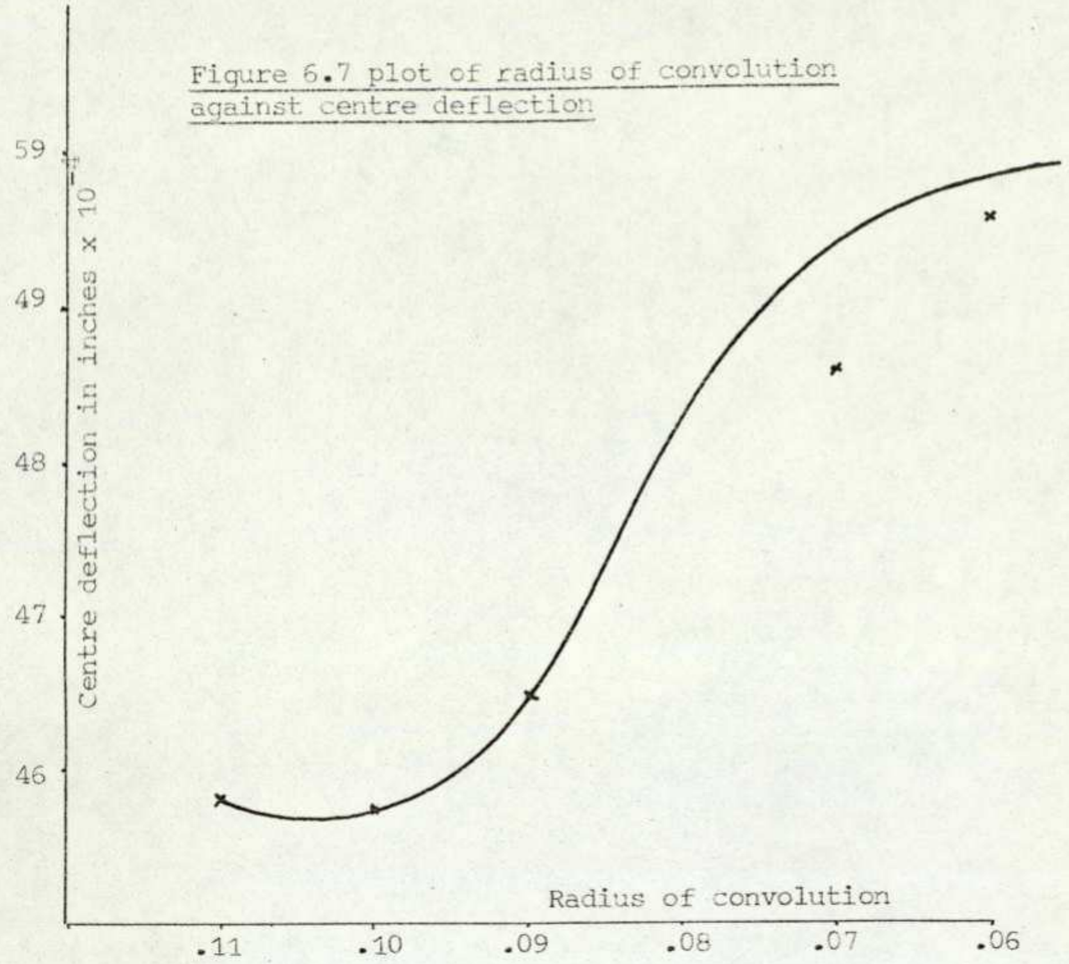

Figure 6.7 plot of radius of convolution against centre deflection

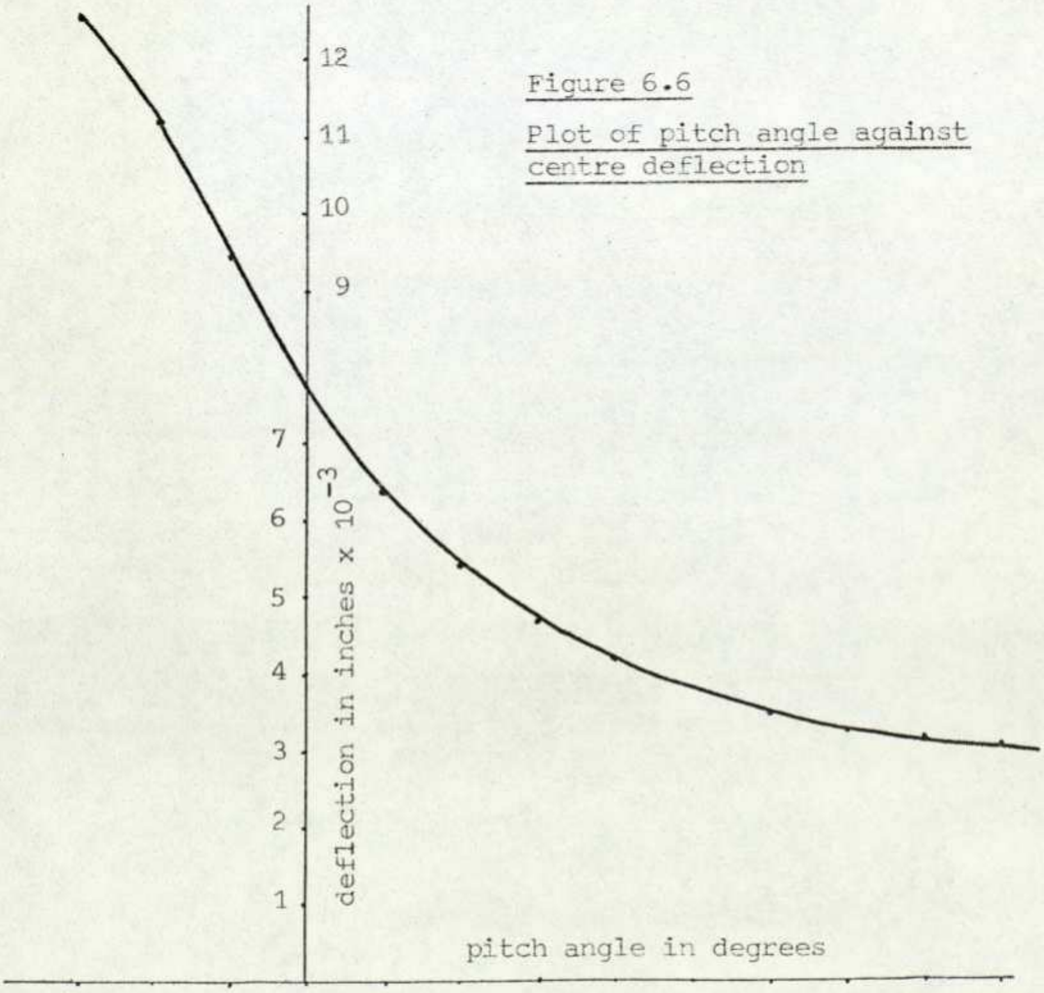

Figure 6.6

Plot of pitch angle against centre deflection

From the figure reproduced from his book, Andreeva states that:

> "The saw-tooth profile diaphragm, although initially more sensitive, has the highest non-linearity, and the trapezoidal profile diaphragm with a sufficiently broad flat section has the lowest non-linearity. The influence of the profile shape on the characteristic is small, however, and it is accordingly more convenient to control the shape of the diaphragm characteristic by varying the material thickness or the corrugation depth."

From a practical point of view, trapezoidal and saw-tooth profiles are much more difficult to manufacture owing to the very tight radii of curvature, which will cause the metal to split. It is, therefore, proposed not to present results of an extensive sensitivity study on various profile shapes, only to indicate that it may be done by using a simple example.

In the example chosen - an arbitrary sinusoidal profile - the radii of curvature were successively reduced so that the diaphragm approximated to a saw-tooth profile. This is shown in Figure 6.7: as the radii are reduced from 0.1 inch down to 0.06 inch, the increase in centre deflection is indicated, verifying the Andreeva statement. If the radius is increased to 0.11 inch (this is the maximum possible with the particular design), the deflection also increases, showing a local minimum, which is of little use when the general requirement is to maximise output.

The work so far discussed is based on results from the linear diaphragm model and can only give the initial sensitivity (the tangent to the curve at the origin). A linear prediction can be obtained by computer in a very short period of time, approximately 40 milliseconds, therefore the design approach may be studied with a view to automating it, as the model does not use an exorbitant amount of computer time.

6.3 Design approach using the linear diaphragm model

This section aims to approach the design problem both from the theoretical and the practical points of view. The design methodology is based on automating a procedure which has been demonstrated in the previous section on sensitivity. Practically, the method is the same as the procedure a designer would take if he had the sensitivity parameters available to him as well as the constraints to the problem. The example problem which is used illustrates the magnitude of the sensitivity parameters and assesses how best to use them.

The second problem attempts a design using an optimisation procedure: this makes the example entirely a computer-orientated problem, mainly because of the number of variables involved and the time required to reach a solution.

6.3.1 Design based on the generation of sensitivity parameters

The method proposes a design based on the variables laid out in Figure 6.2 and, as the linear model is used, a specific deflection for a given pressure is the only criterion to be met. A set of initial or guess values is fed into the program and a deflection found for that particular profile. Assuming that the initial deflection is not the required deflection (unlikely, but possible), small perturbations of the geometric design variables are made and the value of the index n (the Bode sensitivity parameter) is stored. The index is found in both directions, increasing and decreasing the variable; slight differences are apparent for each direction as the typical results shown below indicate. The number of convolutions (N) is strictly a geometric variable, but for ease of computation is kept constant.

		Guess value	Index n	
			Increasing by 5%	Decreasing by 5%
(1)	D_2	0.966"	3.5719	3.6173
(2)	R_s	0.205"	0.7866	0.7570
(3)	l_f	0.0465"	0.0247	0.0102
(4)	H	0.05"	-1.3763	-1.3882
(5)	H_e	0.0817"	-0.2042	-0.2168
(6)	l_e	0.165"	-0.3746	-0.3572
(7)	R_e	0.025"	-0.0131	-0.0127
(8)	R	0.07"	-0.1644	-0.1590
(9)	α	2.0^o	-0.3969	-0.3840
(10)	N	3		
(11)	t	0.004"	-1.2308	-1.2290

Deflection at
150"wg (402 KPa) =
0.01199 inches
$E = 30 \times 10^6$ lbf/in^2
2.068×10^{11} MN m^{-2}

It can be seen that the most sensitive parameters are D_2, H and t, in that order of magnitude, D_2 being much more sensitive than the other two: also it is seen from the sign of the index which direction the sensitivity acts, i.e. if the radius (D_2) is increased, the deflection increases, therefore the index is positive, and if the thickness (t) is increased, then the deflection decreases and n is negative.

If the desired deflection is 0.0125", the present design will have to be altered to give about 4% more deflection. At this point, practical constraints on the problem may be considered by the designer:

(a) The active diameter for the diaphragm will probably be fixed. This is because it may have to fit into an existing space or it may have to be formed with press-tool jigs which accommodate only a certain diaphragm form tool die.

(b) The centre boss size may also be fixed to comply with existing equipment: it will certainly have a minimum size requirement so it can be manufactured and attached to the diaphragm.

(c) The thickness is always a "compromise" variable because the material is usually available in fixed integer thicknesses, e.g. 0.003, 0.004, 0.005 inches, etc.

Therefore, the variable easily adjusted to increase the deflection is the height of convolution (H); any of the non-constrained variables could possibly be considered, but the index of (H) is much larger and only a small adjustment will be necessary. Using $W = kH^{-n}$ as a prediction, a new value of H is proposed and the deflection found. The deflection needs to be increased, hence H needs reducing so n is taken from the second column, i.e. -1.3882. The original design was somewhere near the required deflection and the updated value came within the set design tolerance, in this case 0.2% of the required value. If it did not, the process would have been repeated until it did. This simple iterative procedure using one variable for design adjustment has the advantage that it is inexpensive on computer time, the example given taking only 680 milliseconds C.D.C. 7600 computer time. The obvious disadvantage to the method is that, should the original guess profile give an answer which is a lot different from the desired value and the adjustment on H is such that it affects other variables (e.g. an increase in the height of corrugation can cause the radius of curvature to be too large unless allowed for), then the program will fail.

An extension to the basic method presented above was proposed partly to overcome the previous disadvantage, but partly also to consider other criteria: the variables with the largest sensitivity parameters are also the variables which must be controlled the tightest, because any variations will cause large deviations in output. The centre boss, overall diameter, and thickness are fairly easily controlled to within tight tolerances for manufacturing purposes. But owing to the unavoidable spring-back phenomenon of diaphragms, the height of convolution becomes a very difficult variable to control. It was, therefore, decided to develop a design approach which would minimise the sensitivity of the design to the height of convolution and, in doing this, an upper and lower tolerance band was placed upon the variables, which was able to eradicate the previous problem. This was achieved using a random number generator routine, so when a suitable design was found based upon the previous method, design variables were altered at random between the tolerance band for a preset number of iterations, and the best design based on the desired deflection and minimum index for H was stored and printed out. The example chosen to illustrate this is the same numerically as the one before, except the thickness has been reduced to 0.004 inches to give a larger error between the actual and desired value of deflection, in the order of 20%. The average of the two indexes (increasing and decreasing the variable) is reproduced for ease of comparison:

Variables	Guess Values	Index	First Iteration	Index	Final Optimum Result	Index
(1) D_2	0.966		0.966		0.966	
(2) R_s	0.205	0.725	0.205	0.6758	0.205	0.677
(3) l_f	0.0465	0.0075	0.0465	0.003	*0.0460	0.01336
(4) H	0.05	-1.2218	0.0602527	-1.0351	*0.05657	-0.905
(5) H_e	0.0817	-0.2313	0.0817	-0.2445	*0.081755	-0.243
(6) l_e	0.165	-0.331	0.165	-0.2662	*0.160567	-0.2396
(7) R_e	0.025	-0.0145	0.025	-0.168	*0.02597	-0.0176
(8) R	0.07	-0.0397	0.07	0.064	0.07	0.132
(9) α	2°	-0.2962°	2°	-0.211°	*2.78°	-0.255
(10) N	3		3		3	
(11) t	0.004	-1.353	0.004	-1.4762	0.004	-1.52963
Deflection	0.0157"		0.01267"		0.01256"	

(* variables marked thus were the only values altered by the random number generator routine.)

The main objectives have been achieved, the height of convolution H was increased from 0.05 to 0.0602527 inches to reduce the deflection to 0.01267 inches, but finally a better design was found (albeit at random) which did not increase H so much, i.e. H = 0.05657", but managed to reduce the deflection further: also, the sensitivity of the design to the value of H was reduced from -1.2218 to -0.905, but this seems to be at the expense of increasing the sensitivity to the thickness variable.

The results are encouraging because it appears that some form of automatic design procedure may be applied to find a local optimum result, although the computing time is very much increased, the above example taking 56.81 seconds of C.D.C. 7600 computer time.

6.3.2 Design using the linear model and random shrinkage optimisation

The work was then further extended to use an optimisation routine again based upon a random number generator, in which the design variables were altered between upper and lower values. The random number routine gave the first profile and, therefore, the need for an initial guess shape was removed.

The method consists of a random search with iterative shrinkage, random points for each variable X_1 to X_{NUMR} being generated from the expression

$$X_i = l_i + r_i(u_i - l_i) \qquad i = 1, \ldots\ldots NUMR$$

where l_i = estimated lower limit for X_i
u_i = estimated upper limit for X_i
r_i = random number uniformly distributed between zero and one.

Any generated point that violates an inequality constraint is discarded; if the constraints are violated NSMAX times consecutively, the process will stop. The search is begun by evaluating NUMR random points by the use of the above equation, NUMR being a multiple of the number of variables. From these the best NRET are selected and used as the basis for a new and shrunken range for each variable. NRET is defined by NUMR/NSHRIN, where NSHRIN is a shrinkage factor. Within this new space, NUMR new random points are evaluated. These, plus the previous NRET best, are sorted to yield a new NRET best and a new shrunken space. The process is repeated until the range of each variable is acceptably small or until the range has been shrunken MAXN times. For a complete listing and more information, see ref. (40).

For this particular example, NSMAX = 300
NSHRIN = 4
MAXN = 400.

The optimality criterion was a minimisation and the function chosen utilised the linear model as much as possible by minimising the error between required and actual sensitivity, reducing the sensitivity to variations in thickness and height of corrugation, and minimising the stress level. The function to be minimised is $\bar{U}$ and the required deflection $\bar{W}$ (as before 0.0125 inches).

$$\bar{U} = \alpha(W - \bar{W})^2 + \beta\left(n|_H + n|_t\right)^2 + \text{STRESS} \quad \text{..........} \quad (6.5)$$

α and β are weighting chosen to suit the problem, i.e. the relative importance attached to each function in $\bar{U}$.

$n|_H$ = Bode sensitivity index for height of corrugation,

$n|_t$ = Bode sensitivity index for thickness.

The STRESS quantity was either the numeric value of the maximum stress found in the diaphragm or zero. Usually a designer will wish to keep the stress values below a certain level, e.g. a percentage of the yield, therefore it was decided to run the routine with zero if the value of STRESS was less than a predetermined value, and, if it was greater, penalise the function very heavily so that it acted similarly to a constraint.

Geometrically, the problem of forming a profile from data which is picked at random would be a case of luck unless the freedom of movement in each variable space was very limited. So as not to have this restriction, constraints now have to be rigidly applied. In this particular exercise the number of convolutions was allowed to vary, making a diaphragm profile which had either 2, 3 or 4 corrugations: obviously, there must be a whole number of corrugations and, therefore, a constraint is required to ensure this is indeed the case. The radii of curvature must not be so large that they interfere and the value of D_2 must be at least the sum of l_f and l_e. Inequality constraints, such as the last example, have to be made into equalities of positive magnitude, i.e.

$$D_2 > (l_f + l_e)$$

therefore $\phi_1 = D_2 - (l_f + l_e)$, i.e. $\phi_1 > 0.0$.

All the variables are held in the program as a minimum and maximum quantity, but should they be required as constants, the two values are made equal, as is seen in the example given below, where only eight variables are worked on. The upper and lower limits are the choice of the designer and reflect the freedom available to him.

Example of random optimisation with shrinkage

Design Variable	Upper limit	Lower limit	Final value after 15 iterations
D_2	0.966 inches	0.966 inches	0.966 inches
R_s	0.205 inches	0.205 inches	0.205 inches
l_f	0.045 inches	0.03 inches	0.04295 inches
H	0.06 inches	0.04 inches	0.04883 inches
H_e	0.09 inches	0.08 inches	0.08558 inches
l_e	0.16 inches	0.14 inches	0.14368 inches
R_e	0.03 inches	0.02 inches	0.02608 inches
R1	0.075 inches	0.05 inches	0.06548 inches
α	3.0°	2.0°	2.7675°
N	4	2	3
t	0.005 inches	0.005 inches	0.005 inches

The value of STRESS which could not be exceeded was 0.44 of the yield and the values of α and β, the weighting functions, were 100.0 and 0.01, respectively. The program was allowed to run for 15 cycles, during which $\bar{U}$ had been reduced from 0.3227×10^{-3} down to 0.1432×10^{-8}. The problem converged to the required deflection to within 4 significant figures and the maximum value of stress was only 0.237 of the yield value. The shrinkage range of the H variable over the 15 cycles is shown in Figure 6.8.

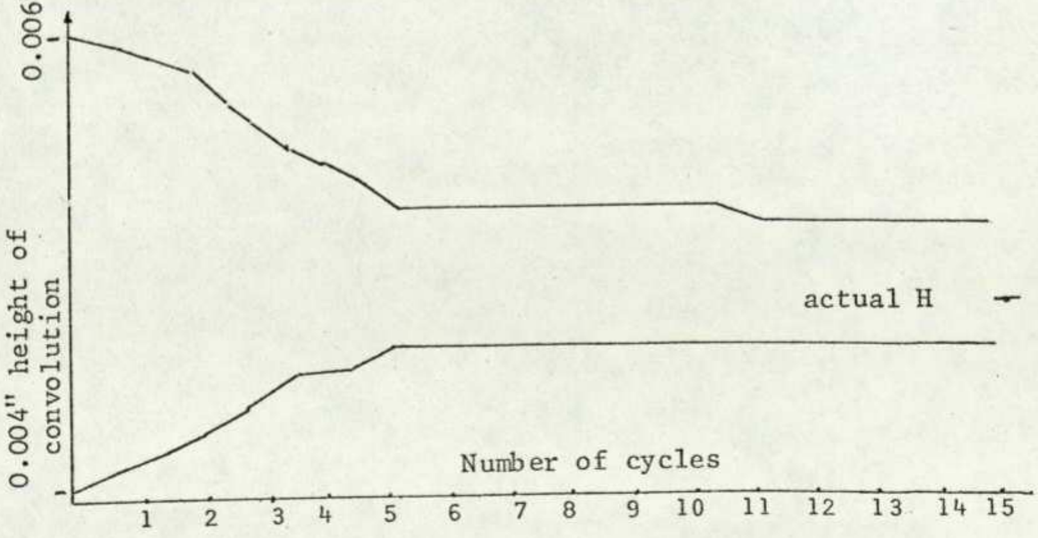

Figure 6.8: The variation of H as the range is shrunken

This method of optimising a design is less expensive on computer time although the search routine is much larger, the reason being that the model itself is run less times and the example cited took 20.865 seconds C.D.C. 7600 computer time.

6.4 Design approach using the non-linear diaphragm model

Once a non-linear model is established it appears to make work with the linear prediction somewhat redundant, except for the fact that the linear model is so much faster and able to lend itself to optimisation routines with a fair degree of success, if with only a small degree of practical usefulness. Therefore, the overall design becomes a hierarchical type where the linear model finds a possible solution which is checked upon the non-linear model to find its deviation from linearity and its actual sensitivity (Figure 6.9).

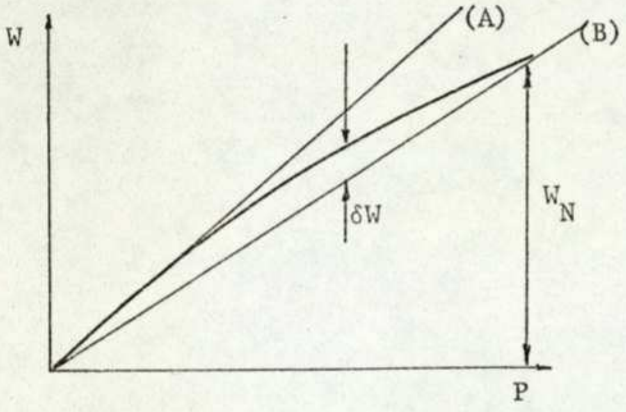

{Refer to Chapter 3 for non-linearity definition}

Figure 6.9: Non-linearity

If these values are not within the tolerances allowed for in the design specification, then the process can be repeated until a suitable solution is found: of course, this process is not automatic and involves a lot of designer interaction. The designer can apply experience gained in undertaking sensitivity analysis with the non-linear model. Results of a sensitivity analysis on the typical corrugated diaphragm shape are included to illustrate the general effect the design variables have upon sensitivity in conjunction with the non-linearity.

6.4.1 Non-linear sensitivity analysis

Referring to Figure 6.9, line (A) is the linear prediction, the curve is the non-linear prediction, and line (B) is a line projected back to the origin from the end of the non-linear range. If the deviation of the actual curve from the two lines (A) and (B) is plotted against working range in both directions, the graph is like Figure 6.10.

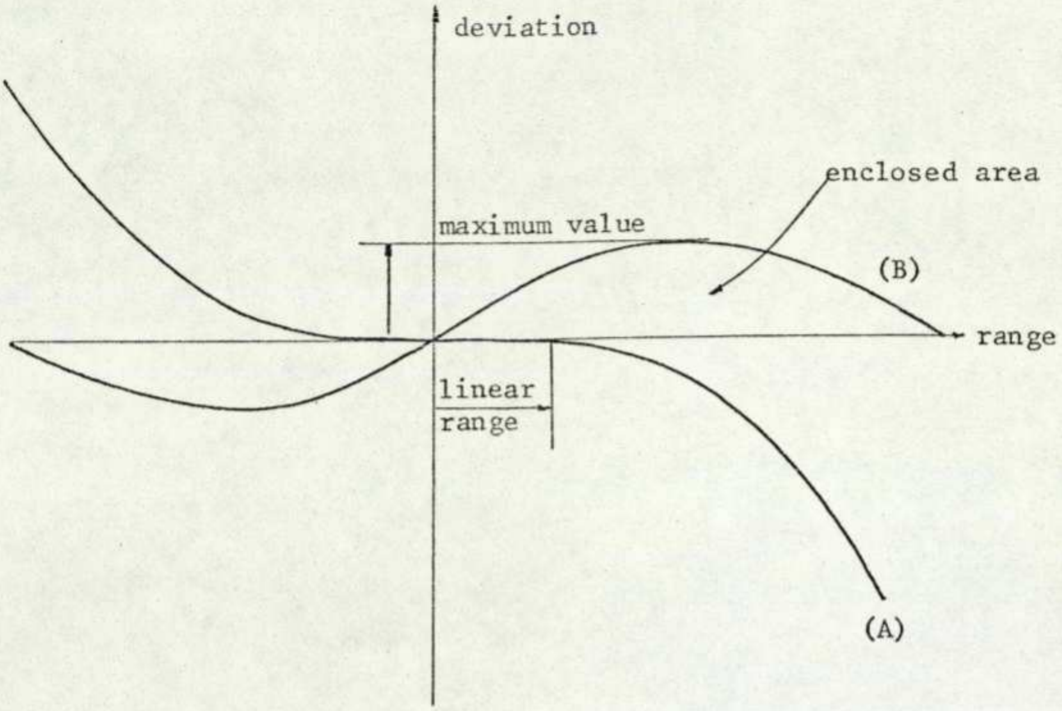

Figure 6.10: Alternative representation of non-linearity

The non-linearity was represented by three parameters: the linear range, the enclosed area, and the maximum value of the deviation from line (B). The linear range was represented as a fraction of the total range, given when the deflection deviated from the linear prediction by more than 0.1%. The profile used in the example is the basic three-convolution diaphragm used in the previous examples with a thickness of 0.005 inches; each of the variables was increased and decreased independently by 5%, except the number of corrugations which was only decreased (down to 2).

	(Slope A x 10^{-3})	(Slope B x 10^{-3})	Area x 10^{-5}	Linear range fraction of total	Maximum deviation %
Basic shape:	2.24800	2.20539	−0.943205	0.4375	−0.75457
l_f	2.24864	2.20603	−0.941961	0.4375	−0.753054
	2.24882	2.20421	−0.943861	0.4375	−0.7559643
α	2.21304	2.17039	−0.909312	0.375	−0.7493231
	2.28348	2.24094	−0.97927	0.4375	−0.7606376
N	3.56516	2.86512	−34.054	0.375	−11.1887
D_2	2.69728	2.62394	−1.99392	0.375	−1.1080
	1.86118	1.83536	−0.45653	0.4375	−0.5317293
R_s	2.3356	2.28808	−1.09169	0.4375	−0.808839
	2.16303	2.12487	−0.813826	0.4375	−0.7034366

(continued over)

	(Slope A x 10^{-3})	(Slope B x 10^{-3}	Area x 10^{-5}	Linear range fraction of total	Maximum deviation %
H	2.10106	2.06645	−0.702219	0.4375	−0.64242
	2.41558	2.36103	−1.31537	0.4375	−0.911653
H_e	2.21664	2.19804	−0.861016	0.4375	−0.70969
	2.28165	2.2339	−1.04742	0.375	−0.8118
R1	2.2334	2.1916	−0.911813	0.4375	−0.7386045
	2.26067	2.21714	−0.974567	0.4375	−0.7712575
R_e	2.24604	2.20369	−0.937949	0.4375	−0.7487389
	2.2499	2.20714	−0.948569	0.4375	−0.75747
l_e	2.21486	2.17026	−0.931317	0.375	−0.77379
	2.28224	2.24093	−0.959248	0.4375	−0.7455875

The noticeable point about this list of results is the effect that the changing of the number of convolutions has upon the linearity; although the sensitivity has risen in reducing the number of convolutions, the non-linearity is substantially increased. This indicates, and is borne out by other runs, that having a high convolution density will reduce non-linearity (in a diaphragm clamped at the outer edge), without penalising sensitivity too much. To complete the picture, the variation to thickness can be shown by reducing to 0.004 inches and increasing to 0.006 inches, giving an index of −1.35:

Thickness (inches)	(Slope A x 10^{-3})	(Slope B x 10^{-3})	Area x 10^{-5}	Linear range fraction of total	Maximum deviation %
0.006	1.76715	1.75084	−0.2913	0.5625	−0.378518
0.004	3.08388	2.95531	3.8885	0.3125	−1.6467

Having thus perturbated all the design variables, the major observation can be pointed out - namely, that if the sensitivity is increased, the linearity is decreased and vice-versa. Therefore, in any design procedure involving the two design criteria a "trade-off" situation will always exist, indicating the possibility of an optimum design dependent upon the constraints. Again, exhaustive tests can be made using the non-linear model to gain the sort of design experience shown here; the same profile was run again, but putting α = zero, not 2°. This is a fairly large change in the profile making the diaphragm more sensitive generally and increasing the values of area and maximum non-linearity as expected, but the linear range was increased: whereas the average figure in the previous example was 0.4375, the average figure for α = zero was between 0.75 and 0.8125. This means that the shape of the two pressure-deflection curves is characteristically different in that one is a smooth gentle curve and the other is initially straight and curves more rapidly towards the end of the range (Figure 6.11), giving a large deviation from linearity as defined by Figure 6.9.

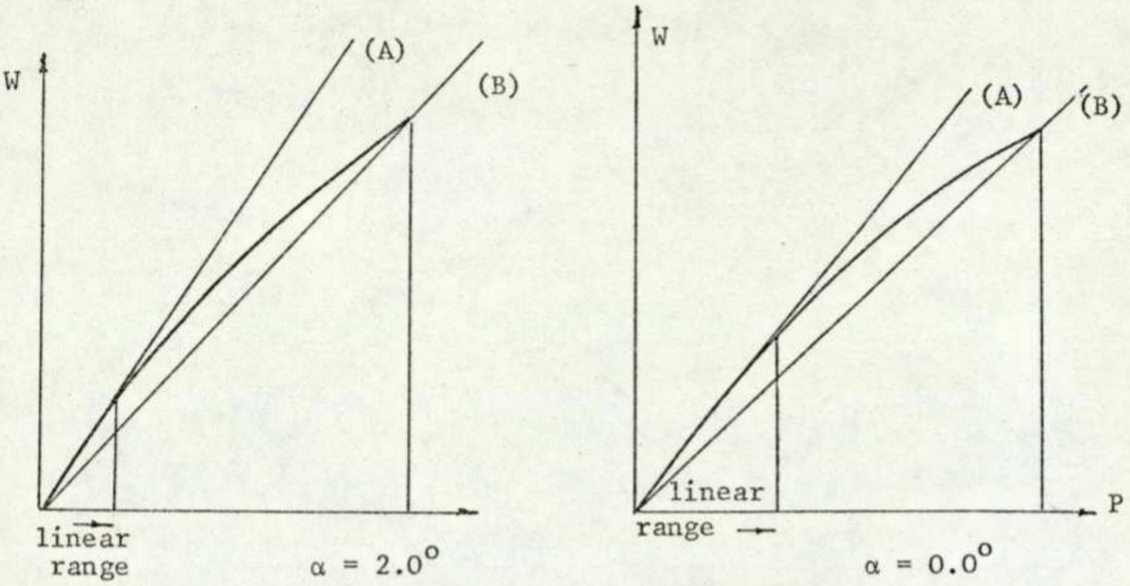

Figure 6.11: Different non-linearity patterns

It is not felt necessary to give more examples of this type of investigation as the work is quite straightforward and, therefore, it is not relevant to present them in any great detail here.

6.4.2 The use of Rosenbrock's "hill climbing" method for designing with the non-linear model

The next logical step in the development of a design methodology for corrugated diaphragms was the investigation of an optimisation routine based upon the two opposing design requirements - sensitivity and linearity. The choice of optimisation routine was somewhat arbitrary and Rosenbrock's "hill climb" was used, being a good general-purpose routine for solving multivariable non-linear problems with non-linear inequality constraints. A full description of the routine is given in Appendix IV.

The main problem with running a design exercise using an optimisation routine is computer time: this disadvantage was highlighted earlier when using the linear model, and will be magnified using the non-linear model because of the additional computer time involved. Bearing this in mind, a problem was set up to design a flat plate clamped at the outer edge with a centre boss, under pressure loading. This may seem a trivial problem, but it introduces the sensitivity versus non-linearity optimality function without getting "bogged down" with too many variables and constraints. The minimisation function was of the form:

$$\bar{U} = \sum_{i=1}^{i=N} \left(\frac{W_1}{P_1} P_i - W_i\right)^2 + \alpha\left(\frac{P_N}{W_N}\right) \quad \ldots\ldots\ldots\ldots\ldots \quad (6.6)$$

where N = the number of pressure points.

The first term is the sum of the squares of the deviation from the linear prediction (the linear prediction of sensitivity being taken as the first displacement, divided by the first pressure point). The second term has a weighting factor α multiplied by the reciprocal of the sensitivity, i.e. the sensitivity is maximised. Upper and lower limits were necessary for the four variables - Young's Modulus E, active radius, centre boss and thickness - and the problem constraint required was that the active radius be greater than the centre boss. To gain an idea of what result to expect, Andreeva, ref. (10), plots the pressure against deflection in non-dimensional form for various centre boss sizes (Figure 6.12). The first run of the program used only the non-linearity part in the optimality function to test the program: the

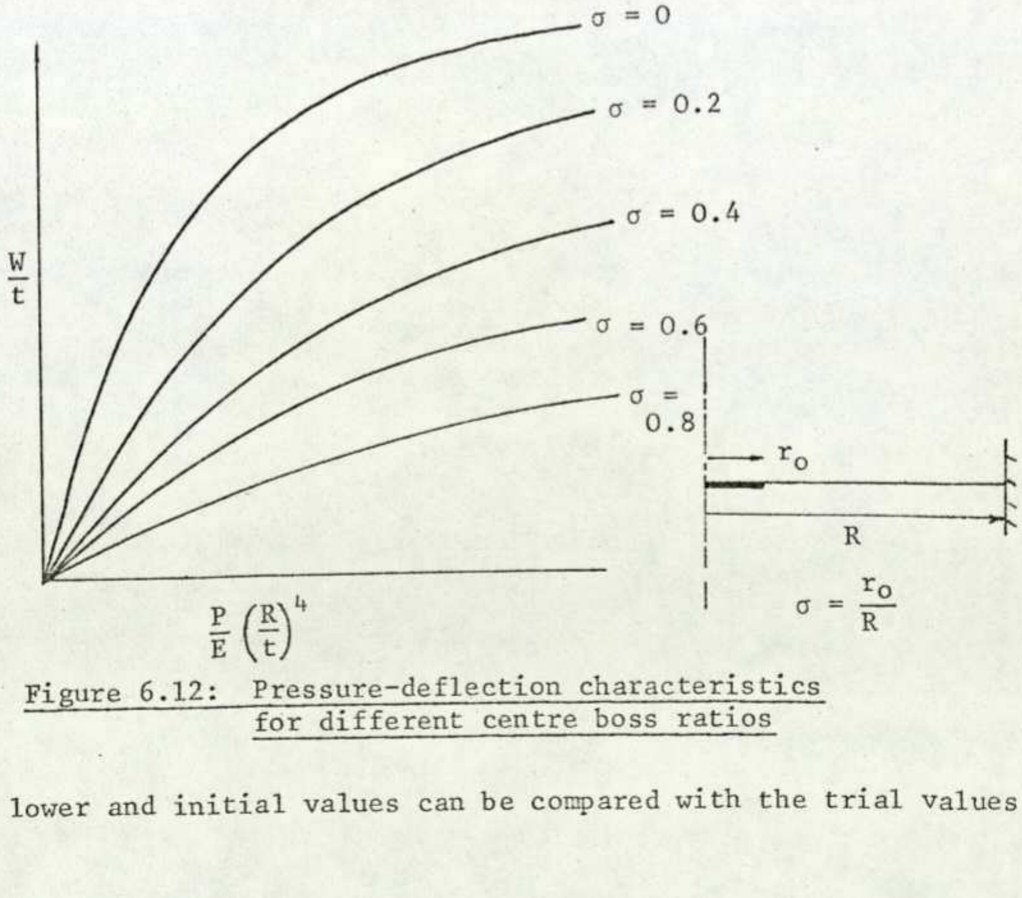

Figure 6.12: Pressure-deflection characteristics for different centre boss ratios

upper, lower and initial values can be compared with the trial values below:

	Upper limit	Lower limit	Initial	Final
E	31×10^6 lbf/in^2	29×10^6 lbf/in^2	30×10^6 lbf/in^2	30.06 lbf/in^2
R	1.4 inches	1.2 inches	1.3 inches	1.9998 inches
r_o	0.4 inches	0.0 inches	0.2 inches	0.85 inches
t	0.028 inches	0.024 inches	0.026 inches	0.027998 inches

Although the program listing, when tested with the sample program, worked satisfactorily, the actual problem caused the problem to jump the limits, as can be seen from the above example of r_o. But still the problem is solved as would be expected. R is pushed down to the bottom limit and t up to the top limit and the centre boss is maximised. The Young's Modulus appears as an experimental variable and gives no definite directions of movement for non-linearity. Exponential penality functions were introduced to prevent the variables jumping the limits.

Runs with the complete optimisation function, Eqn. (6.6), and differing values of the weighting α, gave correspondingly differing optimal results: the balance between sensitivity and non-linearity is, of course, the choice of the designer. For example, if $\alpha = 10^{-8}$, both the sensitivity and non-linearity are reduced from their initial values over the five stages involved in the search, using the same upper and lower limits as before.

	Stage 1	Stage 3	Stage 5
E	29.9025×10^6 lbf/in^2	29.762×10^6 lbf/in^2	29.755×10^6 lbf/in^2
R	1.33125 inches	1.3765 inches	1.3792 inches
r_o	0.1125 inches	0.005824 inches	0.0001852 inches
t	0.025 inches	0.027048 inches	0.027051 inches
$\left(\frac{W}{P}\right)$	1.15934×10^{-3} inches/lbf/in^2	0.90733×10^{-3} inches/lbf/in^2	0.935598×10^{-3} inches/lbf/in^2
Deviation %	17.192	8.4118	9.0657
Function $\bar{U}$	1.2835×10^{-5}	1.21167×10^{-5}	1.2098×10^{-5}

Example of Rosenbrock's search with $\alpha = 10^{-8}$

It can be seen from this example that the weighting factor was probably not the best choice, although in the last stage the sensitivity was increased slightly, but so was the non-linearity. A better choice of α is 10^{-6}: this can be seen by looking at the variations of the design variables and optimality criteria, plotted against the number of stages.

Figure 6.13

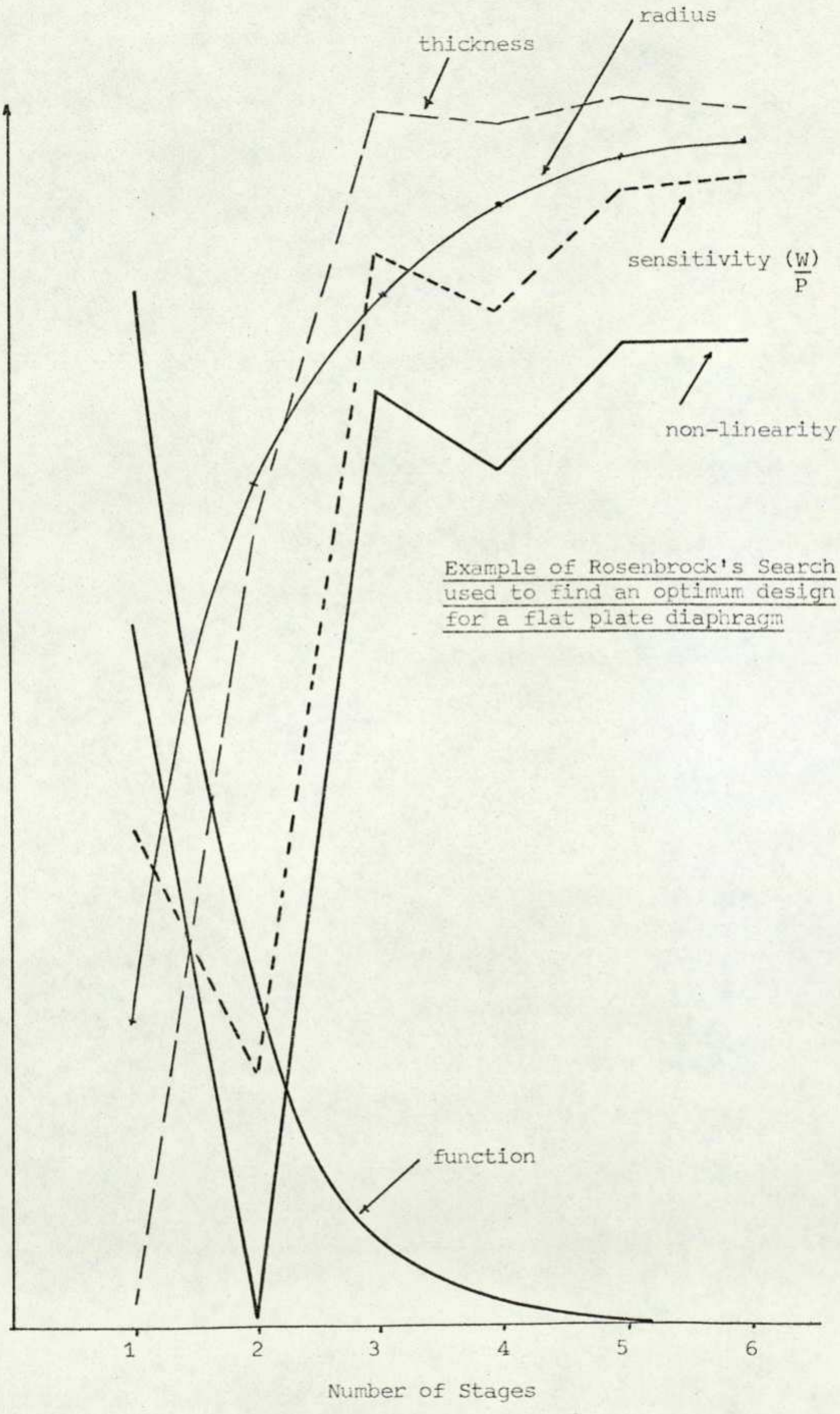

Example of Rosenbrock's Search used to find an optimum design for a flat plate diaphragm

The problem converged at the sixth stage (see Figure 6.13): no attempt has been made to scale the outputs as only the change in directions is of interest. The value of the function decreases quickly at first, but then slowly reaches a minimum value, whereas the radius increases in the same way, both being smooth curves. The movement of the sensitivity and non-linearity are by no means smooth, but they follow each other. The thickness has also increased, as it would have to, to offset the effect of R increasing rapidly. Therefore, using $\alpha = 10^{-6}$ and the particular design variable constraints an optimum design has been found.

The major disadvantage with this type of design procedure, as was to be expected, was the computing time involved: the example with $\alpha = 10^{-8}$ took a total of 209 functions evaluations and 80.522 seconds of C.D.C. 7600 computer time, and the example with $\alpha = 10^{-6}$ took 153 evaluations and 64.095 seconds using the same machine.

Besides using an example with only four unrelated variables, the number of pressure steps used to obtain the characteristic was only five. A corrugated diaphragm would require more pressure points to obtain a reasonable characteristic, also there are more design variables involved, therefore it was decided not to pursue the work in this direction owing to the computing cost. These somewhat theoretical areas of diaphragm design could equally be applied to capsules as well, irrespective of whether they are the nesting or non-nesting type. The design of a nesting type capsule is one of the problems tackled under the heading of Industrial Design Problems.

6.5 The model adapted to various diaphragm applications

The application considered so far has been generally the conversion of pressure into displacement, this being the most widely used application of this type of instrument sensor. Other application areas are also of importance, especially when considering instrument systems. Diaphragms are used in many ways for converting any one of the quantities F, P, W and ΔV (force, pressure, displacement and volume change) into one or more of the remaining ones. The most common uses deal only with the relations between the first three. Generally, one of the quantities (the output) varies as a nearly linear function of the second quantity (the input), when the other two (the modifying quantities) are either zero, a constant value or a certain function of one of the others.

It has been considered worthwhile classifying these differing applications in terms of their input/output relationship and applying the model to some of them. Firstly, some general relationships need to be stated, which are necessarily linear if algebraic models are constructed with "a priori" knowledge of diaphragm performance, but the advantage of having a non-linear model is that the relationships need not necessarily be linear.

(1) $C_F = F/W$ when P is constant (by definition of force constant)

(2) $C_P = P/W$ when F is constant (by definition of pressure constant)

(3) $A_e = \frac{F}{P} = \frac{C_F}{C_P}$ when W is constant (not necessarily zero) by definition pressure effective area.

(4) $A_v = \Delta V/W$ by definition of volumetric effective area.

When the force F causes a deflection in the same direction as an increase in the pressure P, it is positive, and therefore C_P, C_F and A_e are positive. A deflection of the centre always causes a volume change. However, due to a bulging effect, the volume of some diaphragms can change a small amount due to pressure, even though the centre does not move. In many cases the volume change is immaterial when the input or output quantity is deflection or force, it can be amplified or reduced by means of levers.

The first two applications (6.5.1a) and (6.5.1b) are trivial but are included for completeness. (6.5.1b) is obtained by loading the diaphragm with a point load at the centre: this is mentioned in Chapter 3. The next two applications are handled quite simply by the model. By having a fixed point load and incrementing the pressure, (6.4.2a) is achieved, and vice-versa for (6.4.2b).

For the applications of (6.5.3a) and (6.5.3b) the diaphragms are used as the sensing elements for "force-balance" type transmitters and controllers.

The (6.5.4a) condition exists when the diaphragm is deflected by pressure or force to a working position which is other than the equilibrium position. This is done to suppress the zero or to change the effective area.

(6.5.3b) and (6.5.4b) are the reverse of applications of (6.5.3a) and (6.5.4a). These can be achieved practically in two ways: with a completely liquid-filled system or with a pneumatic feedback system,

(6.5.1a)

Pressure into deflection

(force zero)

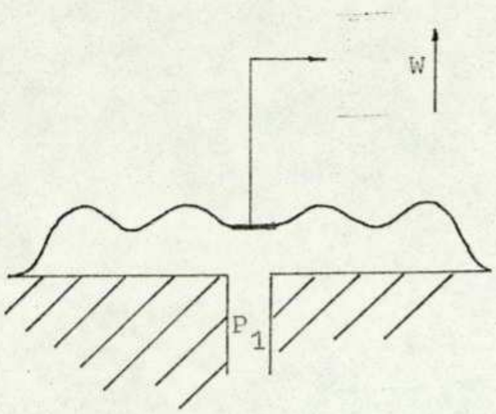

$$W = P_1/C_P$$

(6.5.1b)

Force into deflection

(pressure zero)

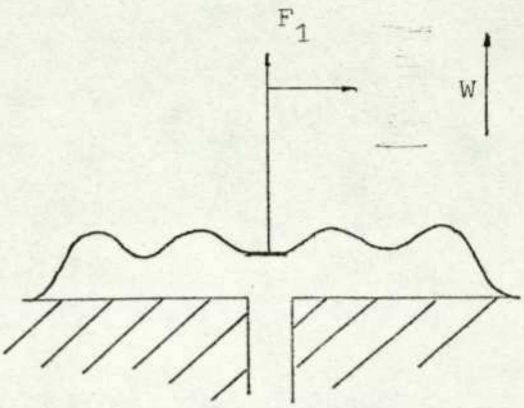

$$W = F_1/C_F$$

(6.5.2a)

Pressure into deflection

force is constant (not zero)

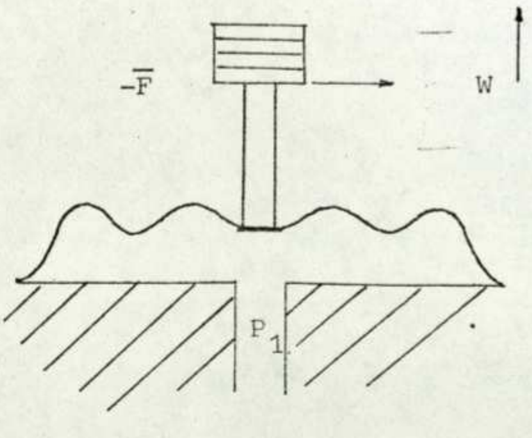

$$W = \frac{P}{C_P} - \frac{\overline{F}}{C_F}$$

(6.5.2b)

Force into deflection

pressure constant (not zero)

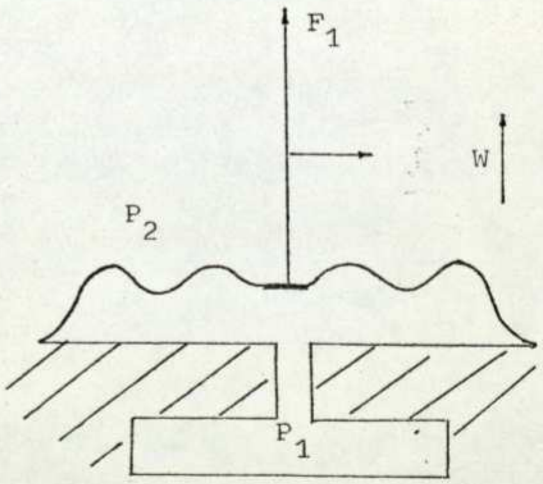

$$\Delta P = P_1 - P_2$$

$$W = \frac{F_1}{C_F} - \frac{\Delta P}{C_P} \text{ or } (F_1 - \Delta PA/_e)/C_F$$

(6.5.3a)

Pressure into force

deflection zero

volume change virtually zero

(very small)

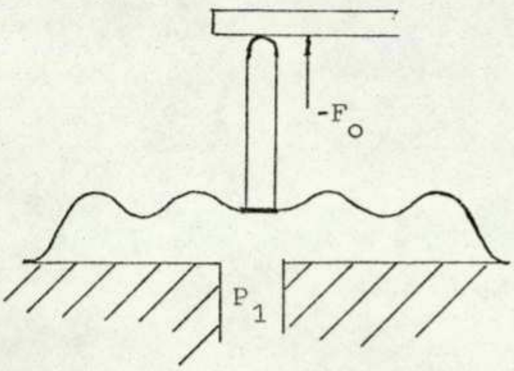

$F_o \;=\; A_eP_1$

(6.5.3b)

Force into pressure

deflection and volume change

are virtually zero (very small)

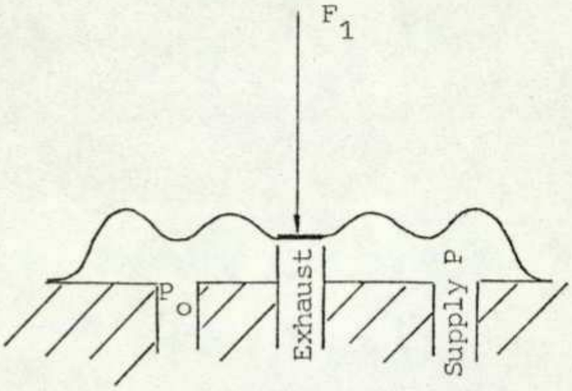

$P_o \;=\; F_1/A_e$

(6.5.4a)

Pressure into force

deflection and volume change

are constant (not zero)

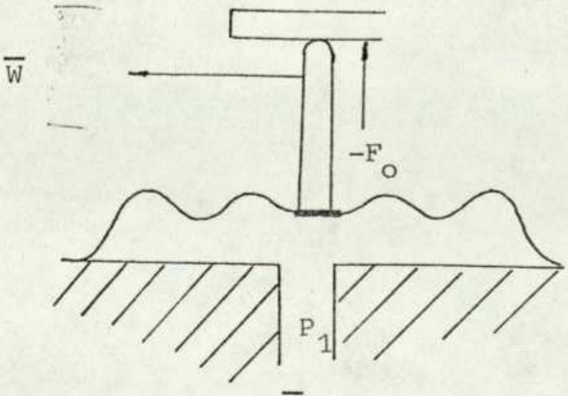

$F_o = (P_1 - C_P\overline{W})\ A_e$

(6.5.4b)

Force into pressure

deflection is constant (not zero)

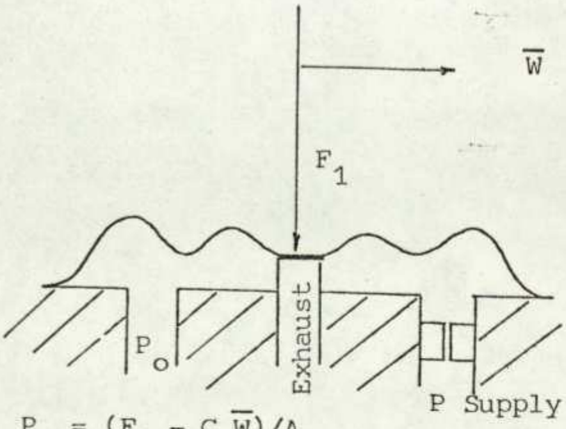

$P_o = (F_1 - C_F\overline{W})/A_e$

such as the nozzle-baffle-orifice combination. In (6.5.3b), the feedback system, the pressure increases to balance the force: this is the force balance type of pneumatic force transmitter. When the deflection is constant at some value other than zero, it can be due to a force or pressure: this is the suppressed zero type of force transmitter.

Simulation of these types of application is not so straightforward as the previous cases. For applications (6.5.3a) and (6.5.4a) the non-linear program is set up to solve an ordinary pressure-deflection situation with the result, pressure difference and deflection printed out. The value of deflection is then stored and a guess value of point load is applied in the opposite direction with the same pressure difference across the diaphragm and a new value of displacement found: this is tested against a suitable tolerance. If zero displacement is required, then the deflection would have to be less than a tolerance near zero, e.g. $\pm 10^{-6}$: for a non-zero displacement the tolerance is placed on that particular value.

Taking the general example of a non-zero displacement and assuming that the guess value of point load (Q_s) did not drive the centre back to the requirement displacement (W_r), then Q_s is modified by multiplying by the factor:

$$\frac{W_o - W_r}{|W_o - W_N|}$$

where W_o = the stored value,

W_N = the updated value.

If the value of Q_s was too great, then W_N would be less than W_r and Q_s would be reduced, but should Q_s be too small, then the factor increases it. The program is arranged so that the latter happens, and W_N approaches W_r from being the greater, the problem then converges quickly. The pressure is increased and the cycle repeated with the guess value of Q_s, the final value from the previous iteration.

This method converges within three iterations and prints the values of A_e, C_F, C_P and point load (force) each cycle: the cost of computing time is quite reasonable, taking only 0.460 seconds per cycle. Figure 6.14 is a model of a production diaphragm showing the variation of A_e (with zero deflection at the centre) as pressure is applied from opposite sides of the diaphragm. If it was a linear relationship the curve would be a horizontal straight line, but this can be seen not to be the case, although the diaphragm has been pressurised well above its intended working range. The systems which convert force into pressure using a

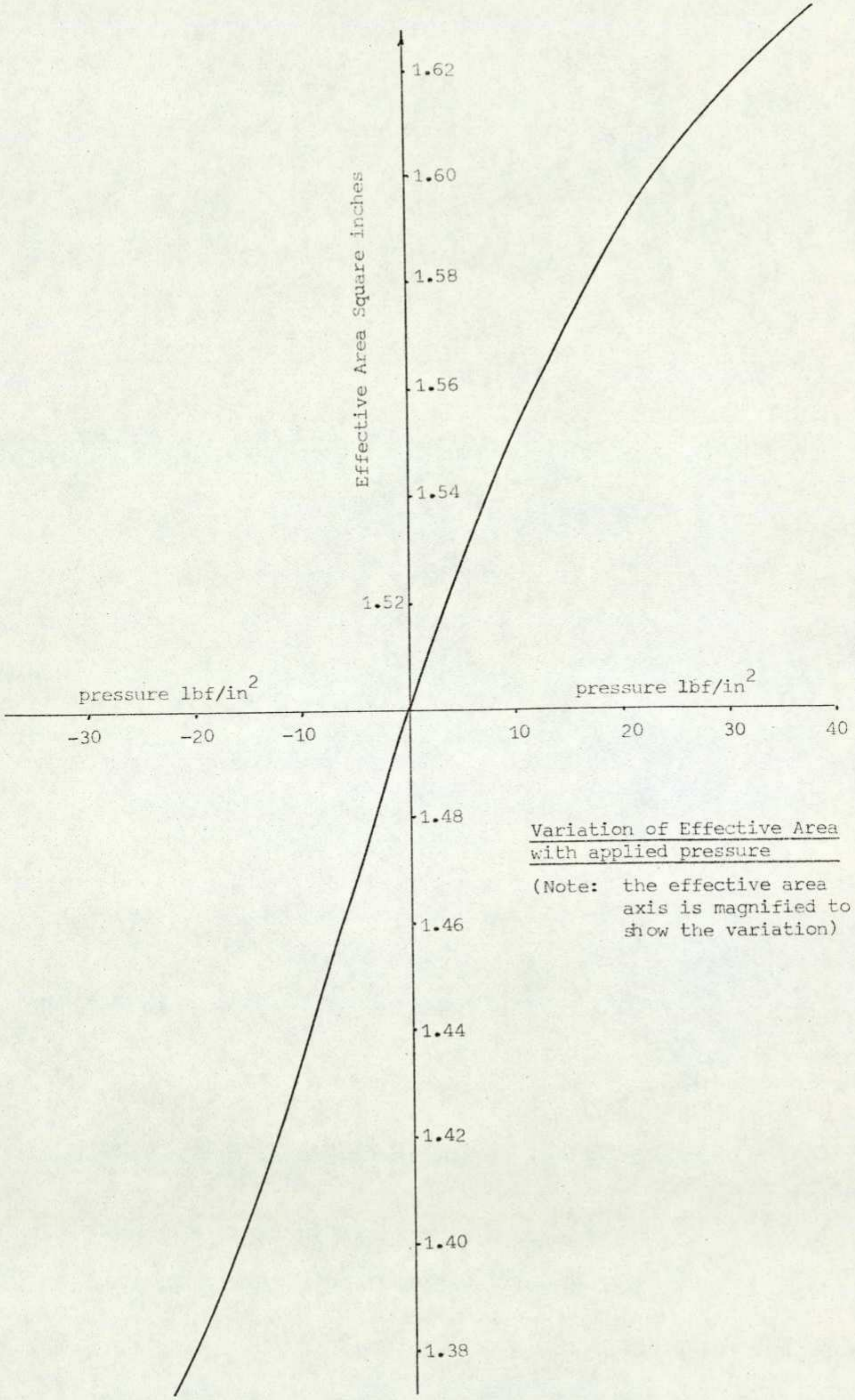

Variation of Effective Area with applied pressure

(Note: the effective area axis is magnified to show the variation) diaphragm, e.g. (6.4.3b) and (6.4.4b) look more complicated because the physical realisation is more complex. A constant loss sytem is used to maintain the pressure balance against applied load, P_0 is a measured value of pressure difference. The force is applied as usual as a point load at the centre, which causes the diaphragm to close the exhaust port: the supply pressure then raises the pressure difference and lifts off the centre of the diaphragm, and a balance is then maintained as the supply pressure fluid exhausts through the annular orifice. The simulation of this by the model is the same as for the case of converting into force but with the respective input quantities reversed.

The other important direct conversion to be considered is the output as a function of the input. For this consider the simple case of converting pressure into deflection, where the resulting force at the centre is a function of the pressure and displacement:

(6.5.5) <u>Pressure into deflection</u>

force is a function of W or P

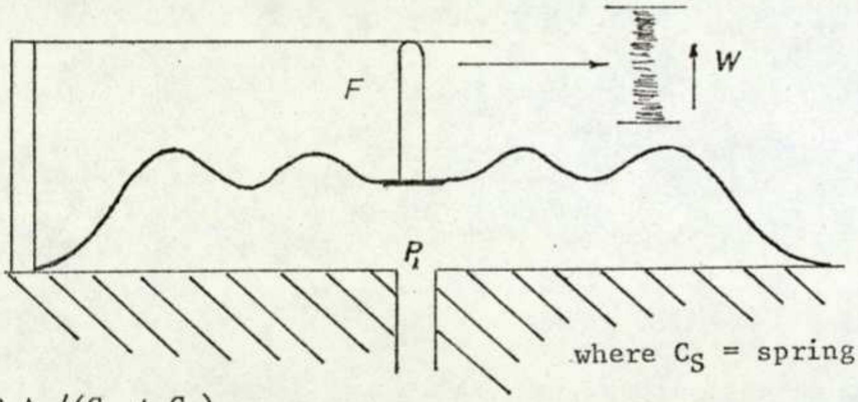

where C_S = spring constant

$W = P_1 A_e/(C_F + C_S)$

Diaphragms are often used in combination with springs in parallel to shift the zero position of the diaphragm, to obtain the desired linearity, to increase the pressure span, or decrease the force. Even in pressure gauges the hairspring in the amplifying levers and spindles sometimes adds an appreciable amount to the force constant. A diaphragm with a spring in parallel obviously does not have the same characteristics as a diaphragm having thicker material.

The simulation is quite straightforward, but, unfortunately, does not converge as rapidly as the method for finding A_e. If a spring of known spring constant is used to "back-off" a diaphragm, then the method proceeds by performing the usual pressure-deflection calculation and obtaining a deflection. The value of deflection is multiplied by the spring constant to give a force which is applied in opposition to the pressure at the centre. The resulting deflection is then much smaller than the first, but the procedure is repeated until the deflection is steady to within a suitable tolerance. Figure 6.15 shows a snap action type diaphragm backed by a coil spring: curve (a) is the plot of displacement against pressure and curve (b) force in the spring against pressure. The bottom plot shows high "over-shoot" obtained by this method. The highly oscillatory nature of the problem can be reduced by taking only 80% of the first deflection and then the problem converges quicker: although it has not been attempted, a non-linear spring could feasibly be used.

All the applications considered so far have dealt with the pressure effective area, i.e. the ratio of (C_F/C_P). The volumetric effective area $(\Delta V/W)$ is in most incidences easier to find, as the displaced volume can be calculated from knowing all the individual deflections along the diaphragm:

$$\Delta V = 2\Pi \sum_{i=1}^{i=N} \left(\sqrt{W_i^2 + U_i^2} \right) ds \; \frac{\left(2(r_i + r_{i-1}) + U_i + U_{i-1} \right)}{4}$$

In the linear region A_v is the same as A_e but, owing to change in shape, the two effective areas are different outside the linear range and this distinction must be borne in mind when undertaking accurate calculations involving effective areas.

The approach to diaphragm applications is somewhat more detailed than that outlined in Chapter 1, which introduces the "through and across" formulation approach, ref. (2), giving a diaphragm as simply:

$$\begin{bmatrix} F \\ \dot{g} \end{bmatrix} = \begin{bmatrix} \left(ms + k + \frac{C_F}{S} \right) & - A_e \\ A_e & 0 \end{bmatrix} \begin{bmatrix} \dot{W} \\ P \end{bmatrix} \qquad \text{see Eqn. (1.1)}$$

From this representation most of the applications detailed here can be derived. The example of pressure into deflection (6.4.5) using a spring applied to the centre was given as:

$$W = \frac{P_1 A_e}{C_F + C_S}$$

Therefore $\underline{W(C_F + C_S) = P_1 A_e}$

Figure 6.15

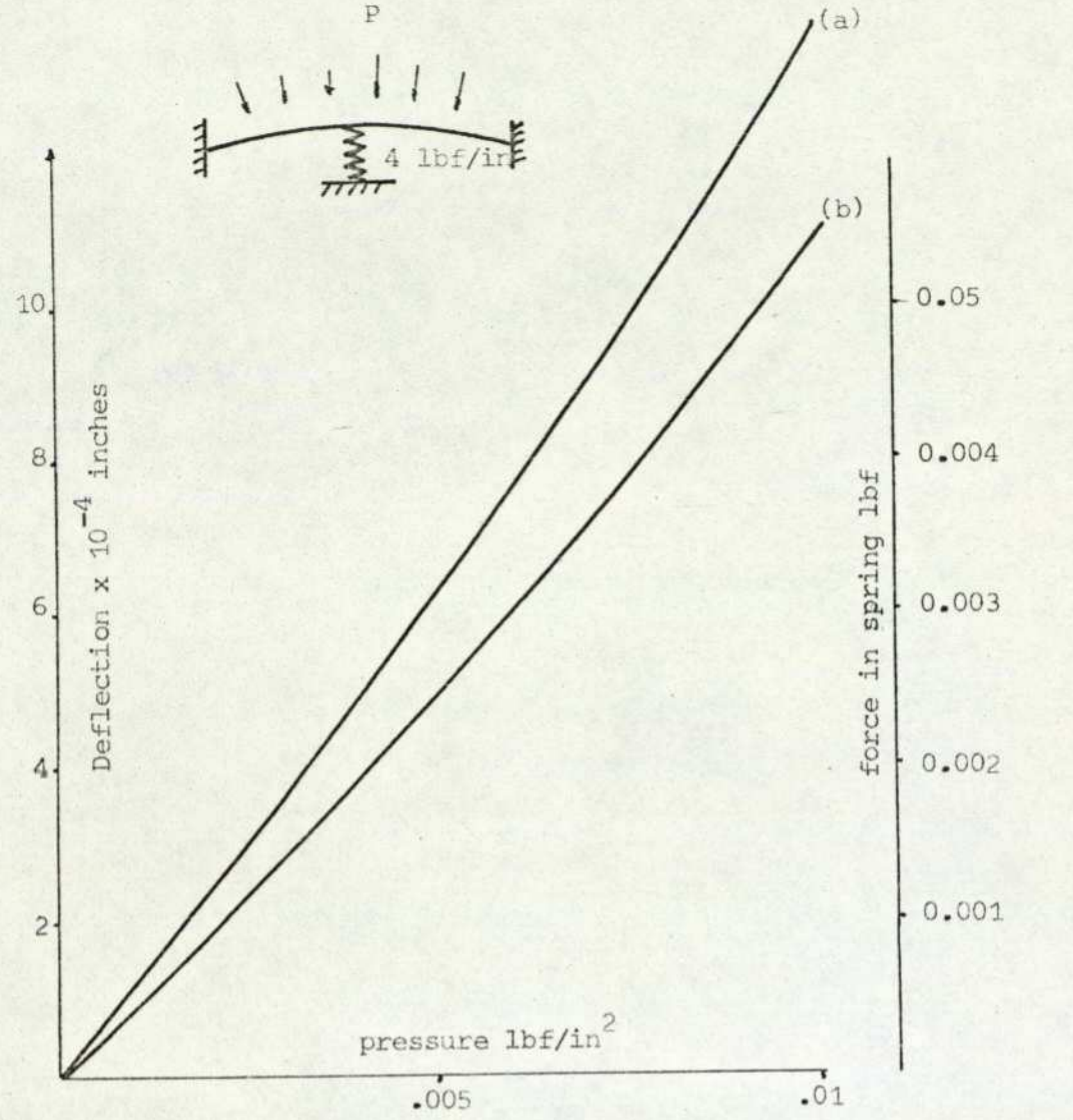

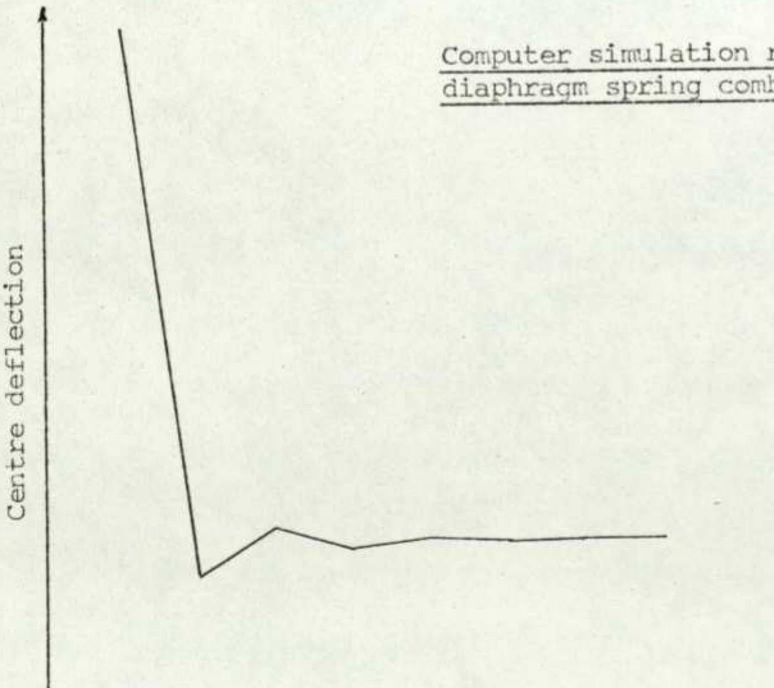

Computer simulation results of a diaphragm spring combination

Now the first row of Eqn. (1.1) in the steady state equals:

$$F = C_F W - A_e P$$

$$\text{and} \quad F - G = W = -A_e P$$

The force F is developed by the displacement and spring constant equal to $C_S W$, but in the opposite direction to that defined in Figure 1.4.

$$\text{Then} \quad -C_S W - C_F W = -A_e P$$

$$\text{hence} \quad \underline{W(C_S + C_F) = A_e P}$$

Therefore the two approaches are synonymous, the latter being a more systematic approach useful for modelling larger systems.

6.6 Industrial design problems

Two actual design problems presented by K.D.G. Instruments, Ltd. have been tackled, each of an entirely differing nature. The first problem was the design of a flexible barrier diaphragm: this ended after the computer study, the results of the investigation showing that the problem could not be solved by the method chosen.

The second problem was the design of a nesting capsule. It was solved by producing a computer design, and this, in turn, created a need for a new production technique which was used to solve the manufacturing difficulties that arose.

The design was subsequently incorporated in instruments and sold as a stock item.

6.6.1 Design of a flexible barrier diaphragm

A need arose for a flexible barrier diaphragm to separate the capsules of a differential pressure transmitter from a hostile medium, but, in so doing, not reduce the pressure seen by the capsules. The proposed scheme involved placing a barrier diaphragm across the inside of the pressure chamber and filling the intervening space with liquid (Figure 6.16). The liquid was assumed incompressible, thereby transmitting the pressure directly to the capsule stack. Ideally, the requirement would be for a completely flexible diaphragm, i.e. with zero rate which would transmit all the pressure across to the sensing capsules, but, in practice, a compromise will have to be reached. The other assumptions in the problem were that the capsules were linear in operation and therefore had constant values of effective area, pressure constant and force constant. The constraints on the problem were the material (E), its minimum thickness and its active diameter. A requirement of the diaphragm was that it also had less than 0.5% non-linearity.

The barrier diaphragm, when subjected to a pressure difference, will deflect (W_d). As indicated previously, its volumetric effective area (A_d) is found quite easily, so at any displacement W_d the volume displaced by the diaphragm equals $W_d.A_a$. This will be equal to the volume displaced by the capsule stack, i.e. the effective area multiplied by the capsule displacement - W_cA_c. As the capsule effective area is known, then its displacement $W_c = \frac{(W_d.A_d)}{A_c}$. As the capsule stack pressure constant is also known (C_p), the pressure required to cause that deflection can be found:

$$P_c = C_P W_c \quad \text{...} \quad (6.7)$$

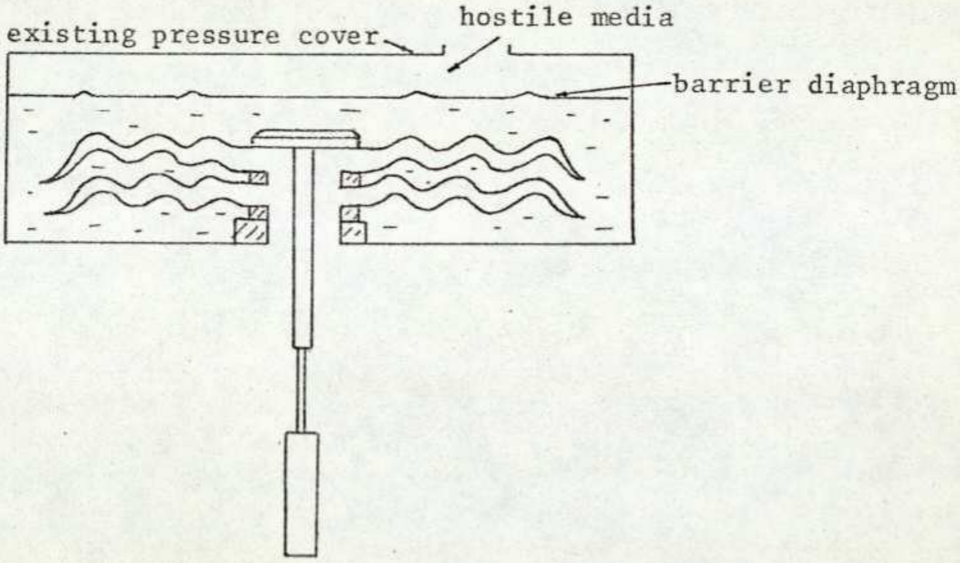

Figure 6.16: A flexible barrier diaphragm

The pressure P_c can be viewed in the same way as the spring in the previous section (application 6.4.5). Normally, applying a pressure to one side or the other of a diaphragm is actually the application of a pressure difference, one side being zero. The solution follows the same argument as for a spring, but, whereas a spring produces a force at the centre, the pressure found by Eqn. (6.7) is subtracted as it opposes the pressure applied to the diaphragm and a new value of W_d is found. The problem is again oscillatory and, after a number of iterations, converges to a value where the applied pressure to the diaphragm is balanced by the dual stiffnesses of the capsule stack and diaphragm itself. A number of design runs were made and the best result which was stable transmitted only 64.5% of the applied pressure across to the capsule stacks; designs which were more sensitive suffered with the stability problems and appear to "snap through" at certain pressures.

Hence, at maximum working pressure only 64.5% of the nominal lift was theoretically available, and coupled with added problems of temperature coefficients, i.e. a zero shift due to the expansion of the liquid when the temperature changed, the idea was not pursued further than the computer study.

6.6.2 Design of a 100 lbf/in^2 (690 KPa) nesting capsule

The design of this capsule forms the main practical illustration of the usefulness of mathematical modelling of instruments and, to help with the understanding, a short description of the actual instrument and its use is included first.

6.6.2.1 The differential pressure transmitter (manufactured by K.D.G. Instruments, Ltd.). A schematic representation of the instrument is shown in Figure 6.17.

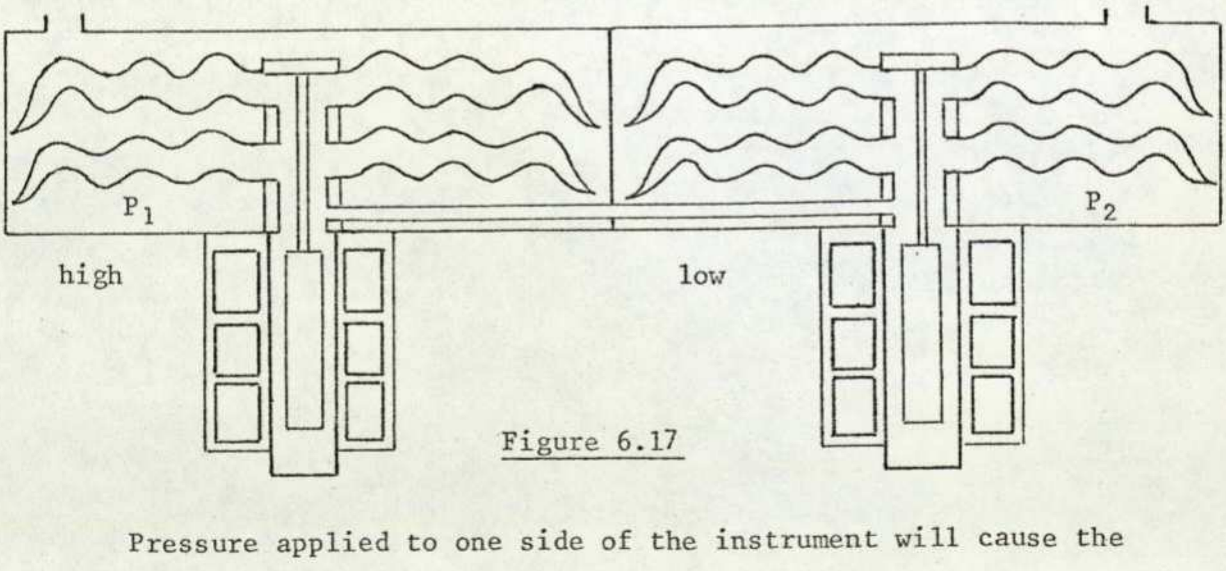

Figure 6.17

Pressure applied to one side of the instrument will cause the capsule stack to deflect, in effect "close down", as the instrument is liquid filled and the filling may for the first part of this explanation be assumed incompressible: the displacement is transferred to another capsule stack which is made to deflect in the opposite direction, "open up". The purpose of the instrument is to measure differential pressure: a pressure P_1 (say) is applied to one side, and a pressure P_2 to the other, and the difference of the displacements measured by the two linear variable differential transforms (L.V.D.T.'s) attached underneath each capsule stack. This is then a direct measure of the differential pressure $\Delta P = P_1 - P_2$. There are a number of advantages for using this method of measurement, which are particularly relevant to the design of the capsules:

(1) The main advantage is that the system can be used to measure a differential pressure on a high static pressure, and should the system malfunction and one side "see" all the static pressure, which is probably many times the working pressure, then the capsule in that side will collapse down, the top diaphragm sitting exactly on the bottom diaphragm. The liquid will be forced into the other side and extend the capsule stack a certain amount, which will be a maximum when the other side has collapsed fully, and any further application of pressure will cause it no more movement. It is therefore said that the instrument is "over load protected".

(2) Sources of secondary effects are to some extent eliminated. Firstly, any liquid is not incompressible and with the application of a high static pressure the liquid will compress. This will cause the capsules to collapse slightly, but as the difference of the outputs is measured, the error is compensated for zero shift. This is termed a "zero shift with static". The same compensation effect is noted when a temperature is applied, causing the liquid to expand. Movement of the centre of a capsule, when an overall temperature rise is applied, is very much less than a diaphragm of similar dimensions clamped at the outer edge: this is because the movement is taken up at the outer edge by a horizontal displacement of the capsule. Capsules under an overall temperature rise have been modelled and the above phenomenon validated.

(3) With one capsule stack working in compression and the other in extension all the time, the non-linearity of each can be matched. Referring to Figure 6.13, the non-linearities are generally equal and opposite, making this possible.

(4) Having a capsule with a stated working range, this range can be doubled when used differentially, i.e. one will compress the

working range and the other extend it, giving a possible differential pressure twice the two working ranges.

Mathematical modelling of the differential pressure transducer has shown that the performance of the complete instrument (including static, dynamic, temperature and vibration response) can be predicted in terms of the sub-assemblies and their various interconnections. This work is summarised in the IMEKO VII paper in Appendix V. Here, of course, we are concerned with the detailed design of the capsule sub-assembly (level B modelling of the paper).

6.6.2.2 Design specification and constraints: It was required to extend the top limit of the range of available differential pressure transmitters; the range went from 0 - 20" Wg (0 - 4.97 KPa) to 0 - 2800" Wg (0 - 696.2 KPa), the extra range needed being 0 - 5600" Wg, approximately 0 - 200 lbf/in^2 (0 - 1380 KPa), i.e. to produce a 0 - 100 lbf/in^2 capsule where the previous maximum was 0 - 50 lbf/in^2. The design had to utilise existing parts, L.V.D.T. connections, etc. and fit into existing equipment, i.e. pressure covers. This means that the active diameter and centre boss sizes were fixed. The material had to be compatible with the rest of the range, therefore Young's Modulus was fixed, and there were two possible material thicknesses which were available: 0.025 and 0.032 inches.

The design specification was then: to produce a capsule subject to the above constraints which gave a nominal 0.05 inch deflection for 100 lbf/in^2 and was linear to within ± 0.5%, as defined in section 6.2, and to withstand an overload pressure of 6000 lbf/in^2 (41.4 MPa), i.e. to dive down without plastically deforming (nesting). The nominal lift of 0.05 inch could be between 0.04 and 0.06 inch. This is a very large tolerance ± 20%, but is a standard facility available in the electronics of the instrument to cope with the differing deflections obtained from the other ranges and the difference in the deflection of compression and extension. It is seen immediately that the sensitivity is not one of the main criteria in this design exercise, but the emphasis for accuracy is placed upon the linearity and the nesting.

6.6.2.3 Design approach: The previous top of the range was examined to see if anything could be learned. The design used 0.025 inch thick material and had three convolutions: a study of this particular capsule in Chapter 4 has shown that the shape takes the theory of thin shells to the limit of acceptability, owing to the radius of curvature to thickness criterion, therefore the number of convolutions which could be incorporated, bearing this in mind, was only two. Studies with the two material thicknesses indicated that 0.032 inch would be a better choice because the stresses within the material were less, and with 0.025 inch material, these were beginning to come near the yield point. Unfortunately, 0.032 inch thick material was later found to be not available, so the design had to be accomplished using 0.025 inch thick Inconel. The number of possible unconstrained design variables was therefore considerably reduced and this made the initial design stages relatively simple. At the start of this work, there only existed a non-linear diaphragm model and a linear capsule model: these were thought sufficient at the time to do the work. A suitable design based upon the linear model was produced in X, Y and R co-ordinates: as there were only two convolutions, this gave only six stations along the diaphragm. The data in that form were read directly into a design program based upon the non-linear diaphragm model. The pressure was then applied from the top of the diaphragm in steps of 15 lbf/in^2(103.4 KPa) from 10 - 145 lbf/in^2 (1000.1 KPa). The deflections and percentage non-linearity were then printed out, based on the range 0 - 100 lbf/in^2. With the diaphragm displaced by a pressure of 145 lbf/in^2 (1.45 the working pressure), the new shape is then obtained by the appropriate adjustment of all the old x_i, y_i co-ordinates ($i = 1, \ldots N$, where N = 240) by all the i^{th} displacements (W_i, U_i) at 145 lbf/in^2. The new values of x_i, y_i were then fed into two subroutines which found the average value of curvature of each peak and trough and the height and radial distance of the peaks and troughs, i.e. the deformed shape, was put back into X, Y, R1 co-ordinates. This new diaphragm was pressurised from the bottom row as it is the proposed bottom diaphragm of the capsule. Over the range 0 - 100 lbf/in^2 (0 - 690 KPa), the deflection and non-linearity is printed out. The procedure is repeated for pressurizing the basic diaphragm shape from the bottom, thus producing the top diaphragm of the capsule. If the deflection is within the nominal range and non-linearity is less than ± 0.5%, the two sets of data for a capsule are punched on cards and fed into the linear capsule model: this procedure was adopted because a picture of the capsule can be produced on the ICL 1905E computer graph plotter, resident at The City University. With a picture, the nesting qualities of the proposed capsule can be studied at any chosen magnification, especially when the capsule is pressurized in compression, as well as the normal position. The example given below is typical of the early attempts of designing a capsule using this method:

Basic shape:

X	Y	R
0.313	0.0	0
0.351	0.0	-0.15
0.556	0.075	0.15
0.761	0.0	-0.15
0.966	0.075	0.15
1.171	0.0	-0.15

Bottom diaphragm:

	X	Y	R
	0.313	-0.0218	0.0
Maximum	0.3504	-0.0218	-0.1499
non-linearity	0.5571	0.0557	0.1521
-0.283%	0.7574	-0.0128	-0.1493
	0.9712	0.0705	0.1489
	1.171	0.0	-0.165

Top diaphragm:

	X	Y	R
	0.313	0.0218	0.0
Maximum	0.3504	0.0218	0.1526
non-linearity	0.5540	0.0942	0.1487
-0.301%	0.7640	0.0130	-0.1519
	0.9605	0.0794	0.1521
	1.171	0.0	-0.135

When the two diaphragms were used in the capsule program, the resulting deflection was 0.02912 inches (.7396 mm) for the stack, giving a total deflection of 0.05824 inches (1.479 mm) for a two-stack device: although this was a little large, it is still within the limit. Unfortunately, the diaphragm had poor nesting qualities, as is seen in Figure 6.18: the problem arises at the outer edge which is shown 50 times full size. The plain lines represent the undeflected capsule, and the lines with small crosses, the deflected. The small crosses are the individual finite difference points which produce the diaphragm profile. It has only been possible to show an end section, but this is where the trouble lies: the capsule not only touches, but appears to pass through itself when used in the compression mode. Of course, it is impossible for one diaphragm to pass through the other so, practically, what would happen is that the diaphragms would touch at some point, thereby shortening the active radius and causing gross non-linearity in the pressure-deflection characteristic.

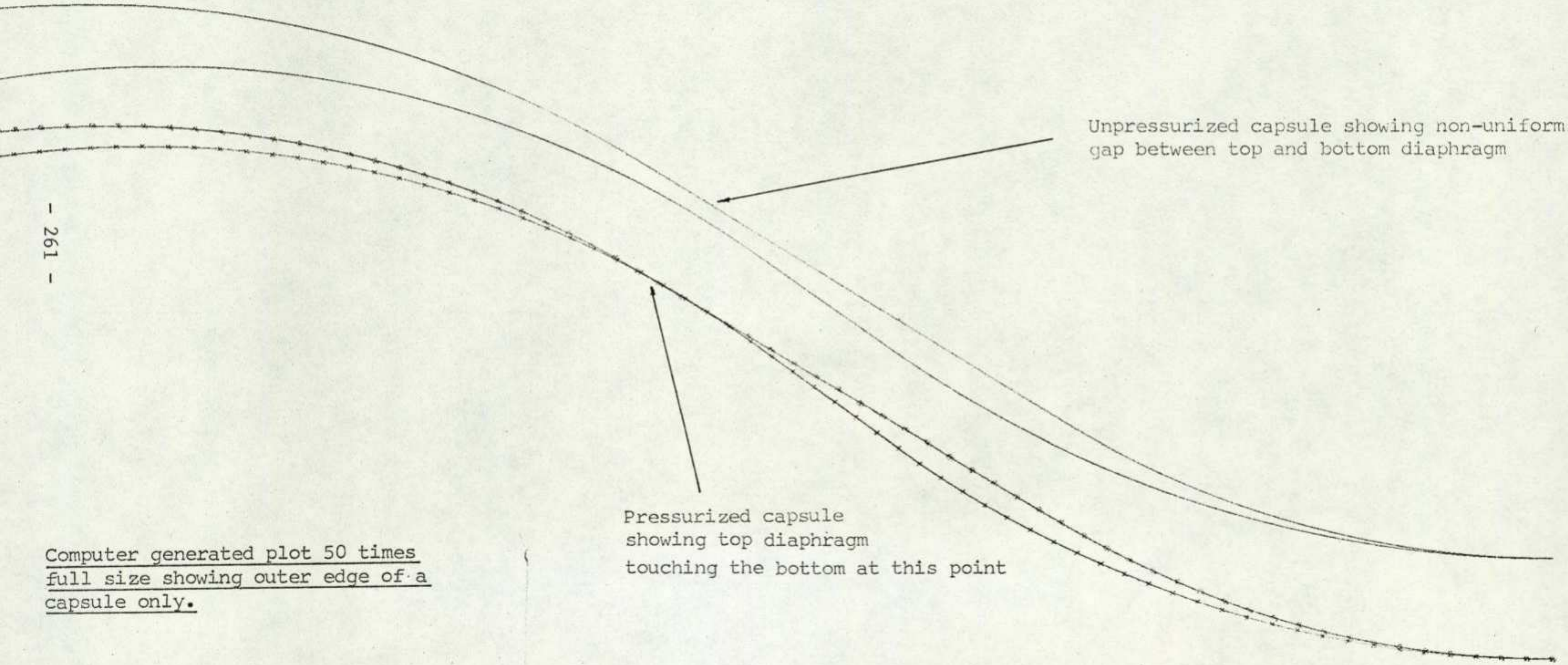

Unpressurized capsule showing non-uniform gap between top and bottom diaphragm

Pressurized capsule showing top diaphragm touching the bottom at this point

Computer generated plot 50 times full size showing outer edge of a capsule only.

Figure 6.18

It was hoped at this stage to be able to ratify this behaviour, possibly by adjusting the peaks of the last corrugation to prevent the pressurised capsule from touching before the end of the working range: this had the effect of slightly reducing the deflection down to 0.02896 inch (.7356 mm) and producing the result shown in Figure 6.19. The gap between the two diaphragms when in compression is shaded in to give a clearer picture of the situation. The section shown is the last corrugation and, although they do not touch, the two diaphragms become very close together at a point nowhere near the outer edge. This would theoretically work as a capsule, but the nesting qualities would be very poor indeed and a large overload pressure would plastically deform the capsule if the trapped liquid compressed or seeped across into the other limb; therefore this was not a good solution. A number of things were tried to eliminate the bad nesting problems associated with this method, but the problems still persisted.

6.6.2.4 Non-linear capsule design model: The answer to the bad nesting problem was a fundamental one: diaphragm behaviour cannot be directly related to capsules, and what was not allowed for was the common horizontal displacements and rotations at the outer edge. Once a non-linear capsule model was developed (described in Chapter 3), the design of a perfectly nesting capsule was a relatively straightforward procedure.

The basic shape was fed into the program in the form of X, Y, R1 co-ordinates. The Y and R1 co-ordinates were then adjusted to form two diaphragms which fitted exactly on top of each other, i.e. the two neutral axes were separated by two half thicknesses. An internal pressure was applied to this capsule, which caused it to open up: when the pressure was 145 lbf/in^2 the same process as had previously been employed was used to form the actual design capsule - in essence, the displaced capsule shape was "frozen" in that position and used for the working design. The method of deriving the new data was somewhat improved by a short cut, which made the method more accurate. Having obtained x_i, y_i ($i = 1, \ldots N$) co-ordinates for the top and bottom diaphragms, instead of converting them to X, Y, R1 co-ordinates to go through subroutine GEOM to produce r_i, rl_i, ϕ_i, ($i = 1, \ldots N$), x_i became r_i directly, rl_i was found from subroutine RADI which simply took three points (x_{i-1}, y_{i-1}), (x_i, y_i), (x_{i+1}, y_{i+1}) and fitted a circle through them of radius rl_i with the appropriate sign of Gaussian curvature,

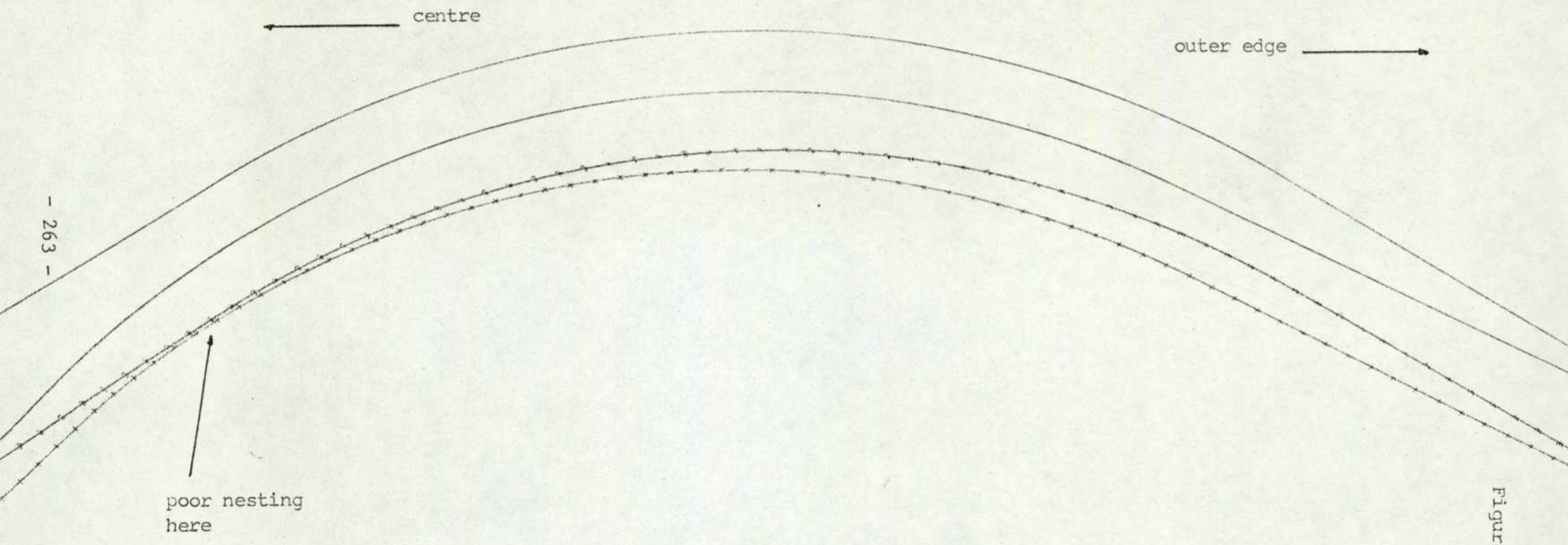

Figure 6.19

Last Convolution of a capsule design showing the poor nesting qualities at the point indicated.

and finally ϕ_i was found from the normal to the slope at each point (x_i, y_i), again with the appropriate sign convention.

The design capsule may then be tested in both directions, compression and extension for sensitivity, non-linearity and stress levels. If all three criteria were satisfied, then the 240 values of x_i and y_i for each diaphragm were punched on cards by the C.D.C. 7600 computer and read into another program for the ICL 1905E computer, which produced a picture of the capsule profile including the thickness. Figure 6.20 shows the first design which was the first attempt to produce an actual capsule: this was, in theory, a perfectly nesting capsule which would collapse at any overload pressure of 145 lbf/in^2 and had a working range of 0 - 100 lbf/in^2 (0 - 690 KPa) with a maximum non-linearity of less than 0.5% in either direction.

6.6.2.5 Manufacture: To produce diaphragms and hence capsules, an oversize blank of the material is placed against a die which is a cylindrical, hardened steel tool with the corrugation pattern machined on one end. The blank is then forced to take the corrugation pattern by a rubber part under hydraulic pressure. The die forms the top face of each diaphragm. This does not eliminate the effect of springback in the material, but gives the springback in the same direction for each diaphragm. The effect of springback was neglected in this particular design, partly because of the reason just mentioned and also because there is less springback with thicker material; this may be seen from the bending equation (6.8), ref. (42):

$$\frac{R}{r} = 4\left(\frac{RS}{E't}\right)^3 - 3\frac{RS}{E't} + 1 \quad \ldots\ldots\ldots\ldots\ldots\ldots\ldots\ldots \quad (6.8)$$

where R = radius around which material is formed,

r = radius material sprung back to

t = thickness

$E' = E/(1 - \nu^2)$

S = stress level.

For the thinner material used for capsules in the range 0.003 inches (.0762 mm), the springback from the tool was 0.010 inches (.254 mm) in some places, but tests with fully annealed 0.025 inch (.625 mm) Inconel showed springback to be minimal.

The program printed out x_i, y_i and rl_i co-ordinates for all the points along both generators; from this, data figures were obtained so that a set of form tools could be made. The required data for initially producing a form tool were much the same format as the data required by GEOM, because these were taken by a toolmaker who attempted to produce the shape using an ordinary centre lathe. The first capsule made was tested and had the correct sensitivity up to 30 lbf/in^2 and then it became very non-linear in a way which would suggest that the capsule was nesting prematurely. Sectioning the capsule did indeed show that this was the case: also, moulds taken of the tools, sectioned along a diaphragm and examined in a shadow graph, showed that the profile was substantially different from that required. Fortunately, springback between the tool and the diaphragm was seen to be insignificant. At this stage two major problems were apparent, one dependent upon the other: (1) was the theoretical design, which gave a perfectly nesting capsule, a practical solution?; and (2) if so, how could it be made accurately? The overall gap between the two diaphragms was small, even at the greatest point: the gap was only 0.0036 inches (.09144 mm) which gradually went to zero at the outer edge, and the clearance between the two down at the last convolution was extremely small. This can be seen on Figure 6.20, which is the complete capsule ten times full size. To overcome the clearance problem, it was decided to re-design the capsule by having increased clearance on the outer convolution (Figure 6.21), but it was decided that this was still not enough, so with keeping this modification the whole capsule was opened up by 200 lbf/in^2 to increase the overall clearance. The second problem in producing the tools was solved by using the x_i, y_i co-ordinates at the 240 points along the generator and making the tool on a numerically controlled lathe.

The principle of the routine to increase the clearance of the last corrugation is shown in Figure 6.22.

The routine stepped along the capsule measuring the gap between the two diaphragms: when this was less than a set amount the distance to the end was calculated and the gap reduced very slightly until the last few points when it is accelerated into zero. Figure 6.23 shows the complete re-designed capsule, ten times full size, with and without the pressure applied in the compressive mode: the effect of the increased clearance may easily be seen.

To produce the data for a numerically controlled lathe, the top surface for each diaphragm had to be programmed, being the surface that was formed in both cases, and allowance for the tool top radius had also

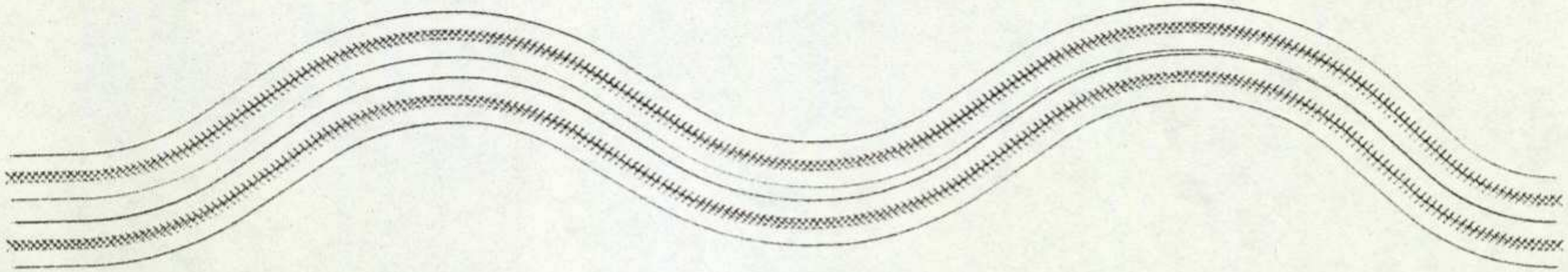

Capsule with working pressure applied in the compressive mode.

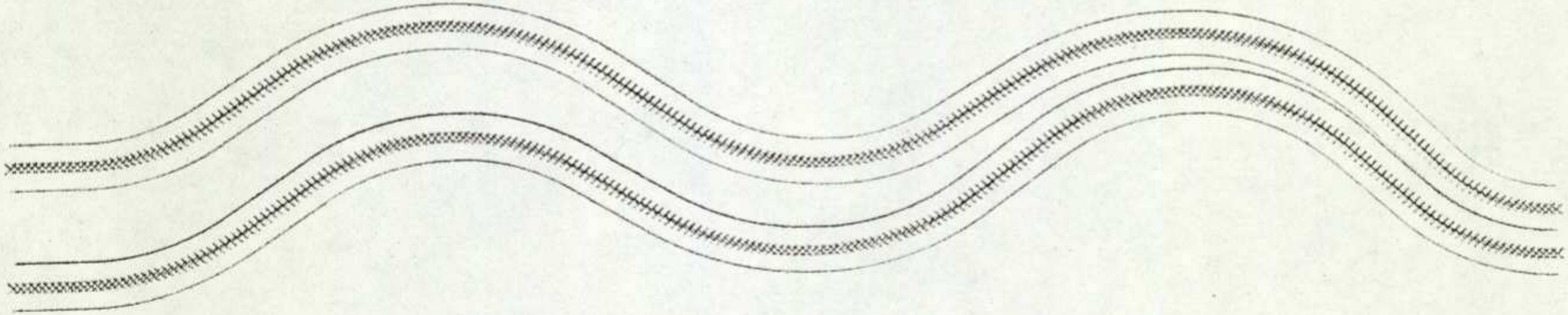

Figure 6.20

First capsule design using the non-linear capsule model computer generated plot 10 times full size.

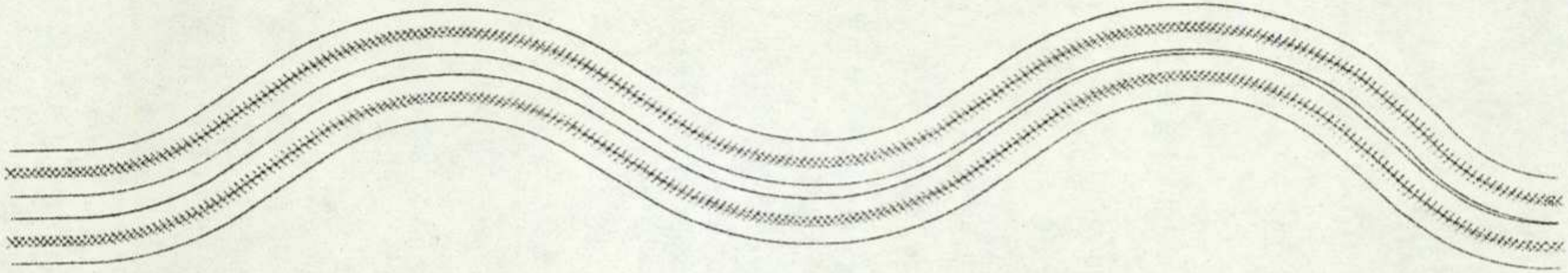

Capsule with working pressure applied in the compressive mode.

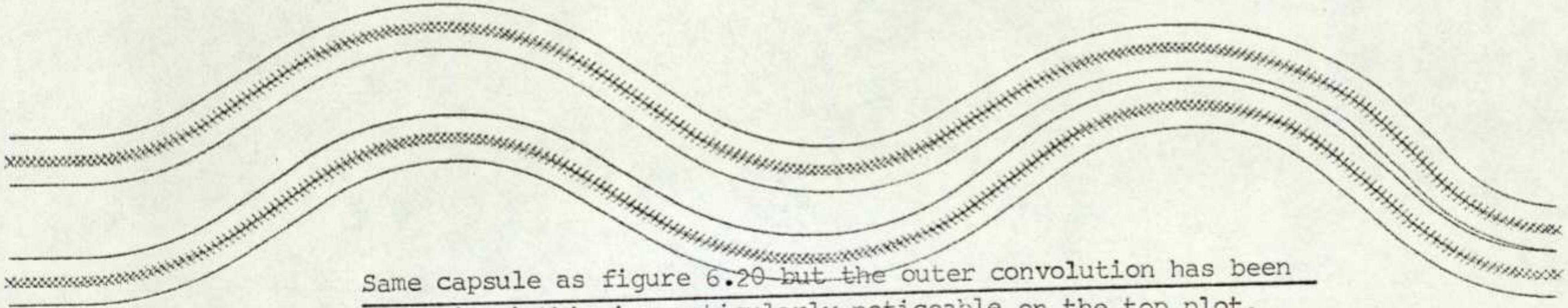

Same capsule as figure 6.20 but the outer convolution has been 'opened up' this is particularly noticeable on the top plot.

Figure 6.21

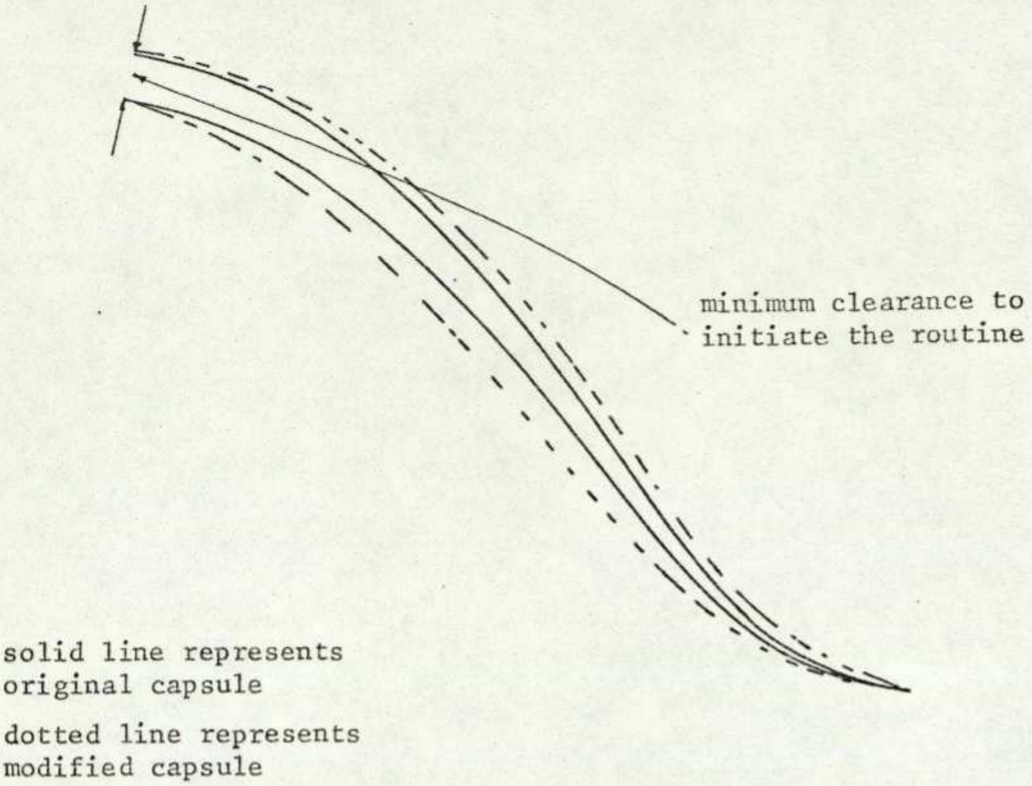

Figure 6.22: Increased clearance

to be incorporated. In most applications involving numerical control work this is a simple allowance calculated by the operator, or even neglected, depending on the size of tool tip and the work piece in question. But as an accurate reproduction of surface was required, therefore this allowance had to be made. Basically the problem is that it is convenient for the machine to assume that the cutting tool is a sharp point, but this is not practical as it would wear off extremely quickly, so the actual tool bit is a small radius and the cutting face a tangent at some point on the circle. For the two diaphragm die tools produced, a 0.020 inch (0.508 mm) radius was used. Figure 6.24 shows the allowance required when cutting a taper on the end of a bar.

To machine the shape indicated by Figures 6.22 and 6.23, assuming there are N, X, Y co-ordinates, requires the machining of N-1 small tapers in a continuous manner. No operator could be expected to make that number of allowances, so a final computer program was written to perform the conversion upon the X, Y co-ordinates for the numerically controlled lathe data. When the two form tools were produced, the profile was magnified twenty-five times and compared with the required form, and no noticeable difference could be detected at that magnification.

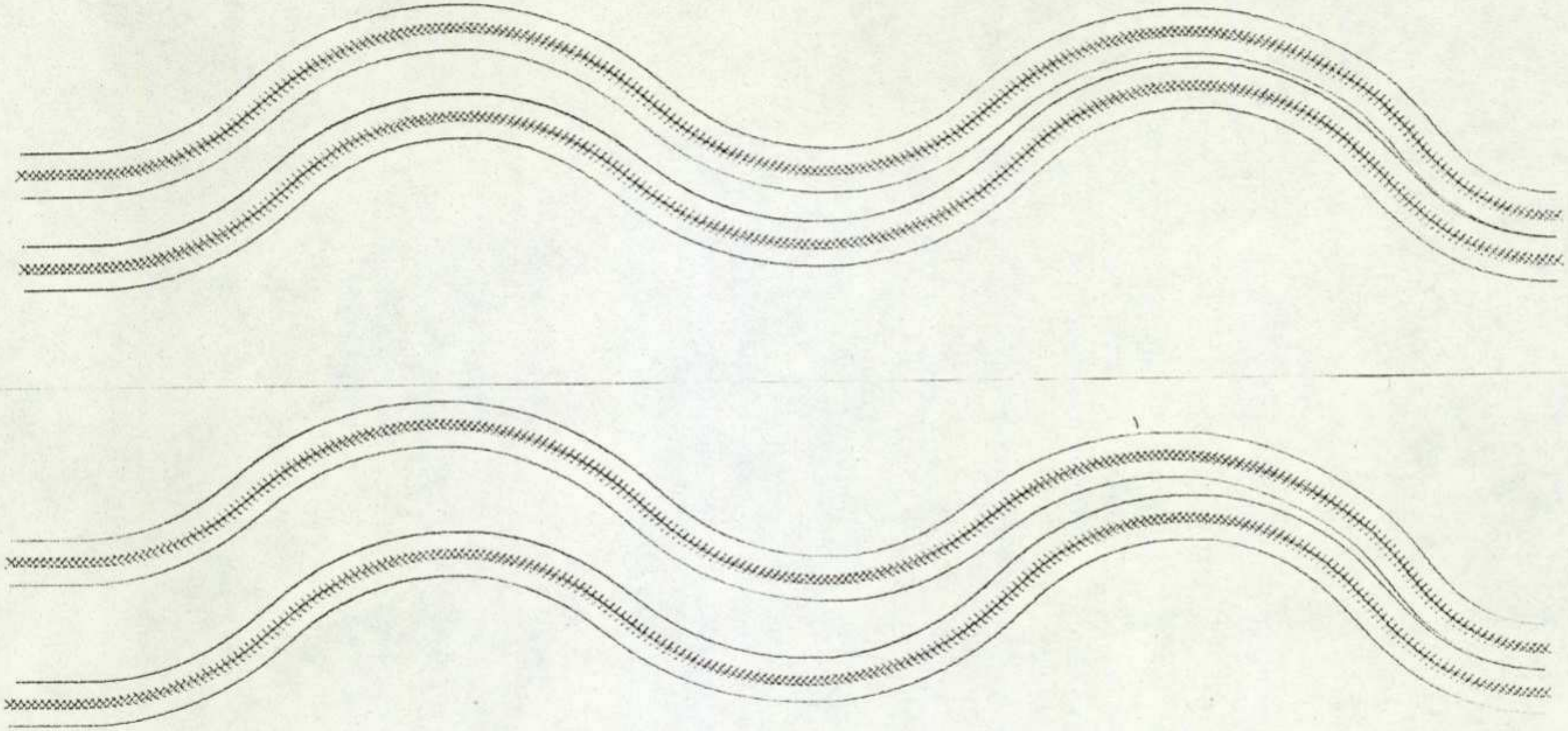

Figure 6.23

Final design for a 100 lbf/in^2 nesting capsule

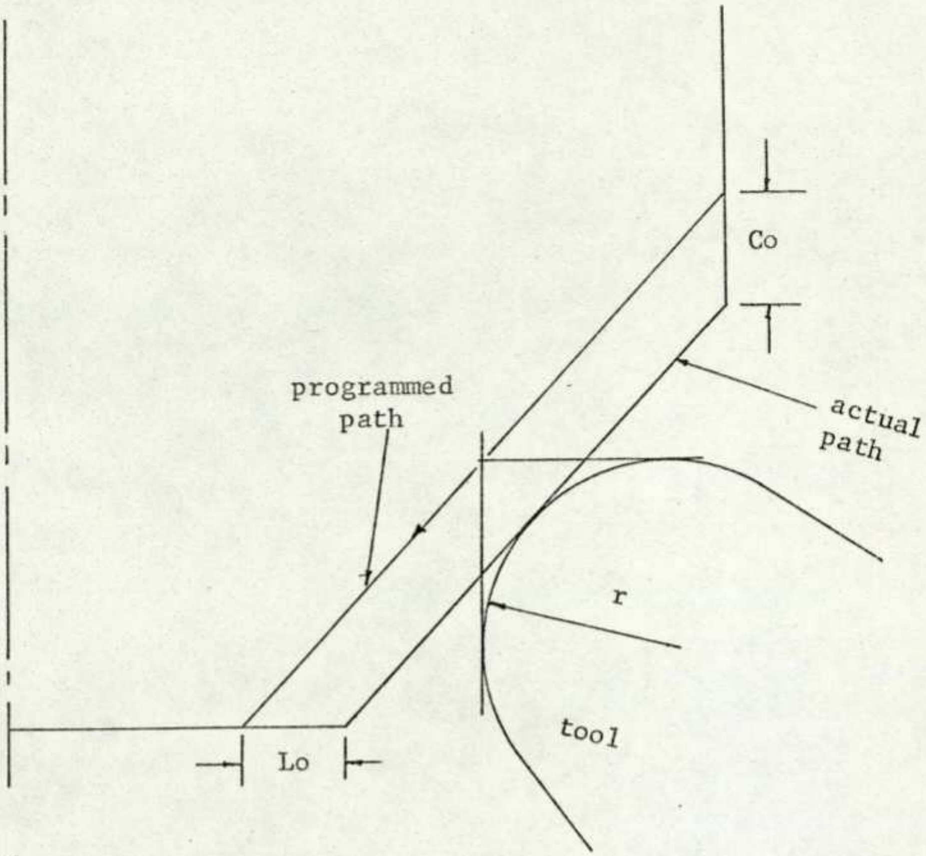

Co = cross offset

Lo = longitudinal offset

Figure 6.24: Taper cutting

Diaphragms made on these tools showed very little spring-off: a maximum of 0.002 inches (0.0508 mm) at the bottom of troughs. A two-stack capsule was made from the diaphragms and tested in compression up to 100 $\mathrm{lbf/in^2}$ (690 KPa). The result of both experimental sensitivity and non-linearity is shown in Figure 6.25, and the sensitivity is compared with the predicted value. The discrepancy in the sensitivity is about 2.6%, an encouraging result, but the non-linearity was not so good: the maximum deviation is over 0.8%, whereas the predicted deviation was -0.313%. The change in sign was to be expected from the results presented in Chapter 4, but not the large absolute value. The capsule had been assembled and tested without the usual manufacturing procedures involved in making capsules of this material and thickness, namely, a re-heat treatment of the weld and a cycling process to stabilise the sensor.

Three more capsule stacks were produced which were re-heated and cycled, two of which were within limits and one which was obviously closing down too soon in compression, which was later shown to be misalignment in the welding process. The results are shown in Table 6.1.

Sensors (1) and (3) were used to make an actual instrument, as both

Figure 6.25

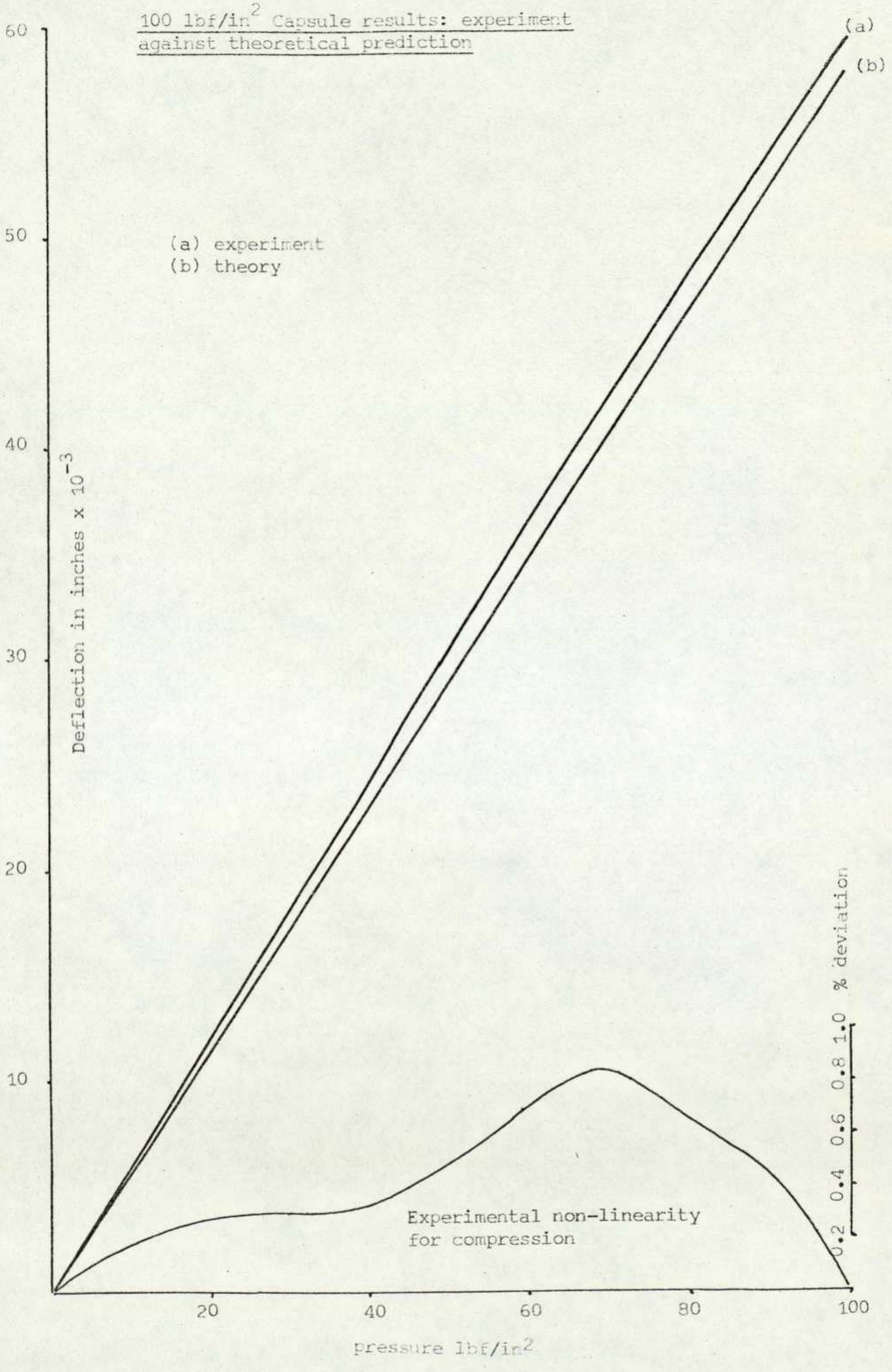

100 lbf/in^2 Capsule results: experiment against theoretical prediction

	Pressure (lbf/in^2)	Deflection extension inches $x 10^{-3}$	Non-linearity deviation %	Deflection compression inches $x 10^{-3}$	Non-linearity deviation %
Capsule stack (1)	0	-	-	-	-
	20	12	0.134	11.95	0.2714
	40	23.85	0.0167	23.75	0.288
	60	35.75	-0.0167	35.65	0.475
	80	47.6	-0.134	47.4	0.407
	100	59.6	-	58.95	-
Capsule stack (2)	0	-	-	-	-
	20	11.85	-0.0	11.75	1.579
	40	23.55	-0.253	23.45	3.067
	60	35.5	-0.0844	34.7	3.728
	80	47.3	-0.164	45.1	2.828
	100	59.25	-	54.45	-
Capsule stack (3)	0	-	-	-	-
	20	11.8	0.017	11.8	-0.017
	40	23.6	0.034	23.7	0.1354
	60	35.4	0.0509	35.5	0.11854
	80	47.2	0.0678	47.25	-0.017
	100	58.95	-	59.05	-

Table 6.1: 100 lbf/in^2 capsule results

the sensitivity and non-linearity were within limits. No trend can be seen from the actual figures for non-linearity as even the sign appears to be inconsistent. A differential pressure transmitter of the type 4000 series was made, and the additional tests for temperature coefficients, reverse overload and zero shift with high static pressure were made. These all gave satisfactory results and it was therefore decided to put this range of sensor into production as part of the standard range of differential pressure transmitters.

6.7 Conclusions

For use in design methodologies a simple but flexible description of a general diaphragm profile is proposed, based on the circle-straight line geometric construction detailed in Chapter 3.

With the aid of the Bode parameter, the sensitivity (centre deflection for a given pressure) of a particular geometric variable can readily be assessed in terms of magnitude and direction. Design procedures can be easily implemented using the linear model and the Bode parameter basically because the model has a fast computer run time. Unfortunately, being able to predict only the sensitivity is of little practical use, and design using the non-linear model is more difficult. There is generally a direct "trade off" situation between sensitivity (which is to be maximised) and non-linearity (which is minimised). A design methodology is proposed using a standard multivariable optimisation routine and is shown to work well for flat circular plate design, but the computer time involved becomes prohibitive when considering design of diaphragms.

The applications of diaphragms other than the usual pressure deflection model are discussed in relation to their input/output characteristics. Section 6.5 illustrates how some of these applications are implemented practically and how the model can be adapted to handle the physical requirements.

The design of a corrugated capsule to perform to a specified pressure-deflection characteristic and non-linearity is described in some detail, including the manufacture of form tools. Thus, this was achieved under the broad heading of a computer-aided design technique and, although in itself it has been successful, it must be compared "cost-wise" with the older established method of empirical design, based to a large extent on trial and error techniques. The costs have been compiled by the manufacturers of the capsules (K.D.G. Instruments, Ltd.) and are based on 1976 figures. These give added justification on a cost effective basis for using a computer-aided design methodology. Below are listed the approximate costs and time required to produce a new nesting capsule for (a) the empirical method and (b) the computer-aided design method:

(a)

1 man-year effort	£ 10,000
Tooling and testing	3,000
Total:	£ 13,000

Time: one year, approximately

(b)

3 months' design effort	£ 2,490
Computing cost	300
Tooling (using N.C. lathe)	100
Testing, 1 man-week effort	200
Total:	£ 3,090

Time: 13 weeks, approximately

7.0 Conclusions

The reasons for undertaking the work presented in this thesis arose mainly from the practical difficulties encountered in designing elastic deformation elements for instrumentation, in particular corrugated diaphragms and capsules, which geometrically are complex, axi-symmetric structures. The demand for high accuracy, accompanied by increased complexity in modern instruments, has meant that design has been largely an expensive and time-consuming process. The author has been able to achieve success in both modelling and design by applying the equations of thin elastic shell theory to the problem, and solving them on a fast digital computer. The important development is the non-linear model: this is adequately illustrated by the industrial design example where the deviation from linearity needed to be much more tightly controlled than the sensitivity. Previous models by Schricker, ref. (13), and Wildhack et al, ref. (11), only gave the linear prediction which has been shown to be of very limited use (Chapter 2).

The models developed, in the form of computer program packages, are extremely flexible in both the profile shapes which can be analysed and types of loading which can be applied (Chapter 3). The extensive validation against experiment shows that the models are accurate (Chapter 4), better than 5 per cent for sensitivity if the assumptions of the thin shell theory are adhered to; the accuracy is then as good as the estimation of the material properties and the interpretation of the geometry. Predictions of the linearity error are entirely adequate, again if the assumptions are adhered to.

With regard to the type and efficiency of the numerical procedures adopted, the finite difference method is far superior to the direct integration method, when program run times are compared. The finite difference method represents a 500:1 saving in time, and even considering the finite element method, which appears to supersede the finite difference method for structural problems, is about fifty times slower. For both alternative techniques mentioned, it has been shown that they are particularly unsuitable for the thin shell problems considered in this thesis.

From the dynamics (Chapter 5) the author has been able to substantiate the work previously done by Alalasundaram, ref. (35), and Franklin, ref. (36), by removing the anomalies which arose with their results. This was achieved by extending the basic Rayleigh principle (which assumes the static deflection shape is approximately the dynamic curve) and working with the actual dynamic shape. This technique gives the value of the first fundamental frequency more precisely and the work was then further extended to apply to Capsule Stacks. The accuracy of the predictions depends upon the accuracy of the static model, but the results are adequate for particular purposes, i.e. better than 10 per cent.

Looking at design aspects (Chapter 6), all the work except the linear prediction is shown to be a man-machine inter-action, a situation which could only be changed if virtually unlimited computer time and storage were available. Fortunately this inter-action has been demonstrated as a practical proposition, with the design of a 100 lbf/in^2 (690 KPa) nesting capsule whose subsequent manufacture demanded a contemporary technology (the use of a Numerically Controlled lathe), and was proved after installation in an instrument to be adequate.

Therefore the successful design of the nesting capsule (section 6.6) may be used to illustrate the potential saving, by comparing the previous empirical method of design with the computer-aided design (CAD) method referred to in Chapter 6 (section 6.7).

It can be seen that CAD cost is less than a quarter,and the time for development also about a quarter, of that required with the empirical method. In addition, the CAD method is capable of producing a perfectly nesting capsule, whereas the empirical method never did.

7.1 Recommendations for future work

The most obvious requirement for future work, which must be realistically tackled, is that of spring-back; this is the unknown amount that the diaphragm will spring away from the forming tool when it is realised from the die (see Chapter 6, section 6.2.5). Theoretically, spring-back in the forming process is a very complicated phenomenon, consisting of three-dimensional bending and stretching, which would involve a major study in the whole mechanics of elasto-plastic metal forming. It is therefore proposed that spring-back may be assessed experimentally, as data is readily available.

It has been stated in the text that finite elements, using the simple one-dimensional "bar-type" element, are not suited to these thin shell problems, but an area where it is seen that they could be usefully applied is in extending the work to include thick shells. These would utilise the two-dimensional curved elements to describe axi-symmetric shells, ref. (24).

Taking a much wider view, software packages or a suite of programs could be developed to cope with design problems which arise generally within the instrument industry. These would be the physical models which exploit the basic principles of physics, like shell theory, and the functional models (see IMEKO paper, appendix V) which rely on prior knowledge of their sub-assembly performance. The two types of model could be assembled to give a complete CAD approach to complex instrument design.

APPENDIX I

The following analysis shows the mathematical derivation of Reissner's linear shell equations formed from the basic equations given in the text.

TO SHOW

$$\beta'' + \frac{(rD/\alpha)'}{(rD/\alpha)}\,\beta' - \left[\left(\frac{r'}{r}\right)^2 - \nu\frac{(rD/\alpha)'}{(rD/\alpha)}\right]\beta + \frac{Z'\psi}{(rD/\alpha)} = \frac{r'}{(rD/\alpha)}\,(rV)$$

given $\alpha Q = -Z'H + r'V$ (3.18)

$$(rM_\xi)' - r'M_\theta - r\alpha Q = 0 \qquad (3.21)$$

$$M_\xi = D(\kappa_\xi + \nu\kappa_\theta) \qquad (3.12c) \qquad \kappa_\xi = \frac{\beta'}{\alpha} \qquad (3.23)$$

$$M_\theta = D(\kappa_\theta + \nu\kappa_\xi) \qquad (3.12d) \qquad \kappa_\theta = \frac{r'}{r}\,\frac{\beta}{\alpha} \qquad (3.24)$$

From (3.18) (3.21)

$$(rM_\xi)' - r'M_\theta + Z'\psi = r'(rV)$$

Substituting

$$(rM_\xi)' - r'D\left[\frac{r'}{r}\,\frac{\beta}{\alpha} + \frac{\nu\beta'}{\alpha}\right] + Z'\psi = r'(rV) \qquad (A1)$$

$$r'M_\xi + M'_\xi r - \left(\frac{Dr}{\alpha}\right)\left[\left(\frac{r'}{r}\right)^2\beta + \nu\frac{r'}{r}\,\beta'\right] + Z'\psi = r'(rV) \qquad (A2)$$

Now taking the first two terms:

$$r'D\left[\frac{\beta}{\alpha} + \frac{\nu r'}{r}\,\frac{\beta}{\alpha}\right] + r\left\{D\left[\frac{\beta'}{\alpha} + \frac{\nu r'}{r}\,\frac{\beta}{\alpha}\right]\right\} \qquad (A3)$$

re-arranging terms for the entire equation.

$$r\left\{D\left[\frac{\beta'}{\alpha} + \frac{\nu r'}{r}\,\frac{\beta}{\alpha}\right]' + D'\left[\frac{\beta'}{\alpha} + \frac{\nu r'}{r}\,\frac{\beta}{\alpha}\right]\right\}$$

$$+ \left(\frac{Dr}{\alpha}\right)\left[\frac{r'\beta'}{r} + \left(\frac{r'}{r}\right)^2\nu\beta\right]$$

$$- \left(\frac{Dr}{\alpha}\right)\left[\left(\frac{r'}{r}\right)^2\beta + \frac{\nu r'\beta'}{r}\right] + Z'\psi = r'(rV) \qquad (A4)$$

considering the first term:-

$$r\left\{D\left[\frac{\alpha\beta'' - \beta'\alpha'}{\alpha^2} + \nu\frac{(r\alpha(r'\beta)' - r'\beta(r\alpha)')}{(r\alpha)^2}\right]\right\}$$

$$rD\left[\frac{\beta''}{\alpha} - \frac{\beta'\alpha'}{\alpha^2} + \nu\,\frac{(r'\beta)'}{r\alpha} - \frac{\nu r'\beta}{(r\alpha)^2}(r\alpha)'\right]$$

$$rD\left[\frac{\beta''}{\alpha} - \frac{\beta'\alpha'}{\alpha^2} + \frac{\nu}{r\alpha}\,(r'\beta' + (r')'\beta) - \frac{\nu r'\beta}{(r\alpha)^2}\,(r'\alpha + \alpha' r)\right]$$

$$\frac{rD}{\alpha}\,\beta'' - \frac{rD}{\alpha^2}\,\beta'\alpha' + \frac{rD}{\alpha}\,\frac{\nu}{r}\,(r'\beta') + \frac{rD\nu}{\alpha r}(r')\beta - \frac{\nu\beta rD}{(r\alpha)^2}\,(\,(r')^2\alpha + \alpha' r r')$$

Now consider the whole equation and collect the terms according to the values of β'', β' and β.

$$\beta'':-\ \frac{rD}{\alpha}$$

$$\beta':-\ -\frac{rD}{\alpha^2}\,\alpha' + \frac{rD}{\alpha}\,\frac{\nu}{r}\,r' + \frac{rD'}{\alpha} + \frac{rD}{\alpha}\,\frac{r'}{r} - \frac{Dr\nu}{\alpha}\,\frac{r'}{r}$$

$$\beta\ :-\ \frac{rD\nu}{\alpha r}\,(r')' + \frac{rD'}{\alpha}\,\nu\,\frac{r'}{r} + \frac{Dr}{\alpha}\left(\frac{r'}{r}\right)^2\nu - \frac{Dr}{\alpha}\left(\frac{r'}{r}\right)^2 - \nu\left(\frac{Dr}{\alpha}\right)\left(\frac{r'}{r}\right)^2 -$$

$$\nu\,\frac{Dr}{\alpha}\,\frac{\alpha'}{\alpha}\,\frac{r'}{r}$$

There is some cancelling of terms to give:-

$$\beta'\left(\frac{rD'}{\alpha} + \frac{r'D}{\alpha} - \frac{rD\alpha'}{\alpha^2}\right) = \beta'\left(\frac{rD}{\alpha}\right)'$$

dividing by $\frac{rD}{\alpha}$ $= \beta'\,\frac{(rD/\alpha)'}{(rD/\alpha)}$

and

$$\beta\left(-\frac{Dr}{\alpha}\left(\frac{r'}{r}\right)^2 + \nu\left[\frac{(r')'D}{\alpha} + \frac{r'D'}{\alpha} - \frac{Dr'\alpha'}{\alpha^2}\right]\right)$$

$$= \beta\left(-\frac{Dr}{\alpha}\left(\frac{r'}{r}\right)^2 + \nu\left(\frac{r'D}{\alpha}\right)'\right) \qquad \text{(A5)}$$

dividing by $\frac{Dr}{\alpha}$ gives :-

$$-\beta\left[\left(\frac{r'}{r}\right)^2 - \nu\frac{(r'D/\alpha)'}{(rD/\alpha)}\right]$$

and the final terms $\frac{Z'\psi}{(Dr/\alpha)}$; $\frac{r'}{(Dr/\alpha)}(rV)$. Therefore

$$\beta'' + \frac{(rD/\alpha)'}{(rD/\alpha)}\beta' - \left[\left(\frac{r'}{r}\right)^2 - \nu\frac{(rD/\alpha)'}{(rD/\alpha)}\right]\beta + \frac{Z'\psi}{(rD/\alpha)} = \frac{r'(rV)}{(rD/\alpha)} \qquad \text{(A6)}$$

TO SHOW

$$\psi'' + \frac{(r/C\alpha)'\psi'}{(r/C\alpha)} - \left[\left(\frac{r'}{r}\right)^2 + \nu\frac{(r'/C\alpha)'}{(r/C\alpha)}\right]\psi - \frac{Z'}{(r/C\alpha)}\beta = \frac{\nu Z'}{r}(rV)'$$

$$- \left[\frac{(r/C\alpha)'}{(r/C\alpha)} + \frac{\nu r'}{r}\right](r\alpha p_H) + \left[\frac{Z'r'}{r^2} + \nu\frac{(Z'/C\alpha)'}{(r/C\alpha)}\right](rV) - (r\alpha p_H)' \qquad \text{(A7)}$$

given

$$\frac{\psi'}{\alpha} + rp_H = N_\theta \quad (3.19) \qquad \frac{\psi}{\alpha}\frac{r'}{r} + \frac{Z}{r\alpha}(rV) = N_\xi \quad (3.17)$$

$$(r\varepsilon_{\theta m})' - r'\varepsilon_{\xi m} = Z'\beta$$

$$C\varepsilon_{\xi m} = N_\xi - \nu N_\theta \quad ; \quad C\varepsilon_{\xi m} = N_\theta - \nu N_\xi \qquad (3.13)$$

from (3.22)

$$r\varepsilon'_{\theta m} + r'(\varepsilon_{\theta m} - \varepsilon_{\xi m}) - Z'\beta = 0 \qquad \text{(A8)}$$

$$r\varepsilon'_{\theta m} + \frac{r'}{C}\left[N_\theta - \nu N_\xi - N_\xi + \nu N_\theta\right] - Z'\beta = 0 \qquad \text{(A9)}$$

Substituting $r\varepsilon'_{\theta m}$ from (3.13) above.

$$r\left[\left(\frac{\psi'}{C\alpha}\right)' + \left(\frac{rp_H}{C}\right)' - \nu\left(\frac{r'\psi}{rC\alpha}\right)' - \left(\frac{Z'\nu(rV)}{rC\alpha}\right)' \right] \tag{A10}$$

Consider the terms containing functions of ψ first:-

$$r\left[\left(\frac{\psi'}{C\alpha}\right)' \right] = r\left[\frac{\psi''}{C\alpha} - \frac{\psi'}{(C\alpha)^2}\,(C\alpha' + C'\alpha) \right]$$

$$= \frac{r}{C\alpha}\left[\psi'' - \psi'\frac{\alpha'}{\alpha} - \psi'\frac{C'}{C} \right]$$

Second term

$$r\nu \left| \frac{r'\psi}{rC\alpha} \right|' = \left| \frac{rC\alpha}{(rC\alpha)^2}(r'\psi)' - \frac{r'\psi}{(rC\alpha)^2}\,(rC\alpha)' \right| r\nu$$

$$r\nu \left[\frac{(r'\psi' + r''\psi)}{rC\alpha} - \frac{r'\psi}{(rC\alpha)^2} \left\{ rC\alpha' + rC'\alpha + r'C\alpha \right\} \right]$$

$$\frac{\nu}{C\alpha}\, r'\psi' + \frac{\nu}{C\alpha}\, r''\psi - \nu \left[\frac{r'\alpha'}{C\alpha^2} + \frac{r'C'}{C^2\alpha} + \frac{(r')^2}{C\alpha r} \right] \tag{A11}$$

Then collecting terms

$$\left(\frac{r}{C\alpha}\right)\psi'' + \left(\frac{r}{C\alpha}\right) \left[\frac{r'}{r}(1 + \nu) - \frac{\alpha'}{\alpha} - \frac{C'}{C} - \nu\left(\frac{r'}{r}\right) \right] \psi' -$$

$$\left(\frac{r}{C\alpha}\right)\left[\left(\frac{r'}{r}\right)^2 + \nu\left(\frac{r''}{r}\right) - \nu\left(\frac{r'}{r}\right) \frac{\alpha'}{\alpha} + \nu\frac{r'}{r}\,\frac{C'}{C} \right] \psi - \frac{Z}{r/C\alpha}\,\beta = \text{Loading terms} \tag{A12}$$

Loading terms on left hand side of equation.

$$\frac{r'}{C}\left[(rp_H) + (rp_H)\nu - \frac{Z}{r\alpha}\,(rV) - \frac{Z}{r\alpha}\,\nu\,(rV) \right] +$$

$$r\left[\left(\frac{rp_H}{C}\right)' - \nu\left(\frac{Z'(rV)}{rC\alpha}\right)' \right] \tag{A13}$$

Second term

$$r\left[\frac{C(rp_H)' - (rp_H)C'}{C^2} - \nu\left\{\frac{(Z'(rV))'\ (C\alpha r) - Z'(rV)\ (C\alpha r)'}{(C\alpha r)^2}\right\}\right]$$

$$= \frac{r}{C\alpha}\left[\alpha(rp_H)' - (r\alpha p_H)\ \frac{C'}{C}\right] - r\nu\left[\frac{(Z'(rV))'}{C\alpha r} - \frac{Z'(rV)}{(C\alpha r)^2}\ (C\alpha r)'\right]$$

Expanding the last part and regrouping

$$-\left(\frac{r}{C\alpha}\right)\nu\left[\frac{Z''}{r}(rV) + \frac{Z'(rV)'}{r}\right] + \left(\frac{r}{C\alpha}\right)\nu\left[\frac{Z'(rV)}{C\alpha r^2}\left\{C'\alpha r + C\alpha' r + C\alpha r'\right\}\right]$$

then

$$\left(-\frac{r}{C\alpha}\right)\nu\left[\frac{Z''}{r}(rV) + \frac{Z'}{r}(rV)'\right] + \left(\frac{r}{C\alpha}\right)\nu\left[\frac{Z}{r}(rV)\frac{C'}{C} + \frac{Z'}{r}(rV)\frac{\alpha'}{\alpha} + \frac{Z}{r^2}(rV)r'\right]$$

Collecting terms of (rV)

$$\left(\frac{r}{C\alpha}\right)\left(\frac{-Z'r'}{r^2}\right) - \left(\frac{r}{C\alpha}\right)\ \frac{Z'r'\nu}{r^2} - \left(\frac{r}{C\alpha}\right)\frac{\nu Z''}{r} + \left(\frac{r}{C\alpha}\right)\nu\left[\frac{Z'}{r}\ \frac{C'}{C} + \frac{Z'}{r}\ \frac{\alpha'}{\alpha} + \frac{Z'r'}{r^2}\right]$$

The second and last terms in the above cancel.

Loading terms on the right hand side of equation.

$$\left(\frac{r}{C\alpha}\right)\left[\frac{Z'r'}{r^2} + \nu\left[\frac{Z''}{r} - \frac{Z'C'}{rC} - \frac{Z'\alpha'}{r\alpha}\right]\right](rV)$$

$$= \left(\frac{r}{C\alpha}\right)\left[\frac{Z'r'}{r^2} + \nu\ \frac{(Z'/C\alpha)'}{(r/C\alpha)}\right]\ (rV) + \nu\ \frac{Z'}{r}\ (rV)'\left(\frac{r}{C\alpha}\right) \tag{A14}$$

Consider now (rp_H) terms

$$-\frac{r'}{C}\left[(rp_H) + (rp_H)\nu\right] - \frac{r}{C\alpha}\left[\alpha(rp_H)' - (r\alpha p_H)\ \frac{C'}{C}\right]$$

$$= -\frac{r}{C\alpha}\left[\frac{r'}{r}\ (r\alpha p_H) - \frac{r'}{r}\ (r\alpha p_H)\nu\right] + \frac{r}{C\alpha}\left[(r\alpha p_H)\ \frac{C'}{C}\right] - \frac{r}{C\alpha}\left[\alpha(rp_H)'\right]$$

$$= \left(-\frac{r}{C\alpha}\right)\ (r\alpha p_H)\ \left[\frac{r'\nu}{r} + \frac{r'}{r} - \frac{C'}{C}\right] - \left(\frac{r}{C\alpha}\right)\ \alpha(rp_H)' \tag{A15}$$

$$= \left(-\frac{r}{C\alpha}\right) \quad r\alpha p_H \left[\frac{r'\nu}{r} + \frac{r'}{r} - \frac{C'}{C} \right] + \alpha(rp_H)'$$

$$\left(-\frac{r}{C\alpha}\right) \left\{ (r\alpha p_H) \left[\frac{r'\nu}{r} + \frac{r'}{r} - \frac{C'}{C} \right] - \frac{\alpha'}{\alpha}(r\alpha p_H) + (\alpha r p_H)' \right\}$$

Multiply by -1 and collect terms

$$\left(\frac{r}{C\alpha}\right) \left[- \left\{ \frac{(r/C\alpha)'}{(r/C\alpha)} + \nu\frac{r'}{r} \right\} (r\alpha p_H) - (r\alpha p_H)' \right] \tag{A16}$$

dividing by (r/Cα) collecting and re-grouping terms in A12

$$\psi'' + \frac{(r/C\alpha)'\psi'}{(r/C\alpha)} - \left[\left(\frac{r'}{r}\right)^2 + \nu\frac{(r'/C\alpha)'}{(r/C\alpha)} \right] \psi - \frac{Z}{(r/C\alpha)}\beta = \text{loading}$$

divide by (r/Cα) in (A14) and (A16) gives finally.

$$\psi'' + \frac{(r/C\alpha)'\psi'}{(r/C\alpha)} - \left[\left(\frac{r'}{r}\right)^2 + \nu\frac{(r'/C\alpha)'}{(r/C\alpha)} \right] \psi - \frac{Z}{(r/C\alpha)}\beta = \nu\frac{Z}{r}(rV)'$$

$$- \left[\frac{(r/C\alpha)'}{(r/C\alpha)} + \nu\frac{r'}{r} \right] (r\alpha p_H) + \left[\frac{Z'r'}{r'} + \nu\frac{(Z'/C\alpha)'}{(r/C\alpha)} \right] (rV)$$

$$- (r\alpha p_H) \tag{A17}$$

APPENDIX II : β, ψ solution algorithm

To find β_i, ψ_i $(i = 2 \;.....\; (N-1))$ form:

$$a_i\beta_{i+1} + b_i\beta_i + c_i\beta_{i-1} + d_i\psi_i = f_i \qquad \ldots\ldots\ldots\ldots\ldots\ldots \qquad (A2.1)$$

$$e_i\psi_{i+1} + g_i\psi_i + h_i\psi_{i-1} + j_i\beta_i = k_i \qquad \ldots\ldots\ldots\ldots\ldots\ldots \qquad (A2.2)$$

knowns are β_1, ψ_1, β_N, ψ_N.

The first equation is then

$$a_2\beta_3 + b_2\beta_2 + c_2\beta_1 + d_2\psi_2 = f_2 \qquad \ldots\ldots\ldots\ldots\ldots\ldots \qquad (A2.3)$$

$$e_2\psi_3 + g_2\psi_2 + h_2\psi_1 + j_2\beta_2 = k_2 \qquad \ldots\ldots\ldots\ldots\ldots\ldots \qquad (A2.4)$$

$$\beta_2 = \left(\frac{f_2 - c_2\beta_1}{b_2}\right) + \left(\frac{-a_2}{b_2}\right)\beta_3 + \left(\frac{-d_2}{b_2}\right)\psi_2 \qquad \ldots\ldots\ldots\ldots \qquad (A2.5)$$

$$\psi_2 = \left(\frac{k_2 - h_2\psi_1}{g_2}\right) + \left(\frac{-e_2}{g_2}\right)\psi_3 + \left(\frac{-j_2}{g_2}\right)\beta_2 \qquad \ldots\ldots\ldots\ldots \qquad (A2.6)$$

Substituting one into the other:

$$\begin{aligned}\beta_2 = {} & \left(\frac{f_2 - c_2\beta_1}{b_2}\right) + \left(\frac{-d_2}{b_2}\right)\left(\frac{k_2 - h_2\psi_1}{g_2}\right) + \left(\frac{-a_2}{b_2}\right)\beta_3 \\ & + \left(\frac{-d_2}{b_2}\right)\left(\frac{-e_2}{g_2}\right)\psi_3 + \left(\frac{d_2}{b_2}\right)\left(\frac{-j_2}{g_2}\right)\beta_2 \qquad \ldots\ldots\ldots\ldots \qquad (A2.7)\end{aligned}$$

$$\begin{aligned}\psi_2 = {} & \left(\frac{k_2 - h_2\psi_1}{g_2}\right) + \left(\frac{-j_2}{g_2}\right)\left(\frac{f_2 - c_2\beta_1}{b_2}\right) + \left(\frac{-e_2}{g_2}\right)\psi_3 \\ & + \left(\frac{-a_2}{b_2}\right)\left(\frac{-j_2}{g_2}\right)\beta_3 + \left(\frac{-j_2}{g_2}\right)\left(\frac{-d_2}{b_2}\right)\psi_2 \qquad \ldots\ldots\ldots\ldots \qquad (A2.8)\end{aligned}$$

therefore, in the form

$$\left.\begin{aligned}\beta_2 &= (BC)_2 + (BB)_2\beta_3 + (BH)_2\psi_3 \\ \psi_2 &= (HC)_2 + (HB)_2\beta_3 + (HH)_2\psi_3\end{aligned}\right\} \qquad \ldots\ldots \qquad (A2.9)$$

$$(BC)_2 = \frac{\left(f_2 - \frac{c_2}{b_2}\beta_1\right) - \left(\frac{d_2}{b_2}\right)\left(\frac{k_2 - h_2\psi_1}{g_2}\right)}{\left\{1 - \left(\frac{d_2}{b_2}\right)\left(\frac{j_2}{g_2}\right)\right\}}$$

Let demon $\equiv 1 - \left(\frac{d_2}{b_2}\right)\left(\frac{j_2}{g_2}\right)$

$$(BB)_2 = \frac{-a_2/b_2}{\text{demon}} \qquad\qquad (BH)_2 = \frac{d_2e_2}{b_2g_2}\Big/\text{demon}$$

$$(HC)_2 = \frac{\left(\frac{k_2 - h_2\psi_1}{g_2}\right) - \left(\frac{j_2}{g_2}\right)\left(\frac{f_2 - c_2\beta_1}{b_2}\right)}{\text{demon}}$$

$$(HB)_2 = \left(\frac{a_2}{b_2}\ \frac{j_2}{g_2}\right) \Big/ \text{demon} \qquad (HH)_2 = \left(\frac{-e_2}{g_2}\right) \Big/ \text{demon}$$

These above six constants then initiate the routine.

Consider the i^{th} equation:

$$\beta_i = \frac{f_i}{b_i} - \frac{c_i}{b_i}\left[(BC)_{i-1} + (HB)_{i-1}\beta_i + (HH)_{i-1}\psi_i \right] + \left(\frac{-a_i}{b_i}\right)\beta_{i+1} + \left(\frac{-d_i}{b_i}\right)\psi_i$$

$$\psi_i = \frac{k_i}{g_i} - \frac{h_i}{g_i}\left[(HC)_{i-1} + (HB)_{i-1}\beta_i + (HH)_{i-1}\psi_i \right] + \left(\frac{-e_i}{g_i}\right)\psi_{i+1} + \left(\frac{-j_i}{g_i}\right)\beta_i$$

$$\beta_i \left(1 + \frac{c_i}{b_i}(BB)_{i-1}\right) = \frac{f_i}{b_i} - \frac{c_i}{b_i}(BC)_{i-1} - \left(\frac{d_i}{b_i} + \frac{c_i}{b_i}(BH)_{i-1}\right)\psi_i - \left(\frac{a_i}{b_i}\right)\beta_{i+1}$$

$$\psi_i \left(1 + \frac{h_i}{g_i}(HH)_{i-1}\right) = \frac{k_i}{g_i} - \frac{h_i}{g_i}(HC)_{i-1} - \left(\frac{j_i}{g_i} + \frac{h_i}{g_i}(HB)_{i-1}\right)\beta_i - \left(\frac{e_i}{g_i}\right)\psi_{i+1}$$

Simplifying the notation to:

$$\beta_i A = B - C\psi_i - D\beta_{i+1}$$

$$\psi_i E = F - G\beta_i - H\psi_{i+1}$$

and getting the equations in the form of (A2.9),
then

$$\beta_i = \frac{\left\{\frac{B}{A} - \frac{CF}{AE}\right\}}{\left(1 - \frac{CG}{AE}\right)} + \left(\frac{-D}{1 - \frac{CG}{AE}}\right)\beta_{i+1} + \left(\frac{\frac{CH}{AE}}{\left(1 - \frac{CG}{AE}\right)}\right)\psi_{i+1}$$

and

$$\psi_i = \frac{\left\{\frac{F}{E} - \frac{BG}{EA}\right\}}{\left(1 - \frac{CG}{AE}\right)} + \left(\frac{\frac{GD}{EA}}{\left(1 - \frac{CG}{AE}\right)}\right)\beta_{i+1} + \left(\frac{-H}{\left(1 - \frac{CG}{AE}\right)}\right)\psi_{i+1}$$

Therefore we have $(BC)_i$ $(BH)_i$ $(BB)_i$ $(HC)_i$ $(HB)_i$ and $(HH)_i$ for every i^{th} point

$$i = (2 \,.....\, N-1).$$

Therefore β_i and ψ_i may be found by an iterative backward substitution in:

$$\beta_j = (BC)_j + (BB)_j \, \beta_{j+1} + (BH)_j \, \psi_{j+1}$$

$$\psi_j = (HC)_j + (HB)_j \, \beta_{j+1} + (HH)_j \, \psi_{j+1}$$

as ψ_N and β_N are known and start the routine.

APPENDIX III

Dynamic Analysis of Capsules using Rayleighs Method

Consider a capsule and a single diaphragm undergoing a static deflection

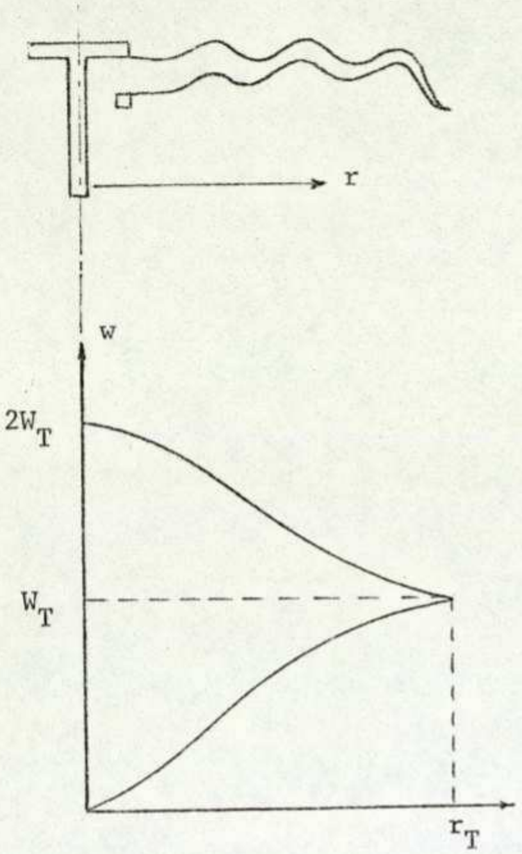

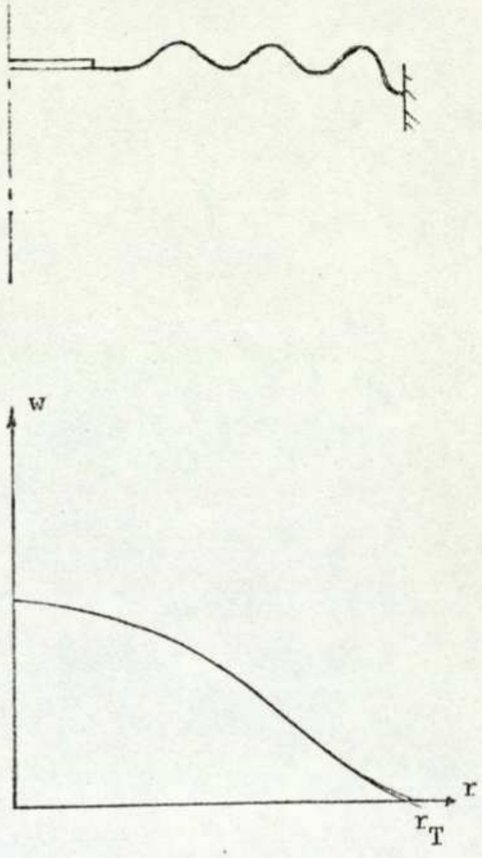

We know that the deflection curve for a circular flat plate clamped at the outer edge deflecting under a uniform pressure takes the form:-

$$w = W_T \quad (1 - \left(\frac{r}{r_T}\right)^2)^2$$

For a corrugated diaphragm the deflection curve is approximately:-

$$w = W_T \; (1 - \left(\frac{r}{r_T}\right)^2)\alpha \qquad \text{where } \alpha \text{ is an unknown index.}$$

For the bottom part of the capsule curve this becomes $w = W_T(1-(1-\left(\frac{r}{r_T}\right)^2)\alpha$

if $\phi(r) = 1 - (1 - \left(\frac{r}{r_T}\right)^2)\alpha$ then $w = W_T \; \phi(r)$ for $r = 0 \to r_T$

$\therefore$ $w = W_T \; (2 - \phi(r))$ for $r = r_T \to 0$ (the top part)

For this analysis material density is represented by ρ and material thickness by h.

The KE for each elemental ring is:- $\frac{1}{2}(\rho h\ 2\pi r\ \delta r)\dot{w}$

$$\therefore \text{ total KE} = \frac{\rho h}{2}\int_0^{r_T} 2\pi r\ \dot{w}_T^2\ \phi^2(r)dr + \frac{\rho h}{2}\int_0^{r_T} 2\pi r\dot{w}_T^2\ (2-\phi(r))^2 dr \quad \text{(A3.1)}$$

$$= \rho h\pi\dot{w}_T^2 \left[\int_0^{r_T} r\phi^2(r)\ dr + \int_0^{r_T} (4 - 4\phi(r) + \phi^2(r))rdr\right]$$

$$= \rho\pi h\dot{w}_T^2 \left[2\int_0^{r_T} r\phi^2(r)dr - 4\int_0^{r_T} r\phi(r)dr + 4\int_0^{r_T} rdr\right]$$

$$= 2\pi\rho h\dot{w}_T^2 \left[r_T^2 + \int_0^{r_T} r\phi^2(r)\ dr - 2\int_0^{r_T} r\phi(r)\ dr\right]$$

from standard form of $\int_0^a x^m(a^n - x^n)^P dx = \int_0^a x^m a^{nP}(1 - \left(\frac{x}{a}\right)^n)^{\ P}\ dx$

$$= \frac{a^{m+1+np}\Gamma\ (m+1)/n\ \ \Gamma(p+1)}{n\ \Gamma\ \left[(m+1)/n + p + 1\right]}$$

now put $m = 1$ $p = \alpha$ $n = 2$

$$a^{2\alpha}\int_0^a x(1 - \left(\frac{x}{a}\right)^2)^\alpha\ dx = a^{2+2\alpha}\ \frac{\Gamma(1)\Gamma\ (\alpha+1)}{2\Gamma\ (2+\alpha)}$$

$$= \frac{a^{2+2\alpha}\Gamma\ (\alpha+1)}{2(1+\alpha)\ \Gamma\ (\alpha+1)}$$

$$\therefore\ 2\pi\rho h\dot{w}_T^2\left[r_T^2 + \int_0^{r_T} r(1-(1-\left(\frac{r}{r_T}\right)^2)^\alpha)^2\ \ dr - 2\int_0^{r_T} r(1-(1-\left(\frac{r}{r_T}\right)^2)^\alpha)dr\right] \quad \text{(i)}$$

$$\text{Now}\quad \int_0^{r_T} r(1-(1-\left(\frac{r}{r_T}\right)^2)^\alpha)^2\ dr = \int_0^{r_T} rdr - 2\int_0^{r_T} r(1-\left(\frac{r}{r_T}\right)^2)^\alpha dr + \int_0^{r_T} r\ (1-\left(\frac{r}{r_T}\right)^2)^{2\alpha}dr$$

$$\text{and}\quad \int_0^{r_T} r(1-(1-\left(\frac{r}{r_T}\right)^2)^\alpha)dr = \int_0^{r_T} rdr - \int_0^{r_T} r(1-\left(\frac{r}{r_T}\right)^2)^\alpha dr$$

$$\text{Then}\quad \int_0^{r_T} r(1-\left(\frac{r}{r_T}\right)^2)^\alpha dr = \frac{1}{r_T^{\ 2\alpha}} \times \frac{r_T^{\ 2+2\alpha}}{2(1+\alpha)} = \frac{r_T^2}{2(1+\alpha)}$$

$$\int_0^{r_T} r(1-\left(\frac{r}{r_T}\right)^2)^{2\alpha}dr = \frac{1}{r_T^{\ 4\alpha}} \times \frac{r_T^{\ 2+4\alpha}}{2(1+2\alpha)} = \frac{r_T^2}{2(1+2\alpha)}$$

.˙. referring to (A3.1) the total K.E. =

$$2\pi\rho h\dot{w}_T^2 \left[r_T^2 + \frac{r_T^2}{2} - \frac{2r_T^2}{2(1+\alpha)} + \frac{r_T^2}{2(1+2\alpha)} - \frac{2r_T}{2} + \frac{2r_T^2}{2(1+\alpha)} \right]$$

$$= \pi\rho h\dot{w}_T^2 r_T^2 \left[\frac{1}{(1+2\alpha)} + 1 \right] = \pi\rho h\dot{w}_T^2 r_T^2 \left[\frac{2(1+\alpha)}{(1+2\alpha)} \right]$$

Now K.E. also $= \frac{1}{2}M_{eq}(2\dot{w}_T)^2$ where M_{eq} = Equivalent Mass

.˙. Equating the two values

$$M_{eq} = \pi\rho h r_T^2 \left[\frac{1+\alpha}{1+2\alpha} \right]$$

Now actual mass (m) not including any addition masses attached at the centre

$$m = 2\pi r_T^2 \rho h$$

.˙. $M_{eq} = \frac{m}{2} \left[\frac{(1+\alpha)}{(1+2\alpha)} \right]$ for a fictitious flat plate capsule $\alpha = 2$

$$.˙.\ M_{eq} = \frac{3m}{10} \qquad \text{(ii)}$$

Calculation of total P.E. of a capsule and hence equivalent stiffness

$$V = \int_0^{W_T}\int_0^{r_T} 2\pi r dr \mid p \mid dw_1 + \int_0^{W_T}\int_0^{r_T} 2\pi r dr |p| dw_2$$

where

$$w_1 = W_T\phi(r) \qquad P = C_p w_T \quad \text{(for a single diaphragm)}$$

$$w_2 = W_T\ (2 - \phi(r))$$

$$V = \int_0^{W_T}\int_0^{r_T} -2\pi r\ dr\ C_p W_T\ \phi(r) dW_T + \int_0^{W_T}\int_0^{r_T} 2\pi r dr C_p W_T\ (2-\phi(r)) dW_T$$

$$V = -\pi W_T^2\ C_p \int_0^{r_T} r dr \phi(r) + \pi W_T^2\ C_p \int_0^{r_T} r(2-\phi(r)) dr$$

$$V = \pi W_T^2\ C_p \left[\int_0^{r_T} 2r dr - 2 \int_0^{r_T} r\phi(r) dr \right]$$

$$V = \pi W_T^2\ C_p \left[\int_0^{r_T} 2r dr - 2 \int_0^{r_T} r(1-(1-\left(\frac{r}{r_T}\right)^2)\alpha) dr \right]$$

$$V = \pi W_T^2\ C_p \left[2 \int_0^{r_T} r(1-\left(\frac{r}{r_T}\right)^2)^{\alpha}\ dr \right] = \pi W_T^2\ C_P \frac{r_T^2}{(1+\alpha)}$$

$$\text{P.E.} = \tfrac{1}{2} K_{eq}\ (2W_T)^2 \equiv \pi W_T^2 \frac{C_p r_T^2}{1+\alpha}$$

for flat plates $\alpha = 2$, $K_{eq} = \frac{\pi C_p\ r_T^2}{6}$

To find the relationship between the natural frequencies of a capsule and a single disc.

If we denote the stiffness of a capsule by $K_{eq}\big|_c$ and a diaphragm by $K_{eq}\big|_d$ then $K_{eq}\big|_c = \frac{\pi C_p\ r_T^2}{6}$ then it is reasonable to assume $K_{eq}\big|_d = 2K_{eq}\big|_c$

also from previous investigations we know $M_{eq}\big|_d = \frac{m}{5}$

$$\therefore\ \omega_n\Big|_d = \frac{\pi C_p r_T^2 5}{3m} = K\ \frac{5}{3}$$

$$\text{and}\ \ \omega_n\Big|_c = \frac{\pi C_p r_T^2 10}{6m3} = K\ \frac{5}{9} = \frac{K}{3}\ \ 5$$

APPENDIX IV: Constrained Rosenbrock Algorithm, ref. (41)

Purpose

The program finds the maximum or minimum of a multivariable non-linear function subject to non-linear inequality constraints:

optimize $F(X_1, X_2, \ldots\ldots X_n)$

subject to $G_K \leqslant X_K \leqslant H_K$, $K = 1, 2, \ldots\ldots M$.

The implicit variables $X_{N+1}, \ldots\ldots X_M$ are dependent functions of the explicit independent variables $X_1, X_2, \ldots\ldots X_N$. The upper and lower constraints H_K and G_K are either constraints or functions of the independent variables.

Method

This method is a sequential search technique which has proven effective in solving some problems where the variables are constrained. The algorithm proceeds per the unconstrained Rosenbrock procedure, ref. (41), until convergence is reached or a boundary zone in the vicinity of the constraints is entered. The boundary zones are defined as follows:

Lower Zone: $G_K \leqslant X_K \leqslant (G_K + (H_K - G_K).10^{-4})$

Upper Zone: $H_K \geqslant X_K \geqslant (H_K - (H_K - G_K).10^{-4})$

$K = 1, 2, \ldots\ldots M$

The procedure requires a starting point that satisfies the constraints and does not lie in the boundary zones. The search computations are then the same as those for the unconstrained case, except that after each function evaluation, the following steps are carried out:

(1) Define by F^o the current best objective function value for a point where the constraints are satisfied, and F^* the current best objective function value for a point where the constraints are satisfied and, in addition, the boundary zones are not violated. F^o and F^* are initially set equal to the objective function value at the starting point.

(2) If the current point objective function evaluation, F, is worse than F^o, or if the constraints are violated, the trial is a failure and the unconstrained procedure is continued.

Flow Diagram of Rosenbrock's Search

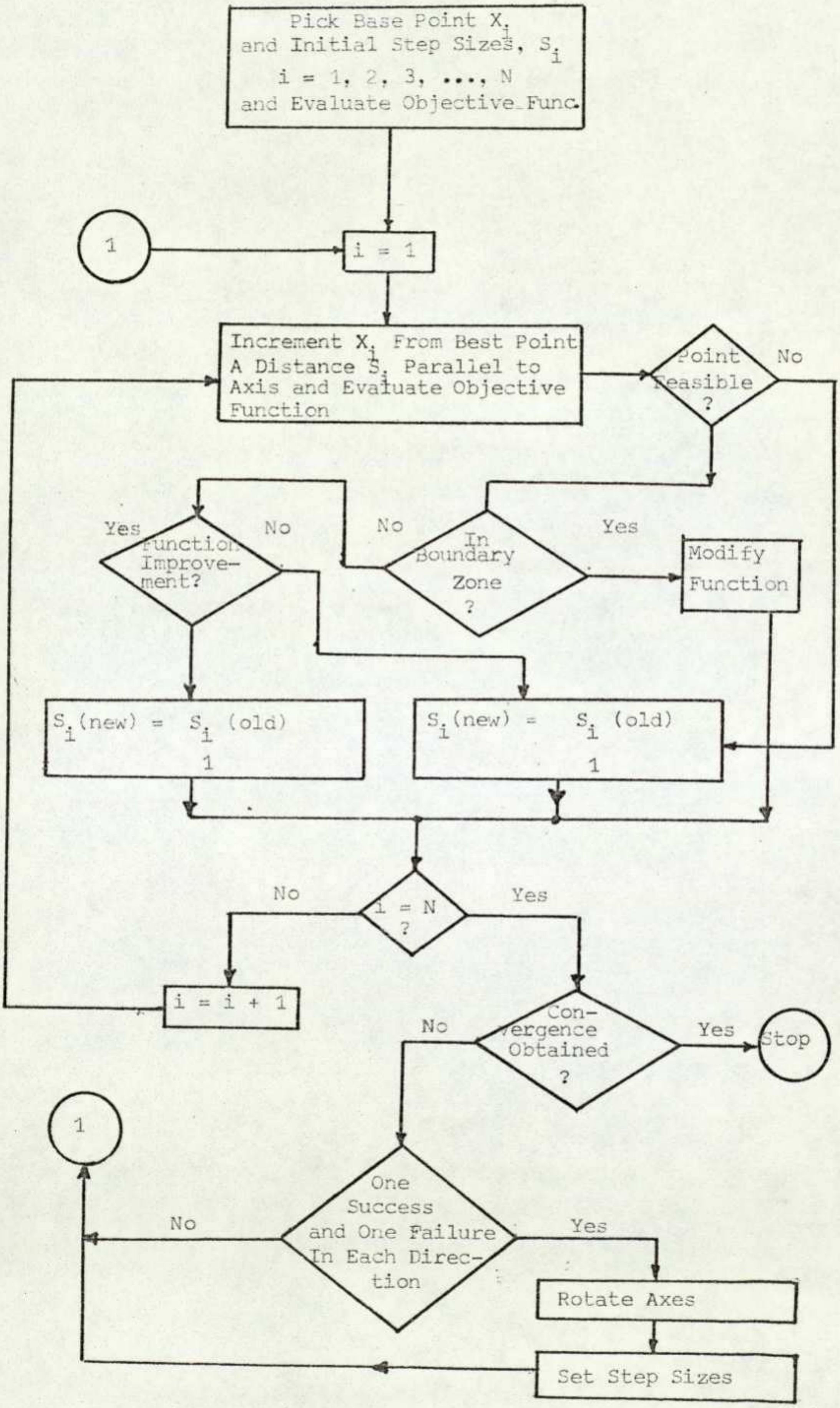

(3) If the current point lies within a boundary zone, the objective function is modified as follows:

$$F(\text{new}) = F(\text{old}) - \left(F(\text{old}) - F^*)(3\lambda - 4\lambda^2 + 2\lambda^3\right),$$

$$\text{where} \quad \lambda = \frac{\text{distance into boundary zone}}{\text{width of boundary zone}}$$

$$= \frac{G_K + (H_K - G_K).10^{-4} - X_K}{(H_K - G_K).10^{-4}} \quad \text{(lower zone)}$$

$$= \frac{X_K - \left(H_K - (H_K - G_K).10^{-4}\right)}{(H_K - G_K).10^{-4}} \quad \text{(upper zone)}$$

At the inner edge of the boundary zone, $\lambda = 0$, i.e. the function is unaltered ($F(\text{new}) = F(\text{old})$). At the constraint, $\lambda = 1$, and thus $F(\text{new}) = F^*$. Thus the function value is replaced by the best current function value in the feasible region and not in a boundary zone. For a function which improves as the constraint is approached, the modified function has an optimum in the boundary zone.

(4) If an improvement in the objective function has been obtained without violating the boundary zones or constraints, F* is set equal to F^o and the procedure continued.

(5) The search procedure is terminated when the convergence criterion is satisfied.

APPENDIX V:

PRACTICAL MEASUREMENT FOR IMPROVING EFFICIENCY

IMEKO VII CONGRESS, 1976

(Organised by the Institute of Measurement and
Control, London, on behalf of the
International Measurement Confederation)

'Mathematical modelling for the evaluation and design of instruments' by Dr. F. Abdullah, A. J. Turley, Prof. L. Finkelstein, presented at VII IMEKO World Congress, London, 10-14 May, 1976, and published in Proceedings.

REFERENCES

1 Zographos, M. "Investigation into the feasibility and use of mathematical models in the design of industrial instruments". Ph.D. Report, June, 1973, The City University, London

2 Koenig, H. E. & Blackwell, W. A. "Electro-mechanical systems theory" McGraw Hill, 1961

3 Rajanna, D., Srindthkumar, S. & Pidmanabha Rao, D. S. "Pressure sensing diaphragms" National Aeronautical Laboratory, Bangalore, Technical Memorandum TM-PR/6202/70

4 Brombacher, W. G. & Jenny, C. V. "Some factors affecting the performance of corrugated diaphragm capsules having a deflection non-linear with pressure" ASME Paper 58.A.169

5 Kandel, A. V. & Whitten, D. C. "Corrugated metal diaphragm performance" A report by The Bristol Company, No. 3102-55

6 Grove, H. J. & Bell, J. C. "Some evaluation of stresses in aneroid capsules" Proceedings of the Society of Experimental Stress Analysis, Vol. 5, 1948, p. 125

7 Rubin, C. "Optimum design of a corrugated diaphragm clamped to a shaft undergoing axial or angular displacement" ASME Journal of Engineering Materials and Technology, Oct., 1975, pp. 363-366

8 Haringx, J. A. "The rigidity of corrugated diaphragms" Applied Scientific Research, The Netherlands, Vol. 2, Sec. A, 1950

Haringx, J. A. "Non-linearity of corrugated diaphragms" Applied Science, Section A, Vol. 6, 1956

9 Haringx, J. A. "Design of corrugated diaphragms" Trans. ASME, Jan., 1957, pp. 55-64

10 Andreeva, L. E. "Elastic elements of instruments" The Israel Programme for Scientific Translation, Ltd., 1966

11 Wildhack, W. A., Dressler, R. F. & Lloyd, E. C. "Investigations of the properties of corrugated diaphragms" Trans. ASME, Vol. 79, 1957, pp. 65-82

12 Dressler, R. F. "Bending and stretching of corrugated diaphragms" ASME Journal of Basic Engineering, Series D.81, pp. 651-657

13 Schricker, H. "An investigation into properties of circular diaphragms used in differential pressure cells" M.Phil. Thesis, 1972, The City University, London

14 Wildhack, W. A. & Goerke, V. H. "Corrugated metal diaphragms for aircraft pressure measuring instruments" NACA Tech. Note No. 738, 1939

15 Meissner, E. "Das Elastizitäts problem fur dünne Schalen von Ringflüchen-, Klugel-, und Kegel-form" Physik. Zeit, 14, 343-349 (1913)

Reissner, H. "Spannungen in Kugelschalen" Müller-Breslau Festschrift, Leipzig Kröner (1912), pp. 181-193

16 Penny, R. K. "Symmetric bending of the general shell of revolution by finite difference methods" Journal of Mechanical Eng. Sci., Vol. 3, No. 4, 1961, p. 369

17 Kraus, H. "Thin Elastic shells" John Wiley & Sons, Lib Con. Cat. No. 67-23328

18 Payne, D. J. "Numerical analysis of axisymmetric bending of a toroidal shell", Journal of Mech. Eng. Sci., Vol. 4, No. 4, 1962, p. 356

19 Abdullah, F. "Computer analysis of the linear and non-linear behaviour of thin elastic shells" Instrument Systems Centre report, March, 1974

20 Kalnins, A. & Lesbingi, J. F. "On the non-linear analysis of elastic shells of revolution" ASME Journal of Applied Mechanics, March, 1967, pp. 59-64

21 Love, A. E. S. "A treatise on the mathematical theory of elasticity" 4th ed., New York; Gover Publications, 1944, Ch. 24

22 Goldenveiser, A. L. "Theory of thin elastic shells", New York, Pergamon Press, 1961

23 Soare, Mirea "Application of finite difference equations to shell analysis" Pergamon Press

24 Zienkiewicz, O. C. "The finite element method in engineering science" 2nd ed., McGraw-Hill, London 1967

25 Flügge, W. "Statik und Dynamik der Schalen" Berlin, Julius Springer Verlag (1934)

26 Reissner, E. "On the theory of thin elastic shells", H. Reissner Anniversary Volume, J. W. Edwards, Ann Arbor, Mich., 1949

27 Billington, D. P. "Note on the finite symmetrical deflections of thin shells of revolution", ASME Series "E", Sept., 1967, pp. 763-4

28 Reissner, E. "On the equations for finite symmetrical deflections of thin shells of revolution", Progress in Applied Mechanics (Prager Anniversary Volume), 1963, pp. 171-178

29 Thurston, G. A. "A numerical solution of the non-linear equations for shells of revolution", J. of Mathematics and Physics, Vol. 4, 1962

30 Inconel Alloy X-750 Huntington Alloy Products Division, The International Nickel Co., Inc., Huntington, West Virginia 25720

31 Ryder, G. H. "Strength of materials", Third ed. enlarged, Cleaver-Hulme Press, Ltd., London

32 Neubert, H. K. P. "Instrument transducers", 2nd ed., Oxford University Press, 1976

33 Nutbourne, A. W., McLellan, P. M. & Kensit, R. M. "Curvature profiles for plane curves", Computer-Aided Design, July, 1972, pp. 176-184

34 Abdullah, F. "Field modelling of a linear variable differential transformer", Instrument Systems Centre report, The City University, London, 1975

35 Alalasundaram, S. "Dynamic characteristics of corrugated diaphragms", October, 1973, M.Sc. report, The City University, London

36 Franklin, N. "The dynamics of corrugated diaphragms", October, 1974, M.Sc. report, The City University, London

37 Thomson, W. T. "Vibration theory and applications", George Allen & Unwin, Ltd., 1966

38 Karnapp, D. & Rosenberg, R. C. "Analysis and simulation of multiport systems. The Bond Graph approach to physical systems dynamics", The M.I.T. Press, 1968

39 Hunt, K. "Electroacoustics", John Wiley & Sons, Inc., 1954

40 Siddall, James N. "Analytical decision-making in engineering design",
1972, Prentice-Hall, Inc., Englewoods Cliffs, New Jersey. Library of Congress Cat. Card No. 79-38246

41 Constrained Rosenbrock (Hill algorithm), reproduced from Optimization Techniques with Fortran, ed. James Kuester, Joc. H. Mize,
McGraw-Hill Book Company, 1973.

Computer Code developed by C. B. Yancey and R. C. Spear, Naval Weapons Centre, China Lake, California, used by permission.

The procedure is based on the automatic method proposed by H. H. Rosenbrock (41, 42) refs. in Optimization Techniques with Fortran:

41 Rosenbrock, H. H. "An Automatic Method for Finding the Greatest or Least Value of a Function", Computer J., 3, 175-184, 1966

42 Rosenbrock, H. H. & Storey, C. "Computational Techniques for Chemical Engineers",
Pergamon Press, New York, 1966

42 Gardiner, F. J. "The spring back of metals",
ASME Trans. 79, Jan., 1957, p. 55

43 Newell, F. B. "Diaphragm characteristics",
ASME, 1958